THE UNIVERSITY OF CHICAGO

IRON ISOTOPE TRACING OF PLANETARY SURFACE PROCESSES AND RUBIDIUM ISOTOPE TRACING OF VOLATILE ELEMENT DEPLETION PROCESSES

A DISSERTATION SUBMITTED TO

THE FACULTY OF THE DIVISION OF THE PHYSICAL SCIENCES

IN CANDIDACY FOR THE DEGREE OF

DOCTOR OF PHILOSOPHY

DEPARTMENT OF THE GEOPHYSICAL SCIENCES

BY

XIKE NIE

CHICAGO, ILLINOIS

AUGUST 2019

TABLE OF CONTENTS

LIST OF FIGURES

LIST OF TABLES

ACKNOWLEDGEMENTS

I am greatly indebted to many people along the journey of my Ph.D. Everything I have accomplished would not have been possible without their help, and I would like to thank them here.

First and foremost, I would like to express my deepest appreciation to my advisor, Nicolas Dauphas, without whom the thesis and all my Ph.D. research would not have been achievable. I am extremely grateful for all his contributions of time, funding and ideas to make my Ph.D. truly beneficial. For his enthusiasm in exploring new things and his extensive knowledge of the field, for his patience in guiding and helping me work through problems, for his resolve during tough times, for his constant support of my work, and for everything I have learned from him.

I would like to extend my sincere thanks to the members of my committee: Andrew Campbell, Andrew Davis, Frank Richter and Jacob Waldbauer, for their valuable guidance, insightful comments and all the helpful discussions, and for the knowledge I gained from their specialties which leads me to diverse exciting projects.

I would like to also acknowledge the help from other professors and staff scientists: Alfred Anderson, Robert Clayton, Philipp Heck, Fred Ciesla, Ruslan Mendybaev and Gerard Olack, for their great patience in explaining while introducing new concepts to me and for their generosity in providing natural and synthetic samples.

Many people around me truly deserve my genuine gratitude. My dear former and current colleagues at the Origins Lab: Christoph Burkhardt, Nicolas Greber, Haolan Tang, Corliss Sio, Francois Tissot, Sarah Aarons, Justin Hu, Cindy Chen, Andrew Heard, Hao Zeng, Matous Ptacek and James Zhang, are really appreciated for making my daily life at work particularly enjoyable,

for their kind help and encouragement during failures, for the useful and stimulating discussions on experiments and for the indispensable snacks in late lab afternoons and evenings.

Special thanks to the CHILI group fellow students: Nan Liu, Levke Koop, Krysten Villalon and Jennika Greer, for their help with experiments and for the wonderful time I spent with them during and after work.

The previous and current administrative staff: Brian Lynch, David Taylor, Katie Casey, Thomas Indelli, James Eason, Susan Hubbard, Jolene Hanchar, Victor Gavin, Thomas Cortellesi are appreciated, for their continued assistance in administrative affairs and for making it easier to focus on research.

Many thanks should also go to my friends outside the department who have backed me up so greatly. Ying Bao, Jinyue Pu, Yin Wu, Jian Yang and Zhixuan Zhou are thanked for making the experience at the University of Chicago particularly worthwhile and enjoyable. I am also very grateful to Liuqin Huang and Zhimin Chen, for their longtime friendship throughout many years.

I would not have been able to pursue my dream and follow my path without the unconditional love, care and support from my parents, my grandparents, my little sister and brother. I would like to say a heartfelt thank you to them. And finally, my deep gratitude to Shuaiyi, my fiancé and my closest friend, for being supportive in all my pursuits, for always believing in me and always being there for me.

ABSTRACT

Stable isotopes are very versatile and effective in tracing geological and geochemical processes. This dissertation uses stable Fe isotopes to trace Fe oxidation and transport on planetary surfaces and uses stable Rb isotopes to trace the depletion of moderately volatile elements in planetary bodies.

The iron UV photo-oxidation process is studied by performing lab UV photo-oxidation experiments and analyzing Fe isotopes in the lab-derived samples and natural banded iron formation samples. It will be demonstrated that this process is a highly possible Fe oxidation mechanism to precipitate banded iron formations and martian hematite spherules (also known as martian "blueberries"). Hematite spherule samples collected in Hawaii are an ideal terrestrial analogue of martian hematite spherules. Here they are studied for their Fe isotopes to investigate their detailed formation history, providing insights into the formation of these enigmatic martian hematite spherules (Chapter 2).

This dissertation also presents a new Rb purification and isotope measurement method that has been developed over the past three years. Rubidium is a new isotopic tracer, and studies on Rb isotopes are very limited due to the difficulty of these measurements. The outlined procedure is capable of achieving high-precision Rb isotopic analyses of even Rb-depleted samples. By performing high-precision Rb isotopic analyses of terrestrial, lunar, martian, and chondrite samples, it will be shown that the depletion of moderately volatile elements in the Moon is related to the status of the protolunar disk after the Moon-forming giant impact. The heavy Rb isotopic composition of the bulk Moon relative to the Earth argues against models of partial condensation as the cause for lunar volatile element depletion. In contrast, a protolunar disk with a vapor layer, which transports volatile elements towards the Earth and is replenished by the underlying magma

layer, can quantitatively explain the moderately volatile element depletion and isotope fractionation of the Moon (Chapter 3).

1 INTRODUCTION

1.1 Objectives

The discovery of the deuterium by H. Urey and of the general occurrence of isotopes of elements in 1930s resulted in numerous studies on the properties of isotopes. Pioneer work on the theory of equilibrium isotope fractionation by Urey, Bigeleisen and Mayer paved the way for the stable isotope geochemistry (Bigeleisen and Mayer, 1947; Urey, 1947). Traditionally, only light elements such as H, O, N, C and S were considered to have measurable isotopic variations. However, as the high-precision isotope measurements became achievable with the invention of the high-resolution Multicollector Inductively Coupled Plasma Mass Spectrometry (MC-ICPMS) in the mid-1990s, more and more nontraditional elements are becoming of great interest and are being explored for their isotopic fractionations in geological systems (Teng et al., 2017).

Stable isotopes of nontraditional elements have great potential in tracing geological processes. Although the isotopic variations of heavy metals are in general small, in per mil (‰) level, these variations allow us to draw important conclusions on questions in geochemistry and cosmochemistry. The aim of this thesis is to study several important processes that occurred in early solar system history, by using nontraditional stable isotopes, and by developing new stable isotope tracers. Stable isotope tracers used in this thesis include iron (Fe) isotopes and rubidium (Rb) isotopes. Specifically, the precipitation mechanisms of banded iron formations on early Earth and of the hematite spherules on early Mars (also dubbed “martian blueberries”) have been investigated using Fe isotopes, and the volatile element depletion of the Moon has been investigated using Rb isotopes. The questions answered in this thesis are as follows:

1) Can Fe UV photo-oxidation explain the precipitation of banded iron formations (BIFs)? This question is important because UV photo-oxidation is the only mechanism that does not involve life among the three mechanisms that have been proposed for BIF formation, and no definitive evidence has been found of the existence of life in the early Archean when the first BIFs were precipitated. To answer this question, lab Fe UV photo-oxidation experiments were conducted, and Fe isotopes were used to investigate the process to see if the isotope signatures during UV photo-oxidation are consistent with that of the BIFs.
2) Can Fe UV photo-oxidation explain the precipitation of martian hematite spherules? On ancient Mars, where the oxygen level was not sufficient to oxidize large amounts of Fe, photo-oxidation might have been played an important role in converting ferrous Fe [Fe(II)] to ferric Fe [Fe(III)]. This work evaluated the efficiency of UV photo-oxidation in oxidizing Fe(II) under martian conditions by constructing a more elaborate model than those in previous work and using more realistic parameters.
3) If Fe oxidation on Mars can be done through UV photo-oxidation, what are the detailed steps of hematite spherule formation? This work investigated Fe isotopes of hematite spherules and associated lithologies from Hawaii, a terrestrial analogue of martian hematite spherules, to trace the detailed spherule formation process such as rock alteration, Fe transport and hematite precipitation.
4) Why is the Moon depleted in moderately volatile elements? One of the distinguishing features of the Moon is that it is depleted in volatile elements relative to the Earth, despite of its similar concentrations in terms of refractory elements. Rb is a moderately volatile element, sensitive to volatilization processes, and its isotopic composition in the Moon contains information on the processes that have caused this depletion. Since Rb isotope

measurement method was not available before this study, a new Rb purification and isotope measurement method was developed. Rubidium isotopic compositions of terrestrial and lunar rocks are measured and volatile loss after the giant impact was constrained.

1.2 Principles of stable isotope fractionation

Isotopes are variants of an element with same numbers of protons but different numbers of neutrons, and consequently different atomic masses. All elements have more than one isotope, either stable or unstable. Unstable isotopes are radioactive and some are critical for geochronology. Since the decay rate of a radioactive isotope is a constant, by determining the number of decayed atoms the temporal information can be retrieved. Here we are more concerned with stable isotopes, *i.e.*, nonradioactive isotopes, and radioactive isotopes with extremely long half-lives that can be considered to be stable over a certain time period.

Partitioning of isotopes between two phases is called isotope fractionation (or isotopic fractionation). Isotope fractionation results in isotopic variations among solar system materials. Most isotopic variations follow clear sets of rules, and they are associated with mass-dependent isotope fractionation, meaning that the extent of isotope fractionation is dependent on the mass differences of the isotopes involved. However, there are some known processes that can cause isotope fractionation deviating from the mass-dependent fractionation (*e.g.,* Dauphas and Schauble, 2016). This type of fractionation is referred to as mass-independent isotope fractionation or as isotopic anomalies. For example, the radioactive decay of an element to its daughter element will cause the isotopic composition of the daughter element to change, which scales with the ratio of the parent/daughter isotopes rather than with the masses of the isotopes. Another example is that stable oxygen isotopic compositions of various chondrites and the calcium-aluminum inclusions (CAIs) within the chondrites do not follow mass-dependent fractionation. In these

samples, the mass-independent fractionation was found to originate from isotope-selective self-shielding during ultraviolet (UV) photolysis of CO in the early solar nebula (Clayton, 2002; Lyons and Young, 2005; Yurimoto and Kuramoto, 2004). Mass-independent isotopic anomalies can provide us with information on the compositions of source materials. If substances are derived from the same source reservoir, they will have the same isotopic anomaly (*e.g.*, Clayton, 2002; Zhang et al., 2012).

1.2.1 Notations and definitions

The isotopic composition of an element (E) is often expressed as the abundance ratio of two isotopes i and j,

$$R^{i/j} = E^i/E^j, \tag{1.1}$$

where the numerator and the denominator are the heavy and light isotopes, respectively. Due to the vary small isotopic variations in nature for nontraditional stable isotopes, isotopic compositions are often reported using δ–notation, which is the per mil (‰) departure of the isotopic ratio of a sample from that of a standard,

$$\delta^{i/j} = (R^{i/j}_{sample}/ R^{i/j}_{standard} - 1) \times 1000. \tag{1.2}$$

If considering isotope partitioning between two phases A and B, the isotope fractionation between the two phases is characterized using fractionation factor α, which is defined as

$$\alpha^{i/j}_{A\text{-}B} = R^{i/j}_A/ R^{i/j}_B = (E^i/E^j)_A/(E^i/E^j)_B. \tag{1.3}$$

The isotopic difference Δ between the two phases A and B is often reported as

$$\Delta^{i/j}_{A\text{-}B} = \delta^{i/j}_A - \delta^{i/j}_B. \tag{1.4}$$

The isotopic difference Δ is thus related to isotope fractionation factor α, by the equation

$$\Delta^{i/j}_{A\text{-}B} \approx 1000 \ln\alpha \approx 1000 (\alpha - 1), \tag{1.5}$$

since $\ln x \approx x-1$ when x approaches 1.

1.2.2 Equilibrium isotope fractionation

Mass-dependent isotope fractionation can be divided into two categories: equilibrium and kinetic isotope fractionation. Equilibrium isotope fractionation arises mainly from the differences in the vibrational frequency of a species when one isotope is substituted for another one, and can this be predicted using quantum mechanics (Urey, 1947).

For an isotope exchange reaction

$$aA_j + bB_i = aA_i + bB_j, \quad (1.6)$$

where A and B are two different molecules and A_i and A_j are two molecules of the same elemental composition with different isotopic composition. The equilibrium fractionation factor α is related to the equilibrium constant K_{eq}, by

$$\alpha^{i/j}_{A\text{-}B} = K_{eq}\ \{[\sigma(A_i)/\sigma(A_j)]^{(1/a)}/[\sigma(B_i)/\sigma(B_j)]^{(1/b)}\}, \quad (1.7)$$

where σ is the molecular symmetry number (Schauble, 2004). Heteronuclear diatomic molecules have a symmetry number $\sigma=1$, while homonuclear diatomic molecules have a symmetry number $\sigma=2$. Equilibrium constant K_{eq} is closely related to the Gibbs free energy (ΔG) of the reaction

$$\Delta G = -RT \ln K_{eq}, \quad (1.8)$$

where R is the molar gas constant (~8.314 J mol K^{-1}) and T is the absolute temperature. A similar equation for Helmholtz free energy and the partition function Q can also be written

$$A = -RT \ln Q, \quad (1.9)$$

where A is the Helmholtz free energy. The partition function Q is the total energy of a system summing over all its possible microstates. Isotope exchange reactions do not change the bond structure or the potential energy of each molecule, and do not involve pressure (p)-volume (V) work. Because $G = A + pV$, for negligible volume change we have

$$\Delta G \approx \Delta A. \tag{1.10}$$

Therefore,

$$\begin{aligned} K_{eq} = Q_{products}/Q_{reactants} &= \{[Q(A_i)]^a\,[Q(B_j)]^b\}/\{[Q(A_j)]^a\,[Q(B_i)]^b\} \\ &= \{[Q(A_i)]/[Q(A_j)]\}^a/\{[Q(B_i)]/[Q(B_j)]\}^b. \end{aligned} \tag{1.11}$$

The partition function Q of a molecule can be written as the product of the four modes of motion (vibrational, translational, rotational and electronic) available to the molecule,

$$Q = Q_{vib}\,Q_{trans}\,Q_{rot}\,Q_{elec}. \tag{1.12}$$

For isotope exchange reactions the electronic configurations are unaffected so Q_{elec} can be ignored, and therefore

$$Q = Q_{vib}\,Q_{trans}\,Q_{rot}. \tag{1.13}$$

All the three modes of partition function Q can be calculated. Compared to Q_{trans} and Q_{rot}, Q_{vib} contributes the most to the total partition function Q for a molecule. Assuming the vibration is harmonic, Q_{vib} takes the form

$$Q_{vib} = \Pi_n\,\{\exp(-h\nu_n/2kT)/\,[1-\exp(-h\nu_n/kT)]\}, \tag{1.14}$$

where the product is taken over all the vibrational frequencies ν_n, k is the Boltzmann's constant and h is Planck's constant (Schauble, 2004). Q_{trans} and Q_{rot} can be approximated by

$$Q_{trans} = V(2\pi mkT)^{3/2}/h^3, \tag{1.15}$$

$$Q_{rot} = 8\pi^2 IkT/(\sigma h^2), \tag{1.16}$$

where V is the volume of the molecule, m is the mass, and I the moment of inertia (Schauble, 2004).

Above equations show that $\alpha^{i/j}_{A\text{-}B}$ can be calculated. However, the resulting formula would be complicated after incorporating everything outlined above. There are some assumptions that can be made to greatly simplify the calculation. In approach of Urey (1947), harmonic vibrations

and rigid-body rotations were assumed, and rotational energies were treated in a simplified way. In this case, the only inputs needed are vibrational frequencies for light and heavy molecules. These assumptions are reasonable for the temperature range of 100 to 1000 K, which is relevant to most geological processes. Generally, for temperatures higher than 1000 K, equilibrium fractionation is very small and can be neglected. For temperatures below 100 K, a full quantum-mechanical treatment is needed (Schauble, 2004).

Since vibrational frequencies are related to bond strengths, knowing the force constants of element bonds of interest in coexisting phases is enough for a simplified calculation of equilibrium isotope fractionation. Isotope fractionation between two phases A and B can be calculated using Eq. 1.5,

$$\Delta^{i/j}_{A\text{-}B} \approx 1000 \times \ln\alpha = 1000\ln\beta_A - 1000\ln\beta_B, \quad (1.17)$$

where β_A and β_B are the reduced partition function ratios or β-factors. Beta-factors can be calculated using the force constants of phases

$$1000\ \ln\beta \approx 1000 \langle F \rangle (1/ m_i - 1/ m_j)\ \hbar^2/(8k^2T^2), \quad (1.18)$$

where <F> is the force constant in N/m, m_i and m_j are the masses of the two isotopes i and j of the element of interest, ħ is the reduced Planck's constant, k is Boltzmann's constant, and T is the temperature (Dauphas et al., 2012). Force constants can be obtained by performing nuclear resonant inelastic X-ray scattering (NRIXS) measurements (Blanchard et al., 2015; Dauphas et al., 2012; 2018). The equilibrium isotope fractionation between the two phases A and B is therefore

$$\Delta^{i/j}_{A\text{-}B} \approx 1000\ (\langle F \rangle_A - \langle F \rangle_B)\ (1/ m_i - 1/ m_j)\ \hbar^2/(8k^2T^2). \quad (1.19)$$

This equation also shows that for two coexisting phases, isotope fractionations at any given temperature can be estimated if the fractionation at one temperature is known.

1.2.3 Kinetic isotope fractionation

Kinetic isotope fractionation occurs when the isotope exchange reaction between two phases are incomplete, which is often associated with relatively fast and unidirectional processes, such as evaporation and diffusion (White, 2013). For an ideal gas, the average kinetic energy is controlled by temperature and all molecules have the same kinetic energy (E_{kin})

$$E_{kin} = (1/2)\, mv^2. \quad (1.20)$$

The movement speed v of a molecule is therefore approximately inversely proportional to the square root of the molecular mass m,

$$v(A_i)/\, v(A_j) = [m(A_j)/m(A_i)]^{0.5}, \quad (1.21)$$

where A_i and A_j are the same molecule with different isotopes. The kinetic isotope fractionation factor α_{kin} (relevant, for example, in evaporation processes) is often parameterized as

$$\alpha^{i/j}_{kin}=[m(A_j)/m(A_i)]^{\beta}, \quad (1.22)$$

where β can have a value close to 0.5 (in the case of evaporation of a melt into vacuum) or lower (if evaporation into a finite pressure) and is often constrained experimentally.

1.2.4 Rayleigh distillation

Rayleigh distillation is one of the most common and important processes in geochemistry. An ideal Rayleigh distillation process is one where the reactant is well-mixed, and the product is removed or does not back-react with the reactant once it forms. Fractional crystallization of a magma, precipitation of a solid from a fluid, evaporation and condensation are all examples of Rayleigh distillation reactions. Because the reaction product does not re-equilibrate with the reactant reservoir, a Rayleigh distillation can lead to very large isotope fractionation. The isotopic evolution of the reactant reservoir and the product reservoir in a Rayleigh distillation can be calculated (see White, 2013 for example). Because the reaction rate is proportional to the amount

present, given two isotopes i and j in a Rayleigh distillation regime, we have for the reactant reservoir

$$dN_i = k_i N_i, \tag{1.23}$$

and

$$dN_j = k_j N_j, \tag{1.24}$$

where k_i and k_j are the rate constants, and N_i and N_j are the numbers of isotopes i and j, respectively. Since we are looking at isotopic effects, k_i is not equal to k_j. The isotopic ratio of the reactant reservoir is

$$R^{i/j}_{reactant} = N_i/N_j, \tag{1.25}$$

and the instantaneous product has an isotopic ratio of

$$R^{i/j}_{inst} = dN_i/dN_j. \tag{1.26}$$

The isotope fractionation factor between the *instantaneous product* and the *reactant reservoir* (called the Rayleigh fractionation factor) is

$$\alpha = R^{i/j}_{inst} / R^{i/j}_{reactant} = (dN_i/dN_j)/(N_i/N_j). \tag{1.27}$$

This equation can be rearranged as

$$dN_i/N_i = \alpha\ (dN_j/N_j). \tag{1.28}$$

Integrating the equation on both sides, we have

$$\ln(N_i/N_{i,0}) = \alpha \ln(N_j/N_{j,0}), \tag{1.29}$$

or

$$N_i/N_{i,0} = (N_j/N_{j,0})^{\alpha}, \tag{1.30}$$

where $N_{i,0}$ and $Nj_{,0}$ are the amount of isotope i and j initially present in the reactant reservoir. To determine the isotopic ratios of the reactant reservoir, by rearranging the equation we are given

$$(N_i/N_j)/(N_{i,0}/N_{j,0}) = (N_j/N_{j,0})^{\alpha-1}. \tag{1.31}$$

Using f, the fraction of isotope j remaining in the reactant reservoir, the equation describes the evolution of the isotopic ratio in the reactant reservoir:

$$R^{i/j}_{reactant} = R_0^{i/j} f^{\alpha-1}. \quad (1.32)$$

The equation can be rewritten using δ-notation,

$$1000[\ln(R^{i/j}_{reactant}/R^{i/j}_{standard}) - \ln(R_0^{i/j}/R^{i/j}_{standard})] = 1000\ (\alpha-1)\ \ln f, \quad (1.33)$$

$$\delta_{reactant} = \delta_0 + 1000\ (\alpha-1)\ \ln f, \quad (1.34)$$

where $R^{i/j}_{standard}$ is the isotopic ratio in the reference standard, $\delta_{reactant}$ is the isotopic composition of the reactant, δ_0 the initial composition, α the Rayleigh fractionation factor, and f the fraction of the element of interest remaining in the reactant reservoir.

The isotopic composition of the instantaneous product is always fractionated by the Rayleigh fractionation factor relative to the reactant,

$$\delta_{inst} = \delta_{reactant} + 1000\ (\alpha-1). \quad (1.35)$$

To calculate the cumulative isotopic composition of the product reservoir ($\delta_{product}$), a mass balance equation can be used,

$$f\ \delta_{reactant} + (1-f)\ \delta_{product} = \delta_0, \quad (1.36)$$

and therefore,

$$\delta_{product} = (\delta_0 - f\ \delta_{reactant})/(1-f). \quad (1.37)$$

1.2.5 Mass dependent isotope fractionation laws

Most natural isotope fractionation processes (including both equilibrium and kinetic isotope fractionations) are mass dependent processes. The partition, or separation of isotopes in a phase ultimately depends on the differences in mass, and it scales in proportion to the isotopic mass differences. For example, for mass-dependent oxygen isotope fractionation, one would always expect the $^{17}O/^{16}O$ ratio to change by about half of the $^{18}O/^{16}O$ ratio, because the mass

difference between ^{17}O and ^{16}O (~1 amu) is about half of the mass difference between ^{18}O and ^{16}O (~2 amu). Therefore, in a conventional three-isotope plot where $\delta^{17/16}O$ is plotted versus $\delta^{18/16}O$, the slope of a mass dependent process should be near 0.5.

To first order, this principle applies to isotope fractionations of all other elements as well, provided that the isotopes are fractionated in a mass-dependent way and no large mass-independent fractionation occurred. However, it has been discovered that the slope of one isotopic system can change slightly in a three-isotope diagram for different processes; these slightly different slopes are termed as mass-dependent isotope fractionation laws. Early studies of the mass-dependent fractionation laws include elements of hydrogen (*e.g.*, Bigeleisen, 1962; Grilly, 1951; Pyper and Christensen, 1975), oxygen (Matsuhisa et al., 1978), and sulfur (Hulston and Thode, 1965), where isotopes have large relative mass differences ($(m_i–m_j)/m$). Determining mass-dependent fractionation laws for heavy metals are not trivial due to the much smaller differences among the laws and extremely high measurement precision is required. Several heavy metals have been studied for their mass-dependent fractionation laws in certain processes such as calcium (Russell et al., 1978; Zhang et al., 2014), titanium (Zhang et al., 2014), Magnesium (Young et al., 2002; Davis et al., 2015), and iron (Nie et al., 2017).

Mass-dependent isotope fractionation laws can potentially be used to distinguish between different processes, because different processes may result in slightly different slopes. In Chapter 2, an example is shown of using the mass-dependent isotope fractionation law of UV Fe photo-oxidation process to tell if the process is consistent with BIF precipitation. Mass-dependent fractionation laws are only briefly introduced here, and detailed discussions of mass-dependent fractionation laws can be found in Cao and Liu (2011), Dauphas and Schauble (2016) and Young et al. (2002). Since the isotope fractionation factor α is the most important parameter in discussing

isotope fractionation, mass-dependent fractionation laws are described in terms of fractionation factors.

Considering two substances A and B, an element E is in both A and B with the three isotopes of i, j and k. Fractionation factor $\alpha_{A\text{-}B}$ is equal to the isotope abundance ratio in substance A relative to substance B. The isotope pairs of i and j, and k and j (here j is used as the denominator of isotope ratios), have fractionation factors of $\alpha^{i/j}_{A\text{-}B}$ and $\alpha^{k/j}_{A\text{-}B}$:

$$\alpha^{i/j}_{A\text{-}B} = R^{i/j}_{A} / R^{i/j}_{B}, \tag{1.38}$$

$$\alpha^{k/j}_{A\text{-}B} = R^{k/j}_{A} / R^{k/j}_{B}, \tag{1.39}$$

where R represents the abundance ratio of two isotopes. As shown above, isotopic composition difference in A and B is related to fractionation factor α by

$$\delta^{i/j}_{A} - \delta^{i/j}_{B} = \Delta^{i/j}_{A\text{-}B} \approx 1000 \times \ln\alpha^{i/j}_{A\text{-}B}, \tag{1.40}$$

$$\delta^{k/j}_{A} - \delta^{k/j}_{B} = \Delta^{k/j}_{A\text{-}B} \approx 1000 \times \ln\alpha^{k/j}_{A\text{-}B}, \tag{1.41}$$

where δ denotes an isotopic composition in δ–notation and $\Delta_{A\text{-}B}$ the difference in the isotopic compositions of the two substances A and B. The slope $\theta^{i,j,k}_{A\text{-}B}$ defined by the two substances in a three-isotope diagram ($\delta^{i/j}$ vs. $\delta^{k/j}$) is therefore

$$\theta^{i,j,k}_{A\text{-}B} = (\delta^{i/j}_{A} - \delta^{i/j}_{B})/(\delta^{k/j}_{A} - \delta^{k/j}_{B}) = \ln\alpha^{i/j}_{A\text{-}B} / \ln\alpha^{k/j}_{A\text{-}B}, \tag{1.42}$$

and when expressing one fractionation factor against the other,

$$\alpha^{i/j}_{A\text{-}B} = (\alpha^{k/j}_{A\text{-}B}) \wedge \theta^{i,j,k}_{A\text{-}B}. \tag{1.43}$$

Maréchal et al. (1999) used a *generalized power law* to describe mass-dependent fractionation laws in general, which takes the form

$$R^{i/j}{}_{B} = R^{i/j}_{A} \times g\wedge(m_i^n - m_j^n), \tag{1.44}$$

where $R^{i/j}{}_{A}$ and $R^{i/j}{}_{B}$ are the isotopic ratios before and after a mass-dependent isotope fractionation process, g is the mass fractionation coefficient, m is the mass of an isotope and the power n is a

free parameter which can have several different values representing different mass fractionation laws. For the isotope pair k and j, we have

$$R^{k/j}_B = R^{k/j}_A \times g\text{^}(m_k^n - m_j^n). \quad (1.45)$$

By taking the logarithm on both sides of the two equations, and dividing the first one by the second one,

$$\ln (R^{i/j}_A / R^{i/j}_B) / \ln(R^{k/j}_A / R^{k/j}_B) = (m_i^n - m_j^n)/(m_k^n - m_j^n). \quad (1.46)$$

Recall that

$$\Delta^{i/j}_{A\text{-}B} = 1000 \times \ln (R^{i/j}_A / R^{i/j}_B) \text{ and } \Delta^{k/j}_{A\text{-}B} = 1000 \times \ln (R^{k/j}_A / R^{k/j}_B), \quad (1.47)$$

therefore, the slope characterizing the mass fractionation law can be written as

$$\theta^{i,j,k}_{A\text{-}B} = (m_i^n - m_j^n)/(m_k^n - m_j^n), \quad (1.48)$$

n can have values of –2, –1, –½, 0, ½, 1, and 2, each value represents a difference mass fractionation law. When n = 0, the slope corresponds to exponential law and takes the form of

$$\theta_{exponential} = \ln(m_i/m_j)/\ln(m_k/m_j), \quad (1.49)$$

which is the law used for correcting for isotope fractionation in mass spectrometers.

1.3 Stable iron isotopes

Iron is ubiquitous and a major element in rocks. It has three valence states, metallic Fe, ferrous iron [Fe(II)] and ferric iron [Fe(III)]. Metallic iron is present mainly in Earth's core, alloying with Ni and a small fraction of light elements, such as S and O. Iron in the silicate Earth is mainly Fe(II) and Fe(III), with more Fe(II) in the mantle and more Fe(III) in the oxygenated Earth's crust. Iron also plays an important role as a micronutrient for life on Earth's surface. In fluids, Fe(II) has a higher solubility than Fe(III). Under acidic conditions, both Fe(II) and Fe(III)

can be dissolved in fluids, but at more alkalic conditions, Fe (III) tends to precipitate as iron oxides and hydroxides.

Iron has four stable isotopes: ^{54}Fe, ^{56}Fe, ^{57}Fe and ^{58}Fe. The relative abundances of the four isotopes are 5.85%, 91.75%, 2.12% and 0.28%, respectively (Berglund and Wieser, 2011; Meija et al., 2016). The Fe isotopic composition is normally reported as $\delta^{56}Fe$, or $\delta^{56/54}Fe$ (the denominator isotope for Fe is ^{54}Fe and is usually omitted; ^{54}Fe and ^{56}Fe are the two most abundant isotopes of Fe, therefore are easier to precisely measure than the other isotopes), which is the deviation in part per thousand (per mil, or ‰) of the isotope abundance ratio of $^{56}Fe/^{54}Fe$ from that of the reference standard. The Fe isotope reference standard is IRMM014, and Fe isotopic compositions are expressed as

$$\delta^{56}Fe = [(^{56}Fe/^{54}Fe)_{sample}/(^{56}Fe/^{54}Fe)_{IRMM014} - 1] \times 1000 \text{ (‰)}. \quad (1.50)$$

Some groups have also reported Fe isotopic compositions as $\delta^{57}Fe$, which uses the $^{57}Fe/^{54}Fe$ ratio instead of $^{56}Fe/^{54}Fe$ ratio (*e.g.*, Poitrasson et al., 2004; Shahar et al., 2008; Sossi et al., 2016b). $\delta^{58/54}Fe$ is very rarely reported, because the relative isotopic abundance of ^{58}Fe is too low to be measured precisely.

Since most natural Fe isotope fractionation processes are mass-dependent, the $\delta^{57}Fe$, $\delta^{58}Fe$ and $\delta^{56}Fe$ values have a relationship of $\delta^{57}Fe \approx 1.5 \times \delta^{56}Fe$ and $\delta^{58}Fe \approx 1.5 \times \delta^{58}Fe$. Terrestrial rocks and bulk meteorites show only mass-dependent Fe isotope fractionation and no mass-independent isotopic anomaly has been detected in these samples (Dauphas et al., 2008; Tang and Dauphas, 2012). Iron isotopic anomalies have been detected in presolar silicon carbide grains (Marhas et al., 2008; Trappitsch et al., 2018) and some FUN (Fractionated and Unknown Nuclear effects) CAIs (calcium-aluminum-rich inclusions) which are the earliest condensates of the solar nebula (Völkening and Papanastassiou, 1989). Another documented mass-independent Fe isotope

fractionation is in the magnetite produced through biomineralization by magnetotactic bacteria, which produces a ^{57}Fe anomaly (Amor et al., 2016).

1.3.1 Iron isotopic variations among planetary bodies

Chondrites are stony, primitive meteorites that have not experienced differentiation and they are considered to be the building blocks of planets. Bulk measurements of carbonaceous chondrites (CC), ordinary chondrites (OC) and enstatite chondrites (EC) show the same Fe isotopic compositions within error. The Fe isotope average of chondrites over 10 carbonaceous chondrites, 15 ordinary chondrites and 16 enstatite chondrites gave a value of $\delta^{56}Fe$ −0.005±0.006 ‰ (Craddock and Dauphas, 2011a), which is identical to the reference standard IRMM-014. Most chondrites contain abundant chondrules, which are quenched silicate spherules. The origin of chondrules is still highly debated, but they were very likely once heated and molten (hence the round shape), and some volatile elements such as Na and K may have been evaporated. The isotope measurements of individual chondrules (Hezel et al., 2010; Mullane et al., 2005; Needham et al., 2009) showed that the Fe isotopic variation among individual chondrules was limited. Most chondrules have $\delta^{56}Fe$ values that fall within ±0.2 ‰ of bulk chondrites. This shows that the Fe isotope fractionation could have occurred under high temperature, near-equilibrium conditions, where equilibrium isotope fractionation is small.

Martian samples of Shergottite-Nakhlite-Chassignite (SNC) meteorites have chondritic Fe isotopic compositions. The isotopic variation is small, from –0.03 to +0.03 ‰ for $\delta^{56}Fe$ (Anand et al., 2006; Poitrasson et al., 2004; Sossi et al., 2016a; Wang et al., 2012; Weyer et al., 2005). Howardite, Eucrite and Diogenite (HED) meteorites from the asteroid 4-Vesta also have Fe isotopic compositions indistinguishable from chondrites within ± 0.05 ‰ (Poitrasson et al., 2004; Schoenberg and Blanckenburg, 2006; Wang et al., 2012; Weyer et al., 2005). In contrast, angrites,

a group of basaltic meteorites from a body that was relatively oxidized (~IW+1), have Fe isotopic compositions heavier than chondrites by ~0.1‰ (Wang et al., 2012). This isotopic composition is comparable to that of terrestrial basalts. It is still unknown why angrites have heavier Fe isotopic compositions than chondrites, SNC and HED meteorites. The isotopic composition might reflect the Fe isotopic composition of precursor materials, or volatilization during accretion.

The samples used to represent bulk silicate Earth in early studies were basalts (Beard and Johnson, 1999; Poitrasson et al., 2004), because basalts are the products of partial melting of the mantle. Terrestrial basalts have average δ^{56}Fe value of ~+0.1 ‰, leading to the conclusion that bulk Earth had a heavier Fe isotopic composition compared with chondrites, which are at ~0 ‰. However, later studies showed that peridotites, which are rocks derived from the shallowest part of the mantle, have Fe isotopic compositions similar to chondrites (Craddock et al., 2013; Huang et al., 2011; Poitrasson et al., 2013; Weyer and Ionov, 2007; Zhao et al., 2010; 2012). Weyer and Ionov (2007) measured Fe isotopes in various mantle peridotites and found a negative trend between δ^{56}Fe vs. Mg# (atomic ratio of Mg/(Mg+Fe)), and interpreted it as a partial melting trend. By extrapolating to Mg# of 0.894, they used the slope of the trend to estimate the Fe isotopic composition of the fertile upper mantle to be 0.02 ± 0.03‰. Other studies measuring mantle peridotites (Craddock et al., 2013; Huang et al., 2011; Poitrasson et al., 2013; Zhao et al., 2012; 2010) also found an average Fe isotopic composition indistinguishable from chondrites, despite of some variations among different samples. This suggests that the Earth may be chondritic in terms of Fe isotopes, and that the heavy Fe isotopic composition of terrestrial basalts may be due to isotope fractionation during partial melting.

Among the lunar rocks that are available to study, mare basalts formed by partial melting of the lunar mantle (Lee et al., 2009) are the best in terms of constraining the composition of the

bulk silicate Moon. There are two types of mare basalts: high-Ti and low-Ti basalts. They are quite different in both age and chemical composition, and cannot be explained by partial melting of a common parental magma to different degrees. Instead, two chemically and isotopically distinct source regions need to be invoked (*e.g.*, Papike et al., 1976). High-Ti and low-Ti mare basalts have different Fe isotopic compositions. High-Ti basalts have an average δ^{56}Fe value of +0.19 ‰ ± 0.02 ‰, while low-Ti basalts have an average value of +0.07 ‰ (Yang Liu et al., 2010; Poitrasson et al., 2004; Weyer et al., 2005; Wiesli et al., 2003), and both of them are heavier than the bulk silicate Earth which is at chondritic value of zero. It has been suggested that the difference in δ^{56}Fe values of low-Ti and high-Ti mare basalts may reflect crystallization of ilmenites during lunar magma ocean crystallization (Craddock et al., 2010). However, ilmenite should be isotopically light when in equilibrium with melt (Nie et al., 2018; Sossi and O'Neill, 2017), meaning that high-Ti basalts should be isotopically lighter compared than low-Ti basalts, but this is not what has been observed. It is still unknown what controlled this difference. One explanation is that the heavy Fe isotopic composition of high-Ti basalts is acquired from heavy ilmenite that formed in the later stages of magma ocean crystallization (Sossi and O'Neill, 2017). The bulk Moon Fe isotopic composition remains uncertain, and the best estimate is an average over high-Ti and low-Ti basalts which gives a value of ~+0.08 ‰ (Yang Liu et al., 2010), similar to terrestrial basalts (~+0.1 ‰) but heavier than the bulk Earth (~0 ‰).

1.3.2 Iron isotope fractionation during BIF formation

As equilibrium isotope fractionation is inversely proportional to the square of temperature (T^2; Eq. 1.19), larger isotope fractionations are expected at lower temperatures. In addition, Fe has two valence states and large Fe isotope fractionations have been observed for redox reactions. Among the questions that used Fe isotopes to trace geochemical and biogeochemical processes,

one of the most extensively studied is how Banded Iron Formations (BIFs) formed. BIFs have played a critical role in discussions on the ancient environment on the Earth surface, because their formation requires redox conditions and Fe transport pathways quite different from the modern Fe cycle (*e.g.*, Johnson et al., 2008a; Klein, 2005).

Banded iron formations are ancient (Archean to early Proterozoic) sedimentary rocks with alternating layers of Fe oxides and silica. The average oxidation state of iron in BIFs is +2.4 (*e.g.*, Klein, 1992). The large inventory of Fe(III) in BIFs requires an oxidation mechanism, since the Fe source has been considered to be hydrothermal Fe(II) based on REE data (Bau et al., 1997). The oxidation mechanism is still in debate, and the proposed mechanisms include 1) oxygen produced during the metabolism of bacteria (Cloud, 1973; 1965), 2) photosynthetic Fe^{2+}-oxidizing bacteria (Garrels et al., 1973; Widdel et al., 1993) and 3) UV photo-oxidation (Braterman et al., 1983; Cairns-Smith, 1978). Oxidation of Fe(II) would produce Fe(III) oxides/hydroxides (ferrihydrite is the most common Fe(II) oxidation product in lab experiments), which would precipitate due to the low solubility. Later on during diagenesis, the Fe(III) oxide/hydroxide precursor would be reduced to form magnetite and siderite (the most common Fe-rich minerals in BIFs), either through dissimilatory iron reduction (DIR; a process in which bacteria utilize Fe(III) as the electron acceptor during anaerobic respiration) or reactions with Fe(II)-rich fluids in the deep marine anoxic layer (Fig. 1.1).

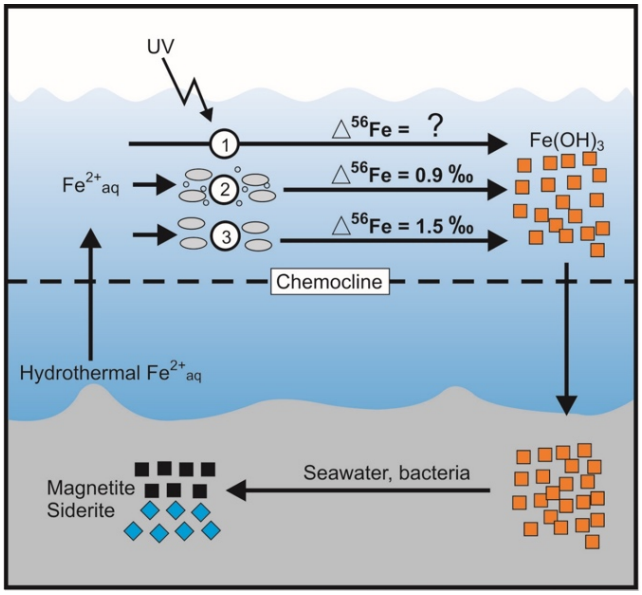

Figure 1.1 An illustration of BIF formation, modified from Johnson et al. (2008a). Here the Fe source is hydrothermal Fe(II). The Fe(II) in the deep water ascends to the upper water column, and gets oxidized to Fe(III) oxides/hydroxides, which "rain" to the site of BIF deposition due to the low solubility. During diagenesis, the Fe(III) oxides/hydroxides are converted to the minerals commonly seen in BIFs (such as magnetite and siderite) through reactions with Fe(II)-containing seawater or through DIR. The oxidation mechanism of Fe(II) to Fe(III) oxides/hydroxides is still in debate, and three pathways have been proposed. Pathway 1 is Fe UV photo-oxidation, and the isotope fractionation factor between Fe(III) oxides/hydroxides and aqueous Fe(II) is determined in Chapter 2. Pathway 2 features oxidation by oxygen produced by bacteria, which produces a fractionation factor of +0.9 ‰ between Fe(III) oxides/hydroxides and Fe(II) (Bullen et al., 2001). Pathway 3 is anoxygenic photosynthesis, in which bacteria use directly Fe(II) as the electron donor. This process has a fractionation factor of +1.5 ‰ (Croal et al., 2004).

In general, the oxidation of aqueous Fe(II) to form ferrihydrite in general produces a ~1–1.5 ‰ isotope fractionation between ferrihydrite and aqueous Fe(II) [$Fe(II)_{aq}$]. Bullen et al. (2001) investigated Fe isotope fractionation during Fe(II) oxidation by oxygen and found that the produced Fe(III) oxides/hydroxides were heavier by ~1‰ compared with the aqueous Fe(II). This fractionation factor is relevant to oxidation by bacteria-generated oxygen, which has been

proposed as a mechanism for BIF precipitation. Oxidation of Fe(II) by Fe(II)-oxidizing phototrophs under anaerobic conditions was studied by Croal et al. (2004); the reaction produced ferrihydrite which was about 1.5 ‰ heavier than $Fe(II)_{aq}$. In this work, iron UV photo-oxidation is investigated in this work and Chapter 2 will show that the process produces a fractionation factor of ~+1.2‰ between Fe(III) products and $Fe(II)_{aq}$.

Reduction of Fe(III) oxides/hydroxides to Fe(II) by DIR can produce Fe(II)-containing minerals that have been observed in BIFs such as magnetite and siderite. Crosby et al. (2007) conducted DIR experiments and found that the $Fe(II)_{aq}$ produced was always enriched in light isotopes. They attributed these light values to the reaction among three Fe components: $Fe(II)_{aq}$, $Fe(II)_{sorb}$ [sorbed Fe(II)], and a reactive Fe(III) component on the Fe(III) oxide surface [$Fe(III)_{reac}$]. The fractionation between $Fe(II)_{aq}$ and $Fe(III)_{reac}$ is constantly –2.95 ‰, independent of the Fe(III) substrate (hematite or goethite). This value is identical within error to the equilibrium fractionation factor between $Fe(II)_{aq}$ and Fe(III) oxides in abiological systems (Johnson et al., 2002; Welch et al., 2003; Wu et al., 2011), suggesting that the role of bacteria during DIR is catalyzing coupled atom and electron exchange between Fe(II)aq and Fe(III)reac so that equilibrium Fe isotope partitioning occurs. The isotopic effects of $Fe(II)_{sorb}$ are relatively small.

The bulk Fe isotopic compositions of BIFs can vary significantly, from ~ –2 to +1 ‰, with a strong mineralogical control (Dauphas et al., 2004; Johnson et al., 2008b). The major Fe-bearing minerals in BIFs are magnetite and siderite. The most well-studied BIFs are the Hamersley group in Australia and Transvaal supergroup in South Africa, which are the largest BIFs deposited at ~2.5 Gyr. Magnetites from Hamersley-Transvaal BIFs have $\delta^{56}Fe$ values ranging from –1 to +1 ‰, centering around ~0 ‰. Modern hydrothermal vents have an Fe isotopic range of ~–0.8 to ~–0.1 ‰, positively correlated with Fe contents, therefore by mass balance the $\delta^{56}Fe$ value of

hydrothermal flux should be near to the high end of the range (Dauphas et al., 2004; Johnson et al., 2008b). In addition, the heat flow in the Archean was higher, and a higher degree of partial melting would result in a near 0‰ Fe isotopic composition for the hydrothermal flux, similar to peridotites which are the major mineral phase of the shallow mantle (Johnson et al., 2008a; Yamaguchi et al., 2005). The average Fe isotopic composition of magnetite (around 0‰) is thought to be inherited from Fe(III) oxide/hydroxide precursors that precipitated due to complete oxidation of Fe(II). Magnetite with heavy Fe isotopic compositions are thought to reflect Fe(III) oxide/hydroxides formed by partial oxidation of aqueous Fe(II) [$Fe(II)_{aq}$], and the ones with light values may be produced by dissimilatory iron reduction (DIR) of Fe(III) oxide/hydroxide (Johnson et al., 2008b; 2008a). The Fe isotopic compositions of siderite from the same BIFs are lower than that of magnetite. The average of the Fe isotopic compositions of siderite is about –0.5‰. This average value is interpreted as reflecting equilibrium isotope fractionation between siderite and sea water $Fe(II)_{aq}$, and the deviation from the average could be explained by DIR of precursor Fe(III) oxides/hydroxides. There is an Fe isotope (and carbon isotope) dichotomy between iron-rich carbonates (siderite and ankerite) and iron-poor carbonates (calcite and dolomite) in Hammersley-Transvaal BIFs. Iron-rich carbonates tend to have relatively high $\delta^{56}Fe$ values and low $\delta^{13}C$ values, while the Fe-poor carbonates have relatively low $\delta^{56}Fe$ values and normal $\delta^{13}C$ values. The Fe and C isotope compositions of Fe-rich carbonates are consistent with DIR driven C oxidation and Fe reduction from precursor materials during diagenesis. The Fe-poor carbonates with normal C values and very low $\delta^{56}Fe$ values can be explained by precipitation from seawater (Craddock and Dauphas, 2011b; Heimann et al., 2010).

1.4 Stable rubidium isotopes

Like potassium, rubidium is an alkali metal, and the two elements have very similar geochemical behaviors. Rb has two isotopes: ^{85}Rb, with a relative abundance of 72.17% and ^{87}Rb, with an abundance of 27.83% (Berglund and Wieser, 2011). Rubidium-85 is stable but ^{87}Rb is radioactive, it decays to ^{87}Sr with a relatively long half-life of 48.8 billion years (Faure and Mensing, 2005), ^{87}Rb-^{87}Sr dating has been widely used in geochronology. For dating purpose, Rb isotopic compositions are usually not measured, and therefore Rb isotope data are still very limited. Rb isotopic compositions are often expressed using the ratio of ^{87}Rb/^{85}Rb, relative to the reference material NIST SRM984,

$$\delta^{87}\text{Rb} = [(^{87}\text{Rb}/^{85}\text{Rb})_{\text{sample}}/(^{87}\text{Rb}/^{85}\text{Rb})_{\text{SRM984}} - 1] \times 1000\ (‰). \quad (1.51)$$

Nebel et al. (2005) measured Rb isotopic compositions of geological materials containing relatively high contents of Rb (tens to hundreds ppm of Rb), such as terrestrial magmatic rocks and K-felspar. They developed a Rb separation method and used a Zr-doping method proposed by Waight et al. (2002) to correct for instrumental isotope fractionation. However, the precision of the measurements (~ ±0.2 ‰) was not precise enough, and the variation of all the samples was within ±1 ‰. Nebel et al. (2011) applied the same method to Rb isotopic analyses of chondrites, and found that Rb isotopic compositions of chondrites are similar to that of the Earth, not deviating more than 1 ‰. Recently, Pringle and Moynier (2017) reported a new Rb isotope separation method and reported a ~ ±0.05 ‰ precision for their Rb isotope measurement. They measured chondrites, terrestrial, and lunar samples and found that lunar magmatic rocks were systematically heavier than terrestrial magmatic rocks, by ~0.1 ‰, and that chondrites had more variable Rb isotopic compositions compared with terrestrial and lunar samples. More high precision measurements are needed to confirm the results and to get better statistics.

Rubidium isotope fractionation can be expected in various processes. Rb is very incompatible and it tends to be partitioned into melts during partial melting. This results in felsic rocks (*e.g.*, granites) that have much higher Rb contents than mafic rocks (*e.g.*, basalts), and some Rb isotope fractionation could happen between these two rock types. Another very important aspect of Rb is that it is a moderately volatile element, with a 50% condensation temperature (the temperature at which half of an element would have condensed from a solar nebular composition; Lodders, 2003; Wood et al., 2019) around 800K. Evaporation processes could evaporate light Rb isotopes, leaving a heavy Rb-enriched residue. This property of Rb makes it a good tracer of the lunar volatile depletion process (Chapter 3). Furthermore, Rb has a high solubility and is mobile, so it has great potential to trace weathering processes.

1.5 Synopsis of chapters

Chapter 2 explores the behavior of the Fe isotopic system in aqueous Fe oxidation-precipitation processes for a better understanding of the mechanisms responsible for the formation of two of the most unique Fe entities involving large quantities of Fe transport: banded iron formations (BIFs) and martian hematite spherules (MHS). Their Fe sources are thought to be $Fe(II)_{aq}$ from hydrothermal vents for BIFs, and leached $Fe(II)_{aq}$ from basalts for MHS. Ferrous Fe from these sources was oxidized to Fe(III), and due to its much lower solubility, Fe(III) precipitated to form BIFs and MHS. The oxidizing mechanism, since ancient Earth and Mars lacked oxygenated atmospheres, had been suggested to be either bioactivity (*i.e.*, oxygen produced by photosynthesis of cyanobacteria, (Cloud, 1973; 1965), or anoxygenic photosynthesis of bacteria (Garrels et al., 1973; Widdel et al., 1993)) or UV photo-oxidation (Braterman et al., 1983; Cairns-Smith, 1978). Chapter 2 focuses on testing the potential of UV photo-oxidation as the cause of BIFs and MHS precipitation. Definitive evidence of life on Earth during the formation of the

earliest BIFs (~3.8 Gyr) is currently nonexistent. UV photo-oxidation, which does not involve life, has been largely ignored in literature despite the fact that the ancient Earth's low-O_2 atmosphere could have allowed about 5 times more UV light than the present-day atmosphere. Chapter 2 tests the UV photo-oxidation hypothesis through two aspects: 1) is the Fe isotope fractionation during UV photo-oxidation consistent with the isotope signature of BIFs? and 2) is UV photo-oxidation efficient enough to oxidize such large quantities of Fe? The latter is of great importance for testing the UV photo-oxidation hypothesis for MHS, considering that samples of MHS are not available yet for isotope measurement.

To answer question 1), lab photo-chemical experiments were designed and performed to mimic UV photo-oxidation, and the isotope evolution of the system was measured. A broad-spectrum UV lamp for mimicking the early Sun was used to irradiate and oxidize $Fe(II)_{aq}$ to Fe(III) precipitate [$Fe(III)_{ppt}$] under anoxic conditions. $Fe(II)_{aq}$ and $Fe(III)_{ppt}$ were sampled at certain time intervals during the experiment. The samples were run through Fe chromatography and measured for Fe isotopic compositions ($\delta^{56/54}Fe$) using the MC-ICP-MS in the Origins Lab at the University of Chicago. With this isotope data, the $Fe(III)_{ppt}$-$Fe(II)_{aq}$ isotope fractionation factor during UV photo-oxidation was constrained to be ~+1.2 ‰. This factor could explain the Fe isotopic variation observed in BIFs. In addition, the mass-dependent isotope fractionation law (*i.e.*, the relationship between $\varepsilon^{56/54}Fe$ and $\delta^{57/54}Fe$) of UV photo-oxidation products was measured carefully. The expectation is that different processes will follow slightly different mass dependent fractionation laws. If UV photo-oxidation was responsible for BIF precipitation, the UV photo-oxidation products and BIFs should follow the same law. This method has not been widely used, because these measurements examining the very small differences between two laws are very analytically challenging. Interestingly, the measured BIF sample and the photo-oxidation run products

followed the same law. This provides further evidence that UV photo-oxidation is consistent with BIF precipitation. To further test the scenario, oxygen isotopes of the UV photo-oxidation experiment products were also measured. Oxygen is known to show some peculiar isotopic effects (mass-independent fractionation) during some processes involving UV light (*e.g.*, Heidenreich and Thiemens, 1983; Thiemens and Heidenreich, 1983; Thiemens and Jackson, 1987). If photo-oxidation produces mass-independent oxygen isotope fractionation, it would not be consistent with BIF formation because mass-independent oxygen isotopes have not been observed in BIFs. We did not observe mass-independent oxygen isotope fractionation in the photo-oxidation products, substantiating that UV photo-oxidation is a possible mechanism accounting for BIF precipitation.

To answer the question 2), a mathematical model was built to calculate rates and timescales for photo-oxidation of Fe in lakes with various depths. The UV photo-oxidation rate of Fe is a function of many parameters, including Fe(II) concentrations, water depths, UV wavelengths and flux, Fe speciation, Fe molar absorptivity and quantum yield. The model aimed to be more realistic than previous models by using more accurate values for the parameters (*e.g.*, the quantum yield determined in the experiments was used in the calculation) and by taking into account the details that could affect the result such as solar incident angle, the distance between Mars and the Sun, water pH change as Fe gets oxidized, diurnal effect and so on. As a result, more realistic timescales were obtained (For example, in this model, it would take ~40 years to oxidize the Fe(II) in a lake with a depth of 100 m, compared to a timescale of 50 days obtained in a previous calculations; Hurowitz et al., 2010). The model suggests that UV photo-oxidation could be very effective, compared with the normal lifetime of a lake and with the timescale of oxidation by oxygen (due to the low oxygen content of the martian atmosphere, oxidizing a lake could be extremely slow).

The main conclusion of this work is that photo-oxidation is a viable oxidation mechanism to form BIFs and MHS.

After studying the UV photo-oxidation mechanism, detailed MHS formation processes was studied; specifically, how Fe was transferred from the source (presumably basalts) to eventually form hematite spherules. Since MHS are not available, a terrestrial analogue, hematite spherules and associated lithologies from Hawaii, were studied in detail using Fe isotopes and elemental concentrations. Various types of alteration that the Hawaii samples experienced (acid-sulfate alteration, low-T and high-T hydrolytic alteration, and hydrothermal alteration under neutral to basic condition) were studied, and acid-sulfate alteration was found to be the only process among them that could effectively leach Fe from basalts. For the first time, the Fe isotope fractionation factor during acid-sulfate alteration was constrained very precisely by looking at rock slabs from a heterogeneously altered basalt. Furthermore, by studying the Fe isotopes of acid-sulfate altered rocks, tephras, and individual hematite spherules, the detailed hematite formation processes of Fe leaching, transport, mixing, precipitation and enrichment were reconstructed. The work provides valuable insights into MHS formation, and a prospective study for the future returned martian samples.

Chapter 3 investigates the volatile depletion in the Moon and in other planetary bodies. Although the giant impact hypothesis is currently the most widely accepted theory, and can explain many features of the Moon, there are still remaining questions concerning the hypothesis. One of the most outstanding problems is the volatile element depletion of the Moon. The Moon is very similar to the Earth in concentrations and isotopic compositions of refractory elements, but it has very low contents of volatile elements such as Zn, K and Rb (depletion by a factor of ~5). This volatile element depletion was thought to be due to volatile loss during the giant impact or through

degassing of lunar magma ocean (Paniello et al., 2012; Pringle and Moynier, 2017; Wang and Jacobsen, 2016). However, the isotopic compositions of these volatile elements in the Moon do not match quantitatively the extents of volatile loss based on evaporation theories, and the specific conditions under which the Moon lost its volatiles are, to a large extent, unconstrained. To better understand the process, a novel isotopic system, Rb isotopes, was developed and applied, for that Rb is volatile and very sensitive to volatilization, and that it makes a good comparison with the recently reported K isotopic system in the Earth-Moon system (Wang and Jacobsen, 2016) due to the very similar chemical behaviors of the two elements. Developing the separation and isotope measurement method of Rb constituted a major challenge because rubidium is a trace element and behaves very similarly to K, and separating it from major elements especially from K is extremely difficult. Chapter 3 describes the Rb isotope measurement method developed in this work over the past several years, including both the experimental tests on Rb purification using various types of resins and the analytical tests to measure Rb isotopes using MC-ICPMS. The method was applied to terrestrial and lunar rocks, chondrites, and martian meteorites, and high-precision (~±0.03 ‰) Rb isotope data were obtained. The Rb isotopic compositions of the bulk Earth and bulk Moon were estimated., the models that have been proposed to explain lunar volatile element depletion were tested by combining these results with published K isotope data. It can be concluded that lunar volatile element depletion most likely occurred in the two-phase (vapor and melt) proto-lunar disk, by draining the vapor phase to the Earth where the vapor was highly viscous due to magnetorotational instability. The Rb isotopic compositions of Mars and chondrites and the implications are also discussed.

Chapter 4 concludes the thesis with a summary of the work. Major findings are summarized, and future directions are discussed.

References

Amor, M., Busigny, V., Louvat, P., Gélabert, A., Cartigny, P., Durand-Dubief, M., Ona-Nguema, G., Alphandéry, E., Chebbi, I., Guyot, F., 2016. Mass-dependent and -independent signature of Fe isotopes in magnetotactic bacteria. Science 352, 705–708.

Anand, M., Russell, S.S., Blackhurst, R.L., Grady, M.M., 2006. Searching for signatures of life on Mars: an Fe-isotope perspective. Philosophical Transactions of the Royal Society B: Biological Sciences 361, 1715–1720.

Bau, M., Höhndorf, A., Dulski, P., Beukes, N.J., 1997. Sources of rare-earth elements and iron in Paleoproterozoic iron-formations from the Transvaal Supergroup, South Africa: evidence from neodymium isotopes. The Journal of Geology 105, 121–129.

Beard, B.L., Johnson, C.M., 1999. High precision iron isotope measurements of terrestrial and lunar materials. Geochimica et Cosmochimica Acta 63, 1653–1660.

Berglund, M., Wieser, M.E., 2011. Isotopic compositions of the elements 2009 (IUPAC Technical Report). Pure and applied chemistry 83, 397–410.

Bigeleisen, J., 1962. Correlation of tritium and deuterium isotope effects. Tritium in the Physical and Biological Sciences. V. 1. Proceedings of a Symposium.

Bigeleisen, J., Mayer, M.G., 1947. Calculation of equilibrium constants for isotopic exchange reactions. The Journal of Chemical Physics 15, 261–267.

Blanchard, M., Dauphas, N., Hu, M.Y., Roskosz, M., Alp, E.E., Golden, D.C., Sio, C.K., Tissot, F., Zhao, J., Gao, L., 2015. Reduced partition function ratios of iron and oxygen in goethite. Geochimica et Cosmochimica Acta 151, 19–33.

Braterman, P.S., Cairns-Smith, A.G., Sloper, R.W., 1983. Photo-oxidation of hydrated Fe^{2+}—significance for banded iron formations. Nature 303, 163.

Bullen, T.D., White, A.F., Childs, C.W., Vivit, D.V., Schulz, M.S., 2001. Demonstration of significant abiotic iron isotope fractionation in nature. Geology 29, 699–702.

Cairns-Smith, A.G., 1978. Precambrian solution photochemistry, inverse segregation, and banded iron formations. Nature 276, 807.

Cao, X., Liu, Y, 2011. Equilibrium mass-dependent fractionation relationships for triple oxygen isotopes. Geochimica et Cosmochimica Acta 75, 7435–7445.

Clayton, R.N., 2002. Solar System: Self-shielding in the solar nebula. Nature 415, 860.

Cloud, P., 1973. Paleoecological significance of the banded iron-formation. Economic Geology 68, 1135–1143.

Cloud, P.E., 1965. Significance of the Gunflint (Precambrian) Microflora: Photosynthetic oxygen may have had important local effects before becoming a major atmospheric gas. Science 148, 27–35.

Craddock, P.R., Dauphas, N., 2011a. Iron isotopic compositions of geological reference materials and chondrites. Geostandards and Geoanalytical Research 35, 101–123.

Craddock, P.R., Dauphas, N., 2011b. Iron and carbon isotope evidence for microbial iron respiration throughout the Archean. Earth and Planetary Science Letters 303, 121–132.

Craddock, P.R., Dauphas, N., Clayton, R.N., 2010. Mineralogical control on iron isotopic fractionation during lunar differentiation and magmatism. Lunar and Planetary Science Conference, p. 1230.

Craddock, P.R., Warren, J.M., Dauphas, N., 2013. Abyssal peridotites reveal the near-chondritic Fe isotopic composition of the Earth. Earth and Planetary Science Letters 365, 63–76.

Croal, L.R., Johnson, C.M., Beard, B.L., Newman, D.K., 2004. Iron isotope fractionation by Fe (II)-oxidizing photoautotrophic bacteria. Geochimica et Cosmochimica Acta 68, 1227–1242.

Crosby, H.A., Roden, E.E., Johnson, C.M., Beard, B.L., 2007. The mechanisms of iron isotope fractionation produced during dissimilatory Fe (III) reduction by *Shewanella putrefaciens* and *Geobacter sulfurreducens*. Geobiology 5, 169–189.

Dauphas, N., Cook, D.L., Sacarabany, A., Froehlich, C., Davis, A.M., Wadhwa, M., Pourmand, A., Rauscher, T., Gallino, R., 2008. Iron 60 evidence for early injection and efficient mixing of stellar debris in the protosolar nebula. Astrophysical Journal 686, 560–569.

Dauphas, N., Hu, M.Y., Baker, E.M., Hu, J., Tissot, F.L., Alp, E.E., Roskosz, M., Zhao, J., Bi, W., Liu, J., 2018. SciPhon: a data analysis software for nuclear resonant inelastic X-ray scattering with applications to Fe, Kr, Sn, Eu and Dy. Journal of Synchrotron Radiation 25, 1581–1599.

Dauphas, N., Roskosz, M., Alp, E.E., Golden, D.C., Sio, C.K., Tissot, F., Hu, M.Y., Zhao, J., Gao, L., Morris, R.V., 2012. A general moment NRIXS approach to the determination of equilibrium Fe isotopic fractionation factors: application to goethite and jarosite. Geochimica et Cosmochimica Acta 94, 254–275.

Dauphas, N., Schauble, E.A., 2016. Mass fractionation laws, mass-independent effects, and isotopic anomalies. Annual Review of Earth and Planetary Sciences 44, 709–783.

Dauphas, N., Van Zuilen, M., Wadhwa, M., Davis, A.M., Marty, B., Janney, P.E., 2004. Clues from Fe isotope variations on the origin of early Archean BIFs from Greenland. Science 306, 2077–2080.

Davis, A.M., Richter, F.M., Mendybaev, R.A., Janney, P.E., Wadhwa, M., McKeegan, K.D., 2015. Isotopic mass fractionation laws for magnesium and their effects on ^{26}Al–^{26}Mg systematics in solar system materials. Geochimica et Cosmochimica Acta 158, 245–261.

Faure, G., Mensing, T.M., 2005. Isotopes: principles and applications. Wiley & Sons, Inc., Hoboken, New Jersey.

Garrels, R.M., Perry, E.A., Mackenzie, F.T., 1973. Genesis of Precambrian iron-formations and the development of atmospheric oxygen. Economic Geology 68, 1173–1179.

Grilly, E.R., 1951. The vapor pressures of hydrogen, deuterium and tritium up to three atmospheres. Journal of the American Chemical Society 73, 843–846.

Heidenreich, J.E., III, Thiemens, M.H., 1983. A non-mass-dependent isotope effect in the production of ozone from molecular oxygen. The Journal of Chemical Physics 78, 892–895.

Heimann, A., Johnson, C.M., Beard, B.L., Valley, J.W., Roden, E.E., Spicuzza, M.J., Beukes, N.J., 2010. Fe, C, and O isotope compositions of banded iron formation carbonates demonstrate a major role for dissimilatory iron reduction in ~2.5 Ga marine environments. Earth and Planetary Science Letters 294, 8–18.

Hezel, D.C., Needham, A.W., Armytage, R., Georg, B., Abel, R.L., Kurahashi, E., Coles, B.J., Rehkämper, M., Russell, S.S., 2010. A nebula setting as the origin for bulk chondrule Fe isotope variations in CV chondrites. Earth and Planetary Science Letters 296, 423–433.

Huang, F., Zhang, Z., Lundstrom, C.C., Zhi, X., 2011. Iron and magnesium isotopic compositions of peridotite xenoliths from Eastern China. Geochimica et Cosmochimica Acta 75, 3318–3334.

Hulston, J.R., Thode, H.G., 1965. Variations in the S^{33}, S^{34}, and S^{36} contents of meteorites and their relation to chemical and nuclear effects. Journal of Geophysical Research 70, 3475–3484.

Johnson, C.M., Beard, B.L., Klein, C., Beukes, N.J., Roden, E.E., 2008a. Iron isotopes constrain biologic and abiologic processes in banded iron formation genesis. Geochimica et Cosmochimica Acta 72, 151–169.

Johnson, C.M., Beard, B.L., Roden, E.E., 2008b. The iron isotope fingerprints of redox and biogeochemical cycling in modern and ancient Earth. Annual Review of Earth and Planetary Sciences 36, 457–493.

Johnson, C.M., Skulan, J.L., Beard, B.L., Sun, H., Nealson, K.H., Braterman, P.S., 2002. Isotopic fractionation between Fe (III) and Fe (II) in aqueous solutions. Earth and Planetary Science Letters 195, 141–153.

Klein, C., 2005. Some Precambrian banded iron-formations (BIFs) from around the world: Their age, geologic setting, mineralogy, metamorphism, geochemistry, and origins. American Mineralogist 90, 1473–1499.

Klein, C., Beukes N.J., 1992. Time distribution, stratigraphy, and sedimentologic setting, and geochemistry of Precambrian iron-formation. Proterozoic Biosphere. J. W. Schopf and C. Klein, Eds., The Proterozoic Biosphere: A multidisciplinary study, Cambridge University Press, New York, 139–146.

Lee, C.T.A., Luffi, P., Plank, T., Dalton, H., Leeman, W.P., 2009. Constraints on the depths and temperatures of basaltic magma generation on Earth and other terrestrial planets using new thermobarometers for mafic magmas. Earth and Planetary Science Letters 279, 20–33.

Liu, Y., Spicuzza, M.J., Craddock, P.R., Day, J.M., Valley, J.W., Dauphas, N., Taylor, L.A., 2010. Oxygen and iron isotope constraints on near-surface fractionation effects and the composition of lunar mare basalt source regions. Geochimica et Cosmochimica Acta 74, 6249–6262.

Lyons, J.R., Young, E.D., 2005. CO self-shielding as the origin of oxygen isotope anomalies in the early solar nebula. Nature 435, 317.

Meija, J., Coplen, T.B., Berglund, M., Brand, W.A., De Bièvre, P., Gröning, M., Holden, N.E., Irrgeher, J., Loss, R.D., Walczyk, T., 2016. Isotopic compositions of the elements 2013 (IUPAC technical Report). Pure and applied chemistry 88, 293–306.

Maréchal, C.N., Télouk, P., Albarède, F., 1999. Precise analysis of copper and zinc isotopic compositions by plasma-source mass spectrometry. Chemical Geology 156, 251–273.

Marhas, K.K., Amari, S., Gyngard, F., Zinner, E., Gallino, R., 2008. Iron and nickel isotopic ratios in presolar SiC grains. Astrophysical Journal 689, 622.

Matsuhisa, Y., Goldsmith, J.R., Clayton, R.N., 1978. Mechanisms of hydrothermal crystallization of quartz at 250 °C and 15 kbar. Geochimica et Cosmochimica Acta 42, 173–182.

Mullane, E., Russell, S.S., Gounelle, M., 2005. Nebular and asteroidal modification of the iron isotope composition of chondritic components. Earth and Planetary Science Letters 239, 203–218.

Nebel, O., Mezger, K., Scherer, E.E., Münker, C., 2005. High precision determinations of $^{87}Rb/^{85}Rb$ in geologic materials by MC-ICP-MS. International Journal of Mass Spectrometry 246, 10–18.

Nebel, O., Mezger, K., van Westrenen, W., 2011. Rubidium isotopes in primitive chondrites: Constraints on Earth's volatile element depletion and lead isotope evolution. Earth and Planetary Science Letters 305, 309–316.

Needham, A.W., Porcelli, D., Russell, S.S., 2009. An Fe isotope study of ordinary chondrites. Geochimica et Cosmochimica Acta 73, 7399–7413.

Nie, N.X., Dauphas, N., Greenwood, R.C., 2017. Iron and oxygen isotope fractionation during iron UV photo-oxidation: Implications for early Earth and Mars. Earth and Planetary Science Letters 458, 179–191.

Nie, N.X., Dauphas, N., Zeng, H., Sio, C.K.I., Hu, J., Alp, E.E., Bi, W., Hu, M.Y., Spear, F.S., 2018. Prospects and pitfalls in calibrating nontraditional stable isotope geothermometers from metamorphic rocks: Insights from Mt. Moosilauke. AGU Fall Meeting Abstracts.

Paniello, R.C., Day, J.M.D., Moynier, F., 2012. Zinc isotopic evidence for the origin of the Moon. Nature 490, 376–379.

Papike, J.J., Hodges, F.N., Bence, A.E., Cameron, M., Rhodes, J.M., 1976. Mare basalts: crystal chemistry, mineralogy, and petrology. Reviews of Geophysics 14, 475–540.

Poitrasson, F., Delpech, G., Grégoire, M., 2013. On the iron isotope heterogeneity of lithospheric mantle xenoliths: implications for mantle metasomatism, the origin of basalts and the iron isotope composition of the Earth. Contributions to Mineralogy and Petrology 165, 1243–1258.

Poitrasson, F., Halliday, A.N., Lee, D.-C., Levasseur, S., Teutsch, N., 2004. Iron isotope differences between Earth, Moon, Mars and Vesta as possible records of contrasted accretion mechanisms. Earth and Planetary Science Letters 223, 253–266.

Pringle, E.A., Moynier, F., 2017. Rubidium isotopic composition of the Earth, meteorites, and the Moon: Evidence for the origin of volatile loss during planetary accretion. Earth and Planetary Science Letters 473, 62–70.

Pyper, J.W., Christensen, L.D., 1975. Equilibrium constants of hydrogen–deuterium–tritium self-exchange reactions in water vapor as studied with a pulsed molecular-beam quadrupole mass filter. The Journal of Chemical Physics 62, 2596–2599.

Russell, W.A., Papanastassiou, D.A., Tombrello, T.A., 1978. Ca isotope fractionation on the Earth and other solar system materials. Geochimica et Cosmochimica Acta 42, 1075–1090.

Schauble, E.A., 2004. Applying stable isotope fractionation theory to new systems. Reviews in Mineralogy and Geochemistry 55, 65–111.

Schoenberg, R., Blanckenburg, von, F., 2006. Modes of planetary-scale Fe isotope fractionation. Earth and Planetary Science Letters 252, 342–359.

Shahar, A., Young, E.D., Manning, C.E., 2008. Equilibrium high-temperature Fe isotope fractionation between fayalite and magnetite: an experimental calibration. Earth and Planetary Science Letters 268, 330–338.

Sossi, P.A., Nebel, O., Anand, M., Poitrasson, F., 2016a. On the iron isotope composition of Mars and volatile depletion in the terrestrial planets. Earth and Planetary Science Letters 449, 360–371.

Sossi, P.A., Nebel, O., Foden, J., 2016b. Iron isotope systematics in planetary reservoirs. Earth and Planetary Science Letters 452, 295–308.

Sossi, P.A., O'Neill, H.S.C., 2017. The effect of bonding environment on iron isotope fractionation between minerals at high temperature. Geochimica et Cosmochimica Acta 196, 121–143.

Tang, H., Dauphas, N., 2012. Abundance, distribution, and origin of ^{60}Fe in the solar protoplanetary disk. Earth and Planetary Science Letters 359, 248–263.

Teng, F.-Z., Watkins, J.M., Dauphas, N., Swainson, I., 2017. Non-traditional stable isotopes. Reviews in Mineralogy and Geochemistry, Volume 82, Mineralogical Society of America.

Thiemens, M.H., Heidenreich, J.E., 1983. The mass-independent fractionation of oxygen: A novel isotope effect and its possible cosmochemical implications. Science 219, 1073–1075.

Thiemens, M.H., Jackson, T., 1987. Production of isotopically heavy ozone by ultraviolet light photolysis of O2. Geophysical Research Letters 14, 624–627.

Trappitsch, R., Stephan, T., Savina, M.R., Davis, A.M., Pellin, M.J., Rost, D., Gyngard, F., Gallino, R., Bisterzo, S., Cristallo, S., 2018. Simultaneous iron and nickel isotopic analyses of presolar silicon carbide grains. Geochimica et Cosmochimica Acta 221, 87–108.

Urey, H.C., 1947. The thermodynamic properties of isotopic substances. Journal of the Chemical Society (Resumed) 562–581.

Völkening, J., Papanastassiou, D.A., 1989. Iron isotope anomalies. Astrophysical Journal 347, L43–L46.

Waight, T., Baker, J., Willigers, B., 2002. Rb isotope dilution analyses by MC-ICPMS using Zr to correct for mass fractionation: towards improved Rb–Sr geochronology? Chemical Geology 186, 99–116.

Wang, K., Jacobsen, S.B., 2016. Potassium isotopic evidence for a high-energy giant impact origin of the Moon. Nature 538, 487–490. doi:10.1038/nature19341

Wang, K., Moynier, F., Dauphas, N., Barrat, J.-A., Craddock, P., Sio, C.K., 2012. Iron isotope fractionation in planetary crusts. Geochimica et Cosmochimica Acta 89, 31–45.

Welch, S.A., Beard, B.L., Johnson, C.M., Braterman, P.S., 2003. Kinetic and equilibrium Fe isotope fractionation between aqueous Fe (II) and Fe (III). Geochimica et Cosmochimica Acta 67, 4231–4250.

Weyer, S., Anbar, A.D., Brey, G.P., Münker, C., Mezger, K., Woodland, A.B., 2005. Iron isotope fractionation during planetary differentiation. Earth and Planetary Science Letters 240, 251–264.

Weyer, S., Ionov, D.A., 2007. Partial melting and melt percolation in the mantle: the message from Fe isotopes. Earth and Planetary Science Letters 259, 119–133.

White, W.M., 2013. Geochemistry. John Wiley & Sons.

Widdel, F., Schnell, S., Heising, S., Ehrenreich, A., Assmus, B., Schink, B., 1993. Ferrous iron oxidation by anoxygenic phototrophic bacteria. Nature 362, 834.

Wiesli, R.A., Beard, B.L., Taylor, L.A., Johnson, C.M., 2003. Space weathering processes on airless bodies: Fe isotope fractionation in the lunar regolith. Earth and Planetary Science Letters 216, 457–465.

Wood, B.J., Smythe, D.J., Harrison, T., 2019. The condensation temperatures of the elements: A reappraisal. American Mineralogist: Journal of Earth and Planetary Materials 104, 844–856.

Wu, L., Beard, B.L., Roden, E.E., Johnson, C.M., 2011. Stable iron isotope fractionation between aqueous Fe (II) and hydrous ferric oxide. Environmental science & technology 45, 1847–1852.

Yamaguchi, K.E., Johnson, C.M., Beard, B.L., Ohmoto, H., 2005. Biogeochemical cycling of iron in the Archean–Paleoproterozoic Earth: constraints from iron isotope variations in sedimentary rocks from the Kaapvaal and Pilbara Cratons. Chemical Geology 218, 135–169.

Young, E.D., Galy, A., Nagahara, H., 2002. Kinetic and equilibrium mass-dependent isotope fractionation laws in nature and their geochemical and cosmochemical significance. Geochimica et Cosmochimica Acta 66, 1095–1104.

Yurimoto, H., Kuramoto, K., 2004. Molecular cloud origin for the oxygen isotope heterogeneity in the solar system. Science 305, 1763–1766.

Zhang, J., Dauphas, N., Davis, A.M., Leya, I., Fedkin, A., 2012. The proto-Earth as a significant source of lunar material. Nature Geoscience 2018 5, 251–255. doi:10.1038/ngeo1429

Zhang, J., Huang, S., Davis, A.M., Dauphas, N., Hashimoto, A., Jacobsen, S.B., 2014. Calcium and titanium isotopic fractionations during evaporation. Geochimica et Cosmochimica Acta 140, 365–380.

Zhao, X., Zhang, H., Zhu, X., Tang, S., Tang, Y., 2010. Iron isotope variations in spinel peridotite xenoliths from North China Craton: implications for mantle metasomatism. Contributions to Mineralogy and Petrology 160, 1–14.

Zhao, X., Zhang, H., Zhu, X., Tang, S., Yan, B., 2012. Iron isotope evidence for multistage melt–peridotite interactions in the lithospheric mantle of eastern China. Chemical Geology 292, 127–139.

2 IRON ISOTOPE GEOCHEMISTRY

2.1 Introduction

Banded Iron Formations (BIFs) are chemical sedimentary rocks composed primarily of laminated iron-rich and silica-rich/iron-poor layers that are confined to the Precambrian, with most occurrences found in the Archean (James, 1954). The iron source is thought to have been predominantly marine hydrothermal ferrous iron Fe(II) (Bau et al., 1997; Dymek and Klein, 1988; Holland, 1973; Jacobsen and Pimentel-Klose, 1988; Klein, 2005), but continental contributions have also been identified (Alexander et al., 2009; Haugaard et al., 2013; Li et al., 2015; Miller and O'Nions, 1985; Viehmann et al., 2014; Wang et al., 2014). In the modern oxic ocean, the solubility and residence time of iron are low, but the globally anoxic conditions in the Archean allowed hydrothermal Fe(II) to be transported over wide distances until it was oxidized to less soluble ferric iron Fe(III), which precipitated to form BIFs. Despite decades of study, the nature of the oxidation mechanism responsible for BIF precipitation has remained elusive. Three scenarios have been proposed to account for Fe(II) oxidation in such an anoxic environment:

1) In the photic zone, local "oxygen oases" could have been produced by the photosynthetic activity of cyanobacteria. Oxygen thus produced could have oxidized dissolved Fe(II) into insoluble Fe(III) that would have rapidly precipitated and sank to form layered deposits known as BIFs (Cloud, 1973; Cloud, 1965). In the following, this is referred to as "O_2-mediated oxidation".
2) A biogenic alternative to O_2-mediated oxidation is anoxygenic photosynthesis, whereby $Fe(II)_{aq}$ is used as the electron donor in place of water (*e.g.,* Croal et al., 2004; Garrels et al., 1973; Hartman, 1984; Kappler et al., 2005; Widdel et al., 1993). In this scenario carbon

fixation and reduction from CO_2 to organic carbon is coupled to intracellular oxidation of Fe(II) into Fe(III).

3) Without oxygen and ozone, the Archean atmosphere was largely transparent to UV photons that could reach the surface layers of the oceans. It was demonstrated experimentally that such UV could induce oxidation of Fe(II) into Fe(III) while releasing H_2 in a process known as photo-oxidation (*e.g.*, Braterman et al., 1983; Cairns-Smith, 1978). Among the three mechanisms considered for BIF formation, this is the only process that does not involve biology.

The viability of the abiological UV photo-oxidation for BIF formation was demonstrated by Braterman et al. (1983). Their experiments used an argon-flushed Fe(II)-containing solution illuminated by a medium-pressure mercury UV lamp. They found that the effective UV wavelength is pH dependent. At near-neutral pH (pH > 6.5), $FeOH^+$ can efficiently absorb 300-450 nm UV light, leading to high Fe(II) oxidation rates. This complex, however, is not abundant at low pH (4.8-6.1) where 100-280 nm UV light induces the oxidation of dissolved Fe(II) to dissolved Fe(III). Anbar and Holland (1992) studied the photo-oxidation of manganese and found that Mn(II) oxidation was much less effective compared to that of Fe(II), the Mn/Fe ratio of precipitates was consistent with field observations of Mn/Fe ratios in BIFs.

The main argument against photo-oxidation was laid out by Konhauser et al. (2007). They performed photo-oxidation experiments with Fe(II) solutions containing chemical species expected to be present in the Archean oceans (Si and Ca specifically). The experiments showed that most $Fe(II)_{aq}$ precipitated rapidly as Fe(II) silicate mineral greenalite and Fe(II) carbonate siderite, hindering Fe(II) photo-oxidation. This mineral precipitation does not occur in oxidation pathways involving O_2 or anoxygenic Fe(II)-oxidizing bacteria. This was used as a circumstantial

argument against photo-oxidation; implicating bacteria as a cause of BIF precipitation. Given the uncertainties surrounding the influences of the faint young Sun and weathering feedbacks on Earth's climate in the Archean, it is not clear to what extent the temperature of 40 °C and high pCO_2-high dissolved silica concentrations used in the experiments of Konhauser et al. (2007) are representative of the conditions that prevailed in Earth's oceans at that time.

Several aspects of this study are worth further scrutiny. Firstly, the photo-oxidation efficiency of UV-A (315–400 nm) was negligible in their experiment, in contradiction with earlier studies indicating that light between 300–450 nm was effective at oxidizing iron when pH > 6.5 (Anbar and Holland, 1992; Braterman et al., 1983). Secondly, while it is not clear how $Fe(II)_{aq}$ would have remained dissolved and been carried over wide distances under the low solubility conditions examined by Konhauser et al (2007), yet iron oxides are an important component of BIFs (Klein, 2005). Thirdly, in the photo-oxidation study of Konhauser et al. (2007), the pH decreased from near neutral to pH~3.5 after approximately 0.1 mM $Fe(II)_{aq}$ was oxidized. pH decrease is expected to slow down the photo-oxidation process significantly (Braterman et al., 1983). Precambrian seawater was probably near neutral or slightly alkaline (Grotzinger and Kasting, 1993; Kempe and Degens, 1985; Morse and Mackenzie, 1998). Under such conditions, the rate of iron photo-oxidation is greatly enhanced by the presence of $FeOH^+$ species. Therefore, the photo-oxidation rate in Konhauser et al. (2007) may have been underestimated.

In this work, we explore the possibility that photo-oxidation was involved in BIF formation by experimentally determining iron and oxygen isotope fractionation induced by this process and comparing the results with BIF isotopic signatures. Iron isotope fractionation between Fe(III) precipitate and dissolved Fe(II) in O_2-mediated oxidation and in anoxygenic photosynthesis has been measured previously (Bullen et al., 2001; Croal et al., 2004), and the two processes yield

similar fractionation factors. However, the extent to which iron isotopes can be fractionated by photo-oxidation is still unknown. The only experiment on photo-oxidation-induced iron isotope fractionation was conducted at a very low pH of ~3 and yielded a fractionation between Fe(III) precipitate and dissolved Fe(II) of +2.5‰ for the $^{56}Fe/^{54}Fe$ ratio (Staton et al., 2006). The results were only reported in abstract form and are not directly applicable to the near-neutral pH conditions that may have prevailed in the Archean ocean (between ~6.5 and 8 depending on the roles of high pCO_2 and alteration of ultramafic rocks; Grotzinger and Kasting, 1993; Kempe and Degens, 1985; Morse and Mackenzie, 1998).

Photo-chemical reactions involving gaseous species of oxygen and sulfur are known to affect the isotopic compositions of those elements in ways that do not follow the rules of mass dependent fractionation (*e.g.*, Chakraborty and Bhattacharya, 2003; Farquhar et al., 2001; Lyons 2007; Thiemens and Heidenreich, 1983). Furthermore, even in systems that do exhibit mass-dependent behaviors, considerable information can be gleaned from a detailed investigation of the relevant mass-fractionation law, as different processes can produce distinct slopes in three-isotope diagrams (*e.g.*, Dauphas and Schauble, 2016). Therefore, in addition to measuring the extent of O and Fe isotope fractionation, we also examine the mass-fractionation laws, or departure therefrom, imparted by iron photo-oxidation.

Photo-oxidation has also been invoked to explain the oxidation of Fe on ancient Mars. (*e.g.*, Burns, 1993; Burns and Fisher, 1993; Hurowitz et al., 2010; Lundgreen et al., 1989; Schaefer, 1996). Martian hematite spherules, or martian blueberries are the product of Fe oxidation. Photo-oxidation of Fe on Mars is evaluated in light of our new results. A terrestrial analogue, Hawaii hematite spherules and associated lithologies, is studied for detailed Fe transport during hematite formation.

2.2 Iron isotope measurement method

2.2.1 Sample preparation

Samples obtained for analyses come in many forms. For example, the products of photo-oxidation experiments are $Fe(II)_{aq}$ solutions and Fe(III) precipitates, and natural samples are often obtained in rock chunks and chips. In the former case, samples are transferred to Teflon beakers and dried on a hotplate at 130 °C. In the latter case, samples are crushed and powdered manually in an agate mortar. The mortar is precleaned by crushing fine silica sand grains in Milli-Q water at least twice, followed by rinsing with Milli-Q water. After crushing, samples are transferred to clean Teflon beakers for digestion.

A general digestion protocol was used to treat most of the samples. For some particular samples, such as the single hematite spherules, the procedure below was adapted to achieve a better result (Sect. 2.4.3). All samples were digested in Savillex Teflon beakers, precleaned with boiling aqua regia (3:1 mixture of HCl and HNO_3, on hotplates overnight at 130 °C) three times, followed by boiling Mill-Q water. The general digestion protocol includes adding and drying acid mixtures on hotplates repeatedly. All the steps are carried out on hot plates at 130 °C if without $HClO_4$. If $HClO_4$ is used for getting rid of organics, a drying temperature of 180 °C is necessary. The first step is to attack samples with 2:1 mixture of HF and HNO_3 (normally 1mL HF + 0.5 mL HNO_3 for ~10-20 mg rock powder), plus several drops of $HClO_4$ if necessary ($HClO_4$ is very effective in dissolving organics, and samples without organics can skip it). Samples are capped and placed on hotplate at 130 °C for at least overnight, and then dried and taken back to acid mixture of 3:1 HCl and HNO_3 (0.75 mL HCl and 0.25 mL HNO_3 for ~ 10-20 mg rock powder), placed on hotplates overnight with lid closed. The samples are then treated with 3:1 mixture of HCl and HNO_3 another time and dried on hotplates, then dissolved in 0.5 mL 6M HCl. If the solution obtained is clear

with no residue left, then it is ready for column chromatography. If there are still residual particles, the following steps are performed.

1) If the residue does not contain Fe, then it can be ignored or discarded by centrifugation. However, this treatment is very rarely performed since there is no easy way to tell if the residue is Fe free or not.
2) Samples are placed in Parr bombs in a mixture of 3:1 HF and HNO_3 at 180 °C for at least 3 days for complete dissolution of refractory phases. Then the samples are taken out of the bombs, treated with acid mixture of 3:1 concentrated HCl and HNO_3 twice as described above, and then dissolved in 6M HCl.

2.2.2 Iron extraction chromatography

The chemical procedure for purifying Fe from unwanted elements is the one routinely used in our laboratory (Dauphas et al., 2004a; 2009; Dauphas and Rouxel, 2006). The procedure is based on the partitioning behavior of elements on anion exchange resin (Strelow, 1980). In general, matrix elements are eluted while Fe is strongly retained on the resin in more concentrated HCl, and Fe is subsequently eluted using diluted HCl. Chromatography columns are made by loading 1 mL AG1-X8 (200-400 mesh) resin into a disposable Bio-Rad Poly-Prep empty column (10 mL total reservoir of 8 mm diameter and 90 mm length). Samples are purified with the columns following the procedure outline in Table 2.1. The procedure is repeated twice.

One thing that requires caution is the total mass of Fe loaded to a column. As Fe is a major element, overloading of Fe can happen if a large sample mass is used or if a sample is very Fe-rich. Overloading can cause some Fe to be eluted early and thus some Fe loss. Because Fe isotopes are fractionated on the column (light and heavy isotopes move in different speeds), loss of Fe can

potentially lead to a fractionated isotopic composition in the collected elution. To avoid the problem, the total Fe mass loaded to a column should be less than 5 mg.

Table 2.1 Chromatography procedure for Fe extraction and purification. Anion resin AG1-X8 200-400 mesh is used. Resin volume is 1 mL.

Step	Acid	Volume	Comment
Column cleaning	Mill-Q H_2O	10 mL	Waste
	1M HNO_3	5 mL	Waste
	Mill-Q H_2O	10 mL	Waste
	0.4M HCl	9 mL	Waste
	Mill-Q H_2O	5 mL	Waste
Conditioning	6M HCl	2 mL	Waste
Sample loading	6M HCl	0.25 mL	Waste
Matrix elution	6M HCl	8 mL	Waste
Iron elution	0.4M HCl	9 mL	Collect Fe

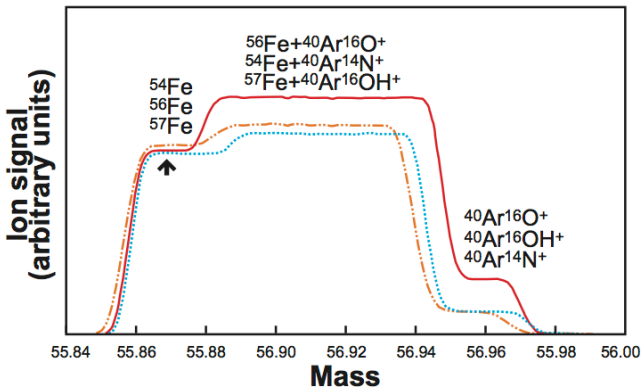

Figure 2.1 Iron isotopes scanned with the MC-ICPMS at the University of Chicago. Iron in 2% HNO_3 was introduced into the mass spectrometer using a dual cyclonic-Scott type spray chamber. The scan was done in medium resolution. The peak shapes are a combination of iron isotopes and argides. Iron isotopes are measured on the left flat-topped peak shoulders (indicated with an arrow). Iron-58 is not shown which has very low abundance and is usually not reported. Iron-54 and ^{57}Fe signal intensities are their real intensities multiplied by factors of 15 and 44 respectively.

2.2.3 Iron mass spectrometry

Iron concentration and isotope analyses were carried out on a Thermo Scientific Neptune MC-ICPMS at the University of Chicago. The extent of isotope fractionation (δ-values) and the departure from a reference mass-fractionation law (ε-values) were measured separately since they require different instrumental settings.

δ-value analyses were performed using sample-standard-bracketing method based on Dauphas et al. (2009). Samples after column chromatography were dried and dissolved in 2% HNO_3, and were introduced into the instrument as 1 ppm solutions (corresponding to ~6–8 V signal intensity on ^{56}Fe in medium resolution) with a dual cyclonic-Scott type quartz spray chamber. A spray chamber (*i.e.,* wet plasma) normally leads to lower sample introduction efficiency and higher argide interference compared with a desolvating nebulizer (*i.e.,* dry plasma), but signals and instrumental mass bias are much more stable. Normal Ni sampler and skimmer cones were installed for the measurements. Measurements were made in medium resolution mode, using the static cup configuration shown in Table 2.2. Medium resolution is good enough to resolve the argide peaks from Fe peaks, and measurements were made on the flat shoulders of Fe peaks (Fig. 2.1).

Table 2.2 Cup configuration for iron isotope measurement.

Configuration	L4	L2	Axial	H1	H2	H4
Mass monitored	53	54	56	57	58	60
Isotope measured	^{53}Cr	^{54}Fe+^{54}Cr	^{56}Fe	^{57}Fe	^{58}Fe+^{58}Ni	^{60}Ni
Amplifier (Ω)	10^{11}	10^{11}	10^{11} for δ-values 10^{10} for ε-values	10^{11}	10^{11}	10^{11}

For ε-value measurements, solutions containing ~1–2 ppm Fe in 2 % HNO_3 were introduced into the plasma torch with an Aridus II desolvating nebulizer without auxiliary N_2.

Desolvating nebulizers have two advantages: 1) they can significantly increase the signal intensity by increasing the fraction of atoms making it into the torch (*i.e.,* high transport efficiency), and 2) they can significantly reduce argide peaks by removing the solvent (*i.e.,* dry plasma) that carries N, O, and H (in the forms of H_2O and HNO_3). A 10^{10} Ω amplifier resistor was used for ^{56}Fe since the signal intensity was approximately 180 V with a combination of jet sampler and X skimmer cones (conventional 10^{11} Ω amplifier resistors are limited <50 V). The measurements were performed in high resolution mode, so that ArN^+, ArO^+, or $ArOH^+$ peak tail interferences were kept to a minimum. Sample-standard-bracketing was used to correct for instrumental fractionation, and the exponential law was used for calculating ε values by fixing the $^{57}Fe/^{54}Fe$ ratio to 0.362549 (the ratio of IRMM-014).

For both δ-value and ε-value measurements, each measurement consisted of 30 to 60 cycles of 4.194 s integration time. Take-up time was 90 s and rinsing time was 120 s. For each sample/standard analysis, typically nine replicate measurements were performed. Background was corrected for by subtracting from the sample signals the signal intensities of 2 % HNO_3 that was used to prepare sample solutions. The contribution of ^{54}Cr and ^{58}Ni to the ^{54}Fe and ^{58}Fe signals were also corrected for, by monitoring ^{53}Cr and ^{60}Ni, and assuming the exponential law for the mass fractionations of $^{58}Ni/^{60}Ni$ and $^{54}Cr/^{53}Cr$ in the mass spectrometer (Maréchal et al., 1999)

$$R^{i/j}_{measured} / R^{i/j}_{true} = (m_i/m_j)^{\beta}, \quad (2.1)$$

where β is the exponential mass fractionation factor, and can be calculated by applying this relationship to $^{57}Fe/^{56}Fe$ ratio as the two isotopes do not have isobaric interferences. For example, the amount of ^{54}Cr deducted from ^{54}Fe is

$$^{54}Cr = {}^{53}Cr_{measured} (^{54}Cr/^{53}Cr)_{ture} (m_{54}/m_{53})^{\beta}, \quad (2.2)$$

$$\beta = \ln[(^{57}Fe/^{56}Fe)_{measured}/(^{57}Fe/^{56}Fe)_{ture}]/\ln(m_{57}/m_{56}), \quad (2.3)$$

with $(^{54}Cr/^{53}Cr)_{true}$ and $(^{57}Fe/^{56}Fe)_{true}$ of 0.2489 and 0.0231 (*i.e.,* the ratios of natural abundances), respectively. The Fe isotopic compositions of samples were calculated by averaging over the replicated measurements, and errors were estimated as

$$\sigma_{sample} = 2\sigma_{standard}/\mathrm{sqrt}(n), \tag{2.4}$$

where $\sigma_{standard}$ is the standard deviation of the standards (bracketed by two adjacent standards) through an analytical session (~12 hours), and n the number of replicates for samples (typically nine). All iron isotope data are reported relative to the average isotopic composition of two bracketing standard solutions of IRMM524, whose isotopic composition is identical to IRMM-014 (Craddock and Dauphas, 2010). The δ and ε values in units of per mil (‰) and per ten thousand are given by,

$$\delta^{i}Fe = [(\,^{i}Fe/^{54}Fe)_{sample}/\,(^{i}Fe/^{54}Fe)_{\,IRMM014} - 1] \times 10^{3}, \tag{2.5}$$

$$\varepsilon^{i}Fe = [(\,^{i}Fe/^{54}Fe)^{*}_{sample}/\,(^{i}Fe/^{54}Fe)^{*}_{\,IRMM014} - 1] \times 10^{4}, \tag{2.6}$$

where i=56, 57, or 58, and the star superscript indicates that the ratios were corrected for mass fractionation by internal normalization to a fixed $^{57}Fe/^{54}Fe$ "true" ratio of 0.362549 using the exponential law,

$$\begin{aligned} \ln\,(^{i}Fe/^{54}Fe)^{*}_{sample} &= \ln(^{i}Fe/^{54}Fe)_{measured} \\ &\quad - \{\ln[(^{57}Fe/^{54}Fe)_{measured}/(^{57}Fe/^{54}Fe)_{true}] \times \ln(m_i/m_{54}) \,/\, \ln(m_{57}/m_{54})\}. \end{aligned} \tag{2.7}$$

The bracketing standards were internally normalized to the same $^{57}Fe/^{54}Fe$ ratio using the exponential law. δ' and ε' notations are also used, which are slightly different expressions from δ and ε notations and are more suitable for describing small departures from a mass dependent fractionation law,

$$\delta'\,^{i}Fe = \ln\,[(^{i}Fe/^{54}Fe)_{sample}/(^{i}Fe/^{54}Fe)_{IRMM\text{-}014}] \times 10^{3}, \tag{2.8}$$

$$\varepsilon'\,^{i}Fe = \ln\,[(^{i}Fe/^{54}Fe)^{*}_{\,sample}/(^{i}Fe/^{54}Fe)^{*}_{IRMM\text{-}014}] \times 10^{4}. \tag{2.9}$$

2.3 UV photo-oxidation as a possible pathway to BIF formation

2.3.1 UV photo-oxidation experiments

2.3.1.1 Experimental setup

The photo-oxidation reactions were conducted in an Ace Glass photo-chemical apparatus (Fig. 2.2). The main body consists of three parts: 1) a 450-Watt Hanovia medium pressure Hg lamp inserted into the center of an immersion well/reaction vessel to serve as a UV source. This lamp delivers a relatively broad and featureless spectrum between 220 and 1370 nm, and is a good proxy for solar light; 2) a quartz immersion well around the lamp connected to a chiller for cooling the system, and 3) a tightly sealed 500 mL borosilicate glass reaction vessel. The vessel has three ports that are used for Fe(II) injection, sampling, and temperature monitoring. UV photons can be damaging to the eyes and generate toxic ozone, so the whole apparatus is placed in a nonreflective enclosure cabinet connected to an exhaust duct hose. The door of the cabinet has an automatic switch that turns off the UV light in case of inadvertent opening.

An air-tight Fe(II) injection section was designed to ensure that O_2 plays no role in Fe(II) oxidation. This section uses Ar-flushing lines, a syringe and a flask filled with Milli-Q water. The Fe(II) salt of $(NH_4)_2Fe(SO_4)_2 \cdot 6H_2O$ in solid form was placed in the syringe. It was dissolved by deoxygenated water just before injection. The sampling section was placed in an Ar-filled glove bag to further avoid air infiltration. It consisted of five sampling lines similar to the one depicted in Fig. 2.2. For each line, two syringes and one 0.1 μm Sartorius™ Minisart™ HF syringe filter were used. Two syringes were used to collect sample aliquots because Fe(III) precipitates tend to clog the filters, which makes it difficult to efficiently draw liquid. Pushing from one syringe to another allows one to apply more force. The detailed steps of an iron photo-oxidation experiment are shown in Fig. 2.2.

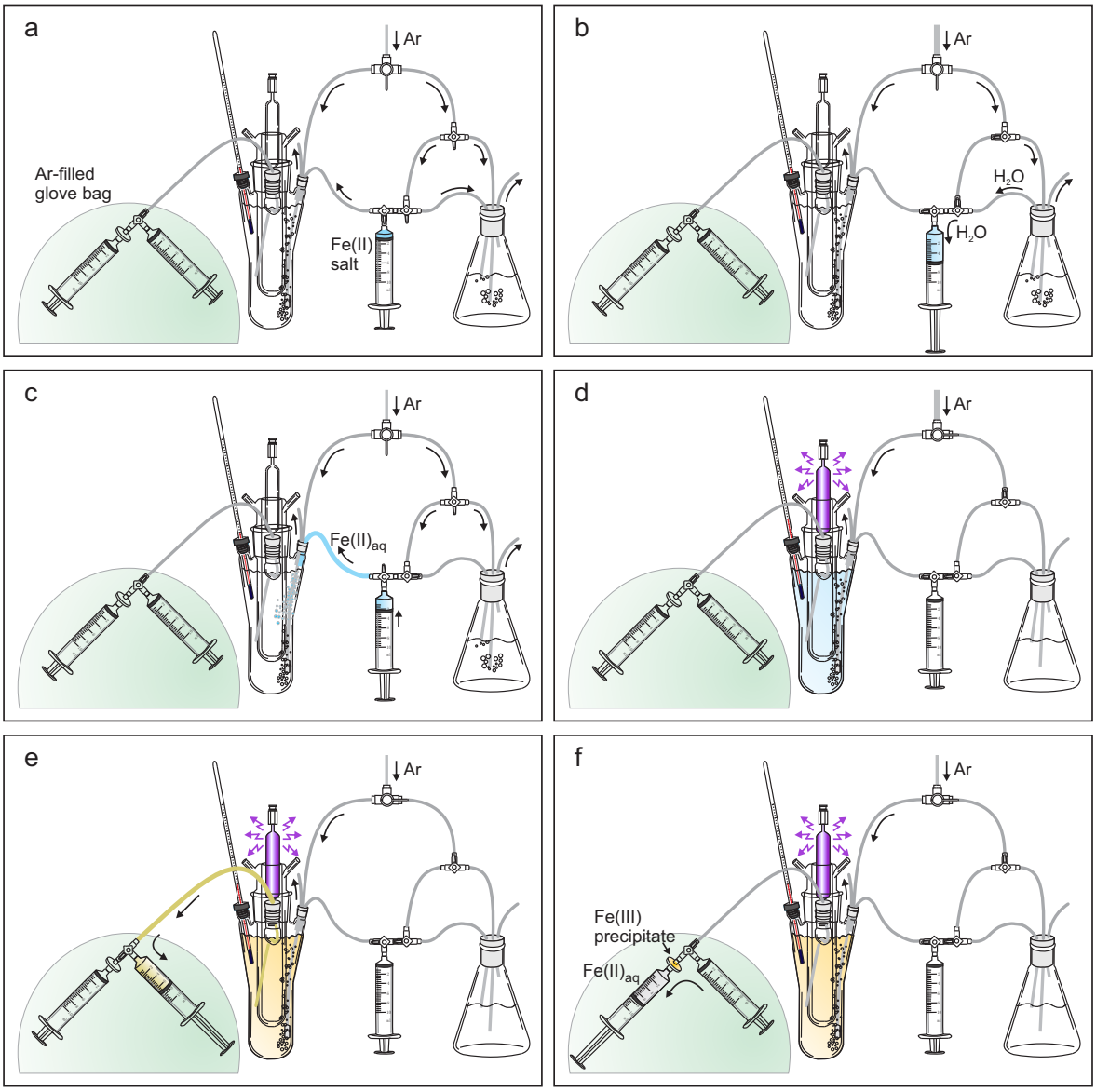

Figure 2.2 Detailed steps in an iron photo-oxidation experiment. (a) About 360 mL borate buffer solution is added to the reaction vessel. Fe(II) salt is placed in the syringe between the reaction vessel and the Mill-Q flask. High-purity argon gas ($O_2 \leq 1$ ppm) flows through the system for 3–4 hours to remove O_2. All the syringes are actuated several times to remove trapped O_2. (b) After the system is deoxygenated, the Fe(II) salt is dissolved in the syringe by drawing some O_2-free water from the flask. (c) Dissolved Fe(II) is added to the buffer solution in the reactor. (d) The UV lamp is turned on. Ferric iron precipitate starts to form due to photo-oxidation of $Fe(II)_{aq}$. (e) A syringe in the sampling section is used to draw an aliquot of the liquid-precipitate mixture from the reaction vessel. (f) The mixture is pushed through a filter into a second syringe to separate Fe(II)-bearing liquid and Fe(III) precipitate.

About 360 mL of borate buffer solution was added to the reaction vessel to keep the reaction at a constant pH of ~7.3. Without the buffer, iron photo-oxidation would drive the solution to more acidic conditions through the reaction $Fe^{2+} + 2H_2O \rightarrow FeO(OH) \downarrow + 2H^+ + 1/2\ H_2 \uparrow$, thereby changing the speciation of iron and the rate of iron oxidation. The buffer was made by adding 0.5 mol L^{-1} NaOH solution to 500 mL 0.6 mol L^{-1} H_3BO_3 solution to a final pH of 7.3. The H_3BO_3 solution was made in volumetric flasks by dissolving 18.55 g of solid H_3BO_3 in 500 mL milli-Q water at room temperature. No pH change was observed during the experiments, consistent with the prediction that the pH should only decrease by about 0.2 units even when all dissolved Fe(II) was oxidized.

High-purity argon gas ($O_2 \leq 1$ ppm) was passed through the system to remove O_2. All the syringes were actuated several times to remove trapped O_2. After the system was deoxygenated, the Fe(II) salt was dissolved in the syringe by drawing some O_2-free water from the flask. Dissolved Fe(II) was then injected into the deoxygenated buffer solution in the reaction vessel and the UV lamp was turned on. A Fe(III) precipitate started to form due to photo-oxidation of $Fe(II)_{aq}$. Several syringes in the sampling section were used to draw an aliquot of the liquid-precipitate mixture from the reaction vessel (a magnetic stirrer was used in the vessel to suspend the precipitate and homogenize the mixture) at regular intervals. The mixture was pushed through a filter into a second syringe. After filtration, the Fe(II)-bearing liquid was in the second syringe while the Fe(III) precipitate was on the filter. All dissolved Fe(II) in the filter was flushed by running deoxygenated Milli-Q water through it and recovering the flushed solution in a pre-cleaned centrifuge tube where it was combined with Fe(II) liquid from the second syringe. The Fe(III) precipitate was recovered from the filter in the glove bag by flushing the filter in the opposite direction with deoxygenated Milli-Q water.

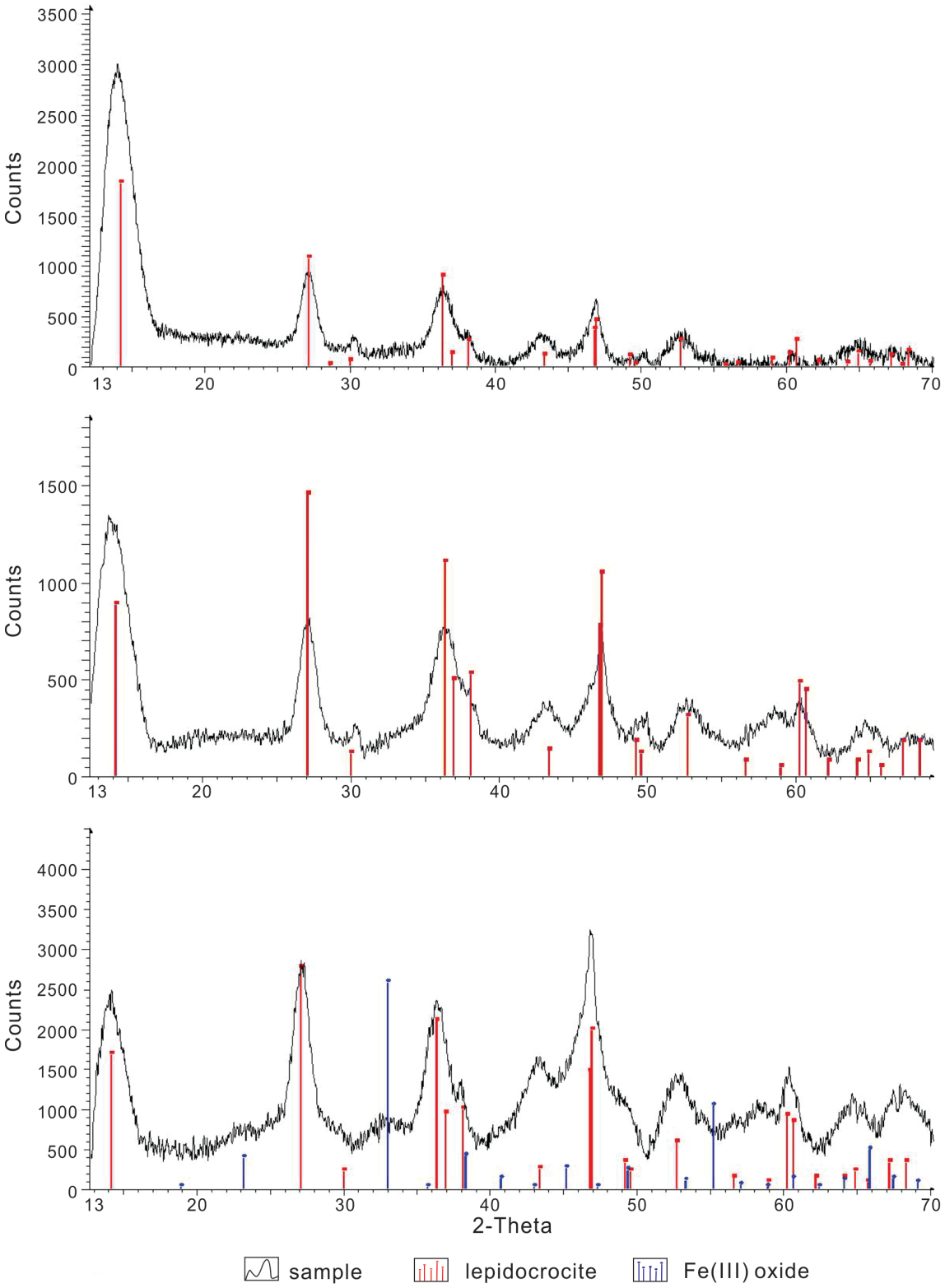

Figure 2.3 XRD patterns of Fe(III) precipitates. The precipitates are mainly lepidocrocite, with minor amount of other Fe(III) oxides.

In the course of the experiments, the temperature increased rapidly (due to the heating of the lamp) at the beginning (~1 °C/min) and stabilized to a steady value of ~45 °C after 20–30 min. Because oxygen isotopic analyses require more precipitate mass than Fe isotopic analyses, two distinct sets of experiments were undertaken: experiment #1 for Fe and experiment #2 for O. The initial concentration of Fe(II) was ~100 ppm or 1.8 mM, which is equivalent to the Fe concentration of some modern deep sea vents (*e.g.,* Edmond et al., 1982) and surface water compositions modeled for the Burns Formation at Meridiani Planum on Mars (Tosca and McLennan, 2009). In experiment #1, 5 aliquots of ~7 mL each of the sample slurry mixture were sampled successively (the first one was sampled before turning on the UV lamp). In experiment #2, 6 aliquots of 18 mL each were sampled. The Fe(II) aliquot and a small fraction of the Fe(III) precipitate from experiment #1 were taken for iron isotopic analyses. The Fe(III) precipitate from experiment #2 was collected, rinsed with Milli-Q water and air dried in a fume hood overnight for oxygen isotopic analysis.

2.3.1.2 Experimental results

Orange-colored particles formed upon irradiation. Orange-colored particles were observed in previous photo-oxidation experiments (Anbar and Holland, 1992; Braterman et al., 1983; Konhauser et al., 2007). XRD analyses indicate that those produced in our experiments were mainly lepidocrocite, with a small quantity of other Fe(III) oxides (Fig. 2.3), instead of amorphous two-line ferrihydrite seen previously (Konhauser et al., 2007). This difference in the nature of the precipitate may stem from differences in pH and silica contents between the two sets of experiments (Mayer and Jarrell, 1996; Schwertmann and Thalmann, 1976). Lepidocrocite is expected to precipitate at near neutral pH (5–7) when Si/Fe ratio of the solution is lower than ~0.01 (our experimental conditions), whereas ferrihydrite would precipitate at a lower pH and a higher

Si/Fe ratio (conditions in Konhauser et al., 2007). Even with active cooling (water surrounding the reaction vessel chilled to 5 °C) and the lamp only inserted half-way, the temperature of the solution increased from ~20 °C to ~45 °C. Higher final temperatures of 60–90 °C were achieved if the lamp was inserted more deeply. At these high temperatures, black-colored particles formed very rapidly; reaching completion in less than half an hour. These black particles were magnetite since they were attracted to a magnet; as was previously documented by Konhauser et al. (2007).

In control experiments below 50 °C, when the UV lamp was switched off, no particles were produced. Above 50 °C, a pale greenish colloid formed, which thermodynamic calculations show that it is most likely ferrous hydroxide $Fe(OH)_2$ (Fig. 2.4). Pure ferrous hydroxide is white in color and the greenish tint probably results from the presence of trace amounts of Fe(III), which could be due to oxidation by O_2 introduced as impurities in Ar gas. Upon exposure to air its color changed to orange within minutes, confirming that the colloid formed above 50 °C contained mainly Fe(II).

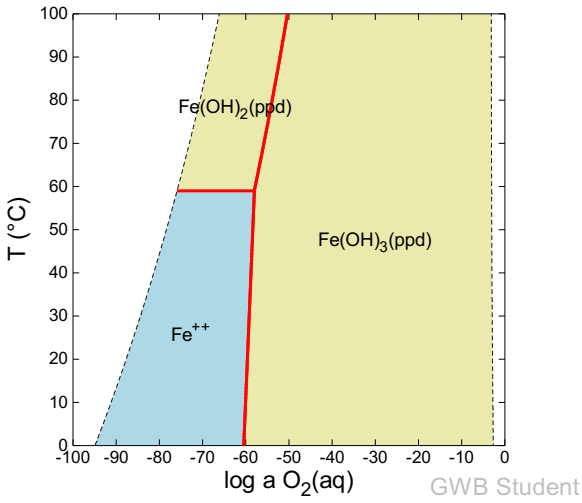

Figure 2.4 Diagram of Fe^{2+} at various temperatures and oxygen fugacities. Fe^{2+} =100 ppm, pH=7, suppressed stable mineral phases: FeO(c), Goethite, Hematite, Magnetite. ppd: precipitated. Dash lines are water limits. The figure was plotted with The Geochemist's Workbench.

The concentrations and isotopic compositions of iron are given in Table 2.3 [$Fe(II)_{aq}$ is used to denote all dissolved Fe(II) species as iron(II) hexaaquo is the main species predicted by Visual MINTEQ (https://vminteq.lwr.kth.se/)]. The $Fe(II)_{aq}$ concentration dropped from ~ 91 to 14 ppm after a 2-hour irradiation. The isotopic compositions of $Fe(II)_{aq}$ and Fe(III) precipitate evolved with time (Figs. 2.5, 2.6). $Fe(II)_{aq}$ had an initial $\delta^{56}Fe$ value of –0.31‰ relative to the IRMM-014 standard, and became enriched in the lighter isotopes as the reaction proceeded, reaching –2.5‰ in the last sampled aliquot. As expected based on mass balance, the $\delta^{56}Fe$ values of the Fe(III) precipitate were always heavier than $Fe(II)_{aq}$ but continuously decreased in response to the light isotope enrichment of the solution.

A three-isotope plot of $Fe(II)_{aq}$ and Fe(III) precipitate yields a straight mass-dependent line with a slope of 0.677 for $\delta'^{56}Fe$ *vs*. $\delta'^{57}Fe$ (Fig. 2.5). No large mass-independent Fe isotope fractionation was observed. The most fractionated samples have small non-zero ε values, which is interpreted to reflect the fact that photo-oxidation follows a mass-fractionation law that differs from the exponential law that is used to correct for mass-dependent fractionation by internal normalization.

The results of experiment #2 dedicated to oxygen isotopic analyses are given in Table 2.4. The iron isotopic compositions follow the same temporal trend as in experiment #1. The oxygen isotopic composition of the Fe(III) precipitate (average +0.33‰) is heavier than that of Chicago tap water used in the experiment, which is about –5.8‰ in terms of $\delta^{18}O$ (measured at the University of Chicago using a Gasbench II connected to a Delta V Isotope Ratio Mass Spectrometer). For comparison, air O_2 has a $\delta^{18}O$ value of +23.5‰. Unlike Fe, where $Fe(II)_{aq}$ and Fe(III) precipitate evolved in the course of the photo-oxidation, no systematic trend of $\delta^{18}O$ with time was seen, consistent with the fact that the solution effectively acted as an infinite reservoir

for oxygen. The $\Delta^{17}O$ values calculated from measured δ-values range between –0.133‰ and –0.048‰, with an average of –0.078‰, where the reference mass fractionation line is the terrestrial fractionation line with a slope of 0.5247 passing through VSMOW (Miller, 2002; Miller et al., 1999). The $\Delta^{17}O$ values are within the range expected for mass-dependent fractionation.

Table 2.3 Iron isotope fractionation in photo-oxidation experiment #1 and the Fe isotopic composition of IF-G.

Sample	Concentration of $Fe(II)_{aq}$ (ppm)	Fraction of Fe precipitated	Illumination time (min)	$\delta^{56}Fe \pm 95\%$ c.i. (‰)	$\delta^{57}Fe \pm 95\%$ c.i. (‰)	$\delta^{58}Fe \pm 95\%$ c.i. (‰)	$\varepsilon^{56}Fe \pm 95\%$ c.i. (‰)
$Fe(II)_{aq}$ solution							
1 Fe(II)	90.8	0	0	−0.311 ± 0.020	−0.471 ± 0.028	−0.632 ± 0.202	−0.009 ± 0.055 (n=12)
2 Fe(II)	51.0	0.44	30	−1.050 ± 0.020	−1.548 ± 0.028	−2.153 ± 0.202	−0.114 ± 0.030 (n=22)
3 Fe(II)	31.4	0.65	55	−1.580 ± 0.020	−2.430 ± 0.028	−3.330 ± 0.202	−0.150 ± 0.055 (n=12)
4 Fe(II)	21.2	0.77	85	−2.138 ± 0.020	−3.153 ± 0.028	−4.226 ± 0.202	−0.218 ± 0.039 (n=14)
5 Fe(II)	14.2	0.84	115	−2.515 ± 0.020	−3.715 ± 0.028	−4.708 ± 0.202	−0.252 ± 0.030 (n=15)
Fe(III) precipitate							
2 Fe(III)	n.a.	0.44	30	0.635 ± 0.027	0.922 ± 0.039	1.209 ± 0.248	0.042 ± 0.055 (n=18)
3 Fe(III)	n.a.	0.65	55	0.389 ± 0.027	0.579 ± 0.039	0.826 ± 0.248	0.001 ± 0.055 (n=18)
4 Fe(III)	n.a.	0.77	85	0.232 ± 0.027	0.352 ± 0.039	0.385 ± 0.248	0.029 ± 0.055 (n=18)
5 Fe(III)	n.a.	0.84	115	0.106 ± 0.027	0.162 ± 0.039	0.345 ± 0.248	0.017 ± 0.069 (n=9)
IF-G	n.a.	n.a.	n.a.	0.611 ± 0.012	0.878 ± 0.019	1.172 ± 0.031	0.052 ± 0.030 (n=24)

δ values are relative to standard IRMM-014. $\varepsilon^{56}Fe$ values are internally normalized to $^{57}Fe/^{54}Fe=0.3625492$ using the exponential law. 95% c.i. are 95% confidence intervals. δ- and ε-values are as defined in Eq. 2.5 and Eq. 2.6. To convert δ- and ε-values to δ'- and ε'-values, the following equations are used: $\delta' = 1000 \times \ln(\delta/1000 + 1)$ and $\varepsilon' = 10000 \times \ln(\varepsilon/10000 + 1)$. n.a.=not applicable.

Table 2.4 Iron and oxygen isotope fractionations in photo-oxidation experiment #2.

Sample	Illumination time (min)	Concentration of $Fe(II)_{aq}$ (ppm)	Fraction of Fe precipitated	$\delta^{56}Fe \pm 95\%$ c.i. (‰)	$\delta^{57}Fe \pm 95\%$ c.i. (‰)	$\delta^{58}Fe \pm 95\%$ c.i. (‰)	$\delta^{18}O \pm 1SD$ (‰)	$\delta^{17}O \pm 1SD$ (‰)
Fe(II) solution								
1 Fe(II)	0	76.9	0	−0.287 ± 0.038	−0.413 ± 0.053	−0.805 ± 0.330	-	-
2 Fe(II)	10	81.0	0	−0.316 ± 0.038	−0.469 ± 0.053	−0.777 ± 0.330	-	-
3 Fe(II)	30	67.4	0.15	−0.691 ± 0.038	−1.038 ± 0.053	−1.198 ± 0.330	-	-
4 Fe(II)	60	53.2	0.33	−0.840 ± 0.038	−1.240 ± 0.053	−1.747 ± 0.330	-	-
5 Fe(II)	120	53.4	0.32	−0.829 ± 0.038	−1.236 ± 0.053	−1.640 ± 0.330	-	-
6 Fe(II)	150	56.7	0.28	−0.868 ± 0.038	−1.258 ± 0.053	−1.622 ± 0.330	-	-
Fe(III) precipitate								
3 Fe(III)	30	n.a.	0.15	1.185 ± 0.044	1.744 ± 0.068	2.068 ± 0.629	−0.135 ± 0.209	−0.121 ± 0.106
4 Fe(III)	60	n.a.	0.33	0.924 ± 0.044	1.375 ± 0.068	1.634 ± 0.629	0.800 ± 0.209	0.372 ± 0.106
5 Fe(III)	120	n.a.	0.32	0.939 ± 0.044	1.392 ± 0.068	1.914 ± 0.629	0.746 ± 0.209	0.309 ± 0.106
6 Fe(III)	150	n.a.	0.28	0.952 ± 0.044	1.442 ± 0.068	2.207 ± 0.629	−0.096 ± 0.209	−0.183 ± 0.106

δ values of iron and oxygen are relative to standards IRMM-014 and SMOW respectively. 95% c.i. are 95% confidence intervals. δ-values are as defined in Eq. 2.5 and Eq. 2.6. To convert δ-values to δ'-values, the following equation is used: $\delta' = 1000 \times \ln(\delta/1000 + 1)$. n.a.=not applicable.

2.3.2 Iron isotope fractionation during UV photo-oxidation

The iron isotopic compositions of minerals in BIFs vary from –2.5 to +1.0‰, which covers almost the entire range encountered on Earth (Dauphas and Rouxel, 2006; Dauphas et al. 2016; Johnson et al., 2003). The heavy isotopic compositions are interpreted to reflect partial iron oxidation (Craddock and Dauphas, 2011; Dauphas et al., 2007; Dauphas et al., 2004b; Heimann et al., 2010; Johnson et al., 2008; Rouxel et al., 2005). It was indeed shown experimentally that partial oxidation of $Fe(II)_{aq}$ into Fe(III) precipitate, either through anoxygenic photosynthesis (Balci et al., 2006; Croal et al., 2004) or O_2-mediated oxidation (Bullen et al., 2001; Welch et al., 2003) imparts a heavy isotopic composition to the Fe(III) precipitate. The low $\delta^{56}Fe$ values could be due to a variety of processes such as reservoir effects in dissolved Fe(II) (Rouxel et al., 2005) and

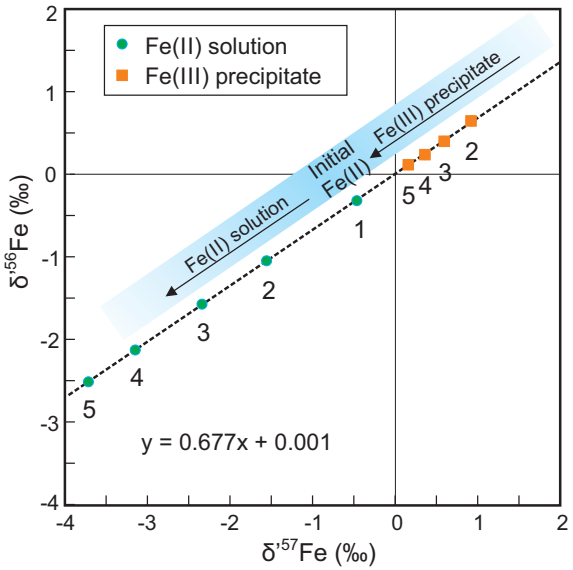

Figure 2.5 Mass-dependent iron isotope fractionation line for photo-oxidation. δ' is calculated as ln (δ/1000 + 1), δ-values are from Table 2.3. Error bars are smaller than the symbols. The $Fe(II)_{aq}$ samples fall on the left side while the Fe(III) precipitate fall on the right side of the initial composition. As the reaction proceeds, $Fe(II)_{aq}$ becomes more fractionated, and the Fe(III) pool gets closer to the initial composition. Sample numbers are labeled next to the data points, with sample 1 the initial iron composition.

postdepositional reworking by dissimilatory iron reduction (*e.g.*, Craddock and Dauphas, 2011; Heimann et al., 2010; Johnson et al., 2008). Regardless of these complications, the first order observation that needs to be explained is the heavy isotope enrichment of BIFs.

The two microbial oxidation mechanisms of O_2-mediated and anoxygenic photosynthesis (Bullen et al., 2001; Croal et al., 2004) can explain the high $\delta^{56}Fe$ values measured in BIFs starting from a hydrothermal $\delta^{56}Fe$ value of ~–0.2‰. Bullen et al. (2001) measured iron isotope fractionation during O_2-mediated $Fe(II)_{aq}$ oxidation at pH around 6 in a natural setting. They used a Rayleigh distillation model to derive a fractionation factor of +1.0‰ between ferrihydrite and $Fe(II)_{aq}$ at room temperature. Croal et al. (2004) measured iron isotope fractionation during anoxygenic photosynthesis at pH around 7 and found that the poorly crystalline ferric oxide produced was enriched in heavier isotopes relative to $Fe(II)_{aq}$ by +1.5±0.2‰. Microbial $Fe(II)_{aq}$ oxidation was also conducted at low pH (< 3) (Balci et al., 2006) and the result is similar to the anoxygenic photosynthesis, with a fractionation factor of +2.2‰ between $Fe(III)_{aq}$ and $Fe(II)_{aq}$, although such low pH conditions are probably irrelevant to Archean seawater.

The photo-oxidation experiments in this study were conducted at pH around 7.3. The iron isotope fractionation during the process can be reproduced by a Rayleigh distillation model with an instantaneous fractionation factor between Fe(III) precipitate and $Fe(II)_{aq}$ of +1.2±0.1‰ in $\delta^{56}Fe$ (Fig. 2.6). A batch equilibrium model fails to reproduce the data, demonstrating that there was no significant isotope exchange with $Fe(II)_{aq}$ after Fe(III) precipitation.

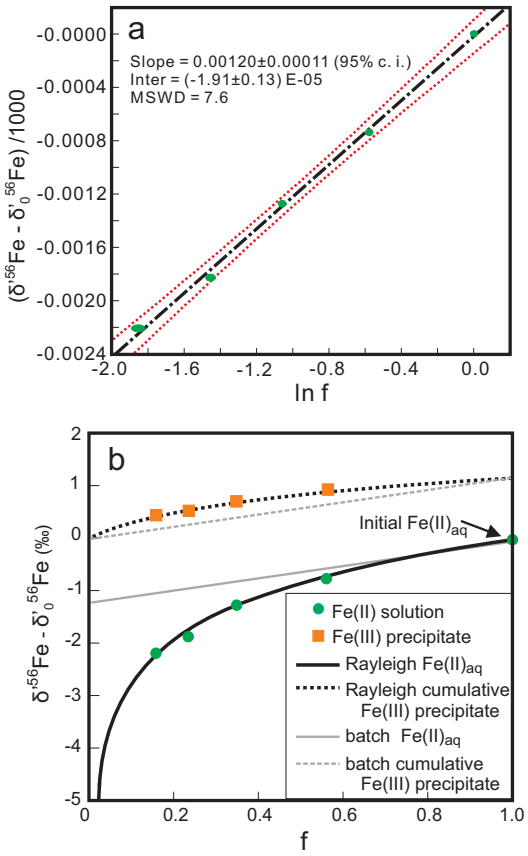

Figure 2.6 Rayleigh fractionation behavior of the photo-oxidation samples. δ' is calculated as ln (δ/1000 + 1), δ-values are from Table 2.3. Error bars are smaller than the symbols. The initial δ'^{56}Fe value was subtracted from all the samples, so that the bulk mix solution+precipitate has a δ'^{56}Fe value of 0. The iron precipitate corresponds to cumulative Fe(III). (a) The regression of $Fe(II)_{aq}$ samples yields an (α –1) value of 0.00012 [$\Delta_{Fe\ (III)\ precipitate-\ Fe(II)aq}$= +1.2‰ at 45 °C]. Distortion of green symbols corresponds to estimated errors. (b) The predicted curves for Rayleigh and batch equilibrium fractionations are shown as black and grey lines respectively. 1.0012 was used as the fractionation factor (α) in the Rayleigh distillation. For batch equilibrium fractionation trends, a fractionation of +1.2‰ between Fe(III) precipitate and $Fe(II)_{aq}$ was used. The formula used to describe a Rayleigh process is $\delta'^{56}Fe(II)_{aq} - \delta'^{56}Fe(II)_{aq,0} = 1000\ (\alpha - 1)\ ln\ f$, where $\delta'^{56}Fe(II)_{aq,0}$ is the isotopic composition of the reactant reservoir, subscript zero denotes the initial composition, f represents the fraction the reactant remains in the reactant reservoir, α is the Rayleigh fractionation factor. f is calculated based on the concentration in the filtrated $Fe(II)_{aq}$ liquid in each aliquot, *i.e.*, $f = C/C_0$, where C_0 is the initial $Fe(II)_{aq}$ concentration. Plotting of $\delta'^{56}Fe(II)_{aq}/1000$ vs. ln f yields a straight line with a slope of α-1.

Equilibrium fractionation factors have been previously estimated for several pairs involving ferric oxide/oxyhydroxide, $Fe(III)_{aq}$, and $Fe(II)_{aq}$ (Fig. 2.7). Those experiments were performed at different temperatures than the one used here, so we converted previous equilibrium fractionation factors to a temperature of 45 °C using Eq. 12 of Dauphas et al. (2012). Wu et al. (2011) determined experimentally the equilibrium fractionation factor between ferrihydrite and $Fe(II)_{aq}$ corresponding to a value of ~+2.7‰ at 45 °C. Welch et al. (2003) studied the effect of temperature on the equilibrium fractionation factor between $Fe(III)_{aq}$ and $Fe(II)_{aq}$. Combining their equation with the equilibrium fractionation factor measured by Skulan et al. (2002) for the system hematite-$Fe(III)_{aq}$ at 98 °C yields a hematite-$Fe(II)_{aq}$ equilibrium fractionation factor of +2.2‰ at 45°C. All these values are significantly higher than the value documented here for Fe(III) precipitate produced by photo-oxidation *vs.* $Fe(II)_{aq}$ (~+1.2‰). Beard et al. (2010) and Frierdich et al (2014) measured a fractionation factor between goethite and $Fe(II)_{aq}$ of ~+0.8‰ when extrapolated to 45 °C, which is more in line with the value reported here. This result, however, would imply that there is an equilibrium fractionation of ~+2‰ between ferrihydrite and goethite (Wu et al., 2011; Beard et al., 2010; Frierdich et al., 2014), which is much larger than the +0.5‰ fractionation predicted between ferrihydrite and hematite (Skulan et al. 2002; Welch et al. 2003; Wu et al., 2011). It is not clear what in the crystal chemistry of goethite would differentiate it so markedly from ferrihydrite and hematite. Independent nuclear resonant inelastic X-ray scattering (NRIXS) experiments on goethite (Blanchard et al., 2015) and ab initio calculations on $Fe(II)_{aq}$ (Rustad et al., 2010), support a larger fractionation between goethite and $Fe(II)_{aq}$ than the measured values. To summarize, the equilibrium fractionation factor between $Fe(II)_{aq}$ and lepidocrocite is unknown and existing data on iron oxides/oxyhydroxides are too uncertain to be of much guidance. The possibility that kinetic effects associated with precipitation may be present, as was

documented previously in mineral precipitation experiments for hematite (Skulan et al., 2002), siderite (Wiesli et al., 2004) and FeS (Butler et al., 2005), also confounds interpretations.

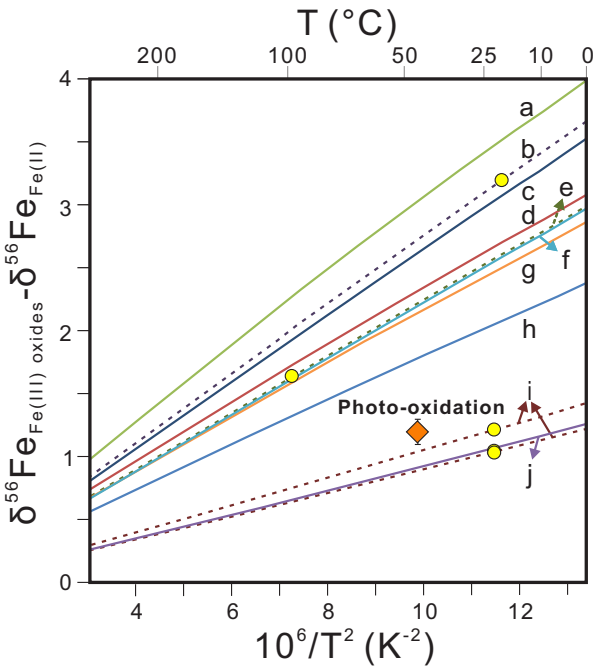

Figure 2.7 Iron isotope fractionation between $Fe(II)_{aq}$ and Fe(III) solid minerals as a function of temperature. The result of the photo-oxidation experiment involving precipitation of lepidocrocite is shown as an orange diamond (labeled photo-oxidation). The solid lines are based on ab initio calculations and NRIXS measurements [the reduced partition function ratios of $Fe(II)_{aq}$ from Rustad et al. (2010) was used when needed]. Dashed lines were calculated by extrapolating experimental data points (yellow dots) in the figure to higher and lower temperatures using Eq. 12 in Dauphas et al. (2012) and the reduced partition function ratios of $Fe(II)_{aq}$ in Rustad et al. (2010). a. Goethite [NRIXS measurement from Blanchard et al. (2015)]; b. Ferrihydrite [extrapolating experimental data from Wu et al. (2011)]; c. Hematite (Polyakov et al., 2007); d. Goethite (Blanchard et al., 2015); e. Hematite [extrapolating experimental data from Skulan et al. (2002) and Welch et al. (2003)]; f. Hematite (Polyakov and Mineev, 2000); g. Hematite (Blanchard et al., 2009); h. Goethite (Blanchard et al., 2015); i. Goethite [extrapolating experimental data from Beard et al. (2010) and Frierdich et al. (2014)]; j. Goethite (Polyakov and Mineev, 2000).

The instantaneous fractionation factor between Fe(III) precipitate and $Fe(II)_{aq}$ given by our experiments is lower than the one obtained in the photo-oxidation experiment of Staton et al. (2006), which may be due to differences in photo-oxidation mechanisms and iron speciation under acidic conditions. This value is, however, similar to the fractionation values in anoxygenic photosynthetic oxidation of $Fe(II)_{aq}$ (+1.5‰; Croal et al., 2004) and in O_2-mediated oxidation (~+1‰; Bullen et al., 2001). This demonstrates that, like the other two oxidation processes, photo-oxidation can also explain the heavy $\delta^{56}Fe$ values measured in BIFs. Therefore, the three processes are not distinguishable based on the extent of iron isotope fractionation alone.

2.3.3 Mass-dependent isotope fractionation law for UV photo-oxidation

2.3.3.1 Mass-dependent fractionation law after a Rayleigh distillation process

As discussed previously, different processes may be characterized by different mass-dependent fractionation laws. It is still not known if a process (*e.g.*, precipitation) folded in a

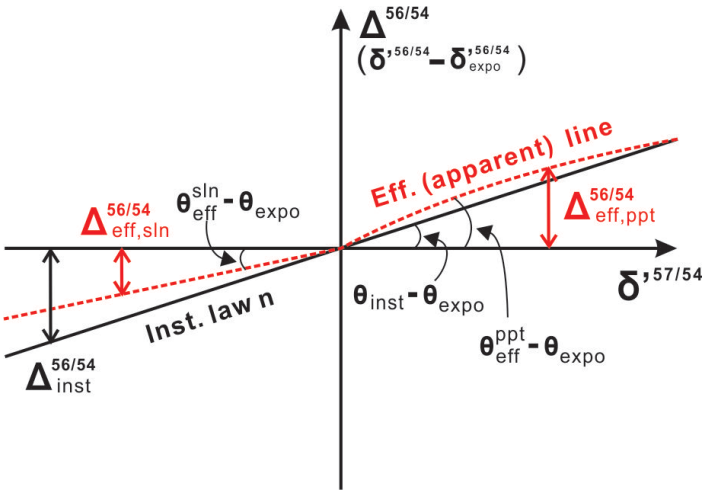

Figure 2.8 Schematic difference between the effective (apparent) curve of a Rayleigh distillation process (red dash line) and the line for the underlying mass fractionation law that the system follows at each step (instantaneous law n). ppt: precipitate. sln: solution. eff: effective. inst: instantaneous. expo: exponential.

Rayleigh distillation would have the same slope (or the same law) as the process itself. Take the photo-oxidation experiment as an example, the photo-oxidation process should follow a law, but since the products are produced in the way of Rayleigh distillation (*i.e.,* products do not backreact with reactants), we want to know if the observed slope records the law that photo-oxidation follows, or the Rayleigh distillation can change the slope of the law. Here we show that the slope is only slightly changed in a Rayleigh distillation, the observed slope should reflect the law that is followed by the investigated process.

The reactant reservoir. For an ideal Rayleigh distillation process, plotting $\delta'^{56/54}$ *vs.* $\delta'^{57/54}$ values of the reactant reservoir (solution) will yield a straight line with an effective (apparent) slope θ_{eff} slightly different from the instantaneous law (θ_{inst}) that the process follows. The two slopes of θ_{eff} and θ_{inst} are compared here to show that the two curves are so close to each other that the difference can be neglected.

The isotopic evolution of the reactant reservoir in a Rayleigh distillation process is given by,

$$\frac{R^{56/54}}{R_0^{56/54}} = f^{(\alpha^{56/54}-1)}, \frac{R^{57/54}}{R_0^{57/54}} = f^{(\alpha^{57/54}-1)}, \tag{2.10}$$

where

$$\alpha^{i/j} = \frac{R^{i/j}_{Fe(III)_{ppt,inst}}}{R^{i/j}_{Fe(II)_{aq}}}. \tag{2.11}$$

Taking the logarithm of the equalities (Eq. 2.10) and rearranging them, it follows,

$$\theta_{eff}^{sln} = \frac{\delta'^{56}Fe(II)_{aq} - \delta'^{56}Fe(II)_{aq,0}}{\delta'^{57}Fe(II)_{aq} - \delta'^{57}Fe(II)_{aq,0}} = \frac{\alpha^{56/54}-1}{\alpha^{57/54}-1}. \tag{2.12}$$

$\alpha^{56/54}$ and $\alpha^{57/54}$ are related through

$$\alpha^{56/54} = (\alpha^{57/54})^{\theta_{inst}}. \tag{2.13}$$

Inserting Eq. 2.13 into Eq. 2.12,

$$\theta_{\mathrm{eff}}^{\mathrm{sln}} = \frac{\alpha^{56/54}-1}{(\alpha^{56/54})^{1/\theta_{\mathrm{inst}}-1}}, \tag{2.14}$$

Since $\alpha^{56/54}$ is very close to one, Eq. 2.14 can be linearized by taking a Taylor series expansion at $\alpha^{56/54} = 1$,

$$\theta_{\mathrm{eff}}^{\mathrm{sln}} \simeq \theta_{\mathrm{inst}} + \frac{1}{2}(\theta_{\mathrm{inst}} - 1)(\alpha^{56/54} - 1), \tag{2.15}$$

which can be solved for θ_{inst},

$$\theta_{\mathrm{inst}} \simeq \frac{\theta_{\mathrm{eff}}^{\mathrm{sln}} + (\alpha^{56/54}-1)/2}{1+(\alpha^{56/54}-1)/2}. \tag{2.16}$$

In our experiments, $\theta_{\mathrm{eff}}^{\mathrm{sln}} = 0.680$ (n=–1; Fig. 2.9) and $\alpha^{56/54} - 1 = 0.0012$. Applying the correction above to $\theta_{\mathrm{eff}}^{\mathrm{sln}}$ yields a θ_{inst} value of 0.6802. The correction is small in regard of the variations in slopes that are expected for different laws.

The product reservoir. Unlike the reactant reservoir, plotting $\delta'^{56/54}$ *vs.* $\delta'^{57/54}$ values (or $\Delta^{56/54}$ *vs.* $\delta'^{57/54}$, $\Delta^{56/54} = \delta'^{56/54} - \delta'^{56/54}_{\mathrm{expo}}$) of the product reservoir will not yield a straight line (Fig. 2.8). The slope changes as a function of f, but the effective departure from the reference law (exponential) $\Delta^{56/54}_{\theta_{\mathrm{eff,ppt}}}$ is always similar to the departure calculated based on the underlying instantaneous fractionation law $\Delta^{56/54}_{\mathrm{inst}}$. For the cumulating product reservoir [Fe(III) precipitate; the right side of the Fig. 2.8], the isotope evolution can be calculated using Eq. 2.10 by mass balance,

$$\frac{R_{\mathrm{ppt}}^{56/54}}{R_0^{56/54}} = \frac{1-f^{\alpha^{56/54}}}{1-f}, \frac{R_{\mathrm{ppt}}^{57/54}}{R_0^{57/54}} = \frac{1-f^{\alpha^{57/54}}}{1-f}. \tag{2.17}$$

The effective slope of the product reservoir is therefore,

$$\theta_{\mathrm{eff}}^{\mathrm{ppt}} = \frac{\delta'^{56/54}_{\mathrm{ppt}} - \delta'^{56/54}_0}{\delta'^{57/54}_{\mathrm{ppt}} - \delta'^{57/54}_0} = \frac{\ln(1-f^{\alpha^{56/54}})-\ln(1-f)}{\ln(1-f^{((\alpha^{56/54})^{1/\theta_{\mathrm{inst}})})-\ln(1-f)}. \tag{2.18}$$

From Eq. 2.18, the slope of the product reservoir is not a constant for given $\alpha^{56/54}$ and θ_{inst}, but changes as a function of the extent of the reaction f, the effective fractionation is thus a curve instead of a straight line (Fig. 2.8). The $\Delta^{56/54}$ difference between the effective fractionation and the instantaneous law is

$$\Delta_{eff,ppt}^{\frac{56}{54}} - \Delta_{inst}^{\frac{56}{54}} = \left(\theta_{eff}^{ppt} - \theta_{inst}\right)\left(\delta'^{\frac{57}{54}}_{ppt} - \delta'^{\frac{57}{54}}_{0}\right) = 1000[(\theta_{inst} - 1)\ln(1-f) + \ln\left(1 - f^{\alpha^{56/54}}\right) - \theta_{inst}\ln(1 - f^{((\alpha^{56/54})^{1/\theta_{inst}})})]. \quad (2.19)$$

Using a third order Taylor series expansion at $\alpha^{56/54} = 1$, the above equation becomes

$$\Delta_{eff,ppt}^{56/54} - \Delta_{inst}^{56/54} = 1000\ \frac{(\theta_{inst}-1)f\ln(f-\ln f-1)(a^{56/54}-1)^2}{2\,\theta_{inst}\,(f-1)^2} + o[\alpha^{56/54} - 1]^3. \quad (2.20)$$

When f goes to 1 (the reaction just starts) or 0 (reaction near completion),

$$\lim_{f\to 1} \Delta_{eff,ppt}^{56/54} - \Delta_{inst}^{56/54} = 0;\ \lim_{f\to 0} \Delta_{eff,ppt}^{56/54} - \Delta_{inst}^{56/54} = 0. \quad (2.21)$$

The maximum value of $\Delta_{eff,ppt}^{56/54} - \Delta_{inst}^{56/54}$ (the largest difference between the effective fractionation and the instantaneous law) would be at f = 0.1556, which is found by calculating where the derivative of $\Delta_{eff,ppt}^{56/54} - \Delta_{inst}^{56/54}$ equals zero. Using f = 0.1556,

$$(\Delta_{eff,ppt}^{56/54} - \Delta_{inst}^{56/54})_{max} = 206.27(\alpha^{56/54} - 1)^2\left(\frac{1-\theta_{inst}}{\theta_{inst}}\right). \quad (2.22)$$

The comparison between $\Delta_{inst}^{56/54}$ and $\Delta_{eff,ppt}^{56/54}$, and the value of $(\Delta_{eff,ppt}^{56/54} - \Delta_{inst}^{56/54})_{max}$ at f = 0.1556 for different n values are shown in Table 2.5, where

$$\Delta_{inst}^{56/54} = (\theta_{inst} - \theta_{expo})\left(\delta'^{57/54}_{ppt} - \delta'^{57/54}_{0}\right) = 1000 * (\theta_{inst} - \theta_{expo})\ \ln(1 - f^{((\alpha^{56/54})^{1/\theta_{inst}})}) - \ln(1-f). \quad (2.23)$$

At f = 0.1556 when the reaction is about 85 % complete and the Δ-value difference between the effective fractionation and the instantaneous law is the maximum, the effective fractionation is still

very similar to the law governing the process. The difference between the two is always much smaller than the precision of the ε-value measurements (95% c.i.) which is about ±0.05.

Table 2.5 $\Delta^{56/54}$Fe difference between the governing instantaneous law and the effective (apparent) fractionation law in the product reservoir for photo-oxidation.

	n=-1	**n=-1/2**	**n=0**	**n=1/2**	**n=1**
$(\Delta^{56/54}_{\text{inst}})_{\text{f=0.1556}}$	0.004068	0.002015	0.000000	0.001977	0.003918
$(\Delta^{56/54}_{\text{eff,ppt}})_{\text{f=0.1556}}$	0.004209	0.002157	0.000145	0.001830	0.003769
$(\Delta^{56/54}_{\text{eff,ppt}} - \Delta^{56/54}_{\text{inst}})_{\text{max,f=0.1556}}$	0.000140	0.000143	0.000145	0.000147	0.000149

2.3.3.2 Equilibrium fractionation law for UV photo-oxidation

Since the extent of iron isotope fractionation shown by the three oxidation scenarios is similar, another way in which these processes might be distinguished is to examine the mass-dependent fractionation laws that govern isotopic variations. In the experiments, no large mass-independent effects were observed that could be used to exclude photo-oxidation as a pathway to BIF precipitation. Terrestrial mass-independent Fe isotope fractionation has only been documented once in magnetite produced by magnetotactic bacterias (Amor et al., 2016), but the process is probably irrelevant to BIF formation since BIFs show only mass-dependent effects.

Beyond mass-independent effects, the mass-dependence of the isotopic fractionation can also provide insights into natural processes (Dauphas and Schauble, 2016 and references therein). Indeed, different processes can impart slightly different slopes in a 3-isotope diagram (*e.g.*, O: Angert et al., 2003; Levin et al., 2014; Luz and Barkan, 2010; Matsuhisa et al., 1978; Miller, 2002;

Pack and Herwartz, 2014; Young et al., 2002; S: Farquhar et al., 2003; Mg: Young et al., 2002; Ca and Ti: Zhang et al., 2014). The slope θ in a 3-isotope diagram is given by,

$$\theta^{i1,i2,i3} = \frac{\delta'^{\,i2/i1}}{\delta'^{\,i3/i1}} = \frac{\ln(R^{i2/i1}/R_{std}^{i2/i1})}{\ln(R^{i3/i1}/R_{std}^{i3/i1})}, \quad (2.24)$$

which can be parameterized as,

$$\theta^{i1,i2,i3} = \frac{m_{i2}^{n} - m_{i1}^{n}}{m_{i3}^{n} - m_{i1}^{n}}, \quad (2.25)$$

where m_i is the mass of an isotopic species. Different mass-fractionation laws define different slopes characterized by different values of n (Dauphas and Schauble, 2016). The most commonly encountered law corresponds to equilibrium fractionation between coexisting phases in the high temperature limit, which gives n=–1. The limit $n \rightarrow 0$ corresponds to the exponential law commonly encountered in mass spectrometry and used in the present study to correct the measurements for instrumental mass fractionation. The laws given above describe mass fractionation when a single process is involved. In our case, this corresponds to the instantaneous fractionation of iron between the last Fe(III) precipitate removed and dissolved $Fe(II)_{aq}$,

$$\theta_{inst} = \frac{\delta'^{56}_{inst}Fe(III)_{ppt} - \delta'^{56}Fe(II)_{aq}}{\delta'^{57}_{inst}Fe(III)_{ppt} - \delta'^{57}Fe(II)_{aq}}. \quad (2.26)$$

This instantaneous fractionation is incorporated in a Rayleigh distillation and what we are interested in is the effective mass fractionation slope θ_{eff} (or apparent θ) of the Rayleigh process for a given θ_{inst}. In a Rayleigh distillation, θ_{eff} of the reactant [$Fe(II)_{aq}$] and product [Fe(III) precipitate] differ from each other and from θ_{inst}. To first order, however, one can safely use the approximation $\theta_{eff}^{solution} \simeq \theta_{eff}^{precipitate} \simeq \theta_{inst}$ (see Sect 2.3.3.1). To facilitate visualization of mass-fractionation laws, isotopic compositions are recast as departures from a reference mass-fractionation law (exponential law) used to correct isotopic ratios through internal normalization

(Eq. 2.7). Different laws are represented by different lines characterized by different n values in ε' *vs*. δ' diagram (Fig. 2.9a),

$$\varepsilon'^{i2/i1} = 10\left(\frac{m_{i2}^{n}-m_{i1}^{n}}{m_{i3}^{n}-m_{i1}^{n}} - \frac{\ln(m_{i2}/m_{i1})}{\ln(m_{i3}/m_{i1})}\right)\delta'^{i3/i1}. \quad (2.27)$$

Tang and Dauphas (2012) derived an approximate equation (Eq. A9 in that paper), based on the above equation using Taylor series expansions, that relates the slope of this relation to n through,

$$\varepsilon'^{i2/i1} \simeq 5(n-k)\frac{(m_{i2}-m_{i1})(m_{i2}-m_{i3})}{m_{i1}}F, \quad (2.28)$$

where F is the degree of isotopic fractionation in ‰/amu; k=0 for exponential law. Applying this equation to the $^{56}Fe/^{54}Fe$ ratio ($m_{i1}=m_{54Fe}$, $m_{i2}=m_{56Fe}$, $m_{i3}=m_{57Fe}$), and $\delta^{57}Fe=(m_{57Fe}-m_{54Fe})$ F,

$$\varepsilon'^{56}Fe = -0.062 \times n \times \delta'^{57}Fe. \quad (2.29)$$

The samples define a slope of 0.0652 ± 0.0087 (Fig. 2.9b), which corresponds to n=–1.05 ± 0.14 using Eq. 2.29. Within error, the samples fall on the high-temperature limit equilibrium-law line (n = –1). However, this does not necessarily imply that the instantaneous Fe(III) precipitate is in equilibrium with $Fe(II)_{aq}$ as it is conceivable that some kinetic processes would display the same mass-dependent exponent as the equilibrium law.

A ~3.7–3.8 Gyr old iron formation from Isua, Greenland was also measured (geostandard IF-G, Table 2.3 and Fig. 2.9a). It is well suited to compare with the experiments because it has a heavy iron isotopic composition relative to most BIFs ($\delta^{57}Fe$ = +0.88‰), thus providing more leverage to distinguish between mass fractionation laws. The isotopic composition of IF-G agrees with the n = –1 law obtained for photo-oxidation.

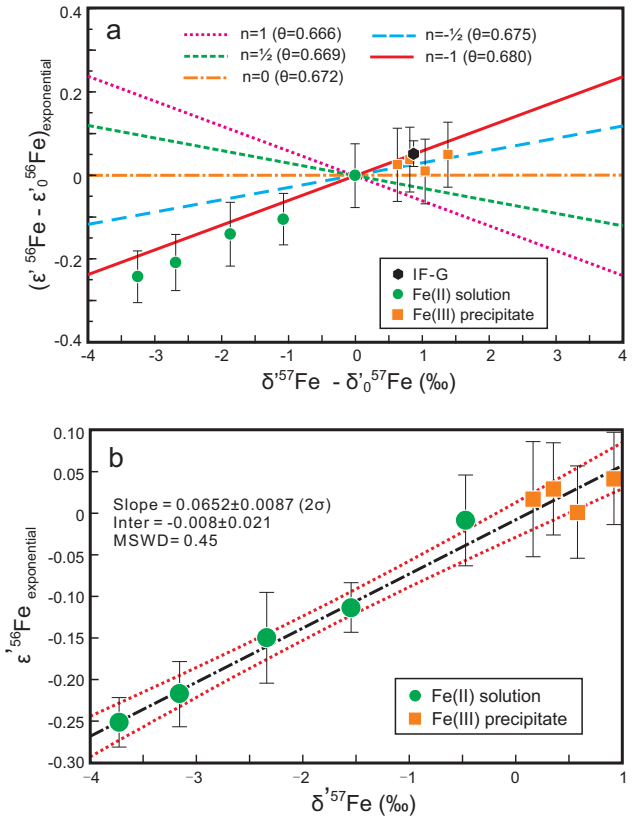

Figure 2.9 Iron mass-fractionation law associated with photo-oxidation. δ' and ε' are calculated as ln (δ/1000 + 1) and ln (ε/10000 + 1) respectively, and δ- and ε- values are from Table 2.3. Samples from the photo-oxidation experiment are plotted as green dots for $Fe(II)_{aq}$ and orange squares for Fe(III) precipitate. The 3.8 Gyr old BIF IF-G is plotted as a black hexagon. (a) The photo-oxidation reaction follows the equilibrium isotope fractionation law (n=–1) within error, so does the BIF sample IF-G. Different lines represent different mass fractionation laws; they are all expressed relative to the exponential law since the measured $\varepsilon^{56}Fe$ values are internally normalized to a fixed $^{57}Fe/^{54}Fe$ ratio using the exponential law. θ is the corresponding slope in the 3-isotope diagram, it is related to n by Eq. 2.25. The δ'- and ε'-values have all had the starting isotopic composition subtracted. (b) A linear regression of the samples (the black line) gives a slope of +0.0652±0.0087, which corresponds to n = -1.05±0.14 using Eq. 2.29. Dashed red lines indicate the 95% confidence interval of the regression.

Although the fractionation is large compared to variations encountered in other natural systems, the maximum iron isotope fractionation expected in BIFs (the products of iron oxidation)

is the instantaneous precipitated Fe(III)-dissolved Fe(II) fractionation factor. In a Rayleigh distillation, much larger fractionation is expected in the source reservoir, that is, the seawater remaining after BIF precipitation. Rouxel et al. (2005) measured the Fe isotopic compositions of sulfides from shales of various ages and found large variations, which they interpreted to result from BIF precipitation and the impact that they have on the Fe isotopic composition of seawater. This interpretation was questioned (Archer and Vance, 2006; Yamaguchi and Ohmoto, 2006), but if correct, high precision Fe isotopic analyses of sulfides in shales could help better constrain the nature of the mass fractionation law associated with BIF formation. The Fe isotopic composition of shales has been extensively studied but the measurements are of insufficient precision to examine the nature of the mass fractionation law.

Adequate high-precision data is also missing for O_2-mediated oxidation and anoxygenic photosynthesis, which is needed to compare with the photo-oxidation presented here. It may be expected, however, that O_2-mediated oxidation in a regime where kinetic isotope effects are limited (at low oxidation rate) would also follow the equilibrium law discussed above, in which case it would be impossible to distinguish between the various oxidation mechanisms that have been proposed to explain the formation of BIFs. Regardless of these complications, this study demonstrates that photo-oxidation remains a viable option for explaining the precipitation of BIFs.

2.3.4 Oxygen isotope fractionation in photo-oxidation

Oxygen isotopic compositions were measured at the Open University using the procedures outlined by Miller (1999). They are reported relative to the VSMOW standard (i=17 or 18) as,

$$\delta^{i}O = [(^{i}O/^{16}O)_{sample} / (^{i}O/^{16}O)_{VSMOW} - 1] \times 10^{3}, \quad (2.30)$$

$$\delta'^{i}O = \ln [(^{i}O/^{16}O)_{sample} / (^{i}O/^{16}O)_{VSMOW}] \times 10^{3}, \quad (2.31)$$

$$\Delta^{17}O = \delta'^{17}O - 0.5247 \times \delta'^{18}O. \quad (2.32)$$

The value 0.5247 for the slope of the mass fractionation line in Eq. 2.32 is based on the data of Miller et al. (1999) and Miller (2002).

The isotopic composition of oxygen was measured to explore whether photo-oxidation by UV light could produce anomalous effects. It is now well established that gas photochemistry can impart mass-independent fractionation for some species of oxygen and sulfur (*e.g.*, Chakraborty and Bhattacharya, 2003; Farquhar et al., 2001; Lyons, 2007; Thiemens and Heidenreich, 1983). UV light can cause photolysis of gaseous O_2 to form ozone which will be enriched in mass-independent heavier oxygen isotopes of ^{17}O and ^{18}O (Heidenreich and Thiemens, 1983; Thiemens and Jackson, 1987). UV photochemistry has also been implicated in creating the pervasive oxygen isotope anomalies documented in planetary materials, including meteorites, the favored mechanism being self-shielding associated with CO photo-dissociation (Clayton, 2002; Lyons and Young, 2005; Yurimoto and Kuramoto, 2004). To our knowledge, there is as yet no known aqueous process that results in mass-independent oxygen isotope fractionation.

In our experiments we did not detect any mass-independent isotope effects for oxygen in the Fe(III) precipitate produced by photo-oxidation. This could either be because photo-oxidation does not induce mass-independent fractionation in oxygen, or alternatively the Fe(III) precipitate equilibrated with atmospheric oxygen or pore water during drying, thus erasing the mass-independent signature. The issue of oxygen isotopic exchange between ferric oxyhydroxides and water upon drying is a known problem in experiments aimed at characterizing equilibrium fractionation factors and may be responsible for discrepancies between published values (Bao and Koch, 1999 and references therein). It is exacerbated when amorphous ferric gels and poorly crystalline phases are present that can exchange with nonstructural water when they transform into

stable ferric oxide phases upon drying. Our experiments were performed at relatively high temperature (45 °C) and most likely the Fe(III) precipitate lepidocrocite produced is relatively stable and not prone to exchange by air-drying at room temperature. Nonstructural water was further removed under vacuum prior to fluorination and isotopic analysis. We take the measured oxygen isotopic composition of the solid as representative of the primary precipitate, but further work is needed to unambiguously confirm this.

Overall, the iron precipitates show $\delta^{18}O$ values with little dispersion, ranging from –0.14 to +0.80‰, with an average of ~ +0.33‰. The isotopic composition of the starting water was –5.8‰, similar to the $\delta^{18}O$ value of lake Michigan (Bowen et al., 2007). There is thus a ~+6‰ fractionation between Fe(III) precipitate and water. This fractionation at ~45 °C is consistent with the limited equilibrium fractionation documented in previous experiments between ferric oxides and water (Fig. 2.10). Previous experimental determinations show that equilibrium oxygen isotope fractionation factors of goethite, hematite and akaganeite are similar, varying between ~-2 and

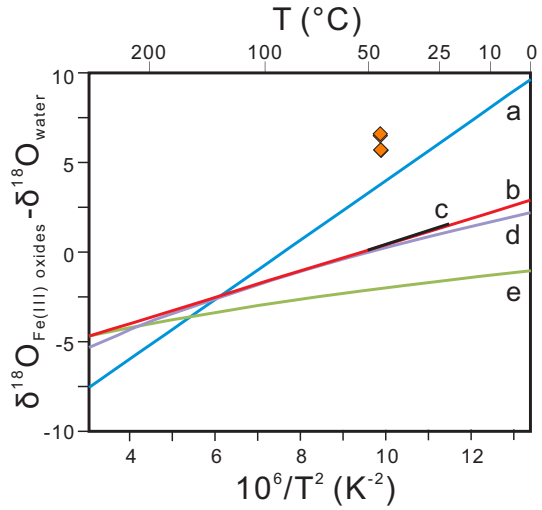

Figure 2.10 Oxygen isotope fractionation between Fe(III) oxyhydroxide minerals and water. Orange diamonds are from this study (fractionation between lepidocrocite and dissolved ferrous iron). Lines a, b, c, and d are previous experimental determinations. a. Goethite (Yapp, 2007); b. Hematite (Bao and Koch, 1999); c. Goethite (Frierdich et al., 2015); d. Akaganeite (Bao and Koch, 1999); e. Goethite (Bao and Koch, 1999).

+4‰ at 45 °C depending on the synthesis protocol and drying procedure involved, but all are centered around zero (Bao and Koch, 1999; Frierdich et al., 2015; Yapp, 2007). The photo-oxidation oxygen isotopes thus seem to record equilibrium isotope fractionation between the precipitate and surrounding water. In the context of BIF genesis, structural oxygen would have exchanged with surrounding pore water and oxygen-bearing phases during diagenesis and maturation to make magnetite and hematite, so comparison with the rock record is not straightforward.

2.3.5 Conclusions

Experiments of Fe(II) photo-oxidation by UV light were performed to measure iron and oxygen isotope fractionation associated with this process and to test whether it is a viable mechanism for BIF formation and iron oxidation on early Mars. The precipitate and solution show a Rayleigh fractionation relationship associated with an instantaneous fractionation factor of +1.2±0.1‰ for the $^{56}Fe/^{54}Fe$ ratio (Fig. 2.6). This value is comparable to previously documented isotope fractionation factors for O_2-mediated oxidation and anoxygenic photosynthesis, the two biogenic alternatives for BIF formation. High-precision iron isotopic analyses show that the mass fractionation law for photo-oxidation is the equilibrium high-temperature limit (n = –1; Fig. 2.9). IF-G, the only banded-iron-formation measured for iron isotopes at high precision has an isotopic composition that falls on the same law (Fig. 2.9). Our results show that photo-oxidation remains a viable pathway to BIF formation.

The oxygen isotopic composition of Fe(III) precipitate formed by photo-oxidation of Fe(II) yields a $\delta^{18}O$ fractionation between the two of +6‰ at 45 °C (Fig. 2.10). This is consistent with previous experiments of equilibrium fractionation between Fe (III) oxyhydroxides and water. No mass-independent effect is observed for oxygen.

2.4 Formation of martian "blueberries"

2.4.1 Martian "blueberries" and terrestrial analogues

The Mars Exploration Rover Opportunity revealed the presence of abundant hematite spherules (also known as "martian blueberries") at its landing site, Meridiani Planum (*e.g.*, Christensen et al., 2004; Klingelhöfer et al., 2004; Squyres et al., 2004). Together with the spherules, sulfur-rich bedrock outcrops have been identified that contain minerals such as jarosite, Mg-, Ca-sulfates, secondary silica, and basaltic rock relics. A model involving interaction between sulfate-rich, acidic water and basaltic rock on ancient Mars was proposed by McLennan et al. (2005) to account for the observed mineral assemblages at Meridiani Planum. In this model, sulfuric acidic water interacted with basaltic rocks to form jarosite and other sulfates in a playa-like environment. Hematite subsequently formed by the breakdown of pre-existing jarosite or other Fe sulfates during a groundwater recharge event. Meridiani Planum is not the only locality on Mars where acid-sulfate alteration might have taken place. For example, the chemical compositions of rocks and soils at Home Plate in Gusev Crater follow the trend expected for acid-sulfate alteration (Squyres et al., 2008). Sulfate minerals have also been detected at Gale crater (Rampe et al., 2016) and Valles Marineris (Milliken et al., 2008).

Two terrestrial analogues have been proposed for studying the formation of martian hematite spherules: Fe-oxide concretions in Navajo sandstone of Utah (Chan et al. 2004) and hematite spherules from Hawaii (Morris et al., 2005). The Fe-oxide concretions in Navajo sandstone formed by mixing reducing Fe(II)-containing fluids with oxygenated water, causing precipitation of Fe(III) as Fe-oxides (Chan et al., 2006; Busigny and Dauphas, 2007). However, the Fe-oxide concretions are not hematite but goethite (Golden et al., 2008) which was not detected in Meridiani hematite spherules. Besides, quartz is a major component in Navajo concretions due

to the interaction between fluids and the sandstone and no acid-sulfate fluid was involved in the concretion formation. This suggests that Navajo concretions are chemically and mineralogically distinct from the martian hematite spherules.

In almost all respects (mineralogy, formation, geologic context) except size (~10–100 μm for Hawaii spherules versus ~5 mm for martian spherules), the hematite spherules found on Mauna Kea (MK) volcano on Hawaii are the best available terrestrial analogue to martian spherules (Morris et al., 2005). Like martian hematite spherules, MK spherules formed by acid-sulfate alteration of basaltic rocks and were found in association with sulfate minerals. Studying their Fe isotopic compositions and the Fe isotopic compositions of the associated lithologies can provide important insights into the formation history of the hematite spherules on Mars.

2.4.2 UV photo-oxidation as a possible Fe oxidation mechanism on Mars

The oxidation mechanism of Fe(II) in forming hematite spherules on ancient Mars is still unclear. Here we explore the possibility of UV photo-oxidation as the oxidation mechanism. The martian blueberries are not available for lab experiments, but one thing we can check is if photo-oxidation is efficient enough to oxidize Fe(II) under martian conditions. In this work, we calculate the rates and timescales of UV photo-oxidation under martian conditions.

2.4.2.1 Quantum yield of UV photo-oxidation

Before calculating UV photo-oxidation timescales on Mars, a very important parameter that needs to be constrained is quantum yield [Fe(II) atoms oxidized per UV photon absorbed]. Although difficult to determine accurately, the quantum yield of $Fe(II)_{aq}$ oxidation is estimated to be ~0.07 based on our photo-oxidation experiments. The value is in general agreement with, but slightly higher than, the value of 0.01–0.05 proposed by Braterman et al. (1983). Calculation of

the quantum yield follows in its main lines the approach used by Anbar and Holland (1992). The quantum yield ϕ here is defined as the number of Fe(II) atoms oxidized per photon absorbed,

$$\phi = \frac{N_{Fe(II)\_oxidized}}{N_{photon}}, \tag{2.33}$$

$N_{Fe(II)\_oxidized}$ is calculated using the measured Fe(II) concentration in the reactant solution. We measured the Fe(II) concentration at 0, 30, 55, 85, and 115 min after starting the photo-oxidation reaction. Since the solution became more and more enriched in Fe(III) colloid which may block some UV light, we use the concentrations at 0 min and 30 min to do the calculation. The number of iron atoms oxidized during that time is given by,

$$N_{Fe(II)\_oxidized} = \frac{6.02 \times 10^{23}\ mol^{-1}\ ([Fe(II)]_0 - [Fe(II)]_{30})\ V}{1000\ mL\ L^{-1}}, \tag{2.34}$$

$[Fe(II)]_0$ and $[Fe(II)]_{30}$ are the ferrous iron concentration at t = 30 min and t = 0 min respectively, in mol L^{-1}. The volume of the solution V is in mL.

The photons absorbed by Fe(II) during the same time can be calculated using the following equations,

$$N_{photon} = [Fe(II)] \int_0^t \int_0^z A \sum_\lambda [\epsilon_\lambda^{Fe(II)}\ F(\lambda, z)] dz dt, \tag{2.35}$$

$$F(\lambda, z) = F_0 10^{-k_\lambda z/\cos\omega}, \tag{2.36}$$

$$k_\lambda = \sum_i \epsilon_\lambda^{X_i} [X_i]. \tag{2.37}$$

In the above equations, $[X_i]$ is the concentration in mol L^{-1} of a light absorbing species; t is time in second; z is the depth of the solution in cm; A is the surface area of the solution; $\sum_\lambda$ is the summation over all wavelengths (the wavelengths below 450 nm of the light emitted by the UV lamp are all taken into account; if the wavelength is continuous, an alternative integral sign $\int_\lambda$ may be used); ϵ is the molar absorptivity (L mol^{-1} cm^{-1}) of a species at a specific λ; F_0 is the photon

flux (quanta cm^{-2} s^{-1}) at the surface of the solution and F is the flux at depth z; k_λ (cm^{-1}) accounts for the absorptivity of the solution; ω is the incident angle.

For the photo-oxidation experiment, the light-absorbing Fe(II) species include both Fe^{2+} and $FeOH^+$. $FeOH^+$ is a strong light absorber which is particularly important for photo-oxidation in the wavelength range between 300 and 450 nm (Braterman et al., 1983). The number of photons absorbed by $FeOH^+$ is close to that absorbed by Fe^{2+} at neutral pH, although the concentration of $FeOH^+$ is only about one thousandth of that of Fe^{2+}, calculated with $K_{eq} = 3.2 \times 10^{-10}$ mol L^{-1} (Anbar and Holland, 1992) and pH of 7.3.

In our calculation, a simplified model of the experimental setup was used; we model the solution as a 1D problem with a surface area of 200 cm^2 and a depth of 1.8 cm with the incident light orthogonal to the water-vessel interface (so that the total volume would be 360 mL, the volume used in our photo-oxidation experiment). The flux F_0 was estimated following the method described in the ACE photochemistry equipment manual. Molar absorptivity of Fe^{2+} and $FeOH^+$ are from the Fig. 3 of Anbar and Holland (1992). Fe(III) solid was treated as spheres with a diameter of 1 μm [the filter used for collecting Fe(III) is 0.1 μm in size] and the absorptivity was calculated using Eq. 8a from Morel and Bricaud (1981). The absorptivity of Fe(III) ion in solution is from Rabinowitch (1942). We further assume that chemical species other than iron such as boron, sodium and sulfate contribute little to the k_λ of the solution (Buck et al., 1954, Rabinowitch, 1942). Initial concentration of Fe(II) (Fe^{2+} + $FeOH^+$) at t = 0 min and concentrations at t = 30 min and later were measured, so instantaneous Fe(II) concentrations were obtained by interpolating exponentially the measured values. $FeOH^+$ was calculated based on $K_{eq} = 3.2 \times 10^{-10}$ mol L^{-1} (Anbar and Holland, 1992) and a pH of 7.3, and Fe(III) precipitate concentrations are the total Fe

subtracted by measured Fe(II). With the above assumptions, the quantum yield is determined to be ~0.07, which is slightly higher than the one determined by Braterman et al. (1983) (0.01–0.05).

In the above calculation, Fe(III) precipitate are considered as 1 μm spheres. How the Fe(III) is treated affects the quantum yield calculated. If Fe(III) is not taken into account, the value of the quantum yield becomes 0.06. If the Fe(III) is treated as dissolved ions; an erroneous assumption [*i.e.*, using the absorptivity of Fe(III) ions in Rabinowitch (1942)], the value becomes 0.13.

In our experiments, the apparatus was covered by aluminum (Al) foil in addition to the protective cabinet. If light reflected by Al foil are taken into account, the quantum yield value would be a little lower. Using the Al foil reflectivity data from Janecke (2012) and the transmittance data of the borosilicate reactor from the product manual, ideally, ~30% UVB (280–315 nm) and ~70% UVA and longer wavelength (315–450 nm) of the initial flux could be reflected to the solution, while UVC (100–280 nm) would be completely blocked by the borosilicate wall of the reactor. If the upper limit 70% reflection was taken (assumed for all wavelength), the quantum yield would decrease from 0.07 to 0.04. Given that we are interested in order of magnitude effects, such correction would not affect our conclusions.

2.4.2.2 Martian photo-oxidation model

Previous studies concluded that photo-oxidation was a viable pathway to BIF precipitation (Anbar and Holland, 1992; Braterman et al., 1983). In the following, we use a model to assess the viability of the photo-oxidation process for forming hematite on Mars. The model investigates the dynamic evolution of water bodies in ancient martian environments. Water bodies are assumed to be at an initial pH of 7 and the pH decreases as Fe(II) gets oxidized. The dissolved ions are Na^+, K^+, Fe^{2+}, Mg^{2+}, Ca^{2+}, SO_4^{2-}, Cl^-, $FeOH^+$ from Fe^{2+} hydrolysis and $FeCl^+$. The chemical reactions follow Hurowitz et al. (2010): dissolved Fe(II) is oxidized to Fe^{3+} by UV photons, and the produced

Fe^{3+} reacts with SO_4^{2-} to precipitate as schwertmannite $[FeO(OH)_{0.75}(SO_4^{2-})_{0.125}]$ (Eq. 2.38), inhibiting the photo-reduction of Fe^{3+} to Fe^{2+}. After all Fe(II) is oxidized, schwertmannite can convert to jarosite and hematite.

$$Fe^{2+} + 1.75H_2O + 0.125SO_4^{2-} \xrightarrow{\hbar\nu} FeO(OH)_{0.75}(SO_4^{2-})_{0.125} \downarrow + 1.75H^+ + 0.5H_2 \uparrow. \quad (2.38)$$

The amount of Fe(II) (including Fe^{2+}, $FeOH^+$ and $FeCl^+$) oxidized is calculated using formulas similar to those used by Anbar and Holland (1992):

$$\eta_{Fe(II)} = \frac{[Fe(II)]}{6.02 \times 10^{23}} \int_0^t \int_0^z \int_{180\ nm}^{450\ nm} [\phi_\lambda^{Fe(II)} \epsilon_\lambda^{Fe(II)} F(\lambda, z)]\ d\lambda dz dt, \quad (2.39)$$

$$F(\lambda, z) = F_0 10^{-k_\lambda z/\cos\omega}, \quad (2.40)$$

$$k_\lambda = \sum_i \epsilon_\lambda^{X_i} [X_i]. \quad (2.41)$$

In the above equations, $\eta_{Fe(II)}$ is the amount of Fe(II) (Fe^{2+} + $FeOH^+$ + $FeCl^+$) oxidized (mol cm^{-2}) in the water column over a depth dz (in cm; the martian surface is at z=0) during time dt (in second); $[X_i]$ is the concentration in mol $L^{-1}$of a light absorbing species; λ is wavelength in nm, the effective wavelength range is assumed to be from 180 nm to 450 nm. ϕ is the quantum yield, and a constant value of 0.07 is used (Sect. 2.4.2.1). ϵ is the molar absorptivity

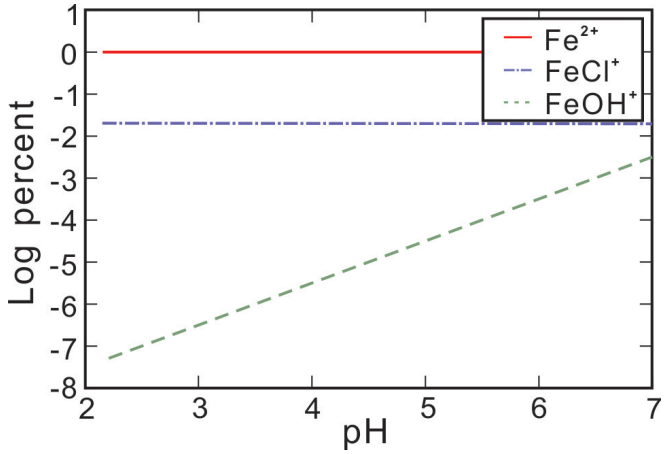

Figure 2.11 Iron speciation as a function of pH. The $FeOH^+$ concentration directly influences the rate of iron photo-oxidation.

(L mol^{-1} cm^{-1}) of a species at a specific wavelength λ; F_0 is the UV flux (quanta cm^{-2} s^{-1} nm^{-1}) at the surface of Mars and F is the UV flux at any specific depth (quanta cm^{-2} s^{-1} nm^{-1}) ; k_λ (cm^{-1}) accounts for the absorptivity of the solution; ω is the incident angle and is assumed to be 35°. When calculating a timescale (in year), the yearly oxidation rate (mol cm^{-2} yr^{-1}) is calculated by multiplying $\eta_{Fe(II)}$ by 3.15×10^7 s $yr^{-1} \times 0.5$. The factor 0.5 corrects for diurnal variations in the incident UV flux.

In the model, Fe^{3+} is not considered as a light absorber because it precipitates as schwertmannite once formed. Na^+, K^+ Mg^{2+} and Ca^{2+} are very stable in solution and their absorption bands are not in the UV-near visible area (Rabinowitch, 1942), so they are assumed to be light insensitive. The concentrations are set to 3.96 mmol L^{-1} for Fe(II), 20.1 mmol L^{-1} for SO_4^{2-}, 2.82 mmol L^{-1} for Cl^- (Tosca and McLennan et al., 2009). $FeOH^+$ and $FeCl^+$ concentrations are calculated using $K_{eq} = 3.2\times10^{-10}$ for $Fe^{2+} + H_2O = FeOH^+ + H^+$ (Anbar and Holland, 1992) and $K_{eq} = 6.686$ for $Fe^{2+} + Cl^- = FeCl^+$ (Lee, 2004) respectively, and the concentrations change as the pH changes. The speciation of Fe(II) as a function of pH is shown in Fig. 2.11. Absorption spectra of these ions can be found in Rabinowitch (1924) and Anbar and Holland (1992). The solar flux at 3.7 Gyr ago is 35% lower than the current flux between 210 and 300 nm (Ribas et al., 2010), and Mars is ~1.52 times farther from the Sun than Earth, therefore the flux at the surface of Mars is assumed to be 0.43 (*i.e.*, $1/1.52^2$) × 65% × the current flux at the top of Earth's atmosphere (solar flux at the top of the Earth's atmosphere is from Fig. 3a in Anbar and Holland (1992), and is wavelength dependent).

The calculation was done numerically. First, the concentrations of each species were calculated by solving a system of equations using the K_{eq} values of the various species and the pH. The absorptivity of the solution k_λ was calculated using Eq. 2.41. With the known k_λ, the flux

profile of a water body (flux for a given wavelength as a function of depth z) can be obtained using Eq. 2.40. The water body is divided into 100 layers to calculate the oxidation rates of Fe^{2+}, $FeOH^{+}$, and $FeCl^{+}$ in each layer over a wavelength range of 180 to 450 nm. Combining the oxidation rates for the three species together we can get the Fe(II) oxidation rate for each layer, then multiplying the rate by a time step Δt to get the amount of Fe(II) oxidized in each layer in Δt. This Δt value is arbitrary and its choice is a trade-off between precision and computation time. We have made the value small enough that it does not affect the results but it is adjusted sometimes so that for each step the oxidized Fe(II) is not less than one thousandth of the initial Fe(II). Summation of oxidized Fe(II) over all the layers gives the total amount of Fe(II) oxidized in Δt. The amount of Fe^{3+} and SO_4^{2-} ions corresponding to the stoichiometry of schwertmannite are removed, and H^{+} produced due to the oxidation of Fe(II) is added to the system. The new composition and pH of the whole system are then obtained, and used as the starting point in the next iteration of photo-oxidation calculation. We assumed that between each step, the remaining species such as Fe(II) and SO_4^{2-} are well mixed in the water column, so that no chemical stratification exists. The program to calculate photo-oxidation on Mars was written in Python.

Braterman et al. (1983) proposed that the oxidation of Fe(II) at near neutral pH was enhanced by the appearance of $FeOH^{+}$. The pH dependence of photo-oxidation rate is shown in Fig. 2.12. The photo-oxidation rate decreases as the pH decreases (Braterman et al., 1983) due to a lower concentration of $FeOH^{+}$ which is a strong UV absorber. Due to the dependence of speciation on pH and light attenuation on speciation, the water depth at which iron photo-oxidation is effective depends on pH. At a near-neutral pH relevant to early Earth oceans, the rate of iron photo-oxidation decreases only slightly at a depth of 1 m compared to the oxidation rate at the

water surface, but for acidic water (pH<4) relevant to Mars hematite-jarosite deposits, a 100-fold decrease in the rate is expected (Fig. 2.12).

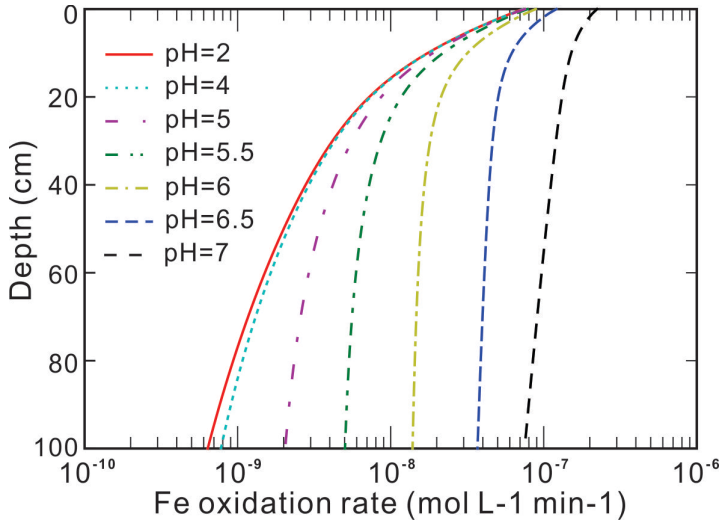

Figure 2.12 pH dependence of iron photo-oxidation rate as a function of depth. Values of initial Fe(II) concentration, quantum yield, and UV flux correspond to early Mars conditions are as discussed in the text.

2.4.2.3 Martian O_2-oxidation model

Like in the photo-oxidation model above, the following reaction is assumed:

$$Fe^{2+} + 0.25O_2 + 0.125SO_4^{2-} + 1.25H_2O \rightarrow FeO(OH)_{0.75}(SO_4^{2-})_{0.125} \downarrow + 1.75H^+. \quad (2.42)$$

The volume change of water is ignored. Water is acidified by oxidizing Fe^{2+} to produce H^+. The rate of oxidation of Fe^{2+} by O_2 is given by Singer and Stumm (1970). We assume that when the pH is lower than 3.5, the oxidation rate is independent of pH,

$$\frac{-d[Fe^{2+}]}{dt} = k\,[Fe^{2+}][O_2], \quad (2.43)$$

where $k = 1.0 \times 10^{-7}$ atm^{-1} min^{-1} at 25 °C. When the pH is greater than 3.5, the rate is calculated using the following equation

$$\frac{-d[Fe^{2+}]}{dt} = k'\,[Fe^{2+}][O_2][OH^-]^2, \tag{2.44}$$

where $k' = 8.0 \times 10^{13}$ L^2 mol^{-2} atm^{-1} min^{-1} at 25 °C.

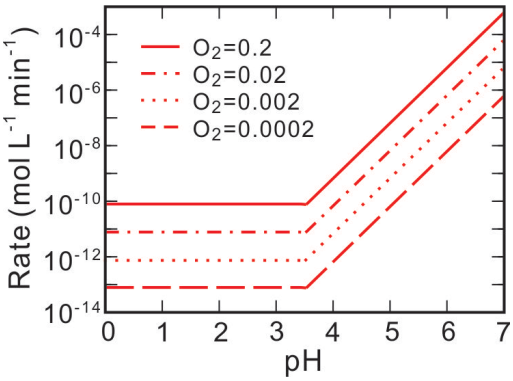

Figure 2.13 Iron oxidation rate by O_2 (in the unit of atm) as a function of pH under different oxygen fugacity conditions.

The model simulates a closed water body with 3.96×10^{-3} mol L^{-1} Fe^{2+} and an initial pH of 7. As the water gets acidified, the oxidation rate diminishes rapidly. The oxidation rates as a function of pH under different oxygen fugacity conditions are shown in Fig. 2.13. The timescales of Fe oxidation can be integrated numerically based on the above rates.

2.4.2.4 Comparison between UV photo-oxidation and O_2-oxidation

Gray hematite was identified remotely on the martian surface in Sinus Meridiani, Aram Chaos and numerous scattered locations by Mars Global Surveyor (Christensen et al., 2001). The presence of gray hematite was confirmed by NASA's Opportunity rover that landed in Meridiani Planum in 2004 (Klingelhöfer et al., 2004). Hematite is hosted in layered sedimentary rocks, which have a thickness of several hundred meters and cover a surface area exceeding 10^5 square kilometers (Arvidson et al., 2006; Hynek and Phillips, 2008). Sulfate minerals such as Mg-, Ca-sulfate, and Fe^{3+}-bearing jarosite coexist with hematite. This mineral assemblage is best explained by chemical precipitation through evaporation of water produced by acid-sulfate alteration of

basaltic rocks followed by diagenetic alteration through interaction with groundwater (Klingelhöfer et al., 2004; McLennan et al., 2005; Tosca et al., 2005). The geologic setting for these deposits is thought to be reworked dry aeolian dune and wet interdune-playa deposits formed in an arid environment with a fluctuating water table (Grotzinger et al., 2005). Those sulfate-rich deposits are of late Noachian to early Hesperian age (~3.8–3.5 Ga), corresponding to a time in the martian history when the climate is thought to have been relatively arid. In such an environment, water ponds would have been ephemeral (Grotzinger et al., 2005). Interestingly, recent *in-situ* observations by the *Curiosity* rover of *ca*. 3.8–3.1 Ga sedimentary deposits in Gale Crater indicate the persistence of a long-lived lake environment (Grotzinger et al., 2015), which suggests a very different climate than that implied by the evaporite deposits at Meridiani Planum. This contrast suggests that the climate record from late Noachian to early Hesperian sedimentary rocks may be more local to regional than global in character. Remote observations also support the existence of paleolakes several hundred meters deep that could have persisted for hundreds to thousands of years or longer (*e.g.*, Dehouck et al., 2010; Ehlmann et al., 2008; Grant et al., 2008; Wray et al. 2011). Those lakes contain phyllosilicate deposits and are mostly of Noachian age (~4.1–3.7 Ga), a period when the martian climate was relatively warm and wet.

Iron in martian basalts is present in its reduced form, Fe^{2+}. One possibility to explain the presence of ferric iron in hematite-sulfate deposits is that iron was photo-oxidized by UV photons (Hurowitz et al. 2010) in a similar manner to the mechanism proposed for BIF formation. One important difference, however, is that while in the case of the early Earth the pH was probably close to neutral, deposition of jarosite suggests that the martian conditions would have been acidic and so have affected the efficiency with which iron was oxidized. Hurowitz et al. (2010) gave a first order estimate of the photo-oxidation rate at 1cm and 1m water depths based on the rates

found in early photo-oxidation experiments (Jortner and Stein, 1962), but these did not take into account the slowing of photo-oxidation as the water body evolved. We have developed a model (see Sect. 2.4.2.2) to more realistically simulate the process of photo-oxidation on Mars using our new estimate of the quantum yield (iron atoms oxidized per photon absorbed) for photo-oxidation. We use the model above to estimate the timescale needed for a water body containing Fe(II) to be oxidized. The initial pH of the water body is set at 7 and then decreases as Fe(II) is oxidized and H^+ ions are produced. The ions in solution are Na^+, K^+, Fe^{2+}, Mg^{2+}, Ca^{2+}, SO_4^{2-}, Cl^-, $FeOH^+$ from Fe^{2+} hydrolysis, and $FeCl^+$. The initial concentrations of Fe^{2+}, SO_4^{2-}, Cl^- are from Tosca and McLennan (2009). The model used here is a closed system, meaning that it does not take into consideration the buffering capacity and replenishment of ions from water-rock interaction.

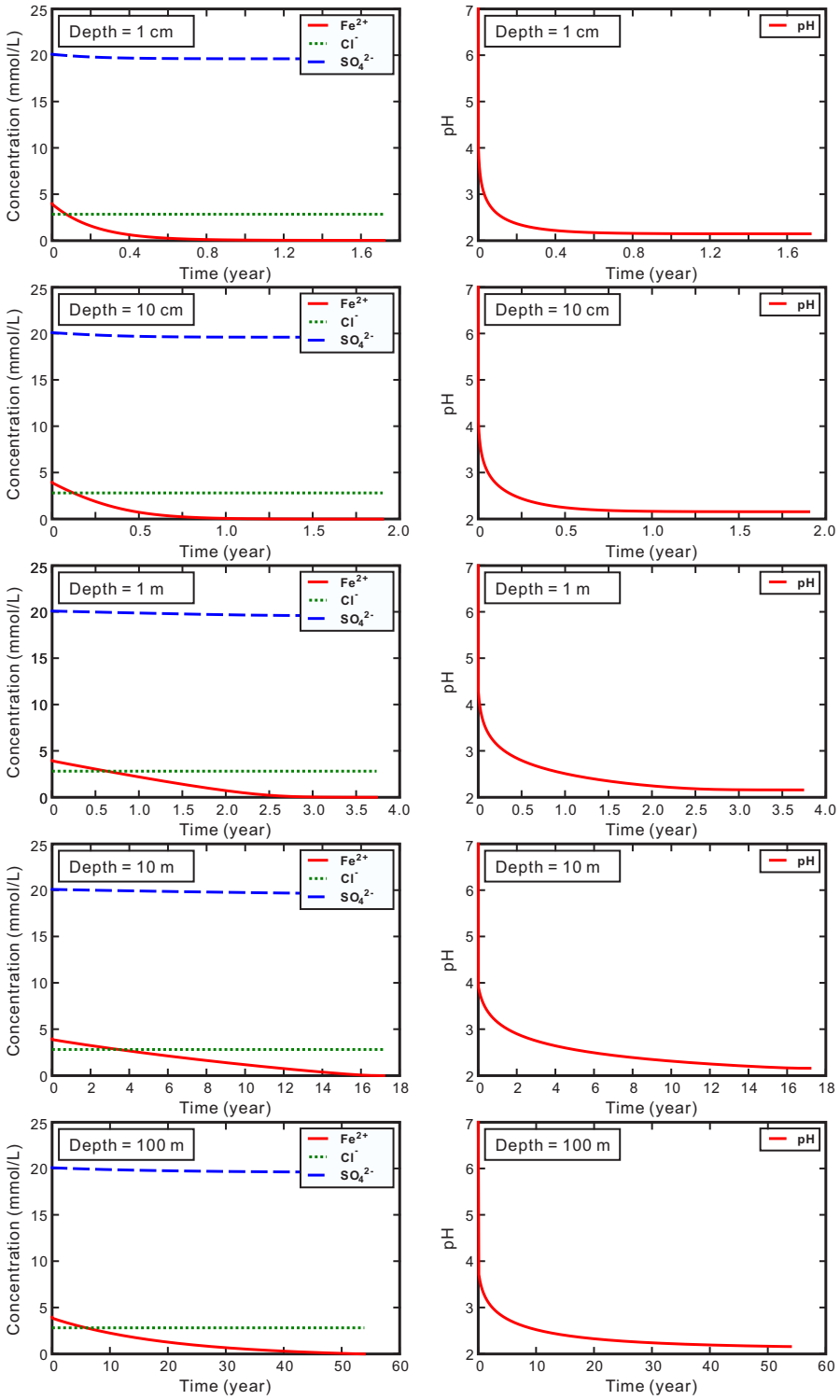

Figure 2.14 Elemental concentration and pH evolution of water bodies with different water depths exposed to UV at the surface of Mars (see text and appendix for details). The initial pH is 7. For 1cm and 1m depth, it takes ~200 and 900 days to oxidize 95% of $Fe(II)_{aq}$ respectively, much longer than the 1–50 days obtained in Hurowitz et al. (2010).

The rate of Fe(II) photo-oxidation decreases quickly (Sect. 2.4.2.2) as the reaction proceeds because the $Fe(II)_{aq}$ concentration decreases and the pH decreases (less $FeOH^+$ is present and UV-photons are less efficiently absorbed). The timescales for Fe(II) oxidation are shown in Fig. 2.14 for five different depths (1, 10 cm, 1, 10, and 100 m). For very shallow water bodies most relevant to playa-type deposits, the rate of Fe(II) oxidation is high at the beginning but decreases rapidly as the pH decreases. For 1 cm water depth, 50% iron oxidation can happen on a timescale of ~50 days, while 95% iron oxidation would take ~200 days. For 1 m depth, the timescales become ~400 days and ~900 days, respectively (Fig. 2.14). These timescales are considerably longer than the 1–50 days obtained in the model of Hurowitz et al. (2010), which

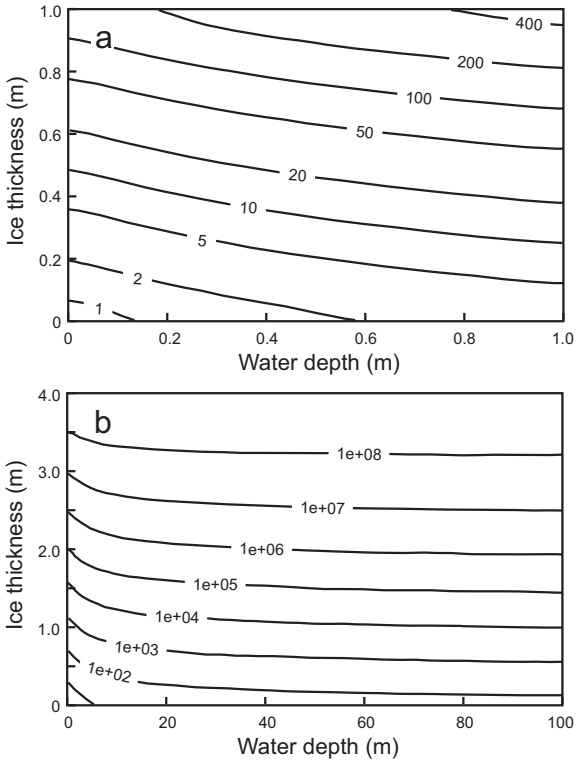

Figure 2.15 Isopleths of photo-oxidation time (95% oxidation) as a function of water depth and ice thickness. (a) for ice thickness and water depth no more than 1m, (b) for ice thickness less than 4 m and water depth less than 100 m. The extinction coefficients of ice are measured young-ice values from Perovich (1995), and extrapolation is necessary to cover the UV wavelength range (180-450 nm) investigated here.

does not take into account pH changes during photo-oxidation, changes in the intensity and spectrum of solar UV, solar incident angle, the greater distance of Mars from the Sun than Earth, and the diurnal effect (*i.e.*, photo-oxidation only works during daytime). Despite these differences, our new results confirm that photo-oxidation is a viable mechanism to explain jarosite-hematite occurrences on Mars provided that shallow water bodies could persist for periods of months to years. For deeper and more persistent water bodies, an additional complication is ice coverage, which would significantly increase the timescales needed to complete photo-oxidation (Fig. 2.15).

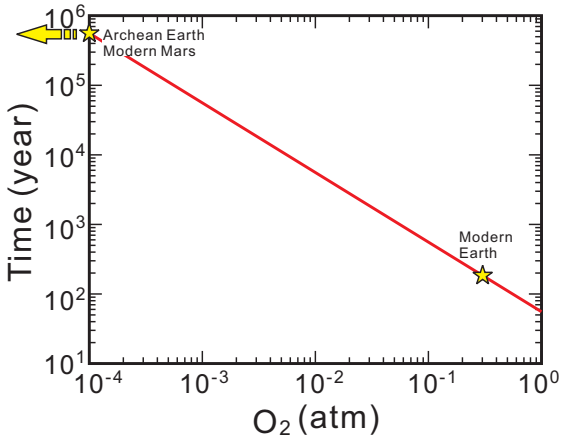

Figure 2.16 Timescale of 95% Fe(II) oxidation by O_2 as a function of O_2 partial pressure. The pH is assumed to be 7 initially and decreases as Fe(II) gets oxidized. The initial $Fe(II)_{aq}$ concentration used is 3.96×10^{-3} mol L^{-1}.

At low pH, oxidation of iron by O_2 is considerably slower than photo-oxidation, with timescales up to hundreds of thousands of years in conditions relevant to early Mars (Hurowitz et al. 2010; Fig. 2.16). Unlike photo-oxidation, however, oxidation by O_2 does not require waters to be exposed to sunlight, so the process can occur in ground water. A difficulty with that scenario is that water-rock interactions would keep the pH near neutral, inhibiting the transport of $Fe(II)_{aq}$ and the formation of jarosite. One possible mechanism that could promote $Fe(II)_{aq}$ transport, described in Baldridge et al. (2009) and Hurowitz et al. (2010), is for iron transport to take place in anoxic, circum-neutral pH groundwater, followed by O_2-mediated oxidation upon groundwater emergence

in the shallow subsurface. On Earth, Fe(II) oxidation by O_2 in low pH environments such as acid mine drainage is largely mediated by bacteria that use iron oxidation as an energy source (Nordstrom and Southam, 1997). Another possibility would therefore be that the oxidation of Fe(II) by O_2 on early Mars involved biological activity. Despite the good preservation and availability of terrestrial BIFs, the involvement of life in their precipitation and diagenesis is very much debated. The difficulty may stem from the fact that bacteria can respire organics using ferric iron as an electron acceptor in a process known as dissimilatory iron reduction, so that organic carbon was mineralized after deposition. If life was ever present on Mars and microbial ecosystems shared any similarity with terrestrial ones, detecting it in hematite-jarosite deposits may prove to be difficult, except possibly by examining stable isotope biosignatures. Unless life is confirmed, photo-oxidation in bodies of standing water is a viable formation mechanism for the Jarosite-hematite deposits on Mars.

2.4.3 Samples from Hawaii as a terrestrial analogue

Studying the iron isotopic composition of terrestrial analogues of martian hematite spherules and associated lithologies can provide important insights into the chemical pathways responsible for the formation of these rocks on Mars (Busigny and Dauphas, 2007; Chan et al., 2006). In most respects (mineralogy, formation, geologic context) except size, the hematite spherules found on Mauna Kea (MK) volcano on the Island of Hawaii are the best available terrestrial analogue to martian blueberries (Morris et al., 2005). Like martian blueberries, MK spherules were formed by acid-sulfate alteration of basaltic rocks and were found in association with sulfate minerals. In the present work, we use iron isotopes to study the acid-sulfate alteration and hematite spherule formation processes. For comparison purpose, iron isotopic data were also

acquired for unaltered tephra, calcined tephra (high-T dry oxidation), palagonite and steam-vent alteration products in Hawaii.

2.4.3.1 Samples from Hawaii

The studied samples (Table 2.6) are from two locations on the Island of Hawaii: Mauna Kea volcano (HWMK) and Kilauea volcano at Sulfur Bank (HWSB). The Mauna Kea samples include two hematite-rich volcanic breccia samples (HWMK745R and HWMK125), 10 tephra samples (HWMK11, HWMK12, HWMK30, HWMK501, HWMK513, HWMK600, HWMK620, HWMK720, HWMK740 and HWMK919) collected in the summit region of Mauna Kea, and one tephra sample (PN64) collected at the Pu'u Nene cinder cone off the saddle road between Mauna Kea and Mauna Loa (Morris et al., 2001; Ruff et al., 2006). The tephra samples are the <1 mm size fractions collected by dry sieving in the field (Morris et al., 2000a). One of them, HWMK 919, also has a <5 μm size fraction obtained by sedimentation in H_2O (Morris et al., 2001).

The breccia HWMK745R contains hematite spherules with diameters of tens of μm. For comparison, martian blueberries are 1~8 mm in diameter, but a second population of spherules with a smaller size is also present that could be more comparable to the Hawaii spherules (Klingelhöfer et al. 2004). A spherule concentrate and 15 individual spherules were separated from the breccia for Fe isotopic analyses. A white-colored piece (HWMK745W) was also sampled from the same breccia and measured for Fe isotopes. A detailed description of breccia HWMK745R can be found in Morris et al. (2005). The other breccia, HWMK125, from the MK "hematite ridge" (Graff et al., 2014) is also rich in hematite (58 wt % Fe_2O_3 total) but is devoid of spherules.

The Sulfur Bank samples include one acid-sulfate leached basaltic rock HWSB820, and 7 tephra <1 mm samples (HWSB531 through HWSB537) collected at active steam vents at Sulfur Bank (Morris et al., 2000a). The altered basaltic rock sample HWSB820 was collected at an active

acid-sulfate fumarole and was partially buried in soil. The exposed part of the rock experienced extensive alteration, as witnessed by its white color, while the buried part is fresher and retains a dark basalt coloration. HWSB820 was cut into slabs ~1 cm thick in a direction parallel to the alteration front (Morris et al., 2000b). The 9 slabs measured in this study (HWSB820 S3.2.2.1 through HWSB820 S3.2.2.9) experienced different extents of alteration and iron mobilization.

The samples cover a variety of alteration conditions (Table 2.6). They include unaltered basaltic tephra (HWMK12 and HWMK513) and basaltic Hawaiian geostandard BHVO-1, palagonitic tephra (hydrolytic alteration under ambient conditions; HWMK600 and HWMK919), tephra from active steam vents (hydrolytic hydrothermal alteration; HWSB531 through HWSB537), calcined tephra oxidized at high temperature in dry conditions (HWMK11 and PN64), tephra that experienced hydrothermal alteration under neutral-to-alkaline conditions (HWMK30 and HWMK720), and samples that experienced hydrothermal alteration under acid-sulfate conditions (HWMK501, HWMK620, HWMK740, HWMK125, HWMK745R and HWSB820). Detailed descriptions of sampling areas, mineralogy, petrology, and spectroscopic features can be found in the Table 2.6 and references listed in it.

Table 2.6 Samples from Mauna Kea volcano and Kilauea volcano in Hawaii.

Sample Name	Description	References
Volcanic tephras and rocks from Mauna Kea volcano		
HWMK11 (<1 mm)	Hematite-bearing tephra (high-T dry oxidation)	(Golden et al., 1993; Hamilton et al., 2008; Morris et al., 1997; Morris et al., 2000a)
HWMK12 (<1 mm)	Unaltered crystalline tephra	(Golden et al., 1993; Morris et al., 2000a)
HWMK30 (<1 mm)	Cristobalite- and phyllosilicate-bearing tephra (hydrothermal, neutral to basic condition)	(Hamilton et al., 2008; Morris et al., 1997).
HWMK125 (breccia)	Hematite-rich volcanic breccia (hydrothermal, acid-sulfate alteration)	
HWMK501 (<1 mm)	Jarosite-bearing tephra (hydrothermal, acid-sulfate alteration)	(Morris et al., 2000a)
HWMK513 (<1 mm)	Unaltered glassy tephra	(Morris et al., 2000a)
HWMK600 (<1 mm)	Palagonitic (phyllosilicate-free) tephra (hydrolytic, low-T alteration)	(Morris et al., 2000a)
HWMK620 (<1 mm)	Jarosite-bearing tephra (hydrothermal, acid-sulfate alteration)	(Morris et al., 2000a)
HWMK720 (<1 mm)	Phyllosilicate-bearing tephra (hydrothermal, neutral to basic condition)	(Hamilton et al., 2008)
HWMK740 (<1 mm)	Sulfate- and phyllosilicate-bearing tephra (hydrothermal, acid-sulfate alteration)	(Hamilton et al., 2008)
HWMK745R (breccia)	Heterogeneous volcanic breccia with embedded hematite spherules (hydrothermal, acid-sulfate alteration)	(Morris et al., 2005)
HWMK745W (breccia)	White-colored piece from HWMK745R (hydrothermal, acid-sulfate alteration)	(Morris et al., 2005)
HWMK919 (<1 mm)	Palagonitic, phyllosilicate-free tephra (hydrolytic, low-T alteration)	(Morris et al., 2001)
HWMK919 (<5 μm)	Palagonitic, phyllosilicate-free tephra (hydrolytic, low-T alteration)	(Morris et al., 2001)
PN64 (<1 mm)	Glassy tephra (high-T dry oxidation)	(Ruff et al., 2006)
Volcanic tephra and rocks from Kilauea volcano		
HWSB531 through HWSB537 (<1 mm)	Tephras from steam vents at Sulfur Bank, altered by steam (hydrolytic, high-T alteration)	(Morris et al., 2000a)
HWSB820 S3.2.2.1 through S3.2.2.9	Rock slabs from HWSB820, vesicular basaltic rock leached by hot acid-sulfate vapors Sulfur Bank fumaroles (hydrothermal, acid-sulfate alteration)	(Morris et al., 2000b)

Table 2.7 Sample chemical compositions[a]

Sample	SiO_2	TiO_2	Al_2O_3	Fe_2O_3T	MnO	MgO	CaO	Na_2O	K_2O	P_2O_5	SO_3R	Total	%LOI	FeO	Fe_2O_3	Fe(3+)/ Fe(Total)	Fe/Ti (mol/mol)	Rb	Sr	Zr	V	Ni	Cr	Cu	Co	Ref[b]
HWMK11 (<1 mm)	50.40	2.97	17.17	12.18	0.19	3.28	6.02	4.87	1.78	0.79	0.02	99.80	3.40	0.59	11.52	0.96	4.10	29	1206	404	125	0	16	18	10	[2]
HWMK 12 (<1 mm)	50.01	2.90	16.90	11.91	0.20	4.32	6.78	4.00	1.76	0.80	0.01	99.74	2.68	6.02	5.22	0.50	4.10	32	1185	397	128	0	14	30	20	[1]
HWMK30 (<1 mm)	56.59	2.97	17.83	12.23	0.07	1.66	4.64	2.14	0.50	1.06	0.01	99.79	6.24	0.65	11.52	0.95	4.12	9	873	405	99	0	12	7	0	[2]
HWMK125 (breccia)	21.11	1.13	7.18	58.01	1.17	6.11	1.75	1.09	1.68	0.50	nd	99.73	2.20	0.00	58.01	1.00	51.36	25	380	254	97	0	24	230	0	[6]
HWMK501 (<1 mm)	49.07	2.77	16.83	14.46	0.17	2.87	5.92	4.57	1.93	0.83	nd	99.42	5.21	4.39	9.58	0.66	5.22	42	nd	nd	135	0	16	22	0	[1]
HWMK513 (<1 mm)	49.78	2.80	16.97	11.81	0.22	4.10	6.60	4.34	1.90	0.89	0.01	99.42	1.39	7.04	3.99	0.34	4.22	34	1138	420	116	0	9	40	9	[1]
HWMK600 (<1 mm)	46.38	3.00	19.87	13.80	0.26	4.29	5.94	3.88	1.37	0.99	nd	99.89	5.39	4.19	9.14	0.72	4.61	27	1150	497	122	62	72	30	12	[1]
HWMK620 (<1 mm)	49.57	3.00	18.79	13.18	0.17	2.38	5.72	4.01	1.69	0.87	nd	99.38	7.69	3.59	9.19	0.70	4.39	38	nd	nd	134	0	15	15	0	[1]
HWMK720 (<1 mm)	50.95	2.47	17.49	11.81	0.22	3.75	6.31	3.36	1.95	0.92	nd	99.23	7.07	3.24	8.21	0.70	4.78	50	1097	511	73	8	34	20	11	[2]
HWMK740 (<1 mm)	51.07	3.16	26.11	8.83	0.11	1.21	2.16	2.48	3.06	1.19	nd	99.39	21.39	0.68	8.07	0.92	2.80	40	1852	572	68	0	71	19	9	[2]
HWMK745 R (breccia)	43.59	2.14	28.02	12.21	0.07	0.98	5.09	3.87	2.21	1.64	nd	100.19	18.76	0.27	11.91	0.98	5.71	20	2131	431	116	150	100	70	0	[3]
HWMK919 (<5 µm)	31.46	5.30	33.63	22.33	0.46	1.28	1.67	1.11	0.22	2.25	nd	99.73	19.69	0.19	22.12	0.99	4.21	49	327	1193	152	17	126	48	8	[4]
HWMK919 (<1 mm)	43.47	3.48	23.50	15.28	0.31	3.46	4.88	3.04	0.93	1.19	0.01	99.74	12.30	2.84	12.12	0.83	4.39	19	958	643	122	64	102	52	12	[4]
PN64 (<1 mm)	49.30	2.80	16.98	11.76	0.22	4.01	6.60	5.00	1.99	0.83	nd	99.57	1.15	0.35	11.37	0.97	4.20	41	1185	402	122	0	12	36	9	[6]
HWSB531 (<1 mm)	30.42	8.41	16.68	40.92	0.06	1.17	0.41	0.09	0.07	0.57	nd	99.06	14.40	1.95	38.75	0.95	4.87	0	nd	nd	893	210	1812	169	10	[1]
HWSB532 (<1 mm)	23.49	10.08	7.43	50.66	0.09	3.85	2.16	0.22	0.13	0.86	nd	99.30	14.11	4.11	46.09	0.91	5.03	5	nd	nd	1076	245	2232	285	34	[1]
HWSB533 (<1 mm)	47.65	4.63	8.11	35.03	0.03	1.73	1.42	0.27	0.14	0.58	nd	99.81	15.96	1.50	33.36	0.95	7.57	5	nd	nd	410	70	1516	110	2	[1]
HWSB534 (<1mm)	40.67	5.43	5.45	27.82	0.17	10.68	7.47	0.72	0.36	0.44	nd	99.41	14.12	7.11	19.92	0.72	5.13	0	nd	nd	671	265	1388	150	45	[1]
HWSB535 (<1 mm)	37.98	6.46	4.24	32.55	0.16	9.74	6.58	0.57	0.35	0.50	nd	99.36	12.64	6.61	25.20	0.77	5.04	5	nd	nd	775	252	1595	170	46	[1]
HWSB536 (<1 mm)	49.25	6.05	3.46	33.71	0.07	3.09	2.04	0.37	0.38	0.77	nd	99.34	10.65	3.95	29.32	0.87	5.57	7	nd	nd	911	72	1001	115	6	[1]
HWSB537 (<1 mm)	nd	nd	nd	nd	nd	nd	nd	nd	nd	nd	nd	nd	nd	nd	nd	nd	nd	nd	nd	nd	nd	nd	nd	nd	nd	
HWSB820 S3.2.2.1	90.72	4.62	2.82	0.92	0.01	0.08	0.22	0.00	0.12	0.14	nd	99.67	10.70	0.27	0.62	0.67	0.20	0	29	271	87	0	121	43	0	[5]
HWSB820 S3.2.2.2	82.37	4.02	7.47	3.61	0.03	0.21	0.30	0.65	0.35	0.33	nd	99.38	16.42	0.72	2.81	0.78	0.90	3	358	239	200	20	241	84	3	[5]
HWSB820 S3.2.2.3	62.39	3.13	13.83	9.64	0.10	3.82	4.68	1.33	0.31	0.34	nd	99.63	14.93	3.25	6.03	0.63	3.08	8	403	180	322	160	414	110	17	[5]
HWSB820 S3.2.2.4	53.20	2.49	17.00	10.51	0.13	5.25	8.58	1.70	0.23	0.30	nd	99.45	10.83	4.34	5.69	0.54	4.22	4	372	143	306	125	398	153	27	[6]
HWSB820 S3.2.2.5	53.41	2.51	17.47	10.52	0.12	4.99	8.18	1.79	0.22	0.31	nd	99.59	11.59	3.98	6.10	0.58	4.19	2	375	146	303	145	451	149	24	[5]
HWSB820 S3.2.2.6	53.72	2.53	17.36	10.38	0.13	5.13	8.08	1.74	0.23	0.29	nd	99.65	10.35	4.16	5.76	0.56	4.10	3	352	147	305	110	434	158	24	[6]
HWSB820 S3.2.2.7	53.93	2.54	16.98	10.50	0.13	5.24	7.99	1.69	0.22	0.29	nd	99.58	9.63	4.41	5.60	0.53	4.14	4	374	148	302	135	470	176	30	[5]
HWSB820 S3.2.2.8	54.94	2.65	17.15	10.20	0.12	4.77	7.37	1.65	0.23	0.30	nd	99.44	11.18	4.19	5.54	0.54	3.85	0	389	153	297	90	393	156	17	[6]
HWSB820 S3.2.2.9	62.25	3.22	14.48	10.23	0.10	3.11	4.22	1.34	0.28	0.36	nd	99.65	14.12	3.50	6.34	0.62	3.18	0	404	185	311	155	382	100	8	[5]

a. Chemical compositions measured on the residue of the LOI measurements.

b. Some major and trace elemental data have been reported in previous work. [1] Morris et al. (2000a). [2] Hamilton et al. (2008). [3] Morris et al. (2005). [4] Morris et al. (2001). [5] Morris et al. (2000b). [6] This study. nd: not determined.

2.4.3.2 Analytical methods

The bulk chemical compositions (Table 2.7) were either reported previously (Morris et al. 2000a; 2001) or measured as a part of this study employing equivalent methods and instruments at Franklin and Marshall College.

The iron isotopic analyses (Table 2.8) were conducted at the University of Chicago following the methodology described in Sect. 2.2. For most samples, about 10–20 mg aliquots were digested using combinations of HF, HNO_3, and $HClO_4$. Iron was purified twice by fixing it onto the AG1-X8 resin in 6 M HCl and releasing it in 0.4 M HCl. Measurements were done using a Thermo Scientific Neptune MC-ICPMS, in medium- or high-resolution wet plasma mode with regular cones (Dauphas et al. 2009). The standard-sample bracketing technique was used to correct for instrumental fractionation. Iron isotopic compositions are expressed using the δ notation.

A spherule concentrate (~5 mg) was extracted from breccia HWMK745R by grinding the spherule-rich portion of the sample, centrifuging the ground material in ethanol, and recovering the high-density part (Morris et al., 2005). This concentrate was measured using the same methodology as that applied to bulk samples, except that only 1.12 mg was digested since this sample is very iron-rich.

Fifteen individual spherules were picked from the spherule concentrate. Given the small size of the individual spherules (10–100 μm), a slurry of the concentrate was prepared and diluted in water so that a given liquid aliquot would only contain a few tens of individual spherules. The isolated spherules were transferred with a pipette under a binocular microscope into clean Teflon beakers. The amount of iron in each spherule is only tens to hundreds of nanograms (Table 2.9). This is equivalent to, or only slightly higher than, the Fe column chromatography blank (~30 ng). Iron column chemistry on the individual spherules was therefore not performed to avoid a

significant contribution from the blank. Because the spherules are very Fe-rich (81.6–96.1 wt% Fe_2O_3T; Morris et al., 2005), the expectation was that bypassing the purification step for those would not affect the accuracy of Fe isotopic analyses. Nevertheless, great care was taken to make sure that the measured values were accurate. The individual spherules were digested in beakers with only small amounts of acids (50 µL HCl + 25 µL HNO_3 + 5 µL $HClO_4$ for each spherule) to minimize the blank. The solutions were then dried, and redissolved in dilute HNO_3 medium for MC-ICPMS analyses. Measurements were performed with an Aridus desolvating nebulizer, with a final sensitivity of 35 V/ppm on ^{56}Fe in medium resolution.

To mitigate any matrix effect associated with the fact that iron in the individual spherules was not purified, the Fe isotopic compositions were measured using the Ni-doping method (Dauphas et al., 2009; Poitrasson and Freydier, 2005). The $^{57}Fe/^{56}Fe$ ratio was measured instead of the $^{56}Fe/^{54}Fe$ ratio because ^{54}Fe has an isobaric interference from ^{54}Cr ($\delta^{57/56}Fe_{sample} = [(^{57}Fe/^{56}Fe)_{sample}/(^{57}Fe/^{56}Fe)_{IRMM014} - 1] \times 1000$). We also report $\delta^{56/54}Fe$ using $\delta^{56/54}Fe = 2 \times \delta^{57/56}Fe$, considering that iron isotopic fractionation follows mass-dependent fractionation (Dauphas et al. 2004a; Dauphas et al., 2017; Wang et al., 2012; Dauphas and Schauble, 2016).

Table 2.8 Sample iron isotopic compositions.

Samples	Alteration/Sample type	Fe_2O_3T (wt.%)	$\delta^{56}Fe$	95 % ci	$\delta^{57}Fe$	95 % ci	$\delta^{58}Fe$	95 % ci
Hawaiitic Basalt Composition Progenitor (Mauna Kea volcano summit region)								
HWMK12 (<1 mm)	Unaltered	11.91	0.165	0.026	0.251	0.037	0.423	0.291
HWMK513 (<1 mm)	Unaltered	11.81	0.140	0.029	0.174	0.042	0.267	0.314
HWMK11 (<1 mm)	Chemically unaltered (high-T dry oxidation)	12.18	0.117	0.029	0.165	0.042	0.185	0.314
PN64 (<1 mm)	Chemically unaltered (high-T dry oxidation)	11.76	0.131	0.029	0.212	0.042	0.114	0.314
HWMK600 (<1 mm)	Palagonitic (passive Fe enrichment)	13.80	0.160	0.030	0.256	0.043	0.280	1.049
HWMK919 (<5 μm)	Palagonitic (passive Fe enrichment)	22.33	0.056	0.031	0.082	0.046	0.225	0.158
HWMK919 (<1 mm)	Palagonitic (passive Fe enrichment)	15.28	0.082	0.030	0.117	0.043	1.598	1.049
HWMK30 (<1 mm)	Hydrothermal (passive Fe enrichment)	12.23	0.128	0.030	0.164	0.043	0.244	1.049
HWMK720 (<1 mm)	Hydrothermal (clay minerals)	11.81	0.178	0.031	0.260	0.046	0.260	0.158
HWMK125 (breccia)	Acid-sulfate (active Fe enrichment as hematite)	58.01	-0.152	0.029	-0.223	0.042	-0.517	0.314
HWMK501(<1 mm)	Acid-sulfate (active Fe enrichment as jarosite)	14.46	0.107	0.030	0.157	0.043	1.361	1.049
HWMK620 (<1 mm)	Acid-sulfate (active Fe enrichment as jarosite)	13.18	0.265	0.026	0.390	0.037	0.236	0.291
HWMK740 (<1 mm)	Acid-sulfate (active Fe depletion)	8.83	0.494	0.030	0.743	0.045	0.850	0.305
HWMK745W(breccia)	Acid-sulfate	8.98	0.517	0.026	0.752	0.037	0.981	0.291
Spherule concentrate from HWMK745R	Acid-sulfate	50.76	0.422	0.026	0.606	0.037	1.039	0.291
Tholeiitic Basalt Composition Progenitor (Sulfur Bank region)								
HWSB531 (<1 mm)	Steam vent (passive Fe enrichment)	40.92	0.213	0.029	0.319	0.043	0.449	0.288
HWSB532 (<1 mm)	Steam vent (passive Fe enrichment)	50.66	0.128	0.030	0.179	0.045	0.169	0.305
HWSB533 (<1 mm)	Steam vent (passive Fe enrichment)	35.03	0.092	0.030	0.128	0.045	0.367	0.305
HWSB534 (<1mm)	Steam vent (passive Fe enrichment)	27.82	0.086	0.030	0.100	0.045	-0.214	0.305
HWSB535 (<1 mm)	Steam vent (passive Fe enrichment)	32.55	0.066	0.030	0.106	0.045	0.300	0.305
HWSB536 (<1 mm)	Steam vent (passive Fe enrichment)	33.71	0.160	0.030	0.245	0.045	0.214	0.305
HWSB537 (<1 mm)	Steam vent (passive Fe enrichment)	nd	0.048	0.030	0.065	0.045	-0.222	0.310
HWSB820 S3.2.2.1	Acid-sulfate (active Fe leaching)	0.92	0.944	0.032	1.388	0.043	1.812	0.140
HWSB820 S3.2.2.2	Acid-sulfate (active Fe leaching)	3.61	0.628	0.032	0.927	0.043	1.186	0.140
HWSB820 S3.2.2.3	Acid-sulfate (active Fe leaching)	9.64	0.281	0.031	0.420	0.046	0.616	0.158
HWSB820 S3.2.2.4	Acid-sulfate (active Fe leaching)	10.51	0.232	0.031	0.344	0.042	0.465	0.133
HWSB820 S3.2.2.5	Acid-sulfate (active Fe leaching)	10.52	0.217	0.031	0.310	0.046	0.285	0.158
HWSB820 S3.2.2.6	Acid-sulfate (active Fe leaching)	10.38	0.234	0.032	0.338	0.043	0.473	0.141
HWSB820 S3.2.2.7	Acid-sulfate (active Fe leaching)	10.50	0.247	0.031	0.350	0.046	0.501	0.158
HWSB820 S3.2.2.8	Acid-sulfate (active Fe leaching)	10.20	0.234	0.031	0.364	0.046	0.519	0.158
HWSB820 S3.2.2.9	Acid-sulfate (active Fe leaching)	10.23	0.310	0.031	0.449	0.042	0.631	0.133
Geostandards								
BHVO-1	Hawaii basalt	12.23	0.102	0.030	0.132	0.043	0.158	1.049
BHVO-1	Hawaii basalt	12.23	0.124	0.027	0.169	0.040	0.206	0.301
BHVO-1	Hawaii basalt	12.23	0.104	0.032	0.149	0.043	0.146	0.140
BCR-2	Columbia River basalt	13.8	0.068	0.029	0.087	0.042	0.131	0.314
BCR-2	Columbia River basalt	13.8	0.114	0.027	0.163	0.040	0.113	0.301
BCR-2	Columbia River basalt	13.8	0.066	0.031	0.093	0.039	0.154	0.086
AGV-2	Guano Valley andesite	6.69	0.107	0.028	0.140	0.041	-0.050	0.305
AGV-2	Guano Valley andesite	6.69	0.098	0.032	0.131	0.043	0.245	0.141
IF-G	Greenland BIFs		0.641	0.026	0.914	0.037	1.110	0.291

nd: not determined.

In Fe isotopic analyses, it is usually important that the bracketing standard match the concentration of the sample to get accurate δ-values. This was difficult to achieve with the spherules due to the very limited amount of Fe available. To correct iron isotope values for mismatched concentrations between samples and standards during the spherule measurements, the individual spherules were measured alternatively with four solutions at different Fe concentrations (50, 100, 200, 500 ppb), prepared by diluting the digested spherule concentrate. Using the four spherule concentrate solutions, a correlation was established between concentration and measured $\delta^{57/56}$Fe values, and between concentrations and reproducibility (quantified using the standard deviation). The two correlations were used to correct the $\delta^{57/56}$Fe values of the individual spherules and to ascribe error bars to the corrected values. After correction, a precision of ±0.2 to 1.4 ‰ was achieved for $\delta^{56/54}$Fe (or ±0.1 to 0.7 ‰ for $\delta^{57/56}$Fe), with iron amounts in the spherules ranging from 30 to 260 ng. John and Adkins (2010) proposed an optimized analytical procedure for measuring small quantities of Fe (*i.e.*, ng level) by MC-ICPMS. They find that in optimal conditions, precisions of ±0.2 to 0.05 ‰ could be achieved for ~6–60 ng of iron. Our uncertainties are larger but sufficient to evaluate whether individual spherules display variable Fe isotopic compositions.

Table 2.9 Fe isotopic compositions of hematite spherules and the white color breccia (HWMK745W) from breccia HWMK745R.

Spherules	Diameter (μm)[a]	Fe amount (ng)	δ^{56}Fe	95 % ci	$\delta^{57/56}$Fe	95 % ci
Hmt1	26	33	-0.36	1.42	-0.18	0.71
Hmt2	26	36	-3.76	1.17	-1.88	0.59
Hmt3	27	37	0.12	1.34	0.06	0.67
Hmt4	27	39	0.81	1.48	0.40	0.74
Hmt5	28	42	0.69	1.16	0.35	0.58
Hmt6	28	44	-0.11	1.00	-0.05	0.50
Hmt7	29	46	0.04	0.98	0.02	0.49
Hmt8	31	57	0.02	0.93	0.01	0.46
Hmt9	31	57	0.11	0.82	0.06	0.41
Hmt10	31	58	0.39	0.82	0.19	0.41
Hmt11	33	71	0.82	0.65	0.41	0.33
Hmt12	37	97	0.28	0.45	0.14	0.22
Hmt13	42	144	-0.03	0.37	-0.02	0.18
Hmt14	42	145	0.25	0.34	0.12	0.17
Hmt15	51	261	0.27	0.17	0.14	0.09
Spherule concentrate			0.422	0.026		
HWMK745W			0.517	0.026		

a. The diameters are calculated based on the measured Fe amount assuming an ideal round shape and pure Fe_2O_3 composition.

2.4.3.3 Elemental and isotopic compositions

Elemental compositions. The major element compositions of the samples are compiled in Table 2.7. Morris et al. (2000a) used LOI and SO_3 concentrations to classify Mauna Kea tephra samples into three distinct groups: unaltered tephra (low LOI and low SO_3) that show little or no alteration, sulfatetic tephra (high SO_3), and palagonitic tephra (high LOI/SO_3 ratios and low SO_3). As an alternative, major elements such as SiO_2 and TiO_2 can also be used as proxies to distinguish these various modes of alteration. This is because Ti is refractory and resistant to alteration, while the mobility of Si depends on the alteration pH (it is more easily mobilized at neutral or higher pH).

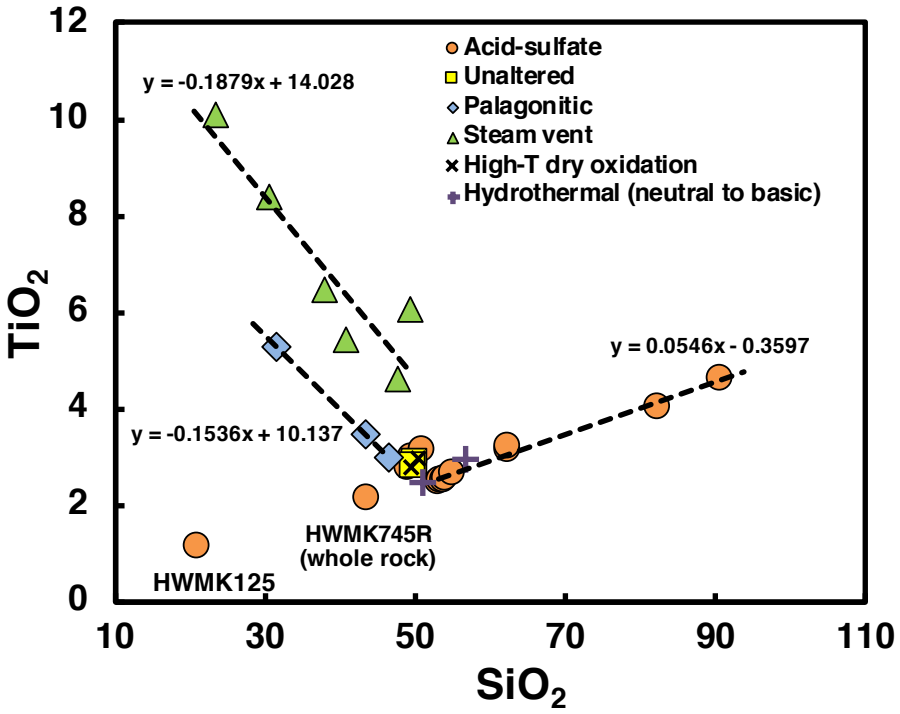

Figure 2.17 TiO_2-SiO_2 (wt%) diagram. Three general trends can be seen from Hawaii samples: 1) acid-sulfate alteration (orange filled circles), characterized by the passive enrichment of SiO_2 and TiO_2 (other ions such as Mg or Fe were mobilized); 2) steam vent alteration (green filled triangles) and 3) palagonitic alteration (blue filled diamonds). Steam vent and palagonitic alteration removed SiO_2 and other fluid mobile elements, causing a passive enrichment in TiO_2.

The alteration types are readily distinguished for acid-sulfate alteration and hydrolytic alteration in a SiO_2-TiO_2 diagram (Fig. 2.17). Three distinct trends are revealed in the diagram corresponding to palagonitic alteration, steam-vent alteration and acid-sulfate alteration. Palagonitic alteration at low-T in the presence of water, and steam-vent alteration at high-T also in the presence of water (hydrothermal) would both cause SiO_2 to be leached and TiO_2 to be passively enriched, resulting in a negative slope in the TiO_2-SiO_2 diagram. Quantitative calculation (see below) shows, however, that the negative slope cannot be accounted for by solely removing SiO_2, and other elements such as CaO, MgO, Na_2O and K_2O must have been leached together with silica. This is consistent with compositional patterns of palagonitic tephra (Morris et al., 2000a).

If SiO_2 and other elements were removed, the concentration of immobile Ti should evolve by mass balance according to

$$[TiO_2] = \frac{[TiO2]_0}{[SiO_2]_0+[others]_0-100} \times \left(1 + \frac{[others]}{[SiO_2]}\right) \times [SiO_2] - \frac{100 \times [TiO_2]_0}{[SiO_2]_0+[others]_0-100}. \quad (2.45)$$

Square brackets denote concentration in wt %, and the subscript 0 denotes the original composition before leaching. If we assume that only SiO_2 was mobilized ($[others] = 0$) and take the SiO_2 and TiO_2 values of unaltered tephra (HWMK12 and HWMK513) as the original compositions, the calculated slope for the SiO_2-TiO_2 relationship is $\frac{[TiO_2]_0}{[SiO2]_0-100}$ =-0.06 (here and throughout this article, the ratios of oxide concentrations are given as wt% ratios, while Fe/Ti ratios are in mol/mol). This value is notably higher than the actual slope (~-0.15; Fig. 2.17) calculated by fitting the palagonitic and steam-vent alteration trends. Assuming that other leached elements include CaO, MgO, Na_2O and K_2O and are removed in constant proportion to SiO_2 (equivalent to the unaltered proportions), the slope becomes –0.11, closer to the fitted slope of –0.15. Therefore, the negative slopes of hydrolytic and steam-vent alteration in Fig. 2.17 are controlled by the removal of both SiO_2 and other fluid-mobile elements. Iron was not removed and was passively increased (Fig. 2.18) due to the removal of other elements. This is confirmed by their limited variation of Fe isotopic compositions (+0.05 to +0.21‰).

For acid-sulfate alteration, both SiO_2 and TiO_2 are passively enriched because of leaching of other elements such as Fe and Mg. The trend of acid-sulfate alteration is mainly defined by rock slabs from a single basaltic rock; HWSB820 (the two most fractionated samples are rock slabs from HWSB820). This trend extends to the origin (*i.e.*, unaltered samples) and is characterized by a constant TiO_2/SiO_2 ratio of ~0.05, indicating the lack of mobilization of these two elements during acid-sulfate alteration. The three acid-sulfate altered tephra samples (HWMK501, HWMK620 and HWMK740) have a similar TiO_2/SiO_2 ratio (~0.06) to HWSB820.

The two acid-sulfate altered breccias, HWMK745R (spherule host breccia) and HWMK125 (hematite-rich breccia) have lower TiO_2 and SiO_2 concentrations than unaltered basalts (Fig. 1) but their TiO_2/SiO_2 ratios are unfractionated (~0.05). The reduced TiO_2 and SiO_2 concentrations are therefore interpreted to be due to the enrichment of other elements. The major element data (Table 2) show large excesses of Al_2O_3 (28 wt % vs. ~17 wt % for unaltered tephras) for HWMK745R (from precipitation of alunite), and of Fe_2O_3T (58 wt %) for HWMK125 (from precipitation of hematite).

The remaining four tephra samples affected by processes other than acid-sulfate alteration (HWMK11, PN 64 and HWMK30 and HWMK720) plot near to the unaltered composition on the TiO_2-SiO_2 diagram. They have Fe/Ti ratios, Fe_2O_3T contents and Fe isotopic compositions similar to those of the unaltered samples, implying that mass transport of Fe did not occur. Mineralogical observations are also consistent with no Fe transport. Dry oxidation of Fe^{2+}-bearing phases (*e.g.*, titanomagnetite) at high temperatures affected both HWMK11 and PN64 (Golden et al., 1993; Ruff et al., 2006). HWMK30 and HWMK720 are phyllosilicate-bearing samples resulting from alteration of basaltic tephra under hydrothermal, circum-neutral, and oxidizing conditions (Hamilton et al., 2008). Since they plot close to the unaltered tephras on the TiO_2-SiO_2 diagram, it is likely that phyllosilicate formation inhibited SiO_2 loss from these samples during leaching compared to palagonitic alteration.

Iron isotopic compositions of the bulk samples. The iron isotopic compositions of the bulk samples range from -0.15 to +0.94 ‰ (relative to IRMM-014; Table 2.8 and Fig. 2.18). The two unaltered tephra samples (HWMK12 and HWMK513) have Fe isotopic compositions ($\delta^{56}Fe$ = +0.15 ‰) similar to BHVO-1 (+0.11 ‰). The samples associated with acid-sulfate alteration display the largest Fe isotopic variation from –0.15 ‰ to +0.94 ‰ compared to the baseline

samples (+0.05 to +0.15 ‰ for Hawaii basaltic rocks previously measured by Konter et al., 2016; Teng et al., 2013, and unaltered tephra samples and BHVO-1 from this study), implying significant Fe transport. The samples that are not associated with acid-sulfate alteration (palagonitic alteration: HWMK600 and HWMK919, high-T dry oxidation: HWMK11 and PN64, steam vent alteration: HWSB531 through HWSB537, and hydrothermal alteration under neutral to basic conditions: HWMK30 and HWMK720) show limited variation of Fe isotopes (from +0.05 to +0.21‰).

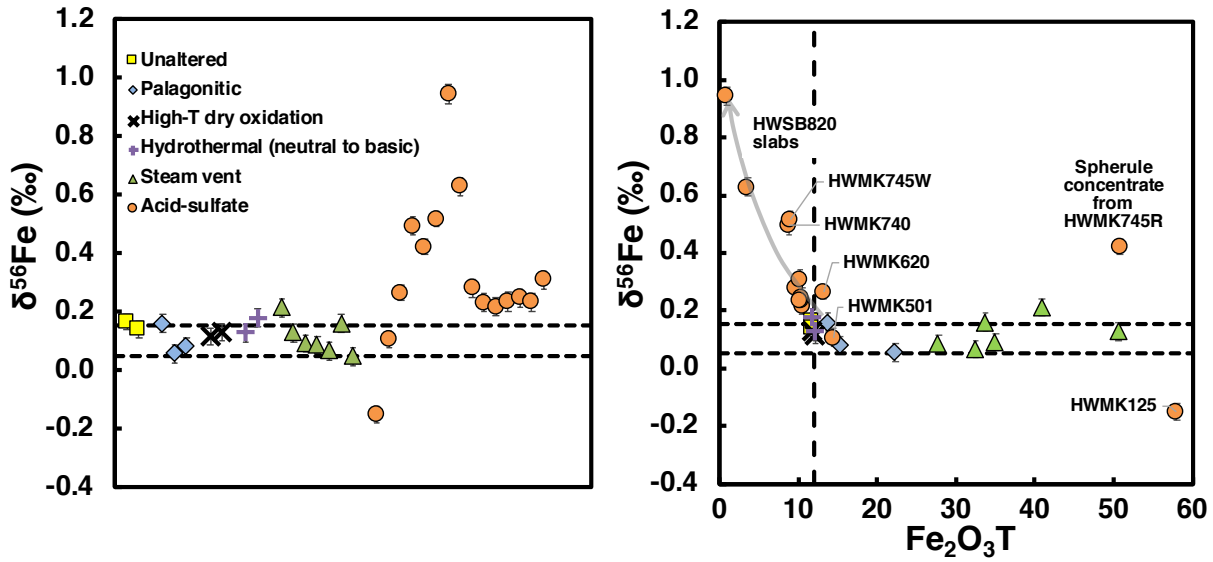

Figure 2.18 Left: Fe isotopic compositions of Hawaii samples (data from Table 2.8). Compared to other types of alteration, acid-sulfate alteration produced large Fe isotopic variation. Right: Fe isotopic compositions vs. Fe_2O_3T contents. The two black horizontal dashed lines delimit the isotopic range of unaltered basaltic rocks and tephras in Hawaii (Konter et al., 2016; Teng et al., 2013; and this study). The vertical dashed line represents the unaltered Fe_2O_3T content.

Among acid-sulfate altered samples, the HWMK820 rock slabs show heavy and large isotopic variation from +0.22 to +0.94 ‰, correlating with the Fe_2O_3T concentrations (Fig. 2.18) and Fe/Ti (mol/mol) ratios (Table 2.7). Tephra HWMK740 has a low Fe_2O_3T concentration, a low Fe/Ti ratio (or high Ti/Fe ratio; Table 2.7), and a heavy isotopic composition (+0.49 ‰) compared to unaltered tephras. It can be explained as a residue of acid-sulfate leaching of Fe. The isotopic

compositions of tephras HWMK501 and HWMK620 (+0.11 and +0.26 ‰, respectively) are heavy but they show slight iron enrichments instead of depletions compared to unaltered tephra, and cannot be explained as leaching residues as advocated for HWMK740. Hematite-rich breccia HWMK125 is the only sample having a light Fe isotopic composition (-0.15 ‰), and it has a very high Fe_2O_3T content of 58 wt% and a high Fe/Ti (mol/mol) ratio of 51. The white-colored piece HWMK745W ("W" represents "White color") and the spherule concentrate obtained from breccia HWMK745R ("R" represents whole rock) both show heavy Fe isotopic compositions of +0.52 and +0.42 ‰, respectively. HWMK745W is depleted in iron, similar to tephra HWMK740, and consistent with being a residue of acid-sulfate leaching of Fe.

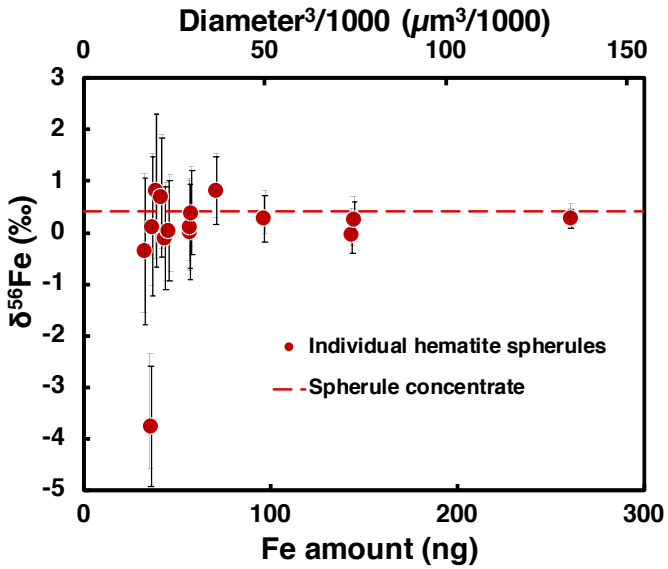

Figure 2.19 Iron isotopic compositions of hematite spherules from acid-sulfate altered breccia HWMK745R. The spherule concentrate and individual spherules are represented by a red dashed line and red solid circles, respectively. All individual spherules except one outlier have identical Fe isotopic composition as the spherule concentrate, regardless of their diameters or Fe amounts, indicating that they more likely formed by transformation from a precursor mineral than directly precipitation from a fluid.

Iron isotopic compositions of hematite spherules. The Fe contents and isotopic compositions of the 15 hematite spherules extracted from breccia HWMK745R are reported in Table 2.9 and Fig. 2.19. The Fe amounts in these spherules are small (33–260 ng). Assuming an ideal round shape and a pure Fe_2O_3 composition, this corresponds to spherules of 26–51 μm in diameter.

The $\delta^{56}Fe$ values for individual spherules are within error of the value for the spherule concentrate (+0.42 ± 0.03 ‰), although the error bars are generally larger (0.2 to 1.4 ‰; smaller spherules have bigger error bars). The large errors result from the very small Fe amount available for isotopic analyses. No correlation between mass analyzed and Fe isotopic composition was found. Fourteen out of 15 spherules have $\delta^{56}Fe$ values identical to the bulk spherule concentrate fraction (+0.42 ‰) within error, regardless of their sizes. One spherule has a very negative $\delta^{56}Fe$ value of –3.34±1.17 ‰, but it is one of the smallest spherules analyzed (Fe = 36 ng), and we cannot exclude that it suffered from an analytical artifact.

2.4.4 Probing Fe transport during spherule formation using Hawaii samples

Below we focus on the samples that are associated with acid-sulfate alteration, as the samples associated with other types of alteration in this study have not involved significant iron mobilization, as attested to by their minimal Fe isotopic variation (+0.05 to +0.21 ‰; Fig. 2.18) and nearly constant Fe/Ti ratios (Table 2.7). As will be discussed below, the processes witnessed by the samples affected by acid-sulfate alteration (nine slabs from HWSB820, breccias HWMK125 and HWMK745R, and tephras HWMK501, HWMK620 and HWMK740) are leaching of basalts (Sect. 2.4.4.1, Figs. 2.20 and 2.21A), precipitation of leached iron from acid-sulfate fluids (Sect. 2.4.4.2 and Fig. 2.21B), and mixing between fluid-derived Fe with solids (Sect. 2.4.4.3 and Fig. 2.21C).

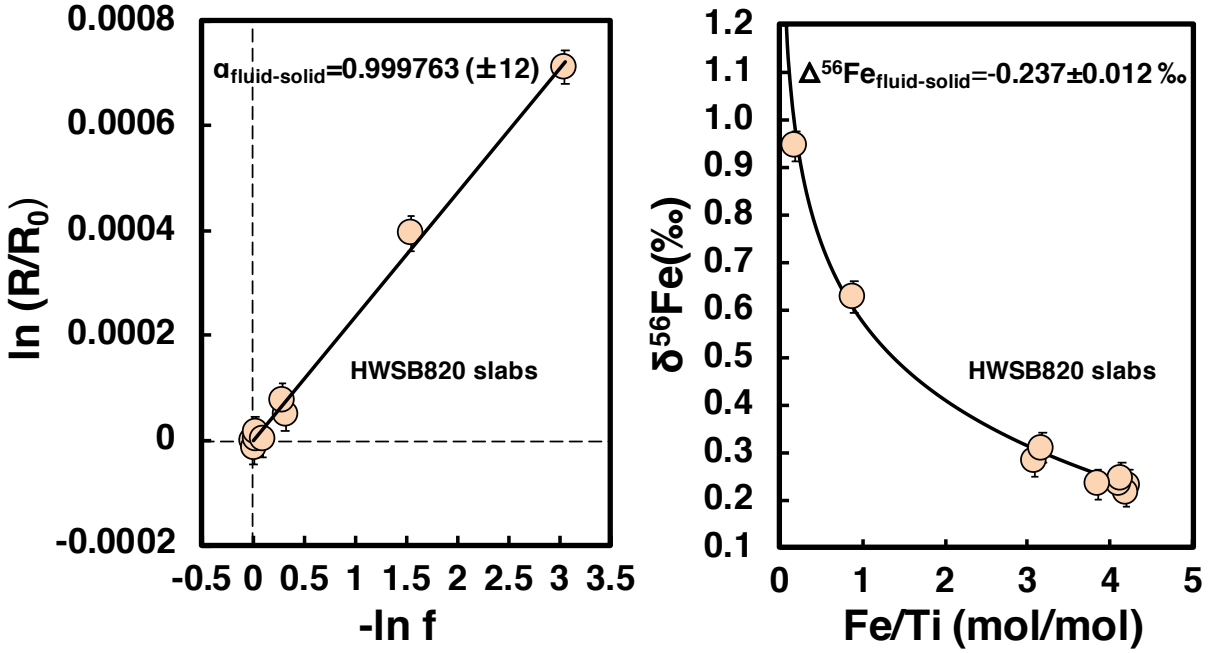

Figure 2.20 Fe isotopic fractionation during acid-sulfate leaching of basalts, constrained by rock slabs from HWSB820. A Rayleigh distillation model explains the iron isotopic variation in the rock slabs. The Fe isotope fractionation factor between acid-sulfate fluid and solid residue is tightly constrained using these rock slabs, to be –0.24 ‰, with the fluid being enriched in the light Fe isotopes. Rock slabs are represented by orange solid circles. Left: by plotting ln (R/R_0) vs. $-\ln f$, the slope of the fitted line is (1-α) in a Rayleigh distillation model. R and R_0 are the isotopic ratios ($^{56}Fe/^{54}Fe$) in altered and unaltered rock slabs respectively, f is the fraction of Fe remaining after leaching ($f = (\mathrm{Fe/Ti})_{\mathrm{sample}}/(\mathrm{Fe/Ti})_0$), and α is the Rayleigh fractionation factor. Right: The Fe isotopic compositions of the rock slabs are fitted very well with the calculated α value, which corresponds to $\Delta^{\mathrm{fluid}}_{\mathrm{residue}} = -0.237 \pm 0.012$ ‰.

2.4.4.1 Acid-sulfate leaching of basalts

Iron isotopic fractionation during acid-sulfate leaching of basalts. Rouxel et al. (2003) showed that during oceanic crust alteration, the altered basalts displayed positive $\delta^{56}Fe$ values, while chemically precipitated alteration products and hydrothermal deposits displayed negative

δ^{56}Fe values. The Fe isotopic compositions of the altered basalts correlated with their iron depletions and the correlation was fitted with a Rayleigh distillation assuming an instantaneous fractionation factor between leached and residual iron ranging from –0.3 to –0.9 ‰ for δ^{56}Fe (the δ^{56}Fe of iron released from the host rock by leaching must be lighter by 0.3 to 0.9 ‰ than that of iron in the residue).

Our samples associated with acid-sulfate leaching in this study show similarly variable extents of iron loss/gain and isotopic fractionation. Among the samples, the nine rock slabs from HWSB820 show an excellent correlation between their heavy isotopic compositions (+0.22 to +0.94 ‰) and Fe loss, as the altered basalts in Rouxel et al. (2003). Because Ti is largely immobile in aqueous fluids, the Fe/Ti ratio (mol/mol) was used to constrain the fraction of residual Fe (f) for each sample [$f = (\mathrm{Fe/Ti})_{\mathrm{sample}}/(\mathrm{Fe/Ti})_0$, where $(\mathrm{Fe/Ti})_0 = 4.2$, the ratio in the least fractionated slab]. The Fe/Ti ratios of the slabs range from 4.2 (similar to that of unaltered tephras and BHVO-1) to 0.2 (significant Fe loss). If iron was removed in a single stage by a batch of liquid equilibrating with the solid (batch equilibrium fractionation), one would be able to write a mass-balance equation,

$$\delta_{\mathrm{residue}} = \delta_0 - (1 - f)\Delta^{\mathrm{fluid}}_{\mathrm{residue}}. \quad (2.46)$$

with $\Delta^{\mathrm{fluid}}_{\mathrm{residue}}$ the isotopic fractionation between the fluid and residue in δ-notation ($\Delta^{\mathrm{fluid}}_{\mathrm{residue}} = \delta_{\mathrm{fluid}} - \delta_{\mathrm{residue}}$). As shown in Fig. 2.20, the data points do not follow such a linear relationship between $\delta_{\mathrm{residue}}$ [or ln(R/R$_0$); 1000ln(R/R$_0$)=$\delta_{\mathrm{residue}}$-$\delta_0$] and f. An alternative model in this context is a Rayleigh distillation, which assumes that iron was leached in small increments and that the liquid thus removed was extracted from the system. In δ-notation, such a distillation model takes the form,

$$\delta_{\text{residue}} \simeq \delta_0 + \Delta^{\text{fluid}}_{\text{residue}} \ln f. \quad (2.47)$$

As shown in Fig. 2.20B, this model reproduces well the dependence of δ_{residue} on f. The model gives a fluid-residue fractionation of –0.237±0.012 ‰, meaning that the fluid is enriched in the light isotopes of iron by 0.237 ‰ compared to the residue.

As discussed above, the fractionation factors between leached Fe and residual Fe during oceanic crust alteration in Rouxel et al. (2003) were –0.3 to –0.9 ‰. This is larger than the fractionation documented in this study but the values reported by Rouxel et al. (2003) show considerable scatter. This might be due to the fact that the basalts experienced several stages of alteration in a range of temperatures and alteration conditions, resulting in variable calculated fractionation factors. In contrast, the Fe isotope fractionation factor for acid-sulfate alteration documented here is very well defined.

Previous dissolution experiments using acids to dissolve rocks also show in general a light Fe isotope enrichment in the leaching fluid. Chapman et al. (2009) did lab experiments on the dissolution of a biotite granite and a tholeiitic basalt with 0.5 M HCl and 5 mM oxalic acid at room temperature to understand how Fe isotopes are fractionated during dissolution of polymineralic systems. They observed that in the first leachate, iron was always isotopically lighter than the source rock. For basalt, Fe leached by HCl was initially lighter by about –1 ‰ relative to the bulk composition while for granite, the fractionation was -1.8 ‰. These values are much larger than the value reported here for acid-sulfate alteration but the isotopic difference between the leaching solution and source rock in their experiments decreased over time as the alteration proceeded, which was ascribed to the formation of a boundary layer. Mineral dissolution of hornblende in the presence of organic ligands and microbes also tends to enrich the solution in the light Fe isotopes (Brantley et al., 2001; Brantley et al., 2004). In contrast, proton-promoted HCl dissolution of

Fe(III) oxides does not produce detectable iron isotopic fractionation, while ligand-controlled and reductive dissolution of Fe(III) oxides caused a kinetic isotope effect in the early dissolved fractions (Brantley et al., 2004; Skulan et al., 2002; Wiederhold et al., 2006). The specific isotopic fractionation between leaching solutions and solids may thus depend on several factors such as the nature of the minerals, the ligands present in solution, the oxidation state of iron, and the degree of under-saturation of the fluid phase.

Iron isotopic fractionation during basaltic rock dissolution in the presence of sulfuric acid has not been examined experimentally. Our study on natural alteration products therefore provides the first estimate of this fractionation factor. It can be compared with theoretical predictions for equilibrium fractionation between the fluid and solid residue. The caveat in this approach is that the reduced partition function ratios (or β-factors) for fluids and solids are calculated or measured using different methodologies. For basalts, the β-factor that is the most relevant is that measured on a Fe^{2+}-rich basaltic glass by the synchrotron technique of Nuclear Resonant Inelastic X-ray Scattering (NRIXS). The study reported a β-factor for a pure Fe^{2+} basaltic glass of ~6.1±0.3 ‰ at 22 °C (Dauphas et al., 2014). To estimate the β-factor of the fluid phase, one must know the speciation of iron. Casas et al. (2000) investigated the speciation of iron in Fe(II)-Fe(III)-H_2SO_4-H_2O concentrated solutions (up to 2.2 M H_2SO_4 and 1.3 M Fe) at 25 and 50 °C. In those conditions, which may be relevant to acid sulfate leaching of iron from basalts, the Fe(II) species are distributed as 78-83% Fe^{2+}_{aq} (hexaaquairon(II); an ion of Fe(II) surrounded by 6 water molecules with oxygen pointing towards iron) and 17–22% $FeSO_4^0$. It is thus reasonable to assume that iron would be dominantly as Fe^{2+}_{aq}. The β-factor of this species is highly uncertain as illustrated by the wide range of values reported in the literature, from 4.8 to 6.8 ‰ at 22 °C (Dauphas et al., 2017 and references therein).

Combining the NRIXS data for the basaltic glass and ab initio results for Fe^{2+}_{aq}, a fluid-solid equilibrium fractionation of –1.3 to +0.7 ‰ at ambient temperature is expected. This encompasses the value of –0.237±0.012 ‰ measured in this study but the uncertainty on the predicted equilibrium fractionation factor is too large to provide any guidance on whether the measured value reflects equilibrium or kinetic processes. The only evidence that this reflects fluid-rock equilibrium is that throughout the leaching, the fluid-rock isotopic fractionation seems to have remained constant so that a simple Rayleigh distillation model can reproduce very well the measured isotopic compositions corresponding to different extents of iron loss. The isotopic fractionation imparted by kinetic effects would not necessarily remain so constant in the course of leaching, as local processes and the extent to which the system departs from equilibrium would be expected to influence the net isotopic fractionation. We therefore suggest that the measured fractionation of –0.24 ‰ may reflect equilibrium isotopic fractionation between Fe^{2+}_{aq} and iron in basaltic rocks.

Iron isotopic composition of fluids. The Fe isotopic composition of the cumulative fluid produced by acid-sulfate leaching of basalts in a Rayleigh distillation can be calculated using the following equation,

$$\delta^{56}Fe_{\text{cumulative fluid}} = \delta^{56}Fe_{\text{bulk}} - \Delta^{\text{fluid}}_{\text{residue}} \times f \times \ln f/(1-f). \quad (2.48)$$

In Fig. 2.21B, we plot the Fe isotopic compositions of the cumulative fluids and residue (connected with tie lines) for different extents of leaching f, assuming the $\delta^{56}Fe_{\text{bulk}} = +0.1$ ‰ (unaltered basalts) and $\Delta^{\text{fluid}}_{\text{residue}}$ of –0.24 ‰ (constrained by HWSB820 slabs). As shown, the cumulative fluid would have a $\delta^{56}Fe$ ranging between –0.14 and +0.1 ‰ for f between 1 and 0. The instantaneous fluids (not shown) would always track the isotopic compositions of the residue and can range from –0.14 to values heavier than +0.1 ‰,

$$\delta^{56}Fe_{\text{instantaneous fluid}} = \delta^{56}Fe_{\text{residue}} - \Delta^{\text{fluid}}_{\text{residue}} = \delta^{56}Fe_{\text{bulk}} + \Delta^{\text{fluid}}_{\text{residue}} (1+ \ln f). \quad (2.49)$$

2.4.4.2 Iron precipitation from acid-sulfate fluids and hematite formation

A previous study by Morris et al. (2005) on breccia HWMK745R suggested that the spherules in the rock could have formed by precipitation from solutions produced by acid-sulfate alteration of basaltic rocks. Two pathways were suggested by them for hematite spherule formation: 1) direct precipitation from the liquid produced by acid-sulfate dissolution of basaltic material, and 2) a two-step process involving precipitation of hydronium jarosite and other sulfates from the fluid in the first, followed by hydrolysis of jarosite ($(H_3O)Fe_3(SO_4)_2(OH)_6 + 2H_2O \rightarrow 3Fe(OH)_3 + 2SO_4^{2-} + 4H^+$; Golden et al., 2008) to form hematite. Our Fe isotope measurements of individual hematite spherules from HWMK745R provide clues to distinguish the two pathways.

The $\delta^{56}Fe$ values of spherules range from –0.4 to +0.8 ‰ with relatively large errors (Fig. 2.19). Although this isotopic range seems big, we consider that the spherules are homogeneous for two reasons: 1) Except for one outlier, the individual hematite spherules have Fe isotopic compositions identical to the spherule concentrate within error. 2) This range is much smaller than what one would expect from direct Fe precipitation. Solid precipitation from a fluid usually follows a Rayleigh distillation process, meaning that once the solid precipitates, it would not be able to exchange isotopes efficiently with the fluid. In this case, isotopic fractionation between the fluid and the solid would drive the isotopic composition of the solid to change quickly as more iron precipitates. Accordingly, the Fe isotopic compositions of the spherules would be variable and some internal heterogeneity within a given spherule would be expected. Assuming a Rayleigh fractionation factor of ~+1 ‰ between precipitates and the fluid (Bullen et al., 2001; Croal et al., 2004; Nie et al., 2017), the expected $\delta^{56}Fe$ variation of precipitates can easily reach several per mil, much larger than the range shown in individual spherules (~ 1 ‰).

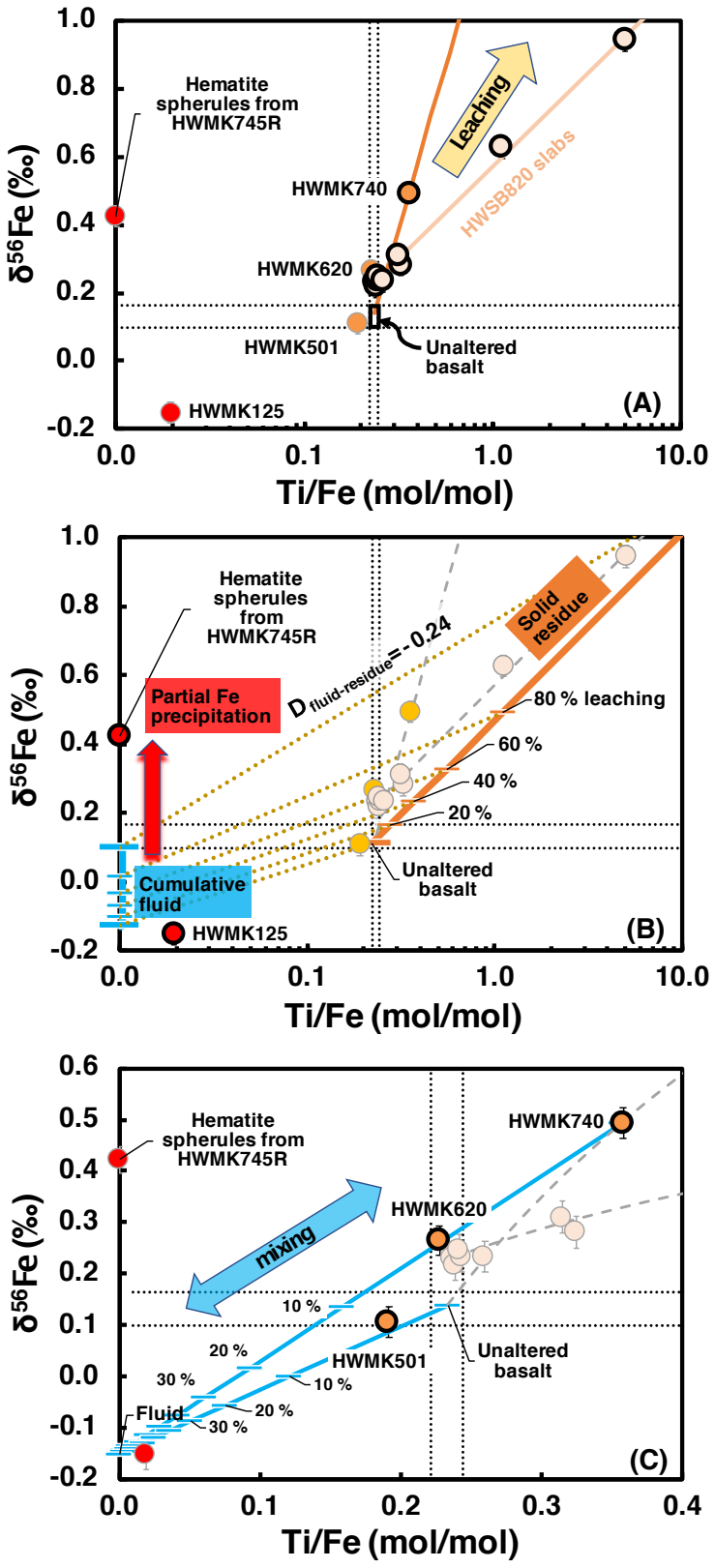

Figure 2.21 Iron isotope fractionations during acid-sulfate alteration related processes.

Figure 2.21 (continued) (A) Leaching of basalts produces a heavy isotopic enrichment in residues characterized by high Ti/Fe ratios. Rock slabs from HWSB820 and tephra HWMK740 can be explained this way but other acid-sulfate samples cannot. (B) Iron precipitation from Fe-carrying fluids produced by acid-sulfate leaching of basalts. The isotopic compositions of cumulative fluids produced by leaching of unaltered basalts are shown in blue, and the fluids and residue corresponding to the same extent of Fe leaching are linked with orange dashed lines. The isotopic compositions of the cumulative fluids range from ~-0.14 to +0.1 ‰, assuming a +0.1 ‰ starting composition and a fractionation factor of -0.24 ‰ between the fluid and the residue. The light isotopic composition of hematite-rich breccia HWMK125 (–0.15 ‰) is best explained by near quantitative Fe precipitation from a fluid with light Fe isotopic composition. The heavy isotopic composition of spherules (+0.42 ‰) from HWMK745R is more consistent with partial precipitation of Fe from an acid-sulfate fluid. (C) Mixing between fluid-derived Fe and solids (altered and unaltered) explains tephra HWMK501 and HWMK620, which cannot be explained simply as leaching residues due to their lower Ti/Fe ratios than unaltered rocks. The altered solid endmember is represented by HWMK740, the most fractionated tephra sample. The unaltered composition (unaltered tephras and basalts) is at the crossover of the dashed lines.

The homogeneity in isotopic composition of the spherules, regardless of their sizes, suggests that they are cogenetic, probably formed during the same event. The fact that the spherules have very similar Fe isotopic composition as the host matrix also supports the idea that the spherules formed by the transformation of a precursor mineral from which they directly inherited their iron isotopic composition. Hematite spherule synthesis through forced hydrolysis of hydronium jarosite under hydrothermal conditions was investigated experimentally by Golden et al. (2008) and shown to be feasible. A hydrothermal pathway through hydronium jarosite is thus reasonable for the Mauna Kea spherules given the acid-sulfate conditions and the presence of jarosite. Other pathways through, for example goethite, ferrihydrite, and schwertmannite (*e.g.*,

Combes et al., 1990; Cornell and Schwertmann, 1996; Fischer and Schwertmann, 1975; Stahl et al., 1993; Tosca et al., 2008) are possible but not supported by the nondetection of those phases.

As discussed above, hematite most likely formed by hydrolysis of precursor jarosite and the conversion was quantitative such that hematite inherited its Fe isotopic composition from that of jarosite. An outstanding question that remains to be answered is why the two hematite precipitates, HWMK125, and spherules from HWMK745R have so different Fe isotopic compositions (–0.15 and +0.42 ‰ respectively). As discussed in Sect. 2.4.4.1, the cumulative fluid produced by acid-sulfate leaching of basalts has δ^{56}Fe values of ~–0.15 to +0.1 ‰. Complete precipitation of a fluid with an isotopic composition of ~–0.15 ‰ can readily explain the Fe isotopic composition of HWMK125. The heavy Fe isotopic composition of spherules from HWMK745R can be explained by two processes that are not mutually exclusive. One scenario is that this sample formed by partial Fe oxidation and precipitation from a fluid. Indeed, precipitates of Fe(III) oxides from Fe(II) fluids through iron oxidation (either by oxygen, UV photons or microbial; Bullen et al., 2001; Croal et al., 2004; Nie et al., 2017) produce ~+1 ‰ fractionation between isotopically heavy precipitates and isotopically light fluids. At equilibrium jarosite is expected to have similar or even heavier Fe isotopic composition than iron oxides such as goethite and hematite (Blanchard et al., 2009; Blanchard et al., 2015; Dauphas et al., 2012; Rustad and Dixon, 2009). Therefore, partial oxidation and precipitation of Fe (*e.g.*, ~80 % Fe precipitation from a fluid of ~0 ‰) would easily drive the Fe isotopic composition of the precipitate to the observed heavy value. Another explanation is that the spherules formed by complete precipitation of a fluid that had heavy Fe isotopic composition to begin with. During acid sulfate alteration, the Fe isotopic composition of the instantaneous fluids (Eq. 2.49) produced by leaching the most extensively iron-depleted (leached and isotopically heavy) samples would have heavy Fe isotopic

composition. We prefer the first scenario because it is not clear whether leaching of an iron-depleted residue would provide enough iron to produce a hematite-rich rock. For example, to get an instantaneous fluid with +0.42 ‰ isotopic composition, ~90 % Fe depletion (assuming an initial composition of +0.1 ‰ and $\Delta^{fluid}_{residue}$ = –0.24 ‰) is needed before leaching.

2.4.4.3 Mixing between fluid-derived Fe and solids

The tephra samples affected by acid-sulfate alteration (HWMK501, HWMK620, and HWMK740) have δ^{56}Fe values of +0.11, +0.27 and +0.49 ‰, respectively. Assuming an unfractionated initial value of ~+0.1 ‰, similar to the unaltered tephras and BHVO-1, and a Rayleigh distillation process with $\Delta^{fluid}_{residue}$ = –0.24 ‰ (as defined by HWSB820 in Sect. 2.4.4.1), these Fe isotopic values would correspond to little Fe loss for HWMK501, but ~ 50 % and 80 % Fe loss for HWMK620 and HWMK740 respectively. However, the Fe/Ti ratios of these samples do not show such extensive Fe loss. HWMK501 and HWMK620 show slightly higher Fe/Ti ratios (5.22 and 4.39; iron-enrichment rather than depletion) than unaltered tephras (~4.2). HWMK740 has a Fe/Ti ratio of 2.8, corresponding to only ~30 % Fe loss, not 80 % Fe loss inferred from its iron isotopic composition. Therefore, acid-sulfate leaching of basalts with $\Delta^{fluid}_{residue}$ = –0.24 ‰ is inconsistent with the Fe isotopic compositions of these samples.

For HWMK740, since it is Fe-depleted, the isotopic composition can be explained still by acid-sulfate leaching, but with a bigger fractionation factor between fluid and solid (Fig. 2.21A). Using the same method as outlined in Sect. 2.4.4.1, a fractionation of ~–0.85 ‰ between fluid and solid is derived. A possible scenario to produce this large fractionation is that the precursor of HWMK740 was leached under quite oxidizing conditions or in long interaction time, so that while leaching, some leached Fe(II) in the fluid got oxidized to Fe(III) and precipitated back. Since

precipitated Fe(III) is isotopically heavier than fluid Fe(II) by ~1 ‰ or bigger (Bullen et al., 2001; Croal et al., 2004; Nie et al., 2017; Sect. 4.2), this mobilization-oxidation-re-precipitation process can significantly enhance the fractionation between the fluid and the solid. One observation supporting this scenario is that HWMK740 has very high Fe(III)/Fe(Total) ratio compared to unaltered tephras (0.9 vs. 0.4), consistent with iron being oxidized.

Both HWMK501 and HWMK620 cannot be explained the same way as for HWMK740. The reason is that they have relatively heavy Fe isotopic compositions but are Fe-enriched (low Ti/Fe ratios). These two samples are most likely mixtures of a solid substrate (altered or unaltered basalts) and Fe-carrying acid-sulfate fluid (Fe mobilized by previous leaching). In Fig. 2.21C, we show the trajectories for mixing between a fluid (-0.15 ‰, and Ti/Fe=0) produced by acid-sulfate leaching of basalts and (1) altered tephra (using HWMK740 as an endmember since it is the most fractionated tephra), and (2) unaltered composition.

2.4.4.4 Application to hematite formation on Mars

The Hawaii hematite spherules resemble the martian hematite spherules in terms of mineralogy, morphology and geochemistry. The coexisting mineralogies of martian hematite spherules, jarosite, and other Mg-, Ca-, Fe-sulfates are consistent with a two-step hematite formation scenario: (1) acidic water interacting with basalts to form jarosite and other sulfates in a playa-like environment, and (2) the breakdown of jarosite and other Fe sulfates led to the formation of hematite during a groundwater recharge event (McLennan et al., 2005). The isotopic compositions of Hawaii rocks and spherules in this study show that the spherules very likely formed in a very similar way, involving acid-sulfate leaching of Fe from basalts, precipitation of jarosite from the fluid thus produced, followed by the transformation of jarosite into hematite. Therefore, the Hawaii spherules represent an excellent terrestrial analogue to martian spherules.

One important difference, however, is that on Earth, $Fe(II)_{aq}$ oxidation and precipitation from a fluid can be readily fulfilled by O_2 or microbes, but it is still unknown how $Fe(II)_{aq}$ on ancient Mars (presumably late Noachian and early Hesperian epoch; Hynek et al., 2002) was oxidized. Indeed, the O_2 partial pressure was presumably small, oxidation kinetics under acidic conditions were slow, and life may be absent on Mars. Photo-oxidation on Mars might have played a role (Hurowitz et al., 2010; Nie et al., 2017), but recent discovery of Mn oxides as filling veins at Gale crater on Mars calls for large amount of O_2 to be present since photo-oxidation of Mn(II) is not efficient (Lanza et al., 2016). Differentiating the two pathways (photo-oxidation vs. oxygen oxidation) could be difficult since they produce similar Fe isotopic fractionations, and one possible way to tell them apart might be measuring the Fe isotopic mass dependent fractionation laws of the two processes. Photo-oxidation of Fe follows the high-T equilibrium fractionation law (Nie et al., 2017) but the law for oxidation by O_2 has not been determined.

The hematite from HWMK745R and the other hematite-rich breccia HWMK125 have very different Fe isotopic compositions (+0.42 ‰ vs. –0.15 ‰). The light composition is consistent with Fe being quantitatively precipitated from an Fe-carrying acid-sulfate fluid, and the heavy composition of the spherules in HWMK745R can be explained by partial precipitation of iron from acid-sulfate fluids. We did not measure other hematite-rich samples, but if the interpretations are correct, it is very likely that a range of hematite isotopic compositions are present. Drawing a similarity with Hawaii, martian spherules may also display variable Fe isotopic compositions at the outcrop scale. Two hematite populations have been identified in the Meridiani planum: relatively big spherules of millimeter size and smaller hematite particles (the size may be comparable to Hawaii spherules) in the surrounding sulfate-rich rock (Klingelhöfer et al., 2004; Morris et al., 2005). Iron isotope measurements of these two spherule populations, together with

other geochemical analyses, may help understand the detailed pathways that led to the formation of martian blueberries. In the present state of advancement of the technology, these iron isotopic variations can only be measured in large Earth-based laboratories, calling for the return of samples for detailed analyses.

2.4.5 Conclusions

UV photo-oxidation as a possible iron oxidation mechanism on Mars to form martian hematite spherules (martian blueberries) was explored. The quantum yield of the iron photo-oxidation reaction and the timescales for Fe(II) photo-oxidation on Mars has been calculated (Fig. 2.14), and compared to that of the oxidation by O_2 (Fig. 2.16). It shows that photo-oxidation is a very likely pathway to form hematite-jarosite deposits on early Mars provided that shallow water bodies persisted for months to years. In acidic conditions, the kinetics of iron oxidation by O_2 are even longer, unless this was mediated by some form of biological activity, which has not yet been detected. UV photo-oxidation within standing bodies of water on early Mars is a viable mechanism to explain the formation of jarosite-hematite deposits, characterized by recent martian remote sensing and rover missions.

Hematite spherules and associated lithologies from Hawaii were studied as a terrestrial analogue. The Fe isotopic compositions of hematite spherules and associated altered basaltic rocks and tephras from Hawaii were measured to constrain iron isotopic fractionation during acid-sulfate alteration and hematite formation processes. Acid-sulfate leaching of basalts is a Rayleigh-type fractionation process, with the leaching fluid being enriched in the lighter Fe isotopes relative to the solid residue, by 0.24 ‰ (Fig. 2.20). The basaltic rock and tephra samples in association with acid-sulfate alteration can be explained either as the residue of acid-sulfate leaching of basalts or as the product of mixing between Fe-carrying acid-sulfate fluids and solids (Fig. 2.21).

Hematite breccia HWMK125 has light Fe isotopic composition (–0.15 ‰), while hematite spherules from HWMK745R have heavy Fe isotopic composition (+0.42 ‰). The contrast between the two most likely reflects different extents of iron oxidation and precipitation from acid-sulfate fluids. Individual hematite spherules in HWMK745R all have similar Fe isotopic composition, suggesting that hematite did not directly precipitate from a fluid, but was instead produced from precipitation of hydronium jarosite from fluids produced by acid-sulfate leaching of basalts, followed by hydrolysis to hematite. This hematite formation process is very similar to the formation mechanism that has been proposed for martian hematite spherules, making Hawaii spherules an excellent terrestrial analogue.

References

Alexander, B.W., Bau, M., Andersson, P., 2009. Neodymium isotopes in Archean seawater and implications for the marine Nd cycle in Earth's early oceans. Earth and Planetary Science Letters 283, 144–155.

Amor, M., Busigny, V., Louvat, P., Gélabert, A., Cartigny, P., Durand-Dubief, M., Ona-Nguema, G., Alphandéry, E., Chebbi, I., Guyot, F., 2016. Mass-dependent and-independent signature of Fe isotopes in magnetotactic bacteria. Science 352, 705–708.

Anbar, A.D., Holland, H.D., 1992. The photochemistry of manganese and the origin of banded iron formations. Geochimica et Cosmochimica Acta 56, 2595–2603.

Angert, A., Rachmilevitch, S., Barkan, E., Luz, B., 2003. Effects of photorespiration, the cytochrome pathway, and the alternative pathway on the triple isotopic composition of atmospheric O_2. Global Biogeochemical Cycles 17(1).

Archer, C., Vance, D., 2006. Coupled Fe and S isotope evidence for Archean microbial Fe (III) and sulfate reduction. Geology 34, 153–156.

Arvidson, R., Poulet, F., Morris, R., Bibring, J.P., Bell, J., Squyres, S., Christensen, P., Bellucci, G., Gondet, B., Ehlmann, B., 2006. Nature and origin of the hematite-bearing plains of Terra Meridiani based on analyses of orbital and Mars Exploration Rover data sets. Journal of Geophysical Research: Planets 111(E12).

Balci, N., Bullen, T.D., Witte-Lien, K., Shanks, W.C., Motelica, M., Mandernack, K.W., 2006. Iron isotope fractionation during microbially stimulated Fe(II) oxidation and Fe(III) precipitation. Geochimica et Cosmochimica Acta 70, 622–639.

Baldridge, A.M., Hook, S.J., Crowley, J.K., Marion, G.M., Kargel, J.S., Michalski, J.L., Thomson, B.J., de Souza Filho, C.R., Bridges, N.T., Brown, A.J., 2009. Contemporaneous deposition of phyllosilicates and sulfates: Using Australian acidic saline lake deposits to describe geochemical variability on Mars. Geophysical Research Letters 36(19).

Bao, H., Koch, P.L., 1999. Oxygen isotope fractionation in ferric oxide-water systems: low temperature synthesis. Geochimica et Cosmochimica Acta 63, 599–613.

Bau, M., Höhndorf, A., Dulski, P., Beukes, N.J., 1997. Sources of rare-earth elements and iron in Paleoproterozoic iron-formations from the Transvaal Supergroup, South Africa: evidence from neodymium isotopes. The Journal of Geology 105(1), 121–129.

Beard, B.L., Handler, R.M., Scherer, M.M., Wu, L., Czaja, A.D., Heimann, A., Johnson, C.M., 2010. Iron isotope fractionation between aqueous ferrous iron and goethite. Earth and Planetary Science Letters 295, 241–250.

Blanchard, M., Dauphas, N., Hu, M., Roskosz, M., Alp, E., Golden, D., Sio, C., Tissot, F., Zhao, J., Gao, L., 2015. Reduced partition function ratios of iron and oxygen in goethite. Geochimica et Cosmochimica Acta 151, 19–33.

Blanchard, M., Poitrasson, F., Méheut, M., Lazzeri, M., Mauri, F., Balan, E., 2009. Iron isotope fractionation between pyrite (FeS_2), hematite (Fe_2O_3) and siderite ($FeCO_3$): a first-principles density functional theory study. Geochimica et Cosmochimica Acta 73, 6565–6578.

Bowen, G.J., Ehleringer, J.R., Chesson, L.A., Stange, E., Cerling, T.E., 2007. Stable isotope ratios of tap water in the contiguous United States. Water Resources Research 43(3).

Brantley, S.L., Liermann, L., Bullen, T.D., 2001. Fractionation of Fe isotopes by soil microbes and organic acids. Geology 29, 535–538.

Brantley, S.L., Liermann, L.J., Guynn, R.L., Anbar, A., Icopini, G.A., Barling, J., 2004. Fe isotopic fractionation during mineral dissolution with and without bacteria. Geochimica et Cosmochimica Acta 68, 3189–3204.

Braterman, P.S., Cairns-Smith, A.G., Sloper, R.W., 1983. Photo-oxidation of hydrated Fe^{2+}; significance for banded iron formations. Nature 303, 163–164.

Buck, R.P., Singhadeja, S., Rogers, L.B., 1954. Ultraviolet absorption spectra of some inorganic ions in aqueous solutions. Analytical Chemistry 26, 1240–1242.

Bullen, T.D., White, A.F., Childs, C.W., Vivit, D.V., Schulz, M.S., 2001. Demonstration of significant abiotic iron isotope fractionation in nature. Geology 29, 699–702.

Burns, R.G., 1993. Rates and mechanisms of chemical weathering of ferromagnesian silicate minerals on Mars. Geochimica et Cosmochimica Acta 57, 4555–4574.

Burns, R.G., Fisher, D.S., 1993. Rates of oxidative weathering on the surface of Mars. Journal of Geophysical Research: Planets 98, 3365–3372.

Busigny, V., Dauphas, N., 2007. Tracing paleofluid circulations using iron isotopes: A study of hematite and goethite concretions from the Navajo Sandstone (Utah, USA). Earth and Planetary Science Letters 254, 272–287.

Butler, I.B., Archer, C., Vance, D., Oldroyd, A., Rickard, D., 2005. Fe isotope fractionation on FeS formation in ambient aqueous solution. Earth and Planetary Science Letters 236, 430–442.

Cairns-Smith, A.G., 1978. Precambrian solution photochemistry, inverse segregation, and banded iron formations. Nature 276, 807–808.

Casas, J.M., Alvarez, F., Cifuentes, L., 2000. Aqueous speciation of sulfuric acid-cupric sulfate solutions. Chemical Engineering Science 55, 6223–6234.

Chakraborty, S., Bhattacharya, S., 2003. Oxygen isotopic fractionation during UV and visible light photodissociation of ozone. The Journal of chemical physics 118, 2164–2172.

Chan, M.A., Beitler, B., Parry, W.T., Ormö, J., Komatsu, G., 2004. A possible terrestrial analogue for haematite concretions on Mars. Nature 429, 731.

Chan, M.A., Johnson, C.M., Beard, B.L., Bowman, J.R., Parry, W.T., 2006. Iron isotopes constrain the pathways and formation mechanisms of terrestrial oxide concretions: A tool for tracing iron cycling on Mars? Geosphere 2, 324–332.

Chapman, J.B., Weiss, D.J., Shan, Y., Lemburger, M., 2009. Iron isotope fractionation during leaching of granite and basalt by hydrochloric and oxalic acids. Geochimica et Cosmochimica Acta 73, 1312–1324.

Christensen, P., Morris, R., Lane, M., Bandfield, J., Malin, M., 2001. Global mapping of martian hematite mineral deposits: Remnants of water-driven processes on early Mars. J. Geophys. Res 106, 23873–23885.

Christensen, P.R., Wyatt, M.B., Glotch, T.D., Rogers, A.D., Anwar, S., Arvidson, R.E., Bandfield, J.L., Blaney, D.L., Budney, C., Calvin, W.M., 2004. Mineralogy at Meridiani Planum from the Mini-TES experiment on the Opportunity Rover. Science 306, 1733–1739.

Clayton, R.N., 2002. Solar system: Self-shielding in the solar nebula. Nature 415, 860–861.

Cloud, P., 1973. Paleoecological significance of the banded iron-formation. Economic Geology 68, 1135–1143.

Cloud, P.E., 1965. Significance of the Gunflint (Precambrian) microflora photosynthetic oxygen may have had important local effects before becoming a major atmospheric gas. Science 148, 27–35.

Combes, J.M., Manceau, A., Calas, G., 1990. Formation of ferric oxides from aqueous solutions: A polyhedral approach by X-ray absorption spectroscopy: II. Hematite formation from ferric gels. Geochimica et Cosmochimica Acta 54, 1083–1091.

Cornell, R.M., Schwertmann, U., 1996. The Iron Oxides. VCH, New York.

Craddock, P.R., Dauphas, N., 2011. Iron isotopic compositions of geological reference materials and chondrites. Geostandards and Geoanalytical Research 35, 101–123.

Croal, L.R., Johnson, C.M., Beard, B.L., Newman, D.K., 2004. Iron isotope fractionation by Fe (II)-oxidizing photoautotrophic bacteria. Geochimica et Cosmochimica Acta 68, 1227–1242.

Dauphas, N., Cates, N.L., Mojzsis, S.J., Busigny, V., 2007. Identification of chemical sedimentary protoliths using iron isotopes in the > 3750 Ma Nuvvuagittuq supracrustal belt, Canada. Earth and Planetary Science Letters 254, 358–376.

Dauphas, N., Janney, P.E., Mendybaev, R.A., Wadhwa, M., Richter, F.M., Davis, A.M., van Zuilen, M., Hines, R., Foley, C.N., 2004a. Chromatographic separation and multicollection-ICPMS analysis of iron. Investigating mass-dependent and-independent isotope effects. Analytical Chemistry 76, 5855–5863.

Dauphas, N., John, S. G., Rouxel, O., 2017. Iron isotope systematics. Reviews in Mineralogy and Geochemistry 82, 415–510.

Dauphas, N., Pourmand, A., Teng, F.-Z., 2009. Routine isotopic analysis of iron by HR-MC-ICPMS: How precise and how accurate? Chemical Geology 267, 175–184.

Dauphas, N., Roskosz, M., Alp, E., Golden, D., Sio, C., Tissot, F., Hu, M., Zhao, J., Gao, L., Morris, R., 2012. A general moment NRIXS approach to the determination of equilibrium Fe isotopic fractionation factors: application to goethite and jarosite. Geochimica et Cosmochimica Acta 94, 254–275.

Dauphas, N., Roskosz, M., Alp, E.E., Neuville, D.R., Hu, M.Y., Sio, C.K., Tissot, F.L.H., Zhao, J., Tissandier, L., Médard, E., Cordier, C., 2014. Magma redox and structural controls on iron isotope variations in Earth's mantle and crust. Earth and Planetary Science Letters 398, 127–140.

Dauphas, N., Rouxel, O., 2006. Mass spectrometry and natural variations of iron isotopes. Mass Spectrometry Reviews 25, 515–550.

Dauphas, N., Schauble, E.A., 2016. Mass Fractionation Laws, Mass-Independent Effects, and Isotopic Anomalies. Annual Review of Earth and Planetary Sciences 44, 709–783

Dauphas, N., van Zuilen, M., Wadhwa, M., Davis, A.M., Marty, B., Janney, P.E., 2004b. Clues from Fe Isotope Variations on the Origin of Early Archean BIFs from Greenland. Science 306, 2077–2080.

Dehouck, E., Mangold, N., Le Mouélic, S., Ansan, V., Poulet, F., 2010. Ismenius Cavus, Mars: A deep paleolake with phyllosilicate deposits. Planetary and Space Science 58, 941–946.

Dymek, R.F., Klein, C., 1988. Chemistry, petrology and origin of banded iron-formation lithologies from the 3800 Ma Isua supracrustal belt, West Greenland. Precambrian Research 39, 247–302.

Edmond, J.M., Von Damm, K., McDuff, R., Measures, C., 1982. Chemistry of hot springs on the East Pacific Rise and their effluent dispersal. Nature 297, 187–191.

Ehlmann, B.L., Mustard, J.F., Fassett, C.I., Schon, S.C., Head III, J.W., Des Marais, D.J., Grant, J.A., Murchie, S.L., 2008. Clay minerals in delta deposits and organic preservation potential on Mars. Nature Geoscience 1, 355–358.

Farquhar, J., Savarino, J., Airieau, S., Thiemens, M.H., 2001. Observation of wavelength-sensitive mass-independent sulfur isotope effects during SO2 photolysis: Implications for the early atmosphere. Journal of Geophysical Research: Planets 106, 32829–32839.

Farquhar, J., Wing, B.A., 2003. Multiple sulfur isotopes and the evolution of the atmosphere. Earth and Planetary Science Letters 213, 1–13.

Fischer, W.R., Schwertmann, U., 1975. The formation of hematite from amorphous iron(III) hydroxide. Clays and Clay Minerals 23, 33–37.

Frierdich, A.J., Beard, B.L., Reddy, T.R., Scherer, M.M., Johnson, C.M., 2014. Iron isotope fractionation between aqueous Fe (II) and goethite revisited: New insights based on a multi-direction approach to equilibrium and isotopic exchange rate modification. Geochimica et Cosmochimica Acta 139, 383–398.

Frierdich, A.J., Beard, B.L., Rosso, K.M., Scherer, M.M., Spicuzza, M.J., Valley, J.W., Johnson, C.M., 2015. Low temperature, non-stoichiometric oxygen-isotope exchange coupled to Fe (II)–goethite interactions. Geochimica et Cosmochimica Acta 160, 38–54.

Garrels, R.M., Perry, E.A., Mackenzie, F.T., 1973. Genesis of Precambrian iron-formations and the development of atmospheric oxygen. Economic Geology 68, 1173–1179.

Golden, D.C., Ming, D.W., Morris, R.V., Graff, T.G., 2008. Hydrothermal synthesis of hematite spherules and jarosite: Implications for diagenesis and hematite spherule formation in sulfate outcrops at Meridiani Planum, Mars. American Mineralogist 93, 1201–1214.

Golden, D.C., Morris, R.V., Ming, D.W., Lauer, H.V., Yang, S.R., 1993. Mineralogy of three slightly palagonitized basaltic tephra samples from the summit of Mauna Kea, Hawaii. Journal of Geophysical Research: Planets 98, 3401–3411.

Graff, T.G., Morris, R.V., Ming, D.W., Hamilton, J.C., Adams, M., Fraeman, A.A., Arvidson, R.E., Catalano, J.G., Mertzman, S.A., 2014. Chemical and Mineralogical Characterization of a Hematite-bearing Ridge on Mauna Kea, Hawaii: A Potential Mineralogical Process Analog for the Mount Sharp Hematite Ridge. Lunar and Planetary Science 45, #2019.

Grant, J.A., Irwin, R.P., Grotzinger, J.P., Milliken, R.E., Tornabene, L.L., McEwen, A.S., Weitz, C.M., Squyres, S.W., Glotch, T.D., Thomson, B.J., 2008. HiRISE imaging of impact megabreccia and sub-meter aqueous strata in Holden Crater, Mars. Geology 36, 195–198.

Grotzinger, J.P., Arvidson, R., Bell, J., Calvin, W., Clark, B., Fike, D., Golombek, M., Greeley, R., Haldemann, A., Herkenhoff, K., 2005. Stratigraphy and sedimentology of a dry to wet eolian depositional system, Burns formation, Meridiani Planum, Mars. Earth and Planetary Science Letters 240, 11–72.

Grotzinger, J.P., Gupta, S., Malin, M.C., Rubin, D.M., Schieber, J., Siebach, K., Sumner, D.Y., Stack, K.M., Vasavada, A.R., Arvidson, R.E., Calef, F., Edgar, L., Fischer, W.F., Grant, J.A., Griffes, J., Kah, L.C., Lamb, M.P., Lewis, K.W., Mangold, N., Minitti, M.E., Palucis, M., Rice, M., Williams, R.M.E., Yingst, R.A., Blake, D., Blaney, D., Conrad, P., Crisp, J., Dietrich, W.E., Dromart, G., Edgett, K.S., Ewing, R.C., Gellert, R., Hurowitz, J.A., Kocurek, G., Mahaffy, P., McBride, M.J., McLennan, S.M., Mischna, M., Ming, D., Milliken, R., Newsom, H., Oehler, D., Parker, T.J., Vaniman, D., Wiens, R.C., Wilson, S.A., 2015. Deposition, exhumation, and paleoclimate of an ancient lake deposit, Gale crater, Mars. Science 350 (6257).

Grotzinger, J.P., Kasting, J.F., 1993. New constraints on Precambrian ocean composition. The Journal of Geology 101(2), 235–243.

Hamilton, V.E., Morris, R.V., Gruener, J.E., Mertzman, S.A., 2008. Visible, near-infrared, and middle infrared spectroscopy of altered basaltic tephras: Spectral signatures of phyllosilicates, sulfates, and other aqueous alteration products with application to the mineralogy of the Columbia Hills of Gusev Crater, Mars. Journal of Geophysical Research: Planets 113 (E12).

Hartman, H., 1984. The evolution of photosynthesis and microbial mats: A speculation on the banded iron formations. Microbial Mats: Stromatolites, 449–453.

Haugaard, R., Frei, R., Stendal, H., Konhauser, K., 2013. Petrology and geochemistry of the~ 2.9 Ga Itilliarsuk banded iron formation and associated supracrustal rocks, West Greenland: Source characteristics and depositional environment. Precambrian Research 229, 150–176.

Heidenreich III, J.E., Thiemens, M.H., 1983. A non-mass-dependent isotope effect in the production of ozone from molecular oxygen. The Journal of Chemical Physics 78, 892–895.

Heimann, A., Johnson, C.M., Beard, B.L., Valley, J.W., Roden, E.E., Spicuzza, M.J., Beukes, N.J., 2010. Fe, C, and O isotope compositions of banded iron formation carbonates demonstrate a major role for dissimilatory iron reduction in~ 2.5 Ga marine environments. Earth and Planetary Science Letters 294, 8–18.

Holland, H.D., 1973. The oceans; a possible source of iron in iron-formations. Economic Geology 68, 1169–1172.

Hurowitz, J.A., Fischer, W.W., Tosca, N.J., Milliken, R.E., 2010. Origin of acidic surface waters and the evolution of atmospheric chemistry on early Mars. Nature Geoscience 3, 323–326.

Hynek, B. M., Arvidson, R. E., Phillips, R. J., 2002. Geologic setting and origin of Terra Meridiani hematite deposit on Mars. Journal of Geophysical Research 107(E10), 5088. doi: 10.1029/2002JE001891, 2002.

Hynek, B.M., Phillips, R.J., 2008. The stratigraphy of Meridiani Planum, Mars, and implications for the layered deposits' origin. Earth and Planetary Science Letters 274, 214–220.

Jacobsen, S.B., Pimentel-Klose, M.R., 1988. A Nd isotopic study of the Hamersley and Michipicoten banded iron formations: the source of REE and Fe in Archean oceans. Earth and Planetary Science Letters 87, 29–44.

James, H.L., 1954. Sedimentary facies of iron-formation. Economic Geology 49, 235–293.

Janecek, M., 2012. Reflectivity spectra for commonly used reflectors. IEEE Transactions on Nuclear Science 59, 490–497.

John, S.G., Adkins, J.F., 2010. Analysis of dissolved iron isotopes in seawater. Marine Chemistry 119, 65–76.

Johnson, C.M., Beard, B.L., Beukes, N.J., Klein, C., O'Leary, J.M., 2003. Ancient geochemical cycling in the Earth as inferred from Fe isotope studies of banded iron formations from the Transvaal Craton. Contributions to Mineralogy and Petrology 144, 523–547.

Johnson, C.M., Beard, B.L., Roden, E.E., 2008. The iron isotope fingerprints of redox and biogeochemical cycling in modern and ancient Earth. Annual Review of Earth and Planetary Sciences. 36, 457–493.

Jortner, J., Stein, G., 1962. The photochemical evolution of hydrogen from aqueous solutions of ferrous ions. Part I. The reaction mechanism at low pH. The Journal of Physical Chemistry 66, 1258–1264.

Kappler, A., Pasquero, C., Konhauser, K.O., Newman, D.K., 2005. Deposition of banded iron formations by anoxygenic phototrophic Fe (II)-oxidizing bacteria. Geology 33, 865-868.

Kempe, S., Degens, E.T., 1985. An early soda ocean? Chemical Geology 53, 95–108.

Klein, C., 2005. Some Precambrian banded iron-formations (BIFs) from around the world: Their age, geologic setting, mineralogy, metamorphism, geochemistry, and origins. American Mineralogist 90, 1473–1499.

Klingelhöfer, G., Morris, R.V., Bernhardt, B., Schröder, C., Rodionov, D.S., De Souza, P., Yen, A., Gellert, R., Evlanov, E., Zubkov, B., 2004. Jarosite and hematite at Meridiani Planum from Opportunity's Mössbauer spectrometer. Science 306, 1740–1745.

Konhauser, K.O., Amskold, L., Lalonde, S.V., Posth, N.R., Kappler, A., Anbar, A., 2007. Decoupling photochemical Fe (II) oxidation from shallow-water BIF deposition. Earth and Planetary Science Letters 258, 87–100.

Lanza, N.L., Wiens, R.C., Arvidson, R.E., Clark, B.C., Fischer, W.W., Gellert, R., Grotzinger, J.P., Hurowitz, J.A., McLennan, S.M., Morris, R.V., 2016. Oxidation of manganese in an ancient aquifer, Kimberley formation, Gale crater, Mars. Geophysical Research Letters 43, 7398–7407.

Lee, M.-S., 2004. Chemical equilibria in ferrous chloride acid solution. Metals and Materials International 10, 387–392.

Levin, N.E., Raub, T.D., Dauphas, N., Eiler, J.M., 2014. Triple oxygen isotope variations in sedimentary rocks. Geochimica et Cosmochimica Acta 139, 173–189.

Li, W., Beard, B.L., Johnson, C.M., 2015. Biologically recycled continental iron is a major component in banded iron formations. Proceedings of the National Academy of Sciences 112, 8193–8198.

Lundgreen, B., Jensen, H.G., Knudsen, J.M., Olsen, M., Vistisen, L., 1989. Photostimulated oxidation of Fe^{2+} (aq): a Mars simulation experiment studied by Mössbauer spectroscopy. Physica Scripta 39, 670.

Luz, B., Barkan, E., 2010. Variations of $^{17}O/^{16}O$ and $^{18}O/^{16}O$ in meteoric waters. Geochimica et Cosmochimica Acta 74, 6276–6286.

Lyons, J., Young, E., 2005. CO self-shielding as the origin of oxygen isotope anomalies in the early solar nebula. Nature 435, 317–320.

Lyons, J.R., 2007. Mass-independent fractionation of sulfur isotopes by isotope-selective photodissociation of SO_2. Geophysical Research Letters 34(22).

Maréchal, C.N., Télouk P., Albarède F, 1999. Precise analysis of copper and zinc isotopic compositions by plasma-source mass spectrometry. Chemical Geology 156, 251–273.

Matsuhisa, Y., Goldsmith, J.R., Clayton, R.N., 1978. Mechanisms of hydrothermal crystallization of quartz at 250 °C and 15 kbar. Geochimica et Cosmochimica Acta 42, 173–182.

Mayer, T.D., Jarrell, W.M., 1996. Formation and stability of iron (II) oxidation products under natural concentrations of dissolved silica. Water Research 30, 1208–1214.

McLennan, S., Bell, J., Calvin, W., Christensen, P., Clark, B.d., De Souza, P., Farmer, J., Farrand, W., Fike, D., Gellert, R., 2005. Provenance and diagenesis of the evaporite-bearing Burns formation, Meridiani Planum, Mars. Earth and Planetary Science Letters 240, 95–121.

Miller, M.F., 2002. Isotopic fractionation and the quantification of 17 O anomalies in the oxygen three-isotope system: an appraisal and geochemical significance. Geochimica et Cosmochimica Acta 66, 1881–1889.

Miller, M.F., Franchi, I.A., Sexton, A.S., Pillinger, C.T., 1999. High precision $\delta^{17}O$ isotope measurements of oxygen from silicates and other oxides: method and applications. Rapid Communications in Mass Spectrometry 13, 1211–1217.

Miller, R.G., O'Nions, R.K., 1985. Source of Precambrian chemical and clastic sediments. Nature 314, 325.

Milliken, R.E., Swayze, G.A., Arvidson, R.E., Bishop, J.L., Clark, R.N., Ehlmann, B.L., Green, R.O., Grotzinger, J.P., Morris, R.V., Murchie, S.L., 2008. Opaline silica in young deposits on Mars. Geology 36, 847–850.

Morel, A., Bricaud, A., 1981. Theoretical results concerning light absorption in a discrete medium, and application to specific absorption of phytoplankton. Deep Sea Research Part A. Oceanographic Research Papers 28, 1375–1393.

Morris, R.V., Golden, D.C., Bell, J.F., 1997. Low-temperature reflectivity spectra of red hematite and the color of Mars. Journal of Geophysical Research: Planets 102, 9125–9133.

Morris, R.V., Golden, D.C., Bell, J.F., Shelfer, T.D., Scheinost, A.C., Hinman, N.W., Furniss, G., Mertzman, S.A., Bishop, J.L., Ming, D.W., 2000a. Mineralogy, composition, and alteration of Mars Pathfinder rocks and soils: Evidence from multispectral, elemental, and magnetic data on terrestrial analogue, SNC meteorite, and Pathfinder samples. Journal of Geophysical Research: Planets 105, 1757–1817.

Morris, R.V., Golden, D.C., Ming, D.W., Shelfer, T.D., Jørgensen, L.C., Bell, J.F., Graff, T.G., Mertzman, S.A., 2001. Phyllosilicate-poor palagonitic dust from Mauna Kea Volcano (Hawaii): A mineralogical analogue for magnetic martian dust? Journal of Geophysical Research: Planets 106, 5057–5083.

Morris, R.V., Graff, T., Lane, M.D., Golden, D.C., Schwandt, C.S., Ming, T.D., Mertzman, S.A., Bell Iii, J.F., Crisp, J., Christensen, P.R., 2000b. Acid sulfate alteration products of a tholeiitic basalt: Implications for interpretation of martian thermal emission spectra. Lunar and Planetary Science 31, #2014.

Morris, R.V., Ming, D.W., Graff, T.G., Arvidson, R.E., Bell, J.F., Squyres, S.W., Mertzman, S.A., Gruener, J.E., Golden, D.C., Le, L., 2005. Hematite spherules in basaltic tephra altered under aqueous, acid-sulfate conditions on Mauna Kea volcano, Hawaii: possible clues for the occurrence of hematite-rich spherules in the Burns formation at Meridiani Planum, Mars. Earth and Planetary Science Letters 240, 168–178.

Morse, J.W., Mackenzie, F.T., 1998. Hadean ocean carbonate geochemistry. Aquatic Geochemistry 4, 301–319.

Nie, N.X., Dauphas, N., Greenwood, R.C., 2017. Iron and oxygen isotope fractionation during iron UV photo-oxidation: Implications for early Earth and Mars. Earth and Planetary Science Letters 458, 179–191.

Nordstrom, D.K., Southam, G., 1997. Geomicrobiology of sulfide mineral oxidation. Reviews in mineralogy 35, 361–390.

Pack, A., Herwartz, D., 2014. The triple oxygen isotope composition of the Earth mantle and understanding variations in terrestrial rocks and minerals. Earth and Planetary Science Letters 390, 138–145.

Perovich, D.K., 1995. Observations of Ultraviolet Light Reflection and Transmission by First-Year Sea Ice. Geophysical research letters 22, 1349–1352.

Poitrasson, F., Freydier, R., 2005. Heavy iron isotope composition of granites determined by high resolution MC-ICP-MS. Chemical Geology 222, 132–147.

Polyakov, V.B., Clayton, R.N., Horita, J., Mineev, S.D., 2007. Equilibrium iron isotope fractionation factors of minerals: reevaluation from the data of nuclear inelastic resonant X-ray scattering and Mössbauer spectroscopy. Geochimica et Cosmochimica Acta 71, 3833–3846.

Polyakov, V.B., Mineev, S.D., 2000. The use of Mössbauer spectroscopy in stable isotope geochemistry. Geochimica et Cosmochimica Acta 64, 849–865.

Rabinowitch, E., 1942. Electron transfer spectra and their photochemical effects. Reviews of Modern Physics 14, 112.

Rampe, E.B., Ming, D.W., Morris, R.V., Blake, D.F., Bristow, T.F., Sj, C., Vaniman, D.T., Yen, A.S., Grotzinger, J.P., Downs, R.T., 2016. Diagenesis in the Murray Formation, Gale Crater, Mars. Lunar and Planetary Science 47, #2543.

Ribas, I., De Mello, G.F.P., Ferreira, L.D., Hébrard, E., Selsis, F., Catalán, S., Garcés, A., do Nascimento Jr, J.D., de Medeiros, J.R., 2010. Evolution of the solar activity over time and effects on planetary atmospheres. II. κ1 Ceti, an analog of the sun when life arose on Earth. The Astrophysical Journal 714, 384.

Rouxel, O., Dobbek, N., Ludden, J., Fouquet, Y., 2003. Iron isotope fractionation during oceanic crust alteration. Chemical Geology 202, 155–182.

Rouxel, O.J., Bekker, A., Edwards, K.J., 2005. Iron isotope constraints on the Archean and Paleoproterozoic ocean redox state. Science 307, 1088–1091.

Ruff, S.W., Christensen, P.R., Blaney, D.L., Farrand, W.H., Johnson, J.R., Michalski, J.R., Moersch, J.E., Wright, S.P., Squyres, S.W., 2006. The rocks of Gusev Crater as viewed by the Mini-TES instrument. Journal of Geophysical Research: Planets 111(E12).

Rustad, J.R., Casey, W.H., Yin, Q.-Z., Bylaska, E.J., Felmy, A.R., Bogatko, S.A., Jackson, V.E., Dixon, D.A., 2010. Isotopic fractionation of Mg^{2+}(aq), Ca^{2+}(aq), and Fe^{2+}(aq) with carbonate minerals. Geochimica et Cosmochimica Acta 74, 6301–6323.

Rustad, J.R., Dixon, D.A., 2009. Prediction of Iron-Isotope Fractionation Between Hematite (r-Fe_2O_3) and Ferric and Ferrous Iron in Aqueous Solution from Density Functional Theory. The Journal of Physical Chemistry A 113, 12249–12255.

Schaefer, M.W., 1996. Are there abiotically-precipitated iron-formations on Mars, Mineral Spectroscopy: A Tribute to Roger G. Burns. The Geochemical Society 5, 381–393.

Schwertmann, U., Thalmann, H., 1976. The influence of Fe(II), Si, and pH on the formation of lepidocrocite and ferrihydrite during oxidation of aqueous $FeCl_2$ solutions. Clay Minerals 11, 189–200.

Singer, P.C., Stumm, W., 1970. Acidic mine drainage: the rate-determining step. Science 167, 1121–1123.

Skulan, J.L., Beard, B.L., Johnson, C.M., 2002. Kinetic and equilibrium Fe isotope fractionation between aqueous Fe (III) and hematite. Geochimica et Cosmochimica Acta 66, 2995–3015.

Squyres, S.W., Arvidson, R.E., Ruff, S., Gellert, R., Morris, R.V., Ming, D.W., Crumpler, L., Farmer, J.D., Des Marais, D.J., Yen, A., 2008. Detection of silica-rich deposits on Mars. Science 320, 1063–1067.

Squyres, S.W., Grotzinger, J.P., Arvidson, R.E., Bell, J.F., Calvin, W., Christensen, P.R., Clark, B.C., Crisp, J.A., Farrand, W.H., Herkenhoff, K.E., 2004. In situ evidence for an ancient aqueous environment at Meridiani Planum, Mars. Science 306, 1709–1714.

Stahl, R.S., Fanning, D.S., James, B.R., 1993. Goethite and jarosite precipitation from ferrous sulfate solutions. Soil Science Society of America Journal 57, 280–282.

Staton, S., Amskold, L., Gordon, G., Anbar, A., Konhauser, K., 2006. Iron isotope fractionation during photo-oxidation of aqueous ferrous iron, AGU Spring Meeting Abstracts, p. 04.

Tang, H., Dauphas, N., 2012. Abundance, distribution, and origin of ^{60}Fe in the solar protoplanetary disk. Earth and Planetary Science Letters 359, 248–263.

Teng, F.Z., Dauphas, N., Huang, S., Marty, B., 2013. Iron isotopic systematics of oceanic basalts. Geochimica et Cosmochimica Acta 107, 12–26.

Thiemens, M.H., Heidenreich, J.E., 1983. The Mass-Independent Fractionation of Oxygen: A Novel Isotope Effect and Its Possible Cosmochemical Implications. Science 219, 1073–1075.

Thiemens, M.H., Jackson, T., 1987. Production of isotopically heavy ozone by ultraviolet light photolysis of O2. Geophysical Research Letters 14, 624–627.

Tosca, N.J., McLennan, S.M., 2009. Experimental constraints on the evaporation of partially oxidized acid-sulfate waters at the martian surface. Geochimica et Cosmochimica Acta 73, 1205–1222.

Tosca, N.J., McLennan, S.M., Clark, B.C., Grotzinger, J., Hurowitz, J.A., Knoll, A.H., Schröder, C., Squyres, S.W., 2005. Geochemical modeling of evaporation processes on Mars: Insight from the sedimentary record at Meridiani Planum. Earth and Planetary Science Letters 240, 122–148.

Tosca, N.J., McLennan, S.M., Dyar, M.D., Sklute, E.C., Michel, F.M., 2008. Fe oxidation processes at Meridiani Planum and implications for secondary Fe mineralogy on Mars. Journal of Geophysical Research: Planets 113(E5).

Viehmann, S., Hoffmann, J.E., Münker, C., Bau, M., 2014. Decoupled Hf-Nd isotopes in Neoarchean seawater reveal weathering of emerged continents. Geology 42, 115–118.

Wang, C., Zhang, L., Dai, Y., Li, W., 2014. Source characteristics of the∼ 2.5 Ga Wangjiazhuang Banded Iron Formation from the Wutai greenstone belt in the North China Craton: Evidence from neodymium isotopes. Journal of Asian Earth Sciences 93, 288–300.

Wang, K., Moynier, F., Dauphas, N., Barrat, J.A., Craddock, P., Sio, C.K., 2012. Iron isotope fractionation in planetary crusts. Geochimica et Cosmochimica Acta 89, 31–45.

Welch, S., Beard, B., Johnson, C., Braterman, P., 2003. Kinetic and equilibrium Fe isotope fractionation between aqueous Fe(II) and Fe(III). Geochimica et Cosmochimica Acta 67, 4231–4250.

Widdel, F., Schnell, S., Heising, S., Ehrenreich, A., Assmus, B., Schink, B., 1993. Ferrous iron oxidation by anoxygenic phototrophic bacteria. Nature 362, 834–836.

Wiederhold, J.G., Kraemer, S.M., Teutsch, N., Borer, P.M., Halliday, A.N., Kretzschmar, R., 2006. Iron isotope fractionation during proton-promoted, ligand-controlled, and reductive dissolution of goethite. Environmental Science & Technology 40, 3787–3793.

Wiesli, R.A., Beard, B.L., Johnson, C.M., 2004. Experimental determination of Fe isotope fractionation between aqueous Fe(II), siderite and “green rust” in abiotic systems. Chemical Geology 211, 343–362.

Wray, J., Milliken, R., Dundas, C., Swayze, G., Andrews-Hanna, J., Baldridge, A., Chojnacki, M., Bishop, J., Ehlmann, B., Murchie, S.L., 2011. Columbus crater and other possible groundwater-fed paleolakes of Terra Sirenum, Mars. Journal of Geophysical Research: Planets 116(E1).

Wu, L., Beard, B.L., Roden, E.E., Johnson, C.M., 2011. Stable iron isotope fractionation between aqueous Fe (II) and hydrous ferric oxide. Environmental Science & Technology 45, 1847–1852.

Yamaguchi, K.E., Ohmoto, H., 2006. Comment on "Iron Isotope Constraints on the Archean and Paleoproterozoic Ocean Redox State". Science 311, 177–177.

Yapp, C.J., 2007. Oxygen isotopes in synthetic goethite and a model for the apparent pH dependence of goethite–water $^{18}O/^{16}O$ fractionation. Geochimica et cosmochimica acta 71, 1115–1129.

Young, E.D., Galy, A., Nagahara, H., 2002. Kinetic and equilibrium mass-dependent isotope fractionation laws in nature and their geochemical and cosmochemical significance. Geochimica et Cosmochimica Acta 66, 1095–1104.

Yurimoto, H., Kuramoto, K., 2004. Molecular cloud origin for the oxygen isotope heterogeneity in the solar system. Science 305, 1763–1766.

Zhang, J., Huang, S., Davis, A.M., Dauphas, N., Hashimoto, A., Jacobsen, S.B., 2014. Calcium and titanium isotopic fractionations during evaporation. Geochimica et Cosmochimica Acta 140, 365–380.

3 RUBIDIUM ISOTOPES TRACING VOLATILE DEPLETION AMONG PLANETARY BODIES

3.1 Introduction

A striking feature of the rocky planetary bodies (*e.g.*, Earth, Moon, Mars and Vesta) is that they are all depleted in volatile elements compared with chondrites which are their building blocks. To avoid confusion, volatile elements here are defined as the elements having 50% condensation temperatures of less than 1135K, when condensing from a solar nebula composition Aat a pressure of 10^{-4} atm (Lodders, 2003). Elements with 50% condensation temperatures above 1135 K are refractory elements. The elemental abundances of the bulk solar system are estimated by measuring CI (Carbonaceous chondrite Ivuna) chondrites, which are considered as the representative of the average solar compositions of most elements except for highly volatile ones such as H, C, O and noble gases (Anders and Ebihara, 1982). As shown in Fig. 3.1, using alkali

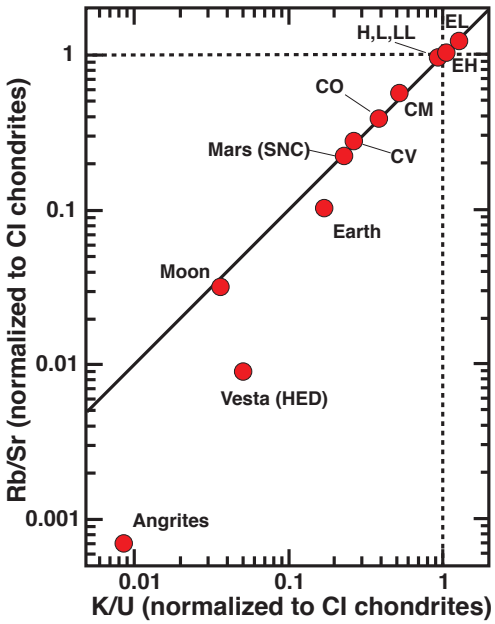

Figure 3.1 CI chondrite normalized Rb/Sr vs. K/U ratios showing volatile depletion in planetary bodies. Modified from Davis (2006).

elements K and Rb as a representative of volatile elements, their ratios relative to the refractory elements U and Sr, respectively, show a depletion trend of volatiles among the planetary bodies compared to CI chondrites (Davis, 2006). Under what conditions these planetary objects acquired this signature is still an enigma.

Studying isotopic compositions of volatile elements in planetary bodies can provide valuable insights into volatile loss processes occurred in the early solar system. In this Chapter, we study the isotopic compositions of Rb, which is a moderately volatile element, in planetary bodies. Rubidium is still an emerging isotopic system and not much work had been done before this study. The measurement method was also not developed before this study. We did extensive lab tests and established the Rb isotope measurement method (Sect. 3.2). Using the method, we measured the Rb isotopic compositions of the Earth-Moon system, chondrites (including carbonaceous, ordinary and enstatite chondrites) and Mars. The Rb isotopic compositions of the bulk Moon and the bulk Earth were estimated to a very high precision, and important conclusions regarding volatile loss during Moon formation were drawn (Sect. 3.3). The Rb isotopic compositions of chondrites and Mars and their implications are reported and discussed in Sect. 3.4.

3.2 Rubidium isotope separation and measurement method

3.2.1 Sample preparation

The sample preparation for Rb isotope measurement is similar to that for Fe isotope measurement described in Chapter 2. The major difference is that the sample mass needed for Rb is quite large, usually around 100 mg or more (in comparison, less than 20 mg is needed for Fe isotope measurement), due to the very low Rb concentrations in rocks (ppm level). Terrestrial

igneous rocks have relatively high Rb contents, tens of ppm for basaltic rocks and a hundred ppm or slightly higher for felsic rocks. Chondrites, lunar and martian rocks have Rb concentrations of ~1 ppm. The relatively high Rb content of terrestrial magmatic rocks is because these rocks are formed by partial melting of Earth's mantle, and the process enriches melts in Rb which is highly incompatible.

In general, about 100 mg powder for each meteorite was digested (~50 mg each was digested for terrestrial rocks). If a meteorite was obtained as chips, the chips were crushed and ground in a precleaned agate mortar (cleaned twice by grinding fine silica grains followed by rinsing with Milli-Q water) which was used exclusively for meteorites (terrestrial rocks are ground in a separate mortar). The total mass of the ground chips was usually two to three hundred mg to make sure that the rock powder was representative of the bulk meteorite. Samples were digested in four steps using mixtures of concentrated HF-HNO_3-HCl-$HClO_4$ acids:

1) 3 mL 28 M HF + 1.5 mL 15 M HNO_3 + 1 mL 10 M $HClO_4$ was added to each sample in a 30 mL precleaned Savillex Teflon beaker. The beaker was closed and placed on a hotplate at 130 °C for 24 hours. Teflon beakers were cleaned with boiling aqua regia (3:1 mixture of HCl: HNO_3).
2) The solution was dried at 130 °C on a hotplate, and then at 180 °C for evaporating remaining $HClO_4$. The evaporation residue was taken up in 3 mL 11M HCl + 1 mL 15M HNO_3 and left on a hotplate at 130 °C for 24 hours with the lid closed. This step was repeated twice.
3) After evaporation to dryness, each sample was redissolved in 4 mL 15M HNO_3 and left on a hotplate at 130 °C for 24 hours with the lid closed.
4) After step 3), if there was still residue in a sample solution (it was very common for meteorites to have residue after step 3)), the solution was centrifuged, and the residue was transferred to

a 7 mL Teflon beaker to be further digested in a Parr bomb. A mixture of 3 mL 28 M HF + 1 mL 15 M HNO_3 was added to the residue and the beaker was closed tightly and placed in a Parr bomb, which was placed in an oven at 175–180 °C. The sample was taken out of the bomb after at least 3 days and the bombed solution was combined with the previously digested solution.

Assuming a Rb concentration of 1 ppm, the total Rb mass from a 100 mg digested mass is 100 ng. About 80 % of the digested mass of a sample was run through chromatographic columns for purification, and the rest 20 % was saved in case a remeasurement was necessary. Therefore, typically ~ 80 ng purified Rb was recovered for isotopic analysis. The total background of digestion and chromatography is ~0.14 ng, which accounts for only less than 0.2 % of the total Rb from a sample and will not affect the isotopic composition of the sample. The total Rb purification yields exceeded 95 % for all the samples.

3.2.2 Rubidium extraction chromatography

In isotope geochemistry, ion-exchange chromatography is widely used for extracting and purifying elements. It separates ions and charged molecules based on their affinity to resins (ion exchanger). Resins contain ionizable functional groups that can have either positively (cation exchanger) or negatively charged ions (anion exchanger), which interact and couple with exchangeable counterions in dissolved samples. The counterions that do not bind or bind weakly with resins are the first to wash away. Then the elution of the counterions that bind to resins can be done by changing pH or acid molarity. Usually, counterions of different kinds (*e.g.*, different elements) compete with each other for binding and have different affinities to resins, so altered conditions can be used to adjust their affinities so that they can be kept on or eluted from resins.

Rubidium separation method had not been established before this work. Therefore, several resins have been tested for Rb separation, and three methods have been developed: 1) separation of Rb using a novel AMP-PAN resin (Sect. 3.2.2.1), 2) separation of Rb with cation resins using a PF-HPLC unit built previously in the lab (Sect. 3.2.2.2), and 3) separation of Rb using Sr resin. The three methods are discussed below.

3.2.2.1 Rubidium separation with AMP-PAN resin

The effective part of the AMP-PAN resin is made of ammonium molybdophosphate (AMP) and is commercially available from Eichrom. Ammonium heteropolyacid salts have been known previously for their cation exchange properties for large alkali ions (Smit et al., 1959a). AMP shows good potential to separate alkali metals, especially high absorbability to Cs (Smit et al., 1959b) and has been used to remove Cs from radioactive waste (*e.g.*, Brewer et al., 1999). The principle is that the big ammonium ion NH_4^+ in the AMP can be substituted by big alkali metal cations. The bigger the alkali ions, the easier the substitution. The resin from Eichrom is AMP embedded in an organic matrix of polyacrylonitrile (PAN) to improve its mechanical characteristics.

Despite its usage in the treatment of radioactive waste solutions, the AMP-PAN resin has not been commonly used for separating alkali metals. The distribution coefficients of alkali metals on AMP have been measured previously (Coetzee, 1972; Smit et al., 1959a; 1959b), but not on the AMP-PAN resin from Eichrom, and the coefficients of other elements on the resin are also missing. Here, we measured the distribution coefficients of multiple elements on the resin in HNO_3 and NH_4NO_3 media and did elution tests based on the measured coefficients. Concentrated ammonium salts such as NH_4NO_3 and NH_4Cl are the only chemicals that can elute Rb and Cs from the resin. NH_4NO_3 was chosen over NH_4Cl in the tests because its higher solubility in water can

give more concentrated ammonium solutions. Accordingly, HNO_3 instead of HCl was used as the sample loading medium.

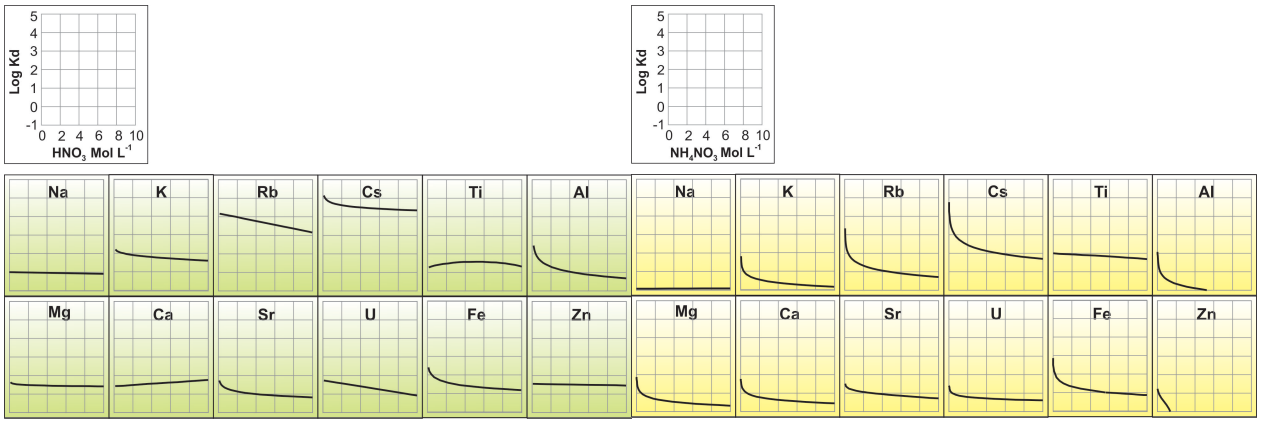

Figure 3.2 Left: Distribution coefficients of alkali metals and several other elements on AMP-PAN resin in HNO_3. Right: Distribution coefficients of alkali metals and several other elements on AMP-PAN resin in NH_4NO_3.

Distribution coefficients (K_d) describes the partition of an element between the sample solution (the acid medium) and the resin at equilibrium. By definition,

$$K_d = C_{resin} / C_{solution}, \quad (3.1)$$

where C_{solid} is the concentration of the element bound to the resin, in mg g^{-1} dry resin, and $C_{solution}$ is the concentration of the element in the solution, in mg mL^{-1}. K_d is very sensitive to the acid type and molarity that elements are dissolved in. The method of determining distribution coefficients is briefly described here. About 200 mg of dry AMP-PAN resin was transferred to 15 mL centrifuge tubes. A multielement solution was prepared for equilibrating with the resin. The solution was made by mixing single-element plasma tuning solutions, with all elements of interest having about the same concentration. Changing the concentration of a solution can be done by either diluting with Milli-Q water for a more diluted solution, or by drying on a hotplate and redissolved in the same acid but less volume for a more concentrated solution The acid medium and morality of a solution can be changed by drying the solution and redissolving residue in the

desired acids. The most convenient way is to make the stock multielement solution more concentrated, and for making solutions for the batch equilibrium experiments, small aliquots of the stock solution are added to Teflon beakers, dried on hotplates and redissolved in acids prepared in different molarities. In this work, batch equilibrium experiments were done with 12 elements in 0.1, 1, 2, 4, 6, 8 and 10 mol L^{-1} HNO_3, and 12 elements in 0.01, 0.1, 1, 2, 4, 6, 8 and 10 mol L^{-1} NH_4NO_3. The solutions were added to centrifuge tubes each filled with ~200 μg of the resin, shaken every 2 hours by hands. After ~8 h of equilibration, the mixtures were filtered using 2 mL Bio-Rad empty columns with frits, which separated liquids from the resin. The liquids were collected in centrifuge tubes or beakers for measuring concentrations.

An extended form of the Eq. 3.1 was used to determine the distribution coefficients,

$$K_d = [(C_0\text{-}C)/w]/(C/V), \quad (3.2)$$

where C is the elemental concentration after equilibration and C_0 the original concentration, w the weight of dry AMP-PAN resin in gram and V the volume of acid solution in mL. The distribution coefficients of elements on AMP-PAN resin in HNO_3 and NH_4NO_3 are shown in Fig. 3.2. A high distribution coefficient means the element is preferentially retained on the resin, and a low distribution coefficient means the element can be released from the resin easily. In HNO_3, Rb and Cs have much higher distribution coefficients than other elements (note that the coefficients are in log scale), suggesting that they can be strongly fixed onto the resin, while other elements cannot. In NH_4NO_3, Rb and Cs have decreasing coefficients as the concentration of NH_4^+ increases. More concentrated NH_4NO_3 solutions can strip them off the resin more easily.

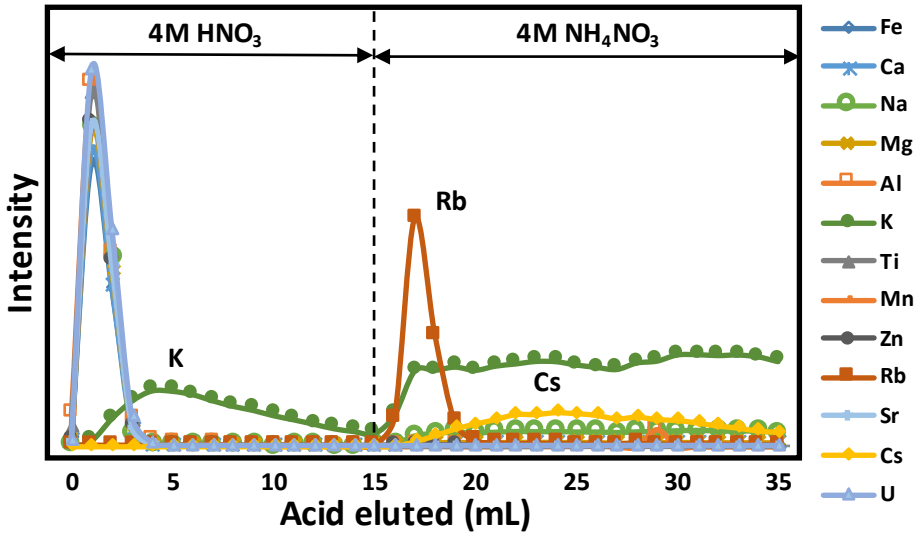

Figure 3.3 Elution curves of elements on AMP-PAN resin. Synthetic multielement solution was loaded onto the resin in 4M HNO_3. Matrix elements including K were eluted using 4M HNO_3 in which Rb was bound to the resin. Rubidium was then eluted from the resin with 4 M NH_4NO_3.

Fig. 3.3 shows the elution curves of elements on AMP-PAN resin using HNO_3 and NH_4NO_3. Elution tests were done first using NH_4NO_3 instead of NH_4Cl, given that HN_4NO_3 has a higher solubility in water and can produce more concentrated ammonium solutions. The resin

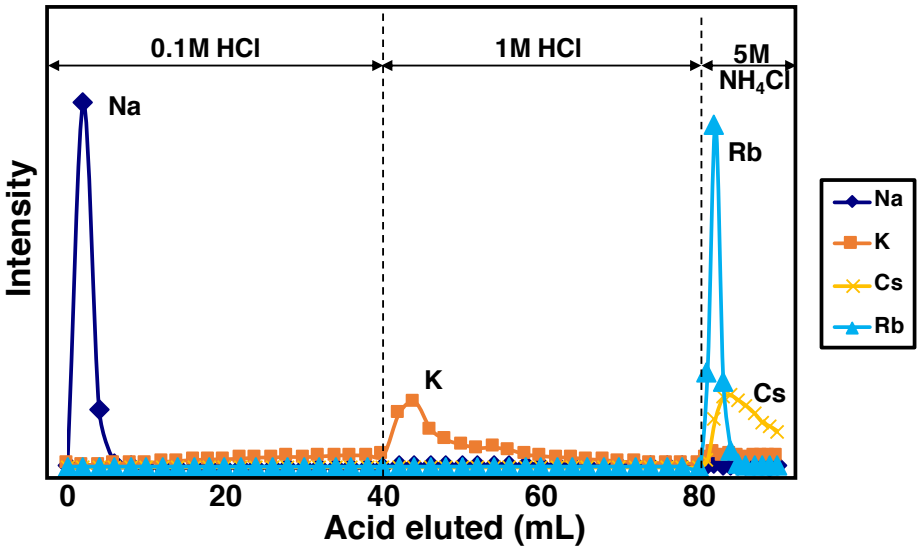

Figure 3.4 Elution of Na, K and Rb with AMP-PAN resin using HCl and NH_4Cl.

volume was 1 mL (resin reservoir was the Bio-Rad Poly-Prep 10 mL empty column of 90 mm height and 8 mm diameter). About 500 μL 20 ppm multielement solution in 4M HNO_3 was loaded onto the resin, then another 15 ml 4M HNO_3 was used to elute matrix elements. 20 mL 4M NH_4NO_3 was then passed through the column to recover Rb.

There are several things noticeable about the elution. First, matrix elements can be easily separated from Rb as they do not stick to the resin and are effectively eluted with 4M HNO_3. Second, as can be seen from the latter part of the elution curves, some K was present together with Rb in NH_4NO_3 solutions. The K was not from the multielement solution loaded to the column, as the amount of K eluted in 4M HNO_3 was about the same as that loaded to the column. The K present in NH_4NO_3 is very likely an impurity in the NH_4NO_3, because the K concentration is a constant in the NH_4NO_3 eluate cuts and should be the background of NH_4NO_3 solution. The NH_4NO_3 used here has the highest purity that is commercially available, but it still has a high alkali-metal background due to the high affinity between alkali metals and NH^{4+}. If not considering K background in NH_4NO_3, the resin is very effective in separating Rb from K. In comparison, separating Rb from K is very difficult with other resins (*e.g.*, cation resins, Sect 3.2.2.2) and the two elements behave quite similarly on various kinds of resins. Another problem of using NH_4NO_3 is that during elution some resin is dissolved in the NH_4NO_3 solution. In the tests, the Rb eluate (NH_4NO_3 solution containing Rb after passing column) was clear initially, but once heated, some small, yellow-colored resin particles formed, and the newly formed particles could not be redissolved. This made further treatment of the Rb eluate (*e.g.*, transferring Rb from NH_4NO_3 solution to dilute HNO_3 media) problematic. Furthermore, large amounts of NH_4NO_3 and Mo (from dissolved AMP) are also present with Rb in the eluate. Removing NH_4NO_3 without

introducing new interferences is very difficult. One way would be to heat NH_4NO_3 at around 200 °C to decompose it, but this can be potentially dangerous due to its explosive properties.

To solve the problems, we switched to HCl-NH_4Cl system. Fixing Rb and removing matrix was done using HCl and recovering Rb using NH_4Cl. It gave similar results as using HNO_3 and NH_4NO_3 in terms of elemental separation, and Rb can be separated from Na and K efficiently (Fig. 3.4). Compared with in HNO_3 and NH_4NO_3, the resin still slightly decomposed in HCl and NH_4Cl, but no resin particles formed from the Rb eluate under further treatment. Another benefit of using NH_4Cl is that it can be commercially obtained with higher purity than NH_4NO_3, therefore less background Rb and K. Not being an explosive, NH_4Cl could be removed from Rb eluate solution by a two-step heating process: 1) transferring the solution to a precleaned Pt crucible (cleaned with double distilled HCl several times), and drying it on a hotplate at relatively low temperature (~90 °C) until all NH_4Cl is solid, and 2) slowly increasing the temperature (to avoid boil-over) to around 350 °C and holding at the temperature until all NH_4Cl decomposed and gone. Molybdenum introduced by the resin can be removed using a small anion exchange column following Dauphas et al. (2001).

Unfortunately, Rb cannot be quantitatively recovered from the resin, either with HNO_3-NH_4NO_3 or HCl-NH_4Cl. The yield was only around 70 %, even when highly concentrated NH_4Cl solution of 5M was used for elution. This is probably because the channels in the AMP crystal lattice are partially blocked after Rb fixation (personal communication with F. Šebesta, who developed the resin). Since Rb has only two isotopes, a high yield of near 100 % is necessary considering the possibility of isotope fractionation on the resin column. The double-spiking technique (Rudge et al., 2009), which can correct for isotope fractionation during sample preparation for which a 100 % yield is not required, can only be applied to elements with four or

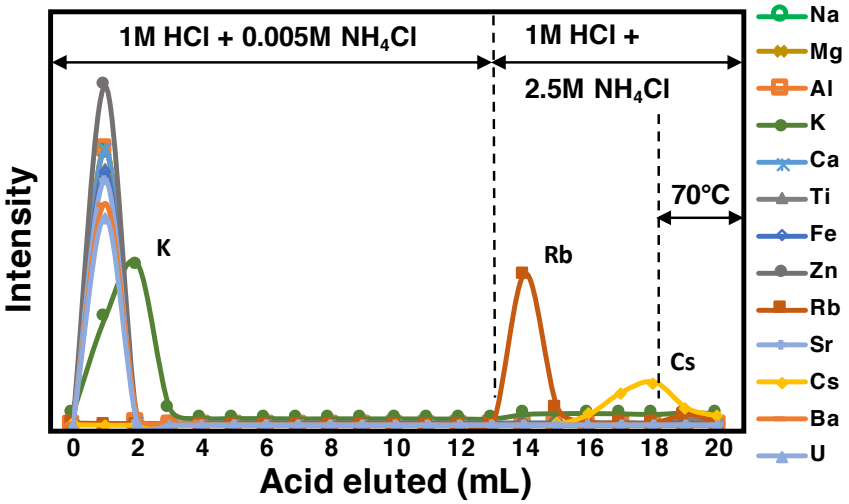

Figure 3.5 Elution scheme of Rb with AMP-PAN resin using HCl and NH_4Cl. Matrix elements are removed with 1M HCl+0.005M NH_4Cl while Rb is bound to the resin. Rb was eluted in two steps. The 1M HCl + 2.5M NH_4Cl is first passed through the resin to collect Rb, which is only partially eluted from the resin, then the remaining Rb in the resin is extracted using the same solution heated at 70 °C, which helps Rb release from the lattice of the AMP-PAN resin.

more isotopes. To solve the low yield problem, a new elution scheme was used and the sample loading medium was adjusted from pure HCl to HCl with a small amount of NH_4Cl to decrease the Rb distribution coefficient, and more importantly, after elution, the resin was partially decomposed by soaking it in the mixture of 1 N HCl and 2.5 N NH_4Cl at 70 °C for several hours twice to fully recover retained Rb (Fig. 3.5). The Rb yield after this treatment was measured to be ~98–100 %.

3.2.2.2 Rubidium separation with PF-HPLC system

Although Rb separation with AMP-PAN resin was successful, the blank of the procedure was relatively high (~80 ng) compared to chemical separation procedures of other elements. For example, the blank of separation procedure is ~20 ng for Fe, which is a major element and should have much higher blank than Rb. The high Rb blank is primarily from two sources: NH_4Cl solution used to elute Rb from AMP-PAN resin, and the resin itself during decomposition for a full recovery of Rb. This blank level is not a problem for measuring rocks with relatively high Rb, for example, terrestrial rocks which have Rb concentrations of tens of ppm or more. A ~50 mg terrestrial basalt would produce several μg of Rb, and the blank Rb would account for only ~2 % of the total Rb,

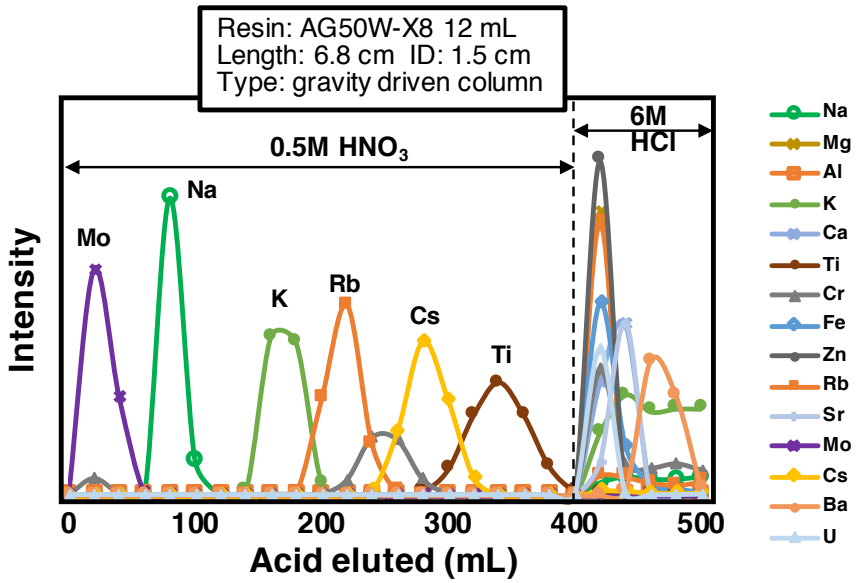

Figure 3.6 Elution curves of elements on 12 mL (length = 6.8 cm) cation resin AG50W-X8. Alkali metals can be eluted with dilute 0.5M HNO_3 while matrix elements are still bound to the resin. Matrix elements can be eluted with concentrated acids such as 6M HCl and 6M HNO_3. Note that there is overlap between K and Rb peaks, and it is very difficult to separate Rb from K using the resin.

which is quite acceptable. However, lunar basalts and chondrites are very low in Rb abundance

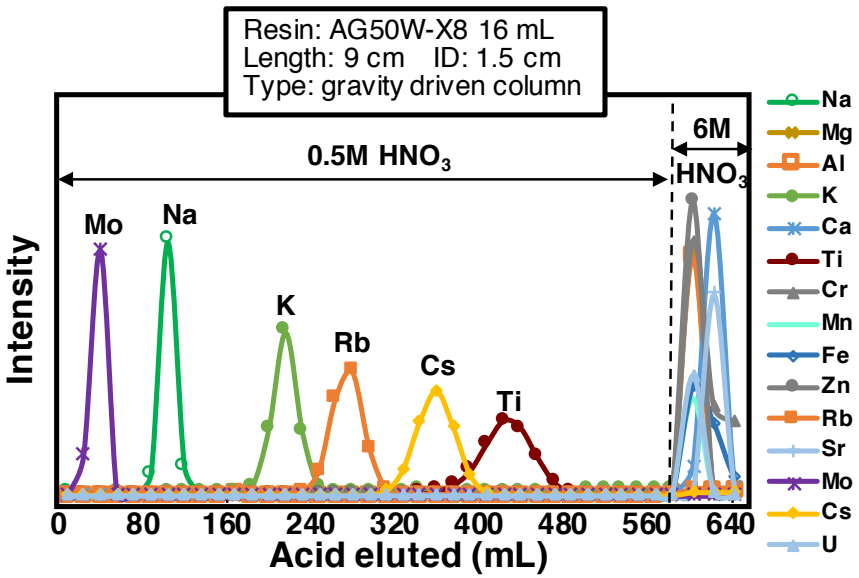

Figure 3.7 Elution curves of elements on 16 mL (length = 9 cm) cation resin AG50W-X8. Compared with 12 mL resin (length = 6.8 cm; Fig. 3.6), the overlap between K and Rb peaks is less but still the resolution is not high enough to separate the two elements from each other.

(concentrations are ~1 ppm). A ~100 mg sample would have a total Rb of ~100 ng, which is only slightly higher than the blank value. A lower blank is therefore needed for high-precision analyses of meteorites.

Since the Rb blank mainly results from the intrinsic properties of AMP-PAN resin, decreasing the blank would require switching to other resins. One option is to use cation exchange resins, which have been well characterized and widely used for cation separation. The major difficulty of using cations resin is that Rb and K are hardly separated from each other on cation resins. The ratio of K/Rb in rocks are ~250 or higher, even a small fraction of K present in Rb cut would cause a significant interference. There was always overlap between K and Rb peaks during elution with gravity-driven cation exchange columns in our tests, although longer columns in general resulted in better separation (Figs. 3.6, 3.7, 3.8). This is consistent with the theory of plates (Martin and Synge, 1941), a theory on chromatography which states that a chromatographic column can be considered as a finite number of theoretical plates of defined height and within each

plate equilibrium is achieved between the liquid and the stationary phase, and therefore increasing the length of a column (*i.e.,* increasing the number of plates) would help to resolve peaks.

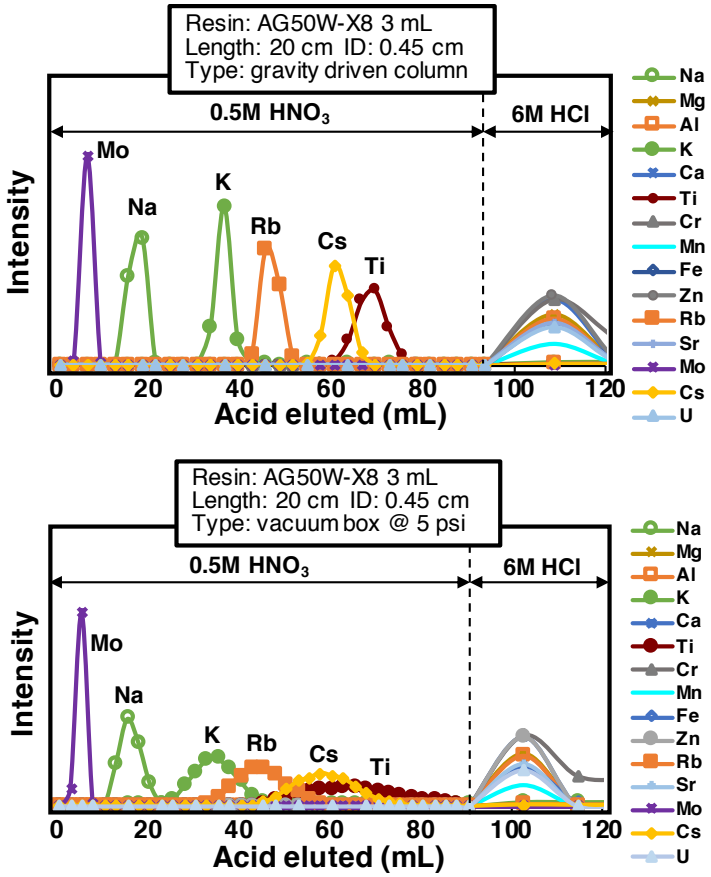

Figure 3.8 Elution curves of elements on AG50W-X8 resin with a column length of 20 cm and an inner diameter of 0.45 cm. The top panel shows the gravity-driven elution while the bottom panel shows the elution of the same column using a vacuum box with pressure set at 5 psi. It can be seen that pressure widened peaks and caused more peak overlaps and worse separation. Compared with gravity-driven columns of 6.8 cm and 9 cm lengths in Figs. 3.6 and 3.7, the 20 cm gravity-driven column gave a better separation between K and Rb.

Several gravity-driven column lengths have been tested, including 6.8 cm (Fig. 3.6), 9 cm (Fig. 3.7) and 20 cm columns (Fig. 3.8). The 20 cm column gave the best separation, and the K and Rb peaks only very slightly overlapped. But the separation is still not good enough to be applied to natural samples, because often a larger acid volume than that of a peak would need to

be collected in case the peak moves slightly due to the interference of large amount of matrix elements in natural samples. Gravity-driven columns longer than 20 cm were not tested (columns longer than 20 cm were tested with the PF-HPLC (Pneumatic Fluoropolymer High Performance Liquid Chromatography system; see below) because increasing length could cause an unrealistic long elution time. A vacuum box where pressure inside the box can be controlled is often used to expedite the elution of long columns (in this case the columns are not just gravity-driven but also pressured by the vacuum box). However, pressure has a negative effect on the separation, as shown in Fig 3.8. To balance the pressure effect, even longer columns would be required. It is therefore critical to find a balance between the two factors. Other factors that could also affect the resolution of a separation are temperature (higher temperature facilitates equilibration between liquids and resins) and resin cross linkage.

To find the right column conditions for Rb separation (pressure, temperature, column length, cross-linkage etc.), we run a series of tests with the PF-HPLC (Pneumatic Fluoropolymer High Performance Liquid Chromatography) system that was built in our lab. The unit was a new version of the previous PF-HPLC unit developed in our lab, which was presented in Ireland et al. (2013). The most distinctive feature of the unit is that column elution is automated through computer control, allowing the use of very long/thin columns that take very long time (*e.g.*, several days) for elution. The unit is also connected to a heating system that can control the elution temperature (up to 80 °C), this is very useful because temperature could affect the efficiency of elemental separation significantly (Ireland et al., 2013). For very long/thin columns the gravity driven flow rate can be extremely low, this PF-HPLC unit can pressurize columns with dry N_2 to reach a reasonable flow rate. The pressure in the unit is adjustable, and the maximum column pressure can reach ~70 psi.

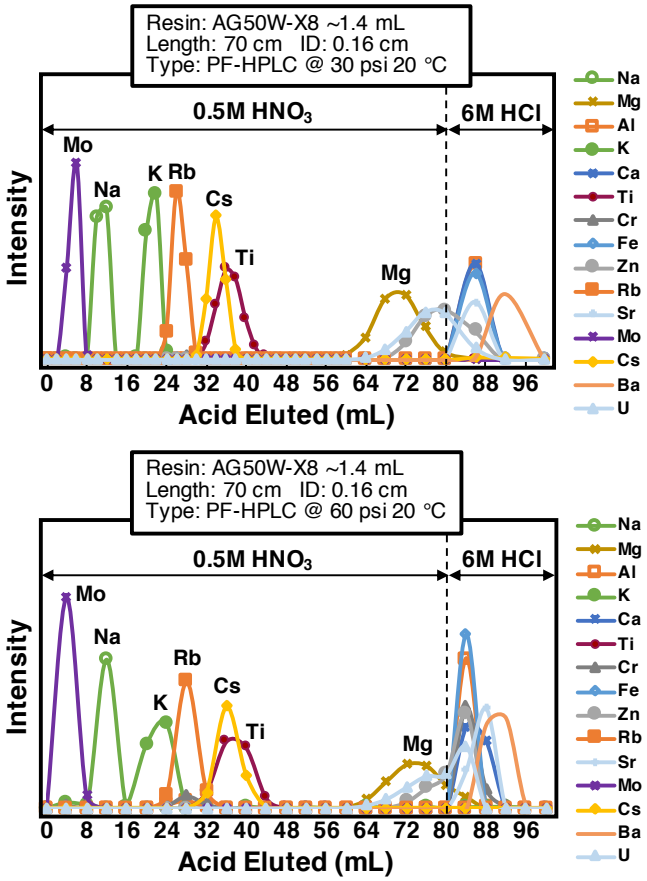

Figure 3.9 Elution curves with PF-HPLC system, using a column of AG50W-X8 resin in a length of ~70 cm. The two elution curves were run under different pressures of 30 psi and 60 psi respectively. The pressure effect (increasing pressure causing more overlap between peaks) can be seen, with 30 psi column showing a slightly better separation (less overlaps).

Pressure. Pressure was tested first with the PF-HPLC system as pressure would affect significantly the flow rate of the elution. A realistic and proper flow rate is required for a routine Rb isotope separation method. Two pressures of 30 psi and 60 psi were tested at room temperature, on a very long and thin column (length=70 cm; ID=0.16 cm; filled with AG50W-X8 resin). The results showed that the separation at 30 psi was slightly better than that at 60 psi (Fig. 3.9), confirming that pressure negatively effects separation. Since at 60 psi the flow rate was higher, we picked 60 psi as the elution pressure and the following tests were all conducted at 60 psi.

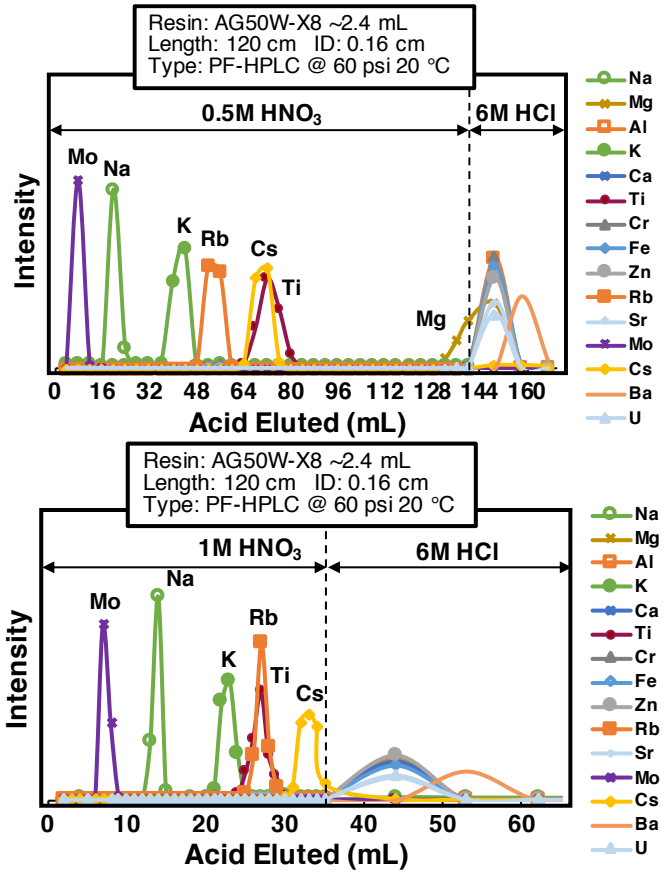

Figure 3.10 The effect of acid molarity on the element separation on AG50W-X8 resin. The column length was 120 cm. The column was run at 60 psi and 20 °C, but first with 0.5 M HNO_3 and second with 1 M HNO_3.The two acid molarities gave similar results in terms of separating Rb from K. The relative position of Ti peak changed.

Acid molarity. The effect of acid molarity on element separation was tested on a 120 cm column filled with AG50W-X8 resin (ID=0.16 cm; pressure=60 psi; temperature=20 °C). Compared with the previous column of 70 cm length (Fig. 3.9), the 120 cm column showed better separation of Rb from K (Fig. 3.10). The two acid molarities of 0.5 M and 1 M on AG50W-X8 resin did not show much difference for this column, but the relatively position of the Ti peak moved slightly ahead from 0.5M HNO_3 to 1M HNO_3. Note that although acid molarity does not have an obvious effect on this PF-HPLC column, it does not mean that it will not affect the separation using PF-HPLC column with cation resin of a different cross-linkage, or using a gravity

driven column. Indeed, as shown for cation resin AG50W-X12 (a higher cross-linkage of X12; Fig. 3.11), and for gravity-driven cation AG50W-X8 columns, acid molarity has a rather large influence on Rb separation, and lower acid molarity yields better Rb separation.

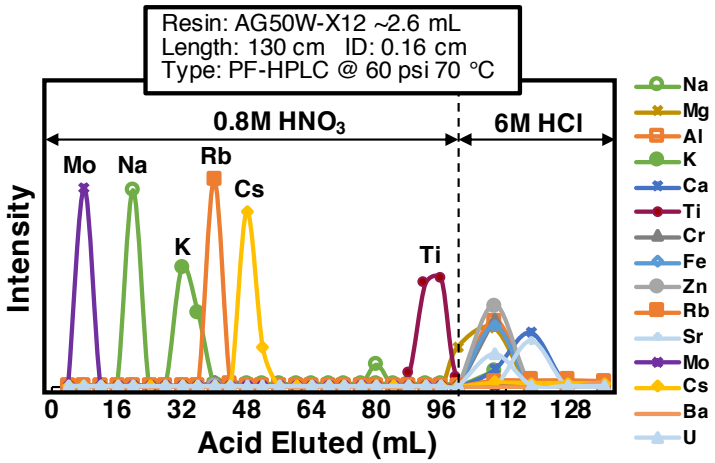

Figure 3.11 Elution curves using AG50W-X12 resin at 70 °C. The separation between K and Rb at 70 °C is not as good as that at 20 °C (Fig. 3.12). The reason is still not known, as theoretically, higher temperature would lead to faster equilibration and thus presumably better separation. It is likely that high temperature leads to faster longitudinal diffusion of elements and thus worse separation.

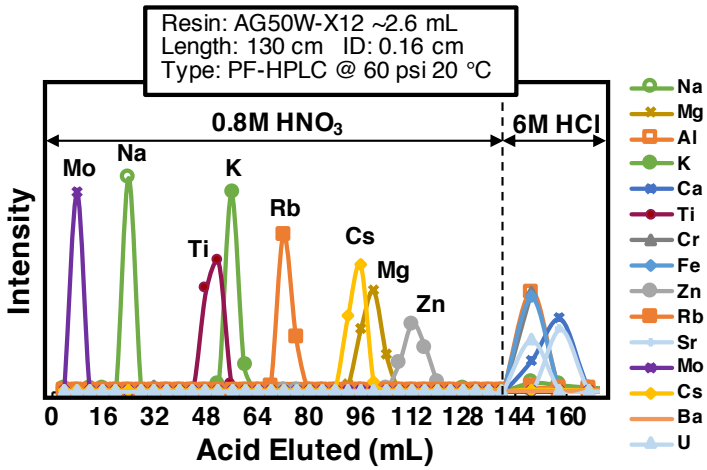

Figure 3.12 Test on elution with a higher resin cross-linkage (AG50W-X12). The separation using the resin is better than the ones using the AG50W-X8 resin shown in previous figures. There was no K and Rb peak overlap in this elution.

Resin cross-linkage. Resin cross linkage also has an effect on elemental separation. Cation resin with a higher cross-linkage (X12 vs. X8) was tested and the result is shown in Fig. 3.11. The AG50W-X12 resin was better than the AG50W-X8 resin for Rb separation, as the K and Rb peaks are separated from each other with the AG50W-X12 resin. Another difference is that on the AG50W-X12 resin Ti came out of the column earlier than K and Rb.

Temperature. For testing the influence of temperature on Rb separation, the same column used in the previous elution (AG50W-X12 resin, 130 cm at 60 psi) was used but the elution was done at 70 °C instead of 20 °C. Theoretically, higher temperature would result in better separation between elements, because higher temperature could facilitate equilibration between the resin and the liquid phase. However, our test showed that the separation between K and Rb at 70 °C (Fig. 3.12) was not as good as the separation at 20 °C (Fig. 3.11). The reason is not known, but it is possible that high temperature may lead to faster longitudinal diffusion of elements in columns, leading to more overlap between elemental peaks (Dybczyński, 1972). The temperature was set at 20 °C (room temperature) for the following tests and sample runs.

Among all the tests running above using PF-HPLC, the only column that successfully separated Rb from K and other elements was the one using AG50W-X12 resin, in a length of 130 cm, at a pressure of 60 psi and a temperature of 20 °C (Fig. 3.13). A longer column of 150 cm was tested after this one since the expectation is that longer columns would give better separation. Two acid molarities of 0.7M HNO_3 and 1M HNO_3 were compared. The best separation was achieved with the 150 cm column filled with AG50W-X12 resin using 0.7M HNO_3 as the eluent.

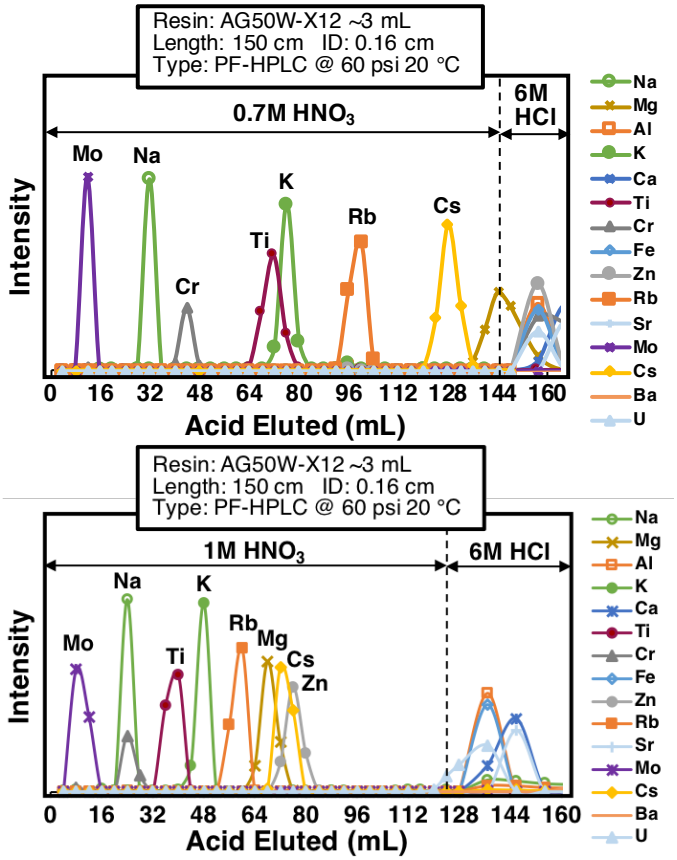

Figure 3.13 Elution curves of elements on AG50W-X12 resin. Eluents with two different acid molarities of 0.7M HNO_3 and 1M HNO_3 were tested. The 0.7M HNO_3 gave a better separation and is used to treat natural samples.

In summary, cation resins with two different cross-linkages were tested for Rb separation from matrix elements especially from K. The tests were performed using the PF-HPLC system developed in the lab. The results showed that high pressure and high temperature had a negative effect on elemental separation. High pressure increases flow rate which might limit the equilibration between resins and liquids. High temperature may lead to faster longitudinal diffusion of elements in columns (Dybczyński, 1972), and make the separation more difficult. In general, longer columns resulted in better separation. Resin with higher cross-linkage (AG50W-X12) gave better separation than resin with low cross-linkage (AG50W-X8), and acids of low molarity was better than acids of high molarity. A complete separation between Rb and K was

achieved with both a 130 cm length and a 150 cm length (ID=0.16 cm) column at 60 psi and 20 °C, filled with AG50W-X12 resin and eluted with ~0.7 M HNO_3. The 150 cm column was adopted for treating natural samples. This PF-HPLC method allows one to separate both K (some Ti may be present in K cut, but Ti can be easily removed with anion resin) and Rb from a sample. The blank for the procedure is less than 1 ng. With this blank level, one can measure low Rb samples such as lunar basalts.

3.2.2.3 Rubidium separation with Sr resin

The disadvantages of the PF-HPLC method are 1) the elution takes very long time (~48 hours) and 2) only one sample could be processed each time (the PF-HPLC unit can only run one column each time). Recently, Zhang et al. (2018) proposed that Rb and K can be separated from each other using Sr-Spec resin. We did a series of tests on the resin and determined the column parameters, such as the inner diameter and the length, suitable for our Rb separation work which will be applied to low Rb samples. The separation using this resin, similar to the PF-HPLC method, is focused on mainly separating K from Rb, as the separation of K and Rb from other elements can be relatively easily done with cation exchange columns (Sect. 3.2.2.2).

The Sr-Spec resin in 3M HNO_3 medium can be used to separate Rb from K. Our tests (Fig. 3.14) showed that a 40 cm Sr resin column resulted in very good separation between Rb and K. This column is used for treating natural samples. The blank of the procedure is less than 0.1 ng. Compared with the PF-HPLC method, the Sr-Spec resin allows us to process several samples each time, and the elution takes about 10 hours, much shorter than the 48 hours needed for PF-HPLC method.

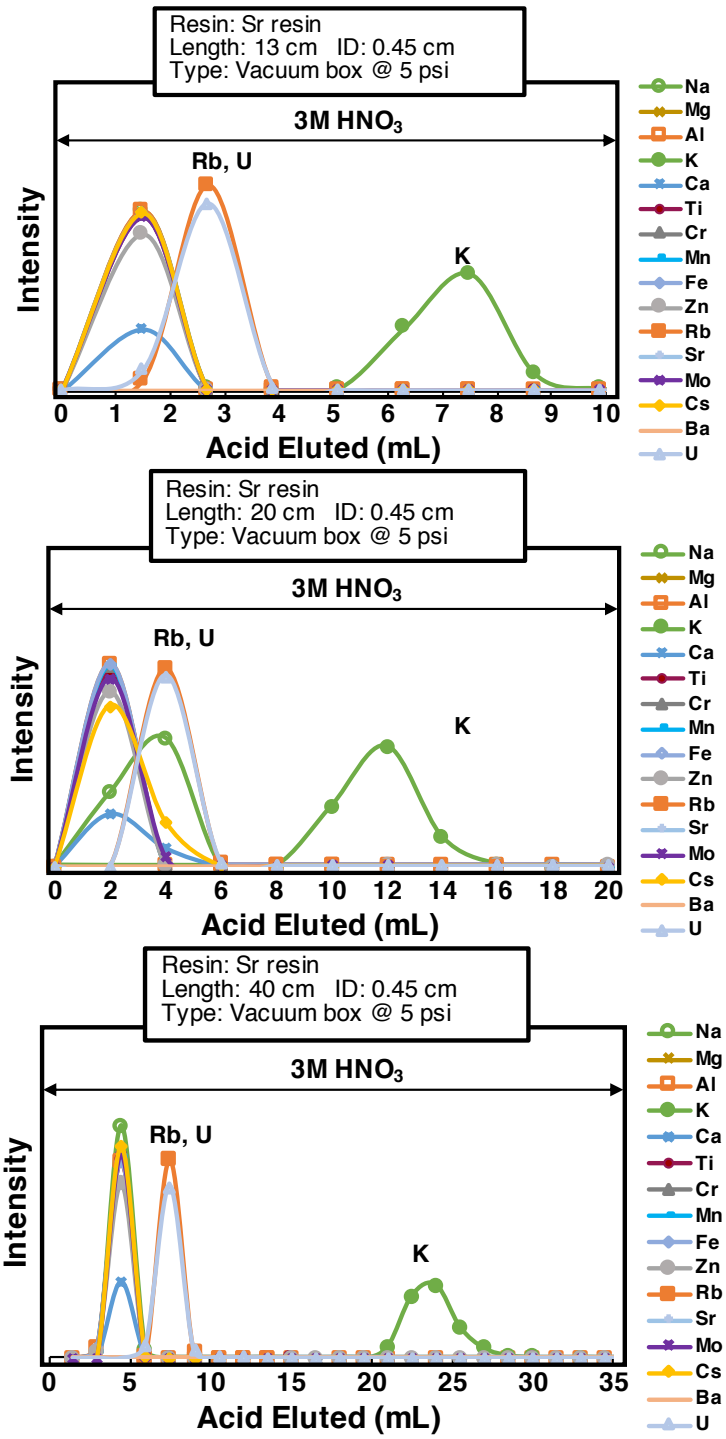

Figure 3.14 Elution curves of Sr resin. Three column lengths (13 cm, 20 cm and 40cm) were tested. All elution was done using vacuum box at a pressure of 5 psi and room temperature. Longer columns resulted in better separation.

3.2.2.4 A complete Rb separation method

The comparison among the three methods (AMP-PAN method, PF-HPLC method and Sr resin method) is shown in table 3.1. In general, all the three methods work for Rb separation, but they have their advantages and disadvantages. For AMP-PAN resin method, the procedure blank is too high (~80 ng) to be applied to low Rb samples like lunar samples and meteorites. The PF-HPLC and the Sr resin methods both have low procedure blank (~ 0.1 ng) but PF-HPLC method is very time consuming; it takes about 48 hours to do one elution and each time only one column can be run with the PF-HPLC unit. For Sr resin, to achieve a good separation between Rb and K, a relatively long (~40 cm; ID=0.45 cm) column is used and a vacuum box is needed for a reasonable flow rate. The Sr resin is much more expensive than the other ion exchange resins.

Table 3.1 Comparison among AMP-PAN, PF-HPLC and Sr resin methods for Rb separation.

Methods	Advantages	Disadvantages
AMP-PAN method	Small column; good separation between Rb and matrix elements	Rb elution from the column is difficult; high procedure background (~80 ng)
PF-HPLC method (using cation resin)	Automated; low background (~ 0.1 ng)	Only one column each time; very time consuming (~48 hours for one elution); separation of Rb from K is not as good as AMP-PAN or Sr resin methods
Sr resin method	Good separation between K and Rb; low background (~0.1 ng)	Relatively long column and vacuum box is needed; resin is very expensive

The Rb isotopic measurement results of synthetic and natural geostandard samples using the three methods are compared and shown in Fig. 3.15. The synthetic samples include NIST SRM984 (the Rb isotope reference standard; treated as a sample and the isotopic composition should thus be zero) and mixtures of peridotites and SRM984. The peridotites used for the mixtures

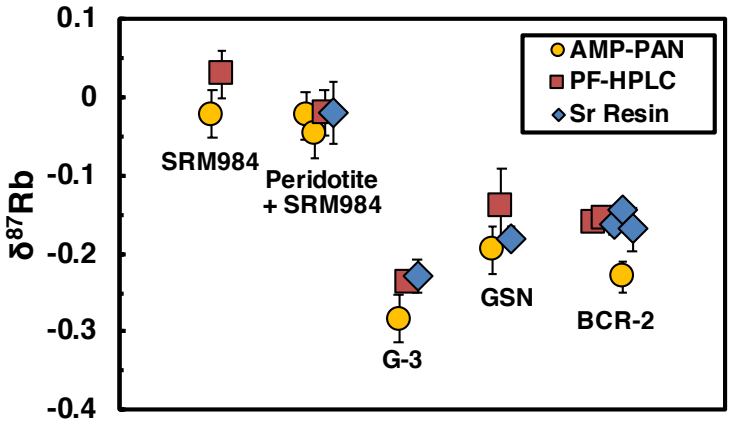

Figure 3.15 Rb isotopic compositions (in ‰) obtained with the three methods (AMP-PAN, PF-HPLC with cation resin and Sr resin methods). In general, the three methods gave the same Rb isotopic compositions within error, suggesting that all the three methods worked.

are PCC-1 and DTS-2b, which have very low Rb concentration (~0.05 ppm). Therefore, the mixtures should have very similar Rb isotopic composition to SRM984 but have matrix element compositions like real rocks. The natural samples include two geostandard granites (G-3 and GSN) and one basalt (BCR-2). In general, the three methods agree within error. It seems however, for BCR-2, the measured Rb value using AMP-PAN method is lower than the values obtained with the other two methods. This can be attributed to the relatively low Rb content in BCR-2 compared with other samples, and therefore Rb background from AMP-PAN method accounted for a nonnegligible fraction of Rb extracted from the rock.

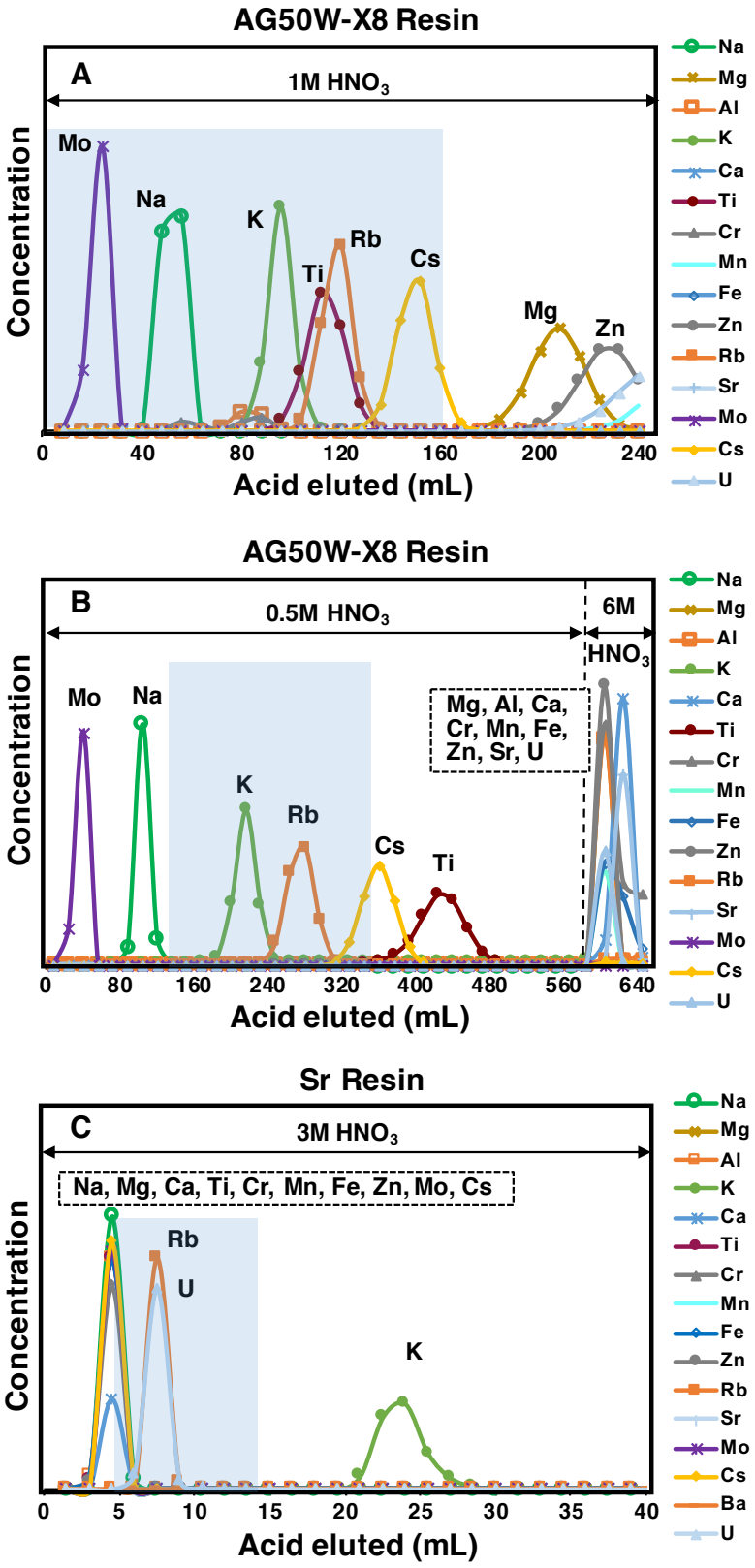

Figure 3.16 Rubidium separation scheme for treating samples including low-Rb meteorites.

Figure 3.16 (continued) The calibration curves were generated using synthetic solutions with equal concentrations of each element. In each panel, the x-axis is the cumulative volume of acids eluted in mL while the y-axis is the concentration. The light-blue shaded areas represent the elution cuts where Rb is collected. (A) Elution curves for various elements on 16 mL AG50W-X8 (200-400 mesh) cation resin in 1M HNO3. Elements not shown in the graph but present in the legend are retained on the column and most of them can be eluted with 6M HNO_3. The first 160 mL of the elution is collected. (B) Elution using the same type of cation resin as in (A) but a lower acid molarity of 0.5M. This step collects eluents around the Rb peak (130-360 mL) and removes almost all matrix elements except for K. (C) Separation of Rb from K using Eichrom Sr resin and 3M HNO3 (5-14 mL is collected). The resin separates Rb and K efficiently.

Among the three methods, the best one to separate Rb from K is using Sr spec resin. The procedure is less time consuming compared with the AMP-PAN and the PF-HPLC methods, and the procedure background is low enough for low Rb samples such as lunar samples and meteorites. A complete Rb separation method including a step of using Sr resin to separate Rb from K has been developed. The method has a sufficiently low total Rb background of ~0.14 ng and has been applied to all the samples measured in this study. The method which consists of five columns, is described below (all the samples were eventually dissolved in 1M HNO_3 before column chemistry).

1) The first column (Fig. 3.16A) of the column chemistry uses 16 mL cation resin (AG50W-X8, 200-400 mesh resin in 20 mL Bio-Rad Econo-Pac columns of 15 mm diameter and 140 mm length). The samples were loaded in 4 mL 1M HNO_3, and 160 mL of 1M HNO_3 was then passed through the column to prepurify Rb from most matrix elements. Element cations have different distribution coefficients on the resin (Dybczyński, 1972; F. Strelow, 1960; F. W. Strelow et al., 1965). This step removes

elements with a higher distribution coefficient than Rb that are retained on the column (*e.g.*, Fe, Mg, Al, Ca, Cr, and Mn), while Rb is eluted. All the matrix elements with distribution coefficients lower than or similar to Rb are collected together with Rb (1-160 mL; light-blue shaded area in Fig. 3.16A). The elution scheme was designed to process relatively large sample masses (low-Rb samples; typically 100 mg). We collect all eluate before the Rb peak to avoid Rb loss, as excessive matrix element concentrations could potentially cause Rb to be eluted early by competing for ion exchange sites on the resin. This step removes a significant portion of matrix elements and all Rb is recovered.

2) The second column (Fig. 3.16B) uses the same type of resin (16 mL AG50W-X8 200–400 mesh in 20 mL Bio-Rad Econo-Pac columns of 15 mm diameter and 140 mm length) but a different HNO_3 molarity of 0.5 M. The reason for using this lower acid molarity is that the elements are better separated from each other (Fig. 3.16), the downside being a larger elution volume compared to the first column (the Rb peaks are at 280 *vs*. 120 mL respectively). Samples were loaded in 4 mL of 0.5 M HNO_3, followed by 360 mL 0.5 M HNO_3 for elution. In this step, only an elution volume around the Rb peak is collected (130–360 mL; light-blue shaded area in Fig. 3.16B). Elements that have a higher or lower partition coefficient than Rb are eliminated. Most Ti is removed in this step, while most K is kept in the Rb elution fraction.

3) After step (ii), a small amount of Ti may remain with Rb. The quantitative removal of remaining Ti was achieved by using a small anion column (1 mL resin of AG1-X8 200–400 mesh in Bio-Rad Poly-Prep 10 mL columns of 8 mm diameter and 90 mm length). The samples were loaded on the resin in 0.5 mL of 2 M HF and then eluted

with 10 mL of the same acid. In 2 M HF, Ti sticks to the anion exchange resin while Rb is eluted (Faris, 1960; Nelson et al., 1960).

4) This step separates Rb from K. Pringle and Moynier (2017) used cation resin AG50W-X8 to separate Rb from K. However, as shown in Fig. 3.16, the elution curves of the two elements largely overlap, even in diluted 0.5 M HNO_3. We used a custom-made PTFE column (40 cm in length and 0.4 cm in diameter) filled with Eichrom Sr resin (50–100 μm) to separate Rb from K. Element partitioning data for the Eichrom Sr resin can be found in Horwitz et al. (1992). Samples were loaded and eluted in 3 M HNO_3. As shown in Fig. 3.16C, complete separation of K and Rb was achieved. This step is similar to the one reported by Zhang et al. (2018) but we use a much longer column (40 cm *vs*. 13 cm) to better separate Rb from K.

5) The solutions from the previous Sr resin step contained pure Rb but were relatively viscous, likely due to dissolution of small amounts of organics from the Sr resin. An additional small clean-up column (1 mL AG50W-X8 resin in Bio-Rad Poly-Prep 10 mL of 90 mm height and 8 mm diameter) was therefore used. Samples were loaded onto the column in 1 mL of 0.5 M HNO_3, followed by another 1 mL 0.5 M HNO_3, and Rb was then collected in 10 mL 6 M HNO_3. This step is not necessary for all Rb samples especially for samples with high Rb contents. Our tests showed that solutions before and after this column gave the same Rb isotopic compositions when measured by MC-ICPMS.

All purified Rb solutions were checked for the presence of potential matrix elements (the elements shown in Fig. 3.16) before measuring their Rb isotopic compositions. After the procedure, K was reduced to about the same concentration level as Rb or lower, and all other

matrix elements had lower concentrations than Rb. The remaining K did not affect the Rb isotopic analyses. Our tests with K-doped Rb solutions showed that the measured isotopic composition of Rb was shifted only when K/Rb concentration ratios (ppm/ppm) were > 50 (Fig. 3.17).

Even small quantities of Sr in the Rb solution can produce a significant isobaric interference of $^{87}Sr^{+}$ on $^{87}Rb^{+}$. The contribution of ^{87}Sr was corrected for by monitoring ^{88}Sr and assuming a constant $^{87}Sr/^{88}Sr$ ratio of 0.085. Our tests with Sr-doped Rb solutions showed that solutions with $^{88}Sr/^{85}Rb$ intensity ratios (V/V) of ≤0.001 yielded accurate $\delta^{87}Rb$ isotopic compositions within ± 0.03 ‰ (Fig. 3.18). The $^{88}Sr/^{85}Rb$ intensity ratios (V/V) of our purified samples were all < 0.0005 (for most samples the ratio was much lower), which is ten times lower than the ratio after purification ($^{88}Sr/^{85}Rb$ < 0.005) in Pringle and Moynier (2017).

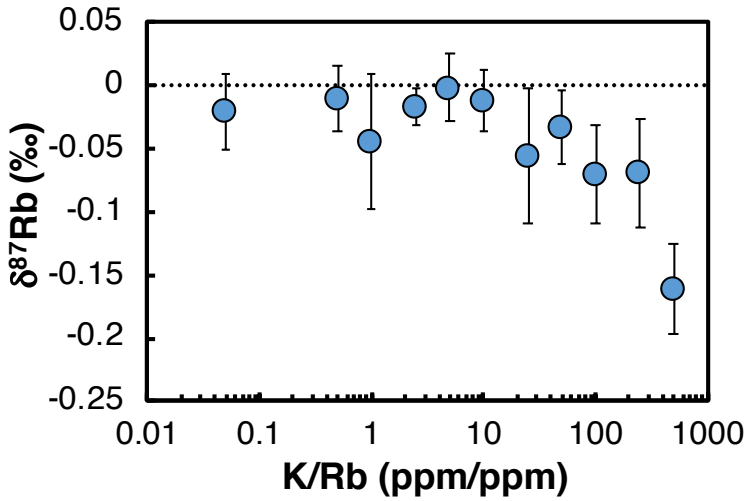

Figure 3.16 Influence of K on the isotopic composition of Rb. The measurements were performed using a spray chamber as the sample introduction system, in low resolution mode, using standard Ni cones, at a Rb concentration of ~20 ppb in 0.3 M HNO_3. The solutions were doped with various amounts of K. The isotopic composition of Rb is unaffected up to a K/Rb (ppm/ppm) ratio of 50. For reference, the K/Rb ratios (ppm/ppm) of terrestrial and lunar rocks are 325 and 450, respectively. The K/Rb ratio after chemical purification is always lower than 1.

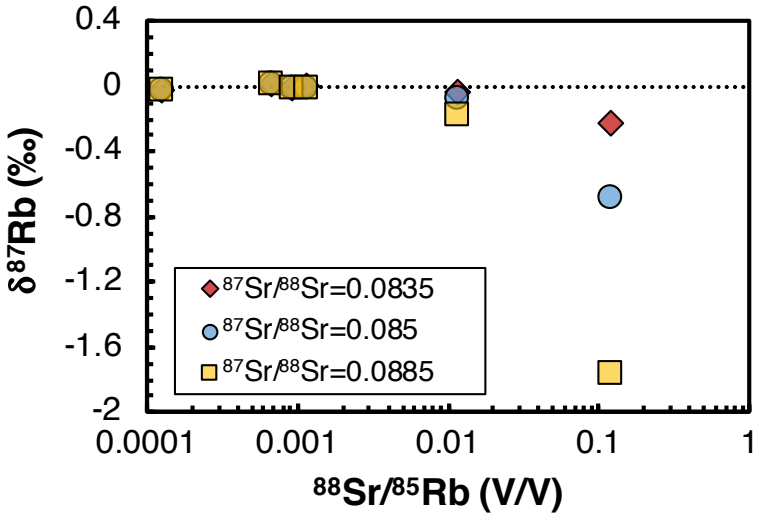

Figure 3.17 Influence of the Sr isobaric interference on the isotopic analysis of Rb. The measurements were performed using a spray chamber as the sample introduction system, in low resolution mode, using standard Ni cones, at a Rb concentration of ~20 ppb in 0.3 M HNO_3. Solutions were doped with various amount of Sr. Strontium-88 was monitored for correcting the interference of ^{87}Sr on ^{87}Rb by assuming a constant $^{87}Sr/^{88}Sr$ ratio of 0.085 (blue circles). The correction is effective for $^{88}Sr/^{85}Rb$ intensity ratios (V/V) equal to or lower than 0.001. All the samples measured in this study have $^{88}Sr/^{85}Rb$ ratios (V/V) lower than 0.0005. Corrections of ^{87}Sr using different $^{87}Sr/^{88}Sr$ ratios of 0.0835 and 0.0885 (corresponding to $^{87}Sr/^{86}Sr$ ratios of 0.70 and 0.74) are also shown in red hexagons and yellow squares, respectively. For samples with $^{88}Sr/^{85}Rb$ ratios (V/V) below 0.001, the shifts in $\delta^{87}Rb$ values are smaller than 0.01 ‰.

3.2.3 Rubidium mass spectrometry

The Rb isotopic analyses were performed using the Thermo Scientific Neptune MC-ICPMS at the University of Chicago. A standard-sample bracketing technique was used. Rubidium sample and standard solutions of ~ 15–25 ppb (Faraday collector voltage of 1–1.5 V for ^{85}Rb in low resolution) in 0.3 M HNO_3 medium were introduced into the MC-ICPMS at a flow rate of 100 μL min^{-1} via a dual cyclonic-Scott type quartz spray chamber. The samples and standards were matched for Rb concentrations within 1 % for MC-ICPMS analyses. Normal Ni sampler and skimmer cones were used, and all measurements were performed in low resolution mode. The

MC-ICPMS at the University of Chicago is equipped with 9 Faraday collectors. Rubidium-85 and ^{87}Rb were measured on the L2 and axial (A) Faraday collectors, respectively, and the isobaric interference of Sr was monitored at mass ^{88}Sr on H1. All three collectors were equipped with the 10^{11} Ω amplifiers. Isobaric interference from ^{87}Sr was corrected for by assuming a constant ^{87}Sr/^{88}Sr ratio of 0.085. For our purified samples, the correction of the ^{87}Sr interference on ^{87}Rb is small enough that uncertainties in the ^{87}Sr/^{88}Sr ratio are largely inconsequential (Fig. 3.18). For example, adopting two extreme ^{87}Sr/^{88}Sr values covering documented variations among chondrites, terrestrial, and lunar rocks (0.0835 and 0.0885, which correspond to ^{87}Sr/^{86}Sr ratios of 0.70 and 0.74, respectively) would shift δ^{87}Rb values of the most Sr-rich purified solutions (^{88}Sr/^{85}Rb intensity ratio of ~ 0.0005) by 0.008 ‰ at most.

Data were collected as a single block of 25 cycles of 4.194 s integration time, with a take up time of 90 s and a washout time (0.45 M HNO_3 for wash) of 60 s. The clean acid solution (0.3 M HNO_3) that was used for diluting Rb for isotopic analysis was measured before and after each sample and standard under conditions identical to the sample or the standard (with the same integration, take up, and washout times). For each sample and standard, the average intensity of the two bracketing blank acids (0.3 M HNO_3) was subtracted. The Rb background was normally around 0.001–0.003 V for ^{85}Rb and increased by 0.001 V after a measurement session (typically ~15 hours or less).

The sample solutions were measured for 5–12 times, depending on the total Rb amount, and the average δ^{87}Rb values were calculated. The uncertainty for a sample was calculated using the formula of $2 \times \sigma/\sqrt{n}$ (Dauphas et al., 2009), with n the number of replicates for the sample and σ the standard deviation of the δ^{87}Rb values of the standards calculated by treating the standards as if they were samples and calculating the δ^{87}Rb values by considering the 2 nearest standards

bracketing each standard. All Rb isotopic compositions are expressed in δ^{87}Rb notation, which is the departure in ‰ of the $^{87}Rb/^{85}Rb$ ratio of a sample from that of the reference material NIST SRM984.

The yield and accuracy of the procedure was checked with the reference standard NIST SRM984 treated as a sample, and with various synthetic and natural samples. Synthetic peridotite samples were made by mixing geostandard (peridotite) powders containing very little Rb with the Rb reference standard SRM984. The matrix elements in these synthetic samples are found in natural peridotites while their Rb isotopic compositions should be identical or very similar to SRM984 (*i.e.,* δ^{87}Rb = 0). Two synthetic samples were made; DTS-2b (dunite) + SRM984 and PCC-1 (peridotite) + SRM984. as shown in Fig. 3.19, the two synthetic Rb-doped peridotite samples, and SRM984 treated as sample gave δ^{87}Rb values of zero within error.

We also measured several geostandards, including basalts and granites (BHVO-2, BCR-2, BE-N, W-2, AGV-2, GSR-1, GS-N, G-A and G-3). The majority of samples were digested and measured more than once and yielded reproducible results, which are in good agreement with previously published results by Pringle and Moynier (2017) and Zhang et al. (2018) (Fig. 3.19). The Allende carbonaceous chondrite (powder from Smithsonian Institution) was also measured to test the method on a low-Rb sample. Compared with the geostandards, Allende has much lower Rb concentration (~1 ppm *vs.* tens of ppm or more in the geostandards). Its Rb concentration is however similar to mare basalts (~1 ppm). It was digested and measured three times and all the three measurements yielded reproducible results that also agree with Pringle and Moynier (2017) (Fig. 3.19).

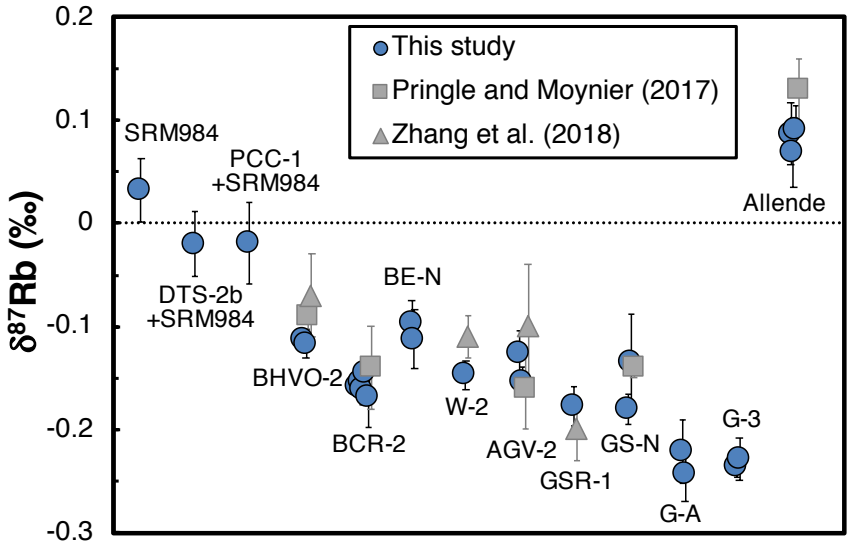

Figure 3.18 Test results for the reference standard SRM984 treated as a sample, synthetic samples (mixtures of DTS-2b+SRM984 and PCC-1+SRM984), geostandards (including basalts and granites) and carbonaceous chondrite Allende. SRM984 treated as a sample and the synthetic samples have Rb isotopic compositions identical to SRM984 within error. Geostandards and carbonaceous chondrite Allende yielded reproducible results (blue circles) that agree with literature data (grey squares and triangles).

3.3 Rubidium isotopes tracing volatile element depletion in the Moon

The Moon and the Earth have very similar refractory element concentrations, except for siderophile elements whose concentrations can be affected by core formation. However, the Moon is depleted in volatile elements comparted to the Earth, and both of them are depleted compared to CI chondrites (Fig. 3.20). Previous work on isotope measurements of refractory and volatile elements in the Moon and the Earth has placed important constraints on the scenarios of Moon formation and its volatile loss. Below the work is briefly summarized. Besides, we have measured high-precision Rb isotope data on terrestrial and lunar rocks. The new Rb isotope data are reported and their implications in the context of Moon formation are discussed.

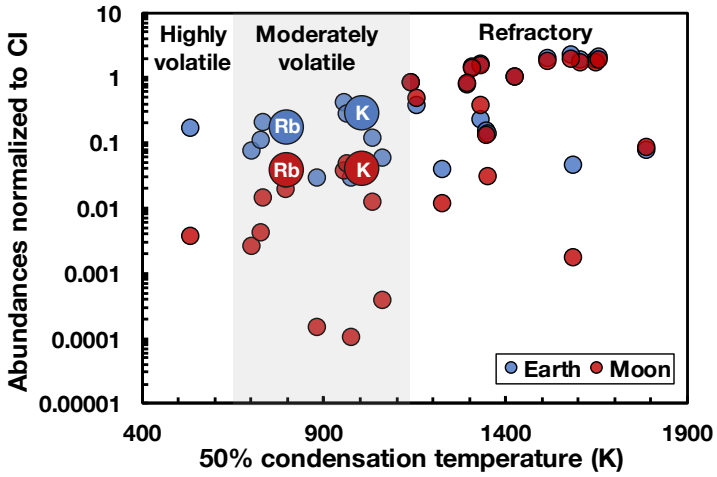

Figure 3.19 Lunar volatile element depletion, modified from Day and Moynier, (2014). The 50% condensation temperatures of elements from Lodders (2003) are plotted on x-axis, which are an indicator of volatility. Elements can be divided into refractory, moderately volatile and highly volatile groups based on their 50% condensation temperatures. The elemental abundances are shown on y-axis. The Moon and the Earth have very similar refractory element concentrations, except for siderophile elements whose concentrations can be affected by core formation. However, the Moon is depleted in volatile elements comparted to the Earth, and both of them are depleted compared to CI chondrites. Elemental concentrations are from McDonough and Sun (1995) and O'Neill (1991).

3.3.1 Giant impact theory and lunar volatile depletion

3.3.1.1 Refractory element isotopes

A widely accepted model for the origin of the Moon is the giant impact model proposed in mid-1970s (Cameron and Ward, 1976; Hartmann and Davis, 1975). According to the model, the Moon formed through a Mars-sized impactor (named Theia) colliding with the proto-Earth. A series of simulations have been done since the proposal of the giant impact hypothesis. Early simulations of the giant impact always yielded a protolunar disk with its most material coming from the impactor (*e.g.,* Canup, 2004; Canup and Asphaug, 2001). Considering the observed

isotopic dissimilarities among planetary bodies (*e.g.,* different oxygen isotopic anomalies; Clayton and Mayeda, 1996), it is very likely that the impactor had a different isotopic composition from the proto-Earth. Therefore, the Moon receiving its most material from the impactor should have a different isotopic composition from the Earth.

This is in contrary to the geochemical observations of isotopes of refractory elements. Measurements of the isotopic anomalies (*i.e.*, mass-independent isotope fractionation, which is used to trace source materials) of refractory elements in the Earth and the Moon showed that the Earth and the Moon have almost the same isotopic compositions. Pioneering work was done by Clayton and colleagues measuring oxygen isotopes of the Earth-Moon system and other planetary bodies (Clayton, 1993; Clayton and Mayeda, 1996). The Earth and Moon fall on the same mass-dependent isotope fractionation line with a slope of ~0.52. Other differentiated parent bodies such as Mars, Vesta (the parent body of HED meteorites) and aubrites fall on different mass-dependent fractionation lines. Following studies on other refractory element isotopes also showed that the Moon and the Earth were strikingly similar. Titanium (Zhang et al., 2012), tungsten (Touboul et al., 2007), chromium (Lugmair and Shukolyukov, 1998) and zirconium (Akram and Schönbächler, 2016) isotopes of lunar rocks all display the same mass-independent isotopic values as that of the Earth. The discrepancy between the isotopic observations and the model simulations is often referred to as "lunar isotopic crisis".

Several scenarios have been proposed to reconcile the disagreement. Pahlevan and Stevenson (2007) proposed that the Earth and the Moon could have the same isotopic composition through isotope equilibration in the aftermath of the giant-impact via turbulent mixing. This was proposed initially to explain the oxygen isotope similarity between the Moon and the Earth. Oxygen might be relatively easier to achieve equilibrium during the intensive mixing after the

giant impact, but highly refractory elements such as Ti and Zr may take significantly long time to reach equilibration (Zhang et al., 2012). Another possibility would be that the impactor and the proto-Earth had similar isotopic compositions (Dauphas, 2017; Dauphas et al., 2014).

Several giant impact models have also been proposed to explain the isotopic similarity between the Moon and the Earth, including 1) hit-and-run giant impact with high impact velocity and impact angle in which a significant part of the impactor escapes so that the protolunar disk is mainly composed of materials derived from the proto-Earth (Reufer et al., 2012); 2) fast-spinning Earth model in which an impact onto a fast-spinning proto-Earth can produce a protolunar disk with materials derived mainly from Earth's mantle (Cuk and Stewart, 2012); 3) a collision between two embryos of comparable mass which produces a disk and a planet with the same composition (Canup, 2012). Compared with canonical models, these models all invoked much higher angular momentum than that of the current Earth-Moon system which has to be reduced to the current value. The drainage of the angular momentum to the Sun through eviction resonance was proposed by Cuk and Stewart (2012) as a way to remove the excess angular momentum from the Earth-Moon system. Recently, a new model without violating the angular momentum constraint was proposed by Hosono et al. (2019). In this model a solid impactor hit the proto-Earth under conventional collision conditions while the proto-Earth was still covered with a magma ocean. This model produces a protolunar disk with a substantial fraction from the magma ocean.

3.3.1.2 Volatile element isotopes

The isotopic compositions of moderately volatile elements Zn, K and Rb have been used to study the volatile element depletion processes of the Moon. Zinc showed mass dependent isotope variation in lunar basalts of ~ –5 to +2 ‰, which is much larger than that in terrestrial basalts (+0.2 to +0.5 ‰) (Herzog et al., 2009; Kato et al., 2015; Moynier et al., 2006; Paniello et

al., 2012). The heavy Zn isotopic compositions measured in lunar samples were interpreted to reflect fractionation by evaporation during the Moon-forming giant impact (Paniello et al., 2012) and/or through degassing and loss of Zn concurrent with lunar magma ocean crystallization (Kato et al., 2015). However, giant-impact volatilization or lunar magma ocean cannot explain the very negative Zn isotopic values (~ –5 ‰) that were also seen in mare basalts. For comparison, chlorine in mare basalts also showed large isotopic variation (–1 to +24 ‰), but the variations were ascribed to volatile loss of metal chlorides such as $ZnCl_2$ during basaltic magma eruption (Sharp et al., 2010). The isotopic compositions of Cl in the terrestrial mantle, crust and carbonaceous chondrites are indistinguishable, so there is no nebular isotope fractionation or isotope fractionation during differentiation of the Earth (Sharp et al., 2007). The large chlorine isotopic variation in lunar materials was explained to reflect that Cl has been lost as metal halides (NaCl, $ZnCl_2$ and $FeCl_2$) during magma eruption on the lunar surface. According to Sharp et al. (2010), evaporation of metal halides is unique to the lunar environment where little H exists, otherwise HCl would have been evaporated which would not result in large isotope fractionation. Whether Zn isotopic variation in lunar basalts is due to or partially due to magma eruption on the lunar surface is still not clear. The large Zn isotopic variation makes constraining precisely the Zn isotopic composition of bulk Moon difficult.

Potassium isotopic compositions in chondrites, achondrites, CAIs, lunar and terrestrial samples were measured first by Humayun and Clayton (1995). They found that K isotopes are homogeneous among the planetary bodies within ±0.5 ‰, even though remarkably different degrees of K elemental depletion were seen. Potassium depletion in the Moon is about 20 times more compared to that of the Earth (Prettyman et al., 2006), but the difference between their K isotopic compositions is small. Wang and Jacobsen (2016) remeasured the K isotopic composition

of the Earth, the Moon and chondrites with higher precision, and found that lunar rocks are enriched in the heavy K isotopes compared with the Earth and chondrites by ~+0.4 ‰. They explained the enrichment of heavy K isotopes in the Moon relative to the Earth as the result of incomplete condensation from a bulk silicate Earth vapor after the giant impact.

Rubidium is comparable to K in that they are both alkali elements and moderately volatile. Pringle and Moynier (2017) measured the Rb isotopic compositions of the Earth, chondrites and the Moon and found also a heavier Rb isotopic composition of the Moon than the Earth by ~+0.17 ± 0.13 ‰. They proposed that Rb could have been lost during or following the giant impact or by evaporation during the accretion of Theia. However, no specific or quantitative explanation was given and the estimated isotopic composition difference between the Earth and the Moon had a large error. We therefore measured high-precision Rb isotopic compositions of lunar and terrestrial samples, trying to constrain the Rb isotopic compositions more precisely and to seek the most reasonable explanation for the lunar volatile element depletion.

3.3.2 Rubidium isotopic composition of the Moon

Six lunar Apollo samples were measured, including 5 mare basalts and 1 norite sample to constrain the Rb isotopic composition of the Moon. To compare to the Earth, terrestrial samples including 3 terrestrial basalts (BCR-2, BHVO-2 and BE-N),1 diabase (W-2), 1 andesite (AGV-2), and 4 granites (GSR-1, GS-N, G-A and G-3), were also measured for Rb isotopic compositions. The Rb isotopic compositions of the samples are reported in Table 3.2 and Fig. 3.21. Lunar samples show in general heavy Rb isotopic compositions compared with terrestrial samples, but the norite sample has a Rb composition lighter than mare basalts and similar to terrestrial rocks. It is still not clear why the norite sample is different from mare basalts in terms of Rb isotopes. Pringle and Moynier (2017) measured a piece of the norite and got a Rb isotopic value similar to that of mare

basalts. The discrepancy is probably because the sample is cataclastic and not homogeneous. The piece we measured is white in color and should contain a large portion of plagioclase, and no detailed description is available for the piece measured in Pringle and Moynier (2017). Possibilities for the light Rb isotopic composition in our norite are as follows. 1) The sample could have reflected Rb isotope fractionation during magmatic differentiation. Terrestrial basalts and granites have slightly different Rb isotopic compositions, implying that magmatic differentiation can cause some Rb isotope fractionation. The Moon experienced magma ocean crystallization and it is likely that rocks forming at different stages would have different Rb isotopic compositions. 2)

Table 3.2 Rb isotopic compositions of lunar and terrestrial rocks.

	Rock type	δ^{87}Rb (‰)	95% c.i.	La/U (ppm/ppm)[a]
Lunar rocks				
12002.613	Olivine basalt	-0.034	0.036	29.6
12018.301	Olivine basalt	0.011	0.043	26.1
12052.353	Pigeonite basalt	-0.003	0.036	18.5
10017.413	Ilmenite basalt (high K)	0.060	0.029	30.3
74275.361	Ilmenite basalt	0.089	0.058	45.3
77215.276	Cataclastic norite (white-colored fragment)	-0.149	0.032	16.8
Terrestrial rocks				
BCR-2	Basalt	-0.155	0.005	14.8
BHVO-2	Basalt	-0.114	0.006	35.7
BE-N	Basalt	-0.103	0.018	34.2
W-2	Diabase	-0.147	0.014	18.9
AGV-2	Andesite	-0.146	0.012	20.2
GSR-1	Granite	-0.178	0.019	2.9
GS-N	Granite	-0.177	0.014	10
G-A	Granite	-0.234	0.020	8
G-3	Granite	-0.234	0.009	43

[a]La/U ratios were calculated using concentration data from the Lunar Sample Compendium (https://curator.jsc.nasa.gov/lunar/lsc/), the USGS website (https://crustal.usgs.gov/geochemical_reference_standards/index.html), and Govindaraju,(1994}. For comparison, the La/U (ppm/ppm) ratio of CI chondrites is 27.6.

plagioclase controls the bulk composition. Compared with other minerals, plagioclase is the one that can very likely fractionates Rb isotopes, because it has been known to fractionate K/Rb ratios to extreme values among terrestrial basalts (Murthy et al., 1970). More work needs to be done regarding how plagioclase fractionate Rb isotopes, and the isotopic compositions of other lunar norite samples and lithologies before conclusions can be drawn.

To estimate the Rb isotopic composition of the bulk Moon, one way is to use the average of the measured mare basalts. However, it is conceivable that Rb isotopes could have been fractionated by magmatic differentiation, for example when an anorthositic flotation crust formed

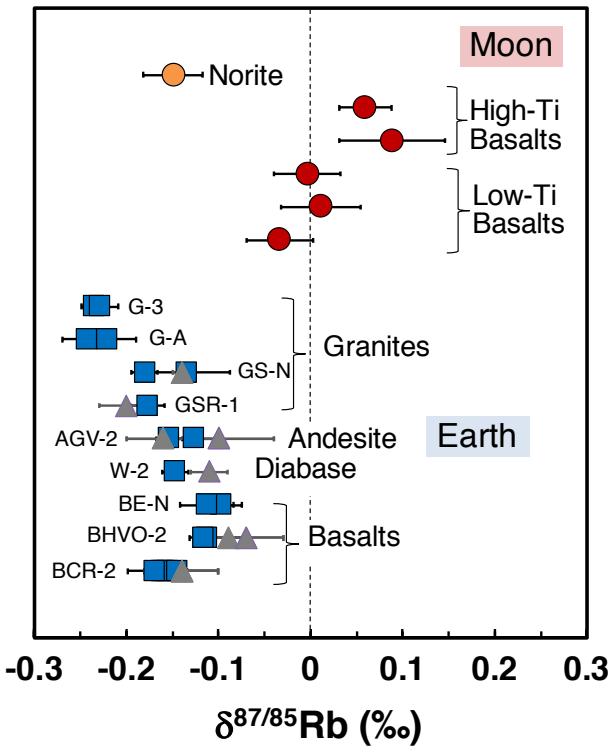

Figure 3.20 Rb isotopic compositions of terrestrial and lunar samples. Red and orange circles are lunar samples and blue squares and grey triangles are terrestrial samples. Grey triangles are from literature data (Pringle and Moynier, 2017; Zhang et al., 2018), while other samples are from this study. Blue squares on the same horizontal line represent a same sample which has been digested and measured more than once. Lunar samples are heavier than terrestrial samples.

from the lunar magma ocean. To mitigate this effect, δ^{87}Rb values of lunar and terrestrial rocks are plotted against the La/U ratio (Fig. 3.22A), because La and U are two refractory elements that have similar geochemical behavior to Rb and K during magmatic processes but have not experienced volatile loss. The data hint at a correlation between δ^{87}Rb and La/U ratios, possibly reflecting isotopic fractionation during magmatic differentiation. By interpolating the trends to a CI chondritic La/U ratio (ppm/ppm; 27.6 for CI chondrites), the bulk Moon and the bulk Earth were estimated to be +0.03 ± 0.01 and –0.13 ± 0.03 ‰ respectively. This means that the Moon is enriched in the heavy isotopes of Rb by +0.16 ± 0.04 ‰. This agrees with the less precise assessment of +0.17 ± 0.13 ‰ Moon-Earth difference reported previously (Pringle and Moynier, 2017).

Potassium has very similar geochemical behavior to Rb, as the two elements are both alkali metals, incompatible, lithophile and moderately volatile. For comparison purpose, we also estimated the K isotopic composition of the bulk moon (Fig. 3.22B), using the same method as for Rb. Potassium isotopic compositions were not measured in this study, and the data used here is from Wang and Jacobsen (2016). They reported the K isotopic compositions of lunar rocks relative to the bulk Earth. Therefore, instead of estimations for both bulk Moon and bulk Earth, the estimation from their data is the difference between the Moon and the Earth. For K isotopes, the Moon was heavier than the Earth by +0.41± 0.07 ‰ (Fig. 3.22B).

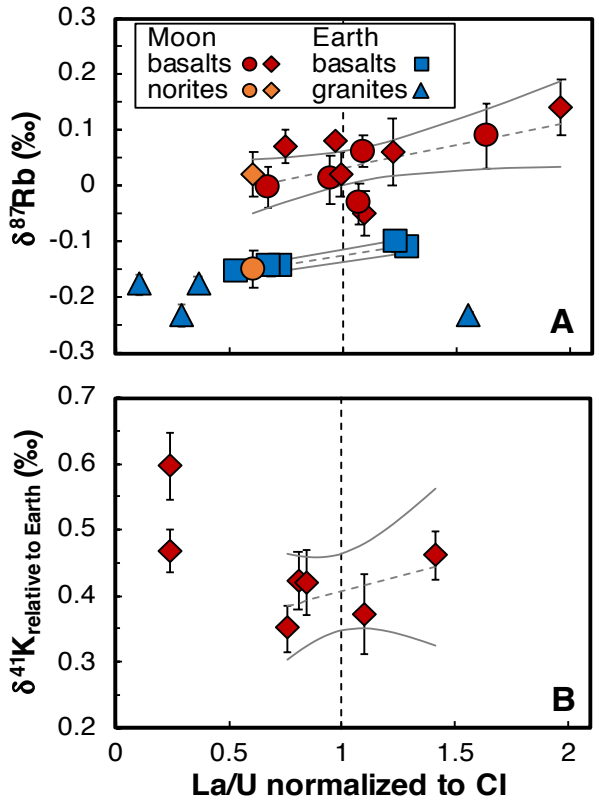

Figure 3.21 Rb and K isotopic compositions of lunar (red and orange circles and hexagons) and terrestrial (blue squares and triangles) samples, plotted against La/U ratios normalized to the CI chondritic ratio (taken here as an indicator of magmatic differentiation). The isotopic compositions of the bulk Moon and the bulk Earth were estimated using linear trends and interpolating to a CI chondrite-normalized La/U ratio of 1. (A) The δ^{87}Rb values of the bulk Moon and the bulk Earth are estimated to be +0.03 ± 0.03 and –0.13 ± 0.01 ‰ respectively, which corresponds to a Moon-Earth difference of +0.16 ± 0.04 ‰. The lunar δ^{87}Rb data are from this study (red circles=lunar basalts, orange circle=norite; Table 3.2) and from Pringle and Moynier (2017) (red hexagons=basalts, orange hexagon=norite), and the La and U concentrations are from the Lunar Sample Compendium (https://curator.jsc.nasa.gov/lunar/lsc/). The norite sample measured in this study (orange circle) was excluded from the regression due to its very light Rb isotopic composition (this sample is heterogeneous and a white-colored piece was measured in the present study). The terrestrial δ^{87}Rb values and the La/U ratios can be found in Table 3.2. (B) The bulk Moon δ^{41}K value is estimated to be +0.41 ± 0.07 ‰ relative to the Earth. The δ^{41}K values of lunar samples relative to the Earth are from Wang and Jacobsen (2016) and the La/U ratios are calculated using concentrations from the Lunar Sample Compendium.

3.3.3 Rubidium isotope fractionation factor during vacuum evaporation

To constrain the behavior of Rb isotopes during evaporation, vacuum evaporation experiments were conducted at the University of Chicago, following the method described in Richter et al. (2007). A MORB-like composition (Gale et al., 2013) was used for the experiments but with ~3 wt% K_2O and ~3 wt% Rb_2O, so that the Rb-depleted evaporation residue can be measured precisely. To make the staring powder, high purity (>99.99 %) oxides and carbonate powders were mixed in proportions shown in Table 3.3. Elements of Ca, Na, K and Rb were added as carbonates since their oxides are not as stable. The mixture was ground in ethanol in an agate mortar for several hours, then the slurry was transferred into an automatic shaker and was shook for several hours to get a homogeneous powder. The powder was dried in air at room temperature, and then heated in a muffle furnace at 950 °C for ~5 hours to get rid of the CO_2 released from carbonate decompose. After decarbonation, about 25–70 mg aliquots were mixed with polyvinyl alcohol (PVA), loaded onto iridium wire (ID = 2.5 mm) loops, and dried at room temperature overnight. They were then placed into a vertical gas-mixing furnace, heated at 1000 °C in air for 2 mins to remove PVA and water. They were then melted at 1200 °C in the furnace flowing with H_2 and CO_2 (fO_2=IW+2) for 5 mins to reduce Fe(III) to Fe(II), and were ready for evaporation.

The evaporation experiments were conducted in a high-temperature vacuum furnace. The pressure around samples was always less than 10^{-6} Torr at run conditions. Two temperature conditions of 1200 °C and 1400 °C were used. For 1200 °C evaporation experiments, temperature was increased to the value within 90 min, and stayed at the value for 5 min, then the heated sample aliquot was quenched in water and was considered as the zero-time sample. For 1400 °C evaporation experiments, temperature was first increased to 1200 °C, kept for 5 min and was then increased to 1400 °C within 8 min, and was kept for different durations for different sample

Table 3.3 The starting composition used for vacuum evaporation experiments.

	Average MORB[a] (wt %)	Mixed powder (wt %; doped with Rb and K)[b]	Oxides and carbonates for making powder mixture[c]	Mass (g) of oxides and carbonates for making 1 g oxide powder[d]
MgO	7.58	7.19	MgO	0.0719
SiO_2	50.47	47.90	SiO_2	0.4790
FeO	10.43	9.90	FeO	0.0990
CaO	11.39	10.81	$CaCO_3$	0.1929
Na_2O	2.79	2.65	Na_2CO_3	0.0453
Al_2O_3	14.7	13.95	Al_2O_3	0.1395
TiO_2	1.68	1.60	TiO_2	0.0159
K_2O		3.0	K_2CO_3	0.0440
Rb_2O		3.0	Rb_2CO_3	0.0371
Total	99.04	100		1.1246

a. Average MORB composition from Gale et al. (2013). b. The final composition of the power used for vacuum evaporation. The elemental proportions are the same as the MORB composition except for K_2O and Rb_2O, for which 3 wt % of each was added. c. CaO, Na_2O and K_2O and Rb_2O were added as carbonates instead of oxides. d. Masses of oxides and carbonates needed for making 1 g oxide powder. The mixed powder was decarbonated before evaporation.

aliquots. The zero-time sample of 1400 °C was quenched right after the temperature reached the value. The Rb isotopic compositions of zero-time samples of 1200 °C and 1400 °C were considered as initial isotopic compositions, and Rb isotopic compositions of samples evaporated in longer time durations were compared with them.

The elemental concentrations and Rb isotopic compositions of the samples were measured using the MC-ICPMS at the Origins Lab at the University of Chicago. The results are shown in Table 3.4 and Fig. 3.23. elemental concentrations are normalized to Al since Al was not expected to be evaporated. All elements except for K, Na and Rb showed more or less unchanged mass during the course of heating. Samples that were heated for different time durations show Na, K and Rb depletion to various extents compare with zero-time samples. The longer heating time

corresponds to more volatile loss. Volatile loss of K and Rb under 1400 °C is much more efficient than that at 1200 °C. Half of K and Rb was lost after ~20-hour heating at 1200 °C. At 1400 °C, however, the same amount of volatile loss occurred after only ~25 min heating.

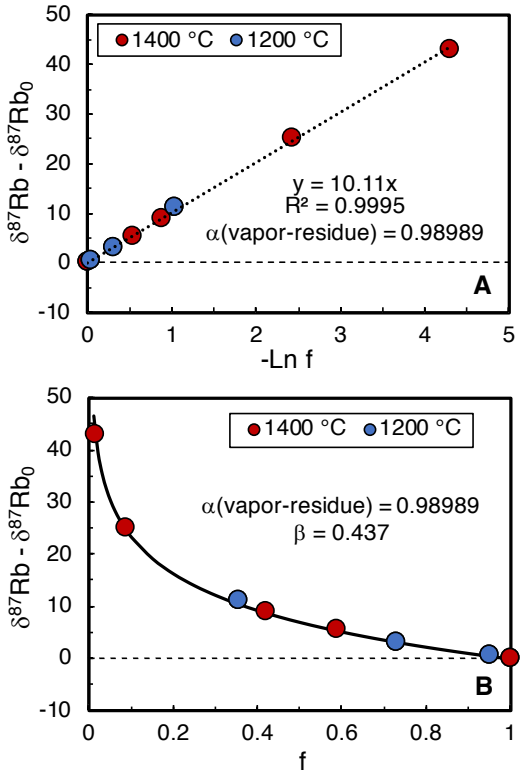

Figure 3.22 Rb isotope fractionation during vacuum evaporation. (A) By plotting Rb isotopic composition vs. lnf, where f is the fraction of Rb remaining in the residue, the slope of the regression line can be used to calculate the fractionation factor α, which is calculated to be 0.98989, corresponding to a fractionation between vapor and liquid of –10.1 ‰ and an evaporation beta factor of 0.437.

Rubidium showed large isotope fractionation due to the evaporative loss (Fig. 3.23). The Rb evaporation is a Rayleigh distillation process, and the isotopic evolution of the residue can be characterized by the following equation,

$$\delta^{87}Rb - \delta^{87}Rb_0 = 1000\,(\alpha - 1)\,\ln f \qquad (3.3)$$

where $\delta^{87}Rb$ and $\delta^{87}Rb_0$ are the Rb isotopic compositions of the evaporation residue and of the initial material respectively, f is the fraction of Rb remaining in the residue, and α is the Rayleigh fractionation factor,

$$\alpha = (^{87}Rb/^{85}Rb)_{vapor} / (^{87}Rb/^{85}Rb)_{residue} \quad (3.4)$$

and the isotope fractionation between vapor and residue is related to α by

$$\Delta^{87}Rb_{vapor\text{-}residue} = \delta^{87}Rb_{vapor} - \delta^{87}Rb_{residue} \cong 1000\ Ln\alpha \cong 1000\ (\alpha\text{-}1) \quad (3.5)$$

By plotting the Rb isotopic compositions of the residue vs. the natural logarithm of the fraction of Rb remaining in the residue, the slope of the line is 1000 (α-1). The Rayleigh fractionation factor α is calculated to be 0.98989 (Fig. 3.23). This value corresponds to a fractionation between the vapor and the residue of ~–10.11 ‰, with the vapor enriched in light Rb isotopes. For evaporation and condensation, the fractionation factor α is often parameterized as,

$$\alpha = (m_i/m_j)^{\beta} \quad (3.6)$$

where m_i and m_j are the masses of the two isotopes of the element of interest, and i and j correspond to the denominator and numerator isotope of the isotopic ratio. For Rb isotopes ^{87}Rb and ^{85}Rb,

$$\alpha = (m_{85}/m_{87})^{\beta} \quad (3.7)$$

and β is thus calculated to be 0.437. The value is very similar to the β value measured for K (0.43) during vacuum evaporation of silicate melts (Richter et al., 2011), demonstrating that K and Rb are behaving very similarly during evaporation of silicate melts.

Table 3.4 Results of the vacuum evaporation experiments.

Sample No.	Duration	Mg/Al (g/g)	Ca/Al (g/g)	Ti/Al (g/g)	Fe/Al (g/g)	Na/Al (g/g)	K/Al (g/g)	Rb/Al (g/g)	f_{Rb}	δ^{87}Rb (‰)	95% c.i.
	1400 °C										
3-2	0 min	0.530	0.940	0.117	0.984	0.167	0.242	0.233	1	1.005	0.023
3-5	15 min	0.531	0.950	0.119	0.986	0.055	0.151	0.137	0.586	6.488	0.023
3-4	30 min	0.530	0.940	0.115	0.969	0.026	0.101	0.097	0.417	9.954	0.023
4-1	60 min	0.532	0.934	0.114	0.967	0.001	0.028	0.021	0.088	25.995	0.023
4-5	90 min	0.533	0.939	0.113	0.964	0.001	0.006	0.003	0.014	44.024	0.046
	1200 °C										
3-1	0 min	0.534	0.934	0.111	0.980	0.192	0.253	0.250	1	0.244	0.046
2-1	1 hour	0.527	0.928	0.117	0.976	0.173	0.238	0.238	0.951	0.821	0.043
2-2	4 hours	0.525	0.935	0.117	0.982	0.088	0.176	0.182	0.729	3.349	0.046
4-2	40 hours	0.538	0.948	0.117	1.001	0.009	0.107	0.088	0.354	11.405	0.046

3.3.4 Vapor loss to the Earth as the cause for lunar volatile depletion

As discussed above, several settings have been considered to explain the volatile element depletion and volatile isotopic compositions of the Moon, including a volatile-depleted Theia, degassing of the lunar magma ocean, and volatile loss due to the Moon-forming giant impact. The scenarios are evaluated here.

3.3.4.1 Volatile-depleted Theia

A mixing between a volatile-depleted impactor and the proto-Earth could produce a volatile depleted Moon. Here we consider a simple mass balance model to calculate the relative proportion of the Theia and the proto-Earth in the protolunar disk (or in the Moon) if the lunar volatile depletion is mainly because Theia was volatile depleted. If we assume f the fraction of the material in the Moon derived from Theia, the fraction of the material derived from the proto-Earth would be 1–f, by mass balance we have (take Rb as the representative of volatile elements)

$$f\,(Rb/Sr)_{Theia} + (1–f)\,(Rb/Sr)_{protoEarth} = (Rb/Sr)_{Moon} \quad (3.8)$$

and therefore

$$f = [(Rb/Sr)_{Moon} - (Rb/Sr)_{protoEarth}] / [(Rb/Sr)_{Theia} - (Rb/Sr)_{protoEarth}] \quad (3.9)$$

To make a volatile depleted Moon, the impactor had to be more volatile-depleted than the Moon. As can be seen in Fig. 3.1, Vesta and angrites are more volatile-depleted than the Moon, and can be used as a proxy for Theia. The Rb/Sr ratio in Vesta, angrites, Earth and Moon are 0.01, 0.001, 0.14, and 0.02 times CI, respectively (Wasson and Kallemeyn, 1988). Assuming that the proto-Earth has a Rb/Sr ratio the same as the current Earth, the f is calculated to be 86 % for angrites and 92 % for Vesta. That is, ~90 % of the material in the Moon should be from the impactor Theia. However, it is difficult to explain the isotopic similarity of refractory elements between the Moon and the Earth if the Moon got such a large contribution from the impactor Theia (Sect. 3.3.1), unless that the impactor and the proto-Earth had similar isotopic compositions.

3.3.4.2 Degassing of the lunar magma ocean

The lithologies of samples from the Moon suggested that the Moon was once at least partially molten and was covered with a magma ocean (*e.g.*, Smith et al., 1970; Wood et al., 1970). The phases crystalized first were olivine and orthopyroxene. At ~80 % crystallization, plagioclase started to crystalize and formed a flotation crust, which served as a conductive lid and reduced the free-radiating heat loss (Elkins-Tanton et al., 2011; Snyder et al., 1992). The early crystalized olivine and orthopyroxene did not likely form a flotation lid, since they were denser than the silicate magma and would founder into the underlying magma. Before the formation of the plagioclase flotation crust, the Moon could radiate freely through the magma ocean from which volatile elements could have been lost to space. While appealing, a potential difficulty is that the heat radiation of the magma ocean could be so efficient that the lifetime of the magma ocean must be very short, on the order of ~1000 yr (Elkins-Tanton et al., 2011). Saxena et al. (2017) modeled Na loss from the lunar magma ocean. During the short time period when the Moon was lidless, the

scale height of the sub-Earth point of the Moon was about 40–50 times the present day Earth's scale height and thermal escape could be efficient. The calculated potential Jean's escape of Na is 4–5 orders of magnitude smaller than the total Na inventory of the Moon. A more accurate estimate by Saxena et al. (2017) by taking the exobase height at the sub-Earth point Roche limit (the exobase height in previous calculation was significantly inwards of the Roche limit for the Moon) yielded ~5–20 % loss of Na from the initial lunar magma ocean. The value is still small compared with the ~90 % Na loss (O'Neill, 1991) from the Moon. Sodium is similar to or even more volatile compared to K and Rb, which means that K and Rb loss through magma ocean degassing must be even smaller. Another complication is that the escaping atmosphere from the Moon would most likely form an Earth-orbiting torus that could potentially be reaccreted by the Moon. Therefore, volatile loss through lunar magma ocean degassing cannot explain the depletion of the Moon.

3.3.4.3 Volatile loss through the Moon-forming giant impact

Three scenarios pertaining to the giant impact have been proposed to explain the loss of the moderately volatile elements from the Moon:

1) Canup et al. (2015) considered a closed system, two-phase protolunar disk composed of silicate vapor and melt. The outer disk (the disk lies exterior to the Roche limit) cools fast to form moonlets which form about 40% Moon's mass rapidly in a few weeks to a year, while the inner disk (the disk lies within the Roche limit) cools more slowly due to the smaller surface and the local production of heat via viscous dissipation. The inner melt disk spreads outwards to supply the remaining 60% mass of the Moon over a longer time period (~100 yr). Melt accretion to the Moon stopes as the inner disk dissipates, disk torques weaken and Moon's orbit expands, and the rest of the inner disk is accreted back to the Earth. During the process, the inner disk has volatile elements stay in the vapor and the

melt clumps accreted to the Moon are substantially depleted in volatile elements, forming a volatile depleted Moon.

2) Lock et al. (2018) proposed a giant impact model in which the impact is much more energetic than that in traditional model so that the post-impact Earth forms a "synestia" structure. The structure features a fast-spinning, high-energy, vaporized state that extends for tens of thousands of kilometers. As it cools by radiation from the optically thin photosphere at the outer edge, silicate condensates form and are not supported by the pressure gradient of the vapor and are falling back to the higher-pressure regions of the structure. The silicate condensates which are volatile depleted form the moonlets which can be reheated by the vapor and/or equilibrate with bulk silicate Earth vapor at high temperature.
3) Charnoz and Michaut (2015) considered a protolunar disk with a vapor layer that is abnormally viscous due to magnetorotational instability (MRI). In their simulation, compared with the case of an inviscid vapor, a viscous vapor would cause the disk to be volatilized efficiently, and the vapor mostly flows inward to the Earth. Volatile elements are depleted in the disk due to their accretion to the Earth.

Here we evaluate these scenarios using our newly constrained Rb and K isotope fractionation in the Earth-Moon system (Sect. 3.3.2) and the isotope fractionation factor during evaporation of Rb and K (Sect. 3.3.3).

In scenario 1), the Moon is accreted from volatile-depleted silicate melt carried across the Roche limit by viscous spreading (Canup et al., 2015) and the vapor containing uncondensed volatile elements stayed and accreted to the Earth. In scenario 2) the Moon is formed via incomplete condensation of a vapor cloud surrounding the Earth (synestia) in the aftermath of a

very energetic impact event (Lock et al., 2018). The two scenarios are essentially partial condensation models and cannot explain the heavy isotopic compositions of Rb and K in the Moon relative to the Earth (by +0.16 ± 0.04 ‰ and +0.41± 0.07 ‰ respectively; Sect. 3.3.2). This is because during condensation, kinetic isotopic fractionation will tend to enrich the partial condensate (*i.e.*, the Moon) in the light isotopes, which is opposite to what is observed. Lock et al (2018) (Scenario 2) argued that the heavy isotopic composition of the Moon could be due to the reequilibration between the condensed moonlets and the vapor, which will enrich the moonlets in heavy isotopes of MVEs. However, at the temperature of ~3500 K considered in the model, equilibrium isotopic fractionation between vapor (as Rb and K atoms) and condensate is too small, as estimated by ab-initio calculations (Dauphas et al., 2018; Li et al., 2019), to account for the observed difference between the Earth and the Moon.

It is likely that ab-initio calculations may suffer from various unrealistic assumptions (*e.g.*, using feldspar as the proxy for condensates and condensed melts) so that the calculated equilibrium fractionation factors are not accurate. Another independent way of distinguishing between kinetic and equilibrium fractionation is to look at the δ^{41}K- δ^{87}Rb slope of the Earth-Moon system. The equilibrium fractionation slope $\theta^{\mathrm{K}}_{\mathrm{Rb}}$ can be calculated using the following formula,

$$\theta^{\mathrm{K}}_{\mathrm{Rb}}(\mathrm{Equilibrium}) = \frac{1/m_{39K} - 1/m_{41K}}{1/m_{85Rb} - 1/m_{87Rb}} = \frac{1/38.963 - 1/40.962}{1/84.912 - 1/86.909} = 4.63. \quad (3.10)$$

The pure kinetic slope is

$$\theta^{\mathrm{K}}_{\mathrm{Rb}}(\mathrm{Kinetic}) = \frac{(m_{39K}/m_{41K})^{\beta_K} - 1}{(m_{85Rb}/m_{87Rb})^{\beta_{Rb}} - 1} = \frac{(39.098/40.962)^{0.43} - 1}{(84.912/86.909)^{0.44} - 1} = 2.1. \quad (3.11)$$

where β_K and β_{Rb} are the beta-factors of K and Rb during evaporation. The β_K of 0.43 is from Richter et al. (2011) and β_{Rb} was constrained to be 0.44 through evaporation experiments (Sect. 3.3.3). The observed slope of the Earth-Moon system has a slope of

$$\theta_{Rb}^{K}(\text{Moon}-\text{Earth}) = \frac{\delta^{41}\text{K}_{\text{Moon}}-\delta^{41}\text{K}_{\text{Earth}}}{\delta^{87}\text{Rb}_{\text{Moon}}-\delta^{87}\text{Rb}_{\text{Earth}}} = \frac{+0.41\pm 0.07\ ‰}{+0.16\pm 0.04\ ‰} = 2.56\pm 0.78. \qquad (3.12)$$

The value is in good agreement with the kinetic isotope fractionation slope rather than equilibrium slope, meaning that equilibrium fractionation between vapor and condensates as proposed in scenario 2 cannot explain the isotope fractionation between the Earth and the Moon.

Most likely, the elevated δ^{87}Rb and δ^{41}K values of the Moon relative to Earth reflect partial evaporation not incomplete condensation. This could have happened through loss of vapor from the protolunar disk onto the proto-Earth (Fig. 3.24), as was advocated by Charnoz and Michaut (2015) in scenario 3. In this model, it is assumed that the protolunar disk is stratified, comprising

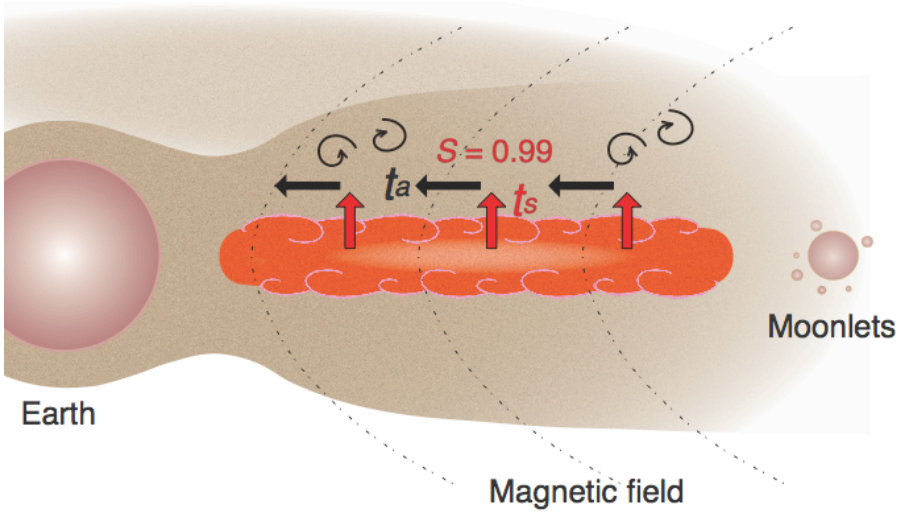

Figure 3.23 Possible setting for the depletion in moderately volatile elements of the Moon. The protolunar disk was composed of a liquid magma layer overlain by a vapor layer. The vapor was drained onto the Earth due to the turbulence and viscosity created by magnetorotational instability (MRI). The elevated δ^{87}Rb and δ^{41}K values of the Moon compared to Earth can be explained by evaporation into a medium that was slightly undersaturated (S≃0.99). For this saturation to be achieved, the evaporation timescale given by the mass of the vapor layer divided by the evaporation flux (t_S) must have been of similar magnitude as the timescale for viscous accretion of the vapor layer onto Earth (t_a). The vapor layer was convecting vigorously and Kelvin-Helmoltz instabilities at the interface between the liquid and vapor layers prevented the development of a viscous layer.

a liquid layer at the midplane surrounded on each side by vapor layers. The fate of moderately volatile elements and the degree of depletion of the Moon in K and Rb depend sensitively on the viscosity of the vapor layer. The reason is that viscosity mediates transport of mass and angular momentum across the disk. Little loss of liquid from the disk could have taken place over much of the cooling history of the disk, because a gravitationally stable low-viscosity region would be present within ~1.7 $R_{\oplus}$ that would have acted as a barrier preventing liquid from being accreted by the Earth. If the viscosity of the vapor was low, it would have remained stagnant and no volatile loss could have occurred. If the viscosity of the vapor was high due to magnetorotational instability (MRI) (Carballido et al., 2016; Gammie et al., 2016), the vapor layer would have been efficiently accreted by the Earth, leaving a disk depleted in volatile elements.

Transport of the vapor layer onto Earth is a complex process that would have involved some evaporation from the liquid to the vapor layer (Charnoz and Michaut, 2015). The kinetics and isotopic fractionation associated with such evaporation depend on the mode of transport inside (advective *vs*. diffusive), and across (equilibrium *vs*. kinetic) the liquid and vapor layers (Craig and Gordon, 1965; Dauphas et al., 2015; Richter, 2004; Richter et al., 2002; 2007). Given the rate of heat loss experienced by the disk through radiation to space, much of the liquid layer would have convected vigorously (Lodders, 2003; Thompson and Stevenson, 1988; Ward, 2011). Furthermore, given the difference in orbital velocities between the vapor and liquid layers, it is likely that Kelvin-Helmholtz instabilities developed (Charnoz and Michaut, 2015; Thompson and Stevenson, 1988) that prevented the development of a viscous layer at the vapor-liquid interface. In this context, where transport within the liquid and vapor layers is entirely advective, the extent of isotopic fractionation of element i during evaporation depends (through the Hertz-Knudsen equation) on its vapor saturation (Dauphas et al., 2015; Richter et al., 2007; 2002), expressed as

$S_i = P_i/P_{i,\,\mathrm{eq}}$ where P_i is the partial vapor pressure of element i and $P_{i,\,\mathrm{eq}}$ is its equilibrium vapor pressure at the relevant temperature.

If $S_i = 1$, there is no net evaporative flux, the vapor is in thermodynamic equilibrium with the liquid, and the isotopic fractionation between vapor and liquid is entirely equilibrium in nature (noted $\Delta_{eq,i}^{v-l}$ hereafter). *Ab initio* calculations give the equilibrium fractionation between monoatomic K vapor (the dominant gas species in conditions relevant to lunar formation) and K-feldspar (taken as a proxy for K in silicate melt) to be $\Delta_{eq,\mathrm{K}}^{v-l} \simeq -0.01$ ‰ at 3500 K (Dauphas et al., 2018; Li et al., 2019). Assuming that Rb forms chemical bonds of similar strengths to K (the two elements have very similar geochemical behaviors), we estimate that the vapor-liquid equilibrium fractionation for Rb should be $\Delta_{eq,\mathrm{Rb}}^{v-l} \simeq -0.002$ ‰ [$\Delta_{eq,\mathrm{Rb}}^{v-l}/\Delta_{eq,\mathrm{K}}^{v-l} \simeq (1/85 - 1/87)/(1/39 - 1/41) = 0.2$].

If $S_i = 0$, the flux is unidirectional (from the liquid to the vapor) and the isotopic fractionation is mostly kinetic in nature (noted $\Delta_{kin,i}^{v-l}$ hereafter). Experiments of K evaporation in vacuum give a kinetic isotopic fractionation with beta-factor of 0.43, $\Delta_{kin,\mathrm{K}}^{v-l} = [(39/41)^{0.43} - 1] \times 1000 = -22$ ‰ (Richter et al., 2011). Our Rb evaporation experiments yielded a similar kinetic isotope fractionation beta-factor of 0.44 (Sect. 3.3.3), which gives $\Delta_{kin,\mathrm{Rb}}^{v-l} = [(85/87)^{0.44} - 1] \times 1000 = -10$ ‰.

If evaporation took place in a medium that was partially saturated ($0 < S_i < 1$), the instantaneous isotopic fractionation factor between vapor and liquid will be intermediate between the equilibrium and kinetic values given above (Dauphas et al., 2015),

$$\Delta_i^{v-l} = \Delta_{eq,i}^{v-l} + (1 - S_i)\Delta_{kin,i}^{v-l} \tag{3.13}$$

This expression gives the instantaneous isotopic fractionation between vapor and liquid. In the model of Charnoz and Michaut (2015) (the scenario 3 above), the vapor is continuously removed

by accretion onto Earth through viscous spreading, leaving behind an MVE-depleted liquid layer. This is a complex process that to first order can be modelled using a Rayleigh distillation,

$$\delta_{i,l} - \delta_{i,0} \simeq \left[\Delta_{eq,i}^{v-l} + (1 - S_i)\Delta_{kin,i}^{v-l}\right] \ln f_i \quad (3.14)$$

where $\delta_{i,l}$ is the isotopic composition (in ‰) of the residual liquid after evaporation, $\delta_{i,0}$ is the initial isotopic composition, and f_i is the fraction of the element remaining after vapor loss. In the context of lunar formation, the present isotopic composition of the Earth would be the starting composition (because in the Earth-Moon system, most of Rb and K resides in the Earth), the lunar composition would be the residual liquid, and the fraction of either Rb or K remaining would be ~0.17 (corresponding to a 6-fold depletion) (Albarède et al., 2015; O'neill, 1991; Ringwood and Kesson, 1977).

Using Eq. 3.14, we can calculate the vapor saturations needed to explain the measured isotopic fractionations between lunar and terrestrial rocks for Rb and K. We find values of $S_{\mathrm{Rb}} = 0.991 \pm 0.002$ and $S_{\mathrm{K}} = 0.990 \pm 0.002$ (Fig. 3.25). If evaporation had occurred in a more undersaturated medium, kinetic isotope effects would have left the Moon more isotopically fractionated in Rb and K than measured. Conversely, if the evaporation had occurred in a medium closer to saturation, the instantaneous fractionation would approach the equilibrium value, leaving the Moon less isotopically fractionated than it is. The extent of Zn depletion ($f_{\mathrm{Zn}} \sim 1/200$; Albarède et al., 2015; O'neill, 1991; Ringwood and Kesson, 1977) and $^{66}Zn/^{64}Zn$ isotopic fractionation in the Moon relative to the Earth (~ +1.4 ‰; (Kato et al., 2015; Paniello et al., 2012)) are more uncertain but we calculate a S_{Zn} value of ~0.98 using $\Delta_{kin,\mathrm{Zn}}^{v-l} = \left(\sqrt{64/66} - 1\right) \times 1000 = -15$ ‰. This suggests that the same process could explain the heavy Zn isotopic composition of the Moon.

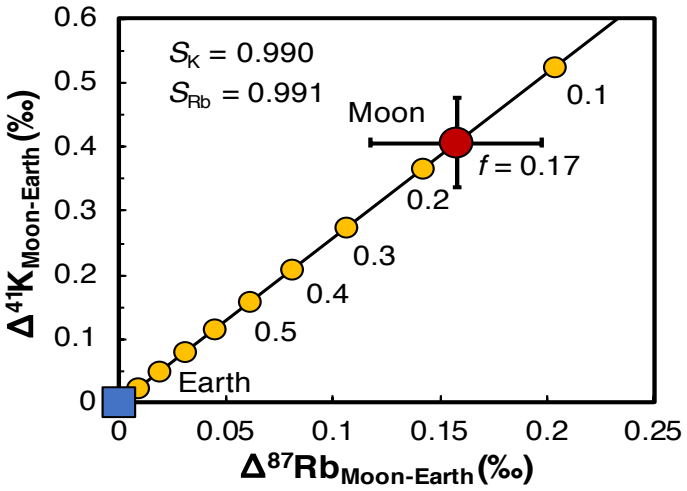

Figure 3.24 Potassium and rubidium isotopic compositions of evaporation residues relative to the starting composition (*f* is the fraction of either K or Rb remaining in the residue). The compositions of the residue (black line and yellow circles; the latter representing the compositions of the residues for 10% evaporation increments) are related to *f* and the vapor saturation state *S* through Eq. 3.14. A slightly undersaturated vapor ($S \simeq 0.99$) associated with kinetic isotopic fractionation can simultaneously explain the heavy Rb and K isotopic compositions of the Moon relative to the Earth ($\Delta^{87}Rb = \delta^{87}Rb_{Moon} - \delta^{87}Rb_{Earth} = +0.16 \pm 0.04$ ‰ and $\Delta^{41}K = \delta^{41}K_{Moon} - \delta^{41}K_{Earth} = +0.41 \pm 0.07$ ‰; Moon=large red circle; Earth=large blue square) for the level of Rb and K depletions in the Moon relative to the Earth ($f \simeq 0.17$; Albarède et al., 2015; O'Neill, 1991; Ringwood and Kesson, 1977).

The finding that both Rb and K evaporations took place in a medium characterized by $S \simeq 0.99$ places severe constraints on scenarios of lunar formation, specifically on the timescale of vapor removal. Indeed, the fact that the vapor was undersaturated means that there was a net evaporative flux from the liquid to the vapor layer, which must have been balanced by vapor removal. We consider a scenario (Fig. 3.24) where the disk is composed of a liquid layer at the midplane of the protolunar disk, overlain by a vapor layer, which is drained efficiently to the Earth due to viscosity powered by MRI (Carballido et al., 2016; Charnoz and Michaut, 2015; Gammie et al., 2016). The timescale for producing a vapor layer with a hydrostatic profile at saturation *S* is

obtained by equating the mass of an element in the vapor layer with the flux across the liquid/vapor interface given by the Hertz-Knudsen equation (see the Saturation timescale calculation below),

$$t_S = \frac{\pi S}{\gamma(1-S)}\sqrt{\frac{R^3}{GM_\oplus}}, \tag{3.15}$$

where γ is a dimensionless evaporation coefficient (available experimental results give values between 0.017 and 0.13 for evaporation of K from silicate melt) (Fedkin et al., 2006; Yu et al., 2003), R is the distance to Earth's center (~1.7 $R_\oplus$=11×10^6 m if we take the outer edge of the gravitationally stable liquid disk; Charnoz and Michaut, 2015), and $M_\oplus$ is Earth's mass. Importantly, this timescale is independent of the volatility ($P_{e,i}$) of the element considered (and the uncertainties attached to it at the elevated temperature considered) because t_S is the ratio of the mass of an element in the vapor layer divided by the evaporation flux across the liquid/vapor boundary, which both scale as $P_{e,i}$. In our preferred scenario (Charnoz and Michaut, 2015; scenario 3), vapor removal would occur by accretion onto the Earth through viscous spreading, which takes place on a timescale,

$$t_a = \frac{2R^2}{3\nu}, \tag{3.16}$$

where ν is the kinematic viscosity (in m^2/s). If $t_a \ll t_S$, vapor is removed more rapidly than it can be replenished by vaporization from the liquid such that the saturation would be lower than $S \simeq 0.99$, and the isotopic fractionation would be larger than that measured in lunar rocks. Conversely, if $t_a \gg t_S$, the saturation would be higher than calculated, and the isotopic fractionation would be smaller than measured in lunar rocks. Equating these two timescales, we can calculate the viscosity needed to maintain the vapor at the saturation level dictated by isotopes,

$$\nu = \frac{2\gamma(1-S)\sqrt{RGM_\oplus}}{3\pi S}. \tag{3.17}$$

To assess whether the calculated kinematic viscosity of the vapor layer is realistic or not, we put it in the context of an α-disk, where the viscosity is expressed as $\nu = \alpha c^2/\Omega$, with α a dimensionless number, $c = \sqrt{kT/m}$ the sound speed (k is the Boltzmann constant, and m the molecular/atomic mass; we use the value of Si because we are concerned with a silicate disk), and $\Omega = \sqrt{GM_\oplus/R^3}$ the Keplerian angular velocity. We calculate that α must have been on the order of 10^{-3} to 10^{-2} in order to explain the inferred saturation of 0.99. Carballido et al. (2016) and Gammie et al. (2016) estimated that in the protolunar disk, where a fraction of alkalis could have been ionized, MRI could have sustained an α value on the order of 10^{-2}. Our estimate of α based on Rb and K isotopic systematics is thus entirely consistent with theoretical expectations, suggesting that MRI-powered viscous drainage is a viable mechanism for explaining the depletion of MVEs in the Moon. At the present time, we cannot tell whether such viscous drainage of vapor would have been a steady process occurring throughout the lifetime of the protolunar disk, or whether it was episodic.

Saturation timescale. Here we calculate the timescale for replenishing a hydrostatic atmosphere above the disk midplane such that the surface pressure is at a set saturation S. The vertical forces acting on a parcel of gas are the pressure forces and the vertical component of the gravitational pull exerted by the Earth,

$$\frac{1}{\rho_g}\frac{\partial P}{\partial z} = -\frac{GM_\oplus z}{(R^2+z^2)^{3/2}}, \tag{3.18}$$

where P is the partial gas pressure, z is the vertical distance from the midplane, ρ_g is the gas density, G is the gravitational constant, $M_\oplus$ is the mass of the Earth, and R is the distance from Earth's center. The gas density ρ_g for the element considered is related to the partial pressure P through the ideal gas law and we have,

$$\frac{1}{P}\frac{\partial P}{\partial z} = -\frac{mGM_{\oplus}z}{kT(R^2+z^2)^{3/2}}, \tag{3.19}$$

where m is the mass of an individual atom (*e.g.*, 6.5×10^{-26} kg for K), k is Boltzmann's constant (1.38×10^{-23} m^2.kg.s^{-2}.K^{-1}), and T is the temperature (in K). Integration of this differential equation with $P(z=0) = P_0$ yields,

$$P = P_0 e^{-\frac{mGM_{\oplus}}{kTR}\left(1-\frac{1}{\sqrt{1+z^2/R^2}}\right)}, \tag{3.20}$$

with $z \ll r$ (the scale height is much smaller than the distance to the Earth), we have,

$$P = P_0 e^{-\frac{mGM_{\oplus}}{2kTR^3}z^2}, \tag{3.21}$$

which can be rewritten as,

$$P = P_0 e^{-\frac{z^2}{2h^2}}. \tag{3.22}$$

with $h = \sqrt{\frac{kTR^3}{mGM_{\oplus}}}$ the scale height of the vapor layer. Introducing the sound speed $c = \sqrt{kT/m}$ and the angular Keplerian velocity $\Omega = \sqrt{GM_{\oplus}/R^3}$, the scale height can be rewritten as $h = c/\Omega$. We now evaluate what the timescale t_S is for an element to be maintained at a given level of saturation S. The total surface density for an element (for the half-space; in kg/m^2) is given by the integral,

$$\Sigma = \int_0^{+\infty} \frac{mP(z)}{kT} dz = \frac{mP_0}{kT}\int_0^{+\infty} e^{-\frac{z^2}{2h^2}} dz = \sqrt{\frac{\pi}{2}}\frac{mhP_0}{kT}. \tag{3.23}$$

The net mass flux of an element (in kg.m^{-2}.s^{-1}) across the liquid/vapor interface is given by the Hertz-Knudsen equation (note that the more commonly used molar flux would have m at the denominator),

$$\phi = \gamma\sqrt{\frac{m}{2\pi kT}}(P_e - P_0), \tag{3.24}$$

where γ is an evaporation coefficient. The saturation timescale t_S is the total mass surface density of an element in the vapor layer at saturation S (Eq. 3.23 with $P_0 = SP_e$) divided by the mass flux across the liquid/vapor layer at the same saturation given by the Hertz-Knudsen equation (Eq. 3.24 again with $P_0 = SP_e$),

$$t_S = \frac{\Sigma}{\phi} = \frac{\pi S}{\gamma(1-S)}\sqrt{\frac{r^3}{GM_\oplus}} = \frac{\pi S}{\gamma(1-S)\Omega}\,. \tag{3.25}$$

This saturation timescale is akin to a residence time and is related to the hydrostatic timescale t_h through $t_S = t_h S/(1-S)$.

3.4 Rubidium isotopic compositions of Mars and chondrites

The Rb isotopic compositions of all the measured samples are summarized in Table 3.5 and Fig 3.26. In general, the terrestrial igneous rocks define a narrow range of Rb isotopic compositions, from –0.22 to –0.11 ‰. There seems to be a slight difference between basaltic and granitic rocks. The granitic rocks are isotopically lighter (–0.14 ~ –0.24 ‰) than basaltic rocks (–0.11 ~ –0.17 ‰), consistent with the observation in Zhang et al. (2018), which reflects Rb isotope fractionation during magmatic differentiation. As discussed in Sect 3.3.2, the best way to estimate the Rb isotopic compositions of bulk silicate Earth and bulk silicate Moon would be to plot the Rb isotopic compositions vs. the La/U ratios (the two refractory elements La and U behaving similarly to Rb during magmatic fractionation can be used to discriminate isotopically fractionated samples) and to look at the Rb isotopic composition corresponding to the CI chondritic La/U ratio. Using the method, we found that the Moon is isotopically heavy compared to the Earth, and our best estimate for the Rb isotopic compositions of bulk Earth and bulk Moon are –0.13 ± 0.01 ‰ and +0.03 ± 0.03 ‰ respectively (Sect. 3.3.2). In this section, we focus on the Rb isotopic

compositions of other planetary bodies than the Earth-Moon system, including Mars, carbonaceous chondrites, ordinary chondrites and enstatite chondrites.

Table 3.5 Rb isotopic compositions of chondrites, terrestrial, lunar and martian samples relative to reference material NIST SRM984.

Samples	Type	$\delta^{87/85}$Rb (‰)	95% C.I.
Chondrites			
Carbonaceous Chondrites			
Orgueil[a]	CI1	0.194	0.034
Orgueil[b]	CI1	0.159	0.042
Ivuna	CI1	0.131	0.042
Allende[a]	CV3	0.087	0.030
Allende[b]	CV3	0.069	0.034
Allende[c]	CV3	0.091	0.024
Vigarano	CV3	0.057	0.020
Murchison[a]	CM2	0.099	0.023
Murchison[b]	CM2	0.119	0.024
Mighei	CM2	0.126	0.032
Ornans	CO3.4	0.100	0.024
Lance	CO3.5	0.029	0.030
Ordinary Chondrites			
Kesen	H4	-1.024	0.026
Queen's Mercy	H6	0.045	0.034
Bald Mountain	L4	-0.512	0.034
Farmington[a]	L5	0.146	0.021
Farmington[b]	L5	0.207	0.034
Krymka	LL3.2	-0.407	0.040
Soko-banja	LL4	-0.821	0.030
Saint-Severin	LL6	0.180	0.034
Enstatite Chondrites			
Abee[a]	EH4	-0.242	0.021
Abee[b]	EH4	-0.193	0.019
Indarch[a]	EH4	-0.096	0.021
Indarch[b]	EH4	-0.035	0.020
Indarch[c]	EH4	-0.079	0.031
Saint-Sauveur	EH5	0.045	0.036

Table 3.5 (continued)

Hvittis	EL6	0.294	0.020
Pillistfer	EL6	0.150	0.052
Terrestrial samples			
BCR-2[a]	Basalt	-0.159	0.008
BCR-2[b]	Basalt	-0.155	0.008
BCR-2[c]	Basalt	-0.162	0.014
BCR-2[d]	Basalt	-0.145	0.011
BCR-2[e]	Basalt	-0.169	0.029
BHVO-2[a]	Basalt	-0.113	0.007
BHVO-2[b]	Basalt	-0.117	0.014
BE-N[a]	Basalt	-0.097	0.023
BE-N[b]	Basalt	-0.113	0.029
AGV-2[a]	Andesite	-0.126	0.023
AGV-2[b]	Andesite	-0.154	0.014
W-2	Diabase	-0.147	0.014
GSR-1	Granite	-0.178	0.019
GS-N[a]	Granite	-0.135	0.047
GS-N[b]	Granite	-0.180	0.014
G-A[a]	Granite	-0.221	0.031
G-A[b]	Granite	-0.243	0.027
G-3[a]	Granite	-0.236	0.010
G-3[b]	Granite	-0.229	0.020
Lunar samples			
12002-613	Olivine basalt	-0.034	0.036
12018-301	Olivine basalt	0.011	0.043
12052-353	Pigeonite basalt	-0.003	0.036
74275-361	Ilmenite basalt	0.089	0.058
10017-413	Ilmenite basalt (high K)	0.060	0.029
77215-276	Cataclastic norite	-0.149	0.032
Martian samples			
Shergotty	Shergottite	0.055	0.021
Zagami	Shergottite	0.052	0.025
Chassigny	Chassignite	0.111	0.063
Nakhla	Nakhlite	0.138	0.063

a, b, c, d, e, f are different aliquots of a sample powder. They are digested, purified and measured separately.

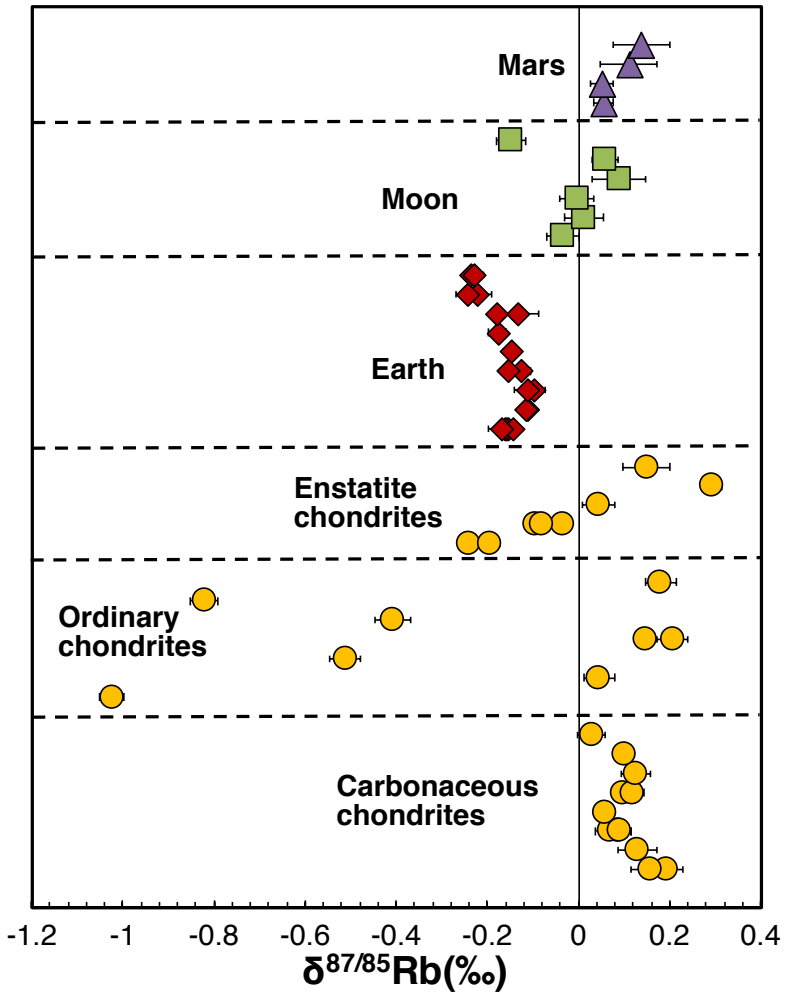

Figure 3.25 Rb isotopic compositions of terrestrial, lunar, Martian samples and chondrites.

3.4.1 Rubidium isotopic composition of Mars

Martian samples (Shergotty, Zagami, Chassigny and Nakhla) were measured for Rb isotopic compositions and their compositions range from +0.05 to +0.14 ‰. Using the same method as for the bulk Moon and bulk Earth, bulk Mars is estimated to have a Rb isotopic composition of +0.10 ± 0.03 ‰ (Fig. 3.27). The value is heavier than those of the bulk Earth and the bulk Moon. This is surprising in that Mars is less depleted in Rb and K compared with the Earth and the Moon (Fig. 3.1). For K isotopes, Mars is lighter than the Moon but is heavier than the Earth (Fig. 3.28). On the K vs. Rb isotope diagram (Fig. 3.28), the Mars does not plot on the

slope defined by the Earth-Moon system. This apparently argues against a simple evaporation or condensation model that isotopic compositions of planetary bodies should correlate with their extents of depletion due to a single evaporation or condensation event. As discussed in Sect. 3.3.4,

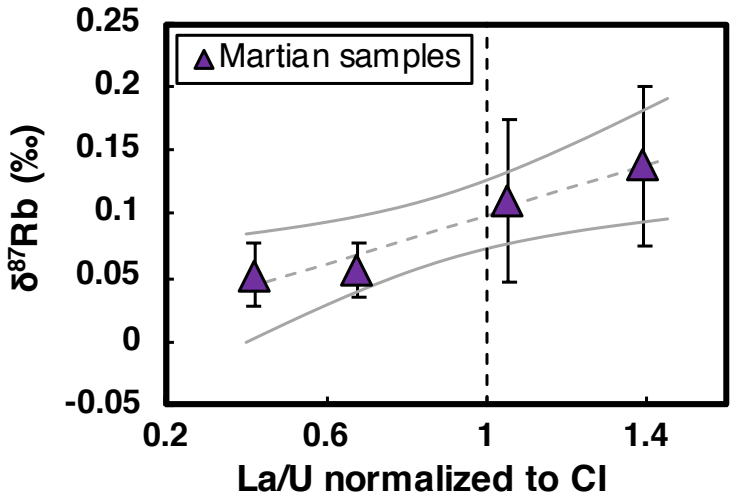

Figure 3.26 Rb isotopic composition of Martian samples, plotted against La/U ratios normalized to the CI chondritic ratio (taken here as an indicator of magmatic differentiation). The δ^{87}Rb value of the bulk Mars is estimated to be +0.10 ± 0.03 ‰. La and U concentrations are from the Martian Meteorite Compendium (https://curator.jsc.nasa.gov/antmet/mmc/).

The Rb and K isotopic fractionation of the Moon relative to the Earth are most likely due to drainage of vapor in the protolunar disk onto the Earth, and the volatile loss occurred in a vapor medium which is only slightly undersaturated (~99 % saturation). There is no reason to expect that the Mars should be on the Earth-Moon trend.

Comparing the Rb isotopic composition of the bulk Mars with the compositions of its building blocks may provide some information on martian volatile element depletion. Based on the elemental compositions of SNC meteorites and their oxygen isotopic compositions, Lodders and Fegley (1997) estimated the building blocks of Mars to be ~85 % H ordinary chondrites, ~11 % CV chondrites and ~4 % CI chondrites. Two CV chondrites were measured in this study (Allende CV3 and Vigarano CV3) and they have an average of +0.07 ‰ for δ^{87}Rb. Two CI

chondrites are measured (Orgueil CI1 and Ivuna CI1), with an average for δ^{87}Rb of +0.16 ‰. For ordinary chondrites, however, it is quite difficult to estimate the bulk composition because their Rb isotopic compositions span a quite large range of –1 to +0.2 ‰. Two H ordinary chondrites were measured, Kesen (H4) and Queen's Mercy (H6), and they have very different Rb isotopic compositions of –1 ‰ and +0.05 ‰ respectively. A Rayleigh distillation model for evaporation can be used to calculate the Rayleigh fractionation factor α,

$$\delta^{87}Rb_{Mars} = \delta^{87}Rb_0 + 1000\,(\alpha-1)\,\ln f. \tag{3.26}$$

where $\delta^{87}Rb_0$ denotes the initial Rb isotopic composition (the isotopic composition of the building blocks), f can be calculated by using the Rb/Sr ratios of these materials $f = (Rb/Sr)_{Mars}/(Rb/Sr)_0$. The Rb/Sr ratios of H chondrites, CV, CI and Mars are (g/g) ~0.29, 0.08, 0.27 and 0.07 respectively, (from MetBase, Martian Meteorite Compendium, and Wasson and Kallemeyn, 1988), and f is therefore calculated to be ~0.26.

For an H chondrite composition of –1 ‰ (the isotopic composition of Kesen meteorite), the initial Rb isotopic composition $\delta^{87}Rb_0$ would be –0.83 ‰ (the average of 85 % H ordinary chondrites, ~11 % CV chondrites and ~4 % CI chondrites) and the fraction factor α would be 0.9993, corresponding to a fractionation between the vapor and the residue of –0.7 ‰. If the H chondrite composition was assumed to be that of the Queen's Mercy (H6) meteorite (+0.05 ‰), the fractionation factor would be 0.99997, corresponding to a fractionation of -0.033 ‰ between the vapor and the residue.

The equilibrium isotope fractionation between the vapor and the residue in an evaporation process can be calculated using the following equation (Dauphas et al., 2012):

$$1000 \ln \beta_{i/j} \simeq 1000 \left(\frac{1}{m_j} - \frac{1}{m_i}\right) \frac{\hbar^2}{8k^2T^2} \langle F \rangle. \tag{3.27}$$

For Rb isotopes, the equation becomes

$$1000 \ln \beta_{^{87}\mathrm{Rb}/^{85}\mathrm{Rb}} \simeq 1189\langle F\rangle/T^2, \quad (3.28)$$

where $\ln \beta_{^{87}\mathrm{Rb}/^{85}\mathrm{Rb}}$ is the Rb reduced partition function ratio and $\langle F\rangle$ is the mean force constant of Rb bonds. The mean force constant of Rb bonds in Rb-feldspar, which is used here as a proxy of melt, is 26 N m^{-1} based on ab-initio calculations (paper submitted). At a temperature of 1500 K relevant to the melting temperature of silicate magma, the reduced partition function ratio of Rb-felspar is 0.014 ‰ (*i.e.*, the fractionation between vapor and residue is –0.014 ‰). At the Rb half-condensation temperature of 800 K, the reduced partition function ratio of feldspar is 0.048 ‰.

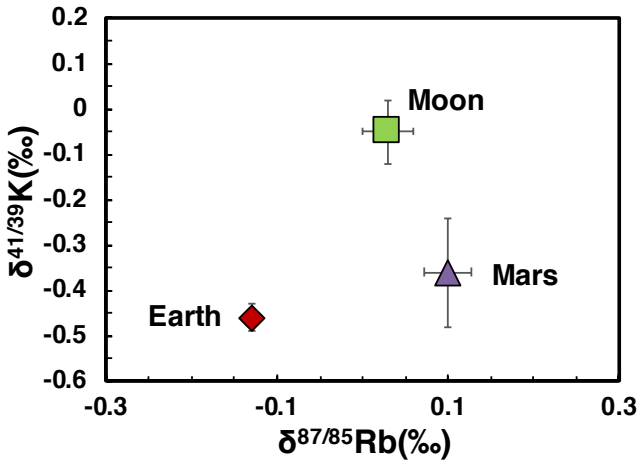

Figure 3.27 K versus Rb isotopic compositions of bulk Earth, Moon and Mars. The K isotopic compositions are from Wang and Jacobsen (2016) and Tian et al. (2018).

The Rb isotope fractionation between vapor and residue during vacuum evaporation (kinetic isotope fractionation) is -10.1 ‰ (Sect. 3.3.3). The fractionation factors calculated based the Rb isotopic compositions of martian building blocks (–0.033 ‰ if H chondrite composition is assumed to be +0.05 ‰ (the isotopic composition of Queen's Mercy; H6) for δ^{87}Rb and –0.7 ‰ if the composition is –1 ‰ (the isotopic composition of Kesen; H4)) fall in between the theoretical equilibrium and kinetic fractionation factors. The calculated –0.033 ‰ fractionation factor is more consistent with equilibrium isotope fractionation between the vapor and the residue during evaporation. The –0.7 ‰ fractionation factor however, would need an evaporation into a medium

that is not saturated. It is difficult to know which fractionation factor (–0.033 versus –0.7 ‰) is more relevant to martian volatile depletion and whether the evaporation occurred under equilibrium or kinetic conditions. The K isotopic compositions of ordinary chondrites also show significant variations (Ku and Jacobsen, 2019), and further work measuring Rb and K isotopic compositions on the same samples with large sample masses might be helpful to enlighten the reason behind the unusually large Rb and K isotopic variations of ordinary chondrites and to obtain the bulk composition of the martian building blocks.

Although evaporation may explain the volatile depletion and Rb isotope fractionation of the Mars, under what conditions could the Mars have lost its volatiles remain unclear. It is very unlikely to lose vapor from fully grown planetary bodies because of their strong gravity. Volatile loss may occur during their accretion when planetesimals colliding with each other, and some melt production and/or impact vaporization could be expected at the stage (Young et al., 2019). Large impacts such as the Moon forming-giant impact can cause large scale melting and vaporization but for smaller objects like Mars, impact vaporization is likely not significant. To first order, impact melting and vaporization is controlled by the normal component of the impact velocity (Pierazzo and Melosh, 2000). Dauphas et al. (2015) calculated the vaporized fraction of a planetary body during its accretion as a function of mass. The effect of short-lived heat-producing ^{26}Al on the impact vaporization was accounted for by assuming that the impacts involved molten rather than solid bodies. For a Mars-sized body (~0.1 Earth mass), due to the low escape/impact velocity, the vaporized fraction through the growing of Mars is negligible. However, higher fractions of vaporization can result from higher impact velocities (Hin et al., 2017) which may happen as a result of the Grand Tack movement of Jupiter and Saturn.

Another possibility is that volatile loss can happen to the ^{26}Al-bearing planetesimals during their melting. Young et al. (2019) studied the transient "magma ocean" on planetesimals produced by ^{26}Al heating. A magma ocean produces steady-state rock vapor within hours, balanced by magma evaporation and atmospheric escape, and equilibrium fractionation between vapor and melt is expected. For planetary bodies with mass smaller than 10^{22} kg (~1/50 Mars mass), hydrodynamic escape would occur which does not fractionate much the isotopic composition of the atmosphere. For bigger bodies, however, magma evaporation would be balanced by Jeans escape and isotopic composition of the atmosphere and the melt could be changed (Young et al., 2019). Therefore, a vapor produced by a melt and balanced by Jeans escape at the exobase would be needed to produce heavy Rb and K isotopic compositions of the martian precursors. This could happen to the large planetesimals with sufficient mass forming the Mars. Note that a melt formed from the transient "magma ocean" on planetesimals would always be in near-equilibrium isotope fractionation with the atmosphere (Young et al., 2009). In this case, the calculated –0.033 ‰ Rayleigh fractionation factor for martian volatile loss based on the isotopic composition of Queen's Mercy (H6) might be more likely compared with the –0.7 ‰ fractionation factor based on Kesen (H4), although Kesen (H4) is less metamorphosed than Queen's Mercy (H6).

In summary, the H chondrites as the most important building blocks of Mars have Rb isotopic compositions varying significantly from –1 to +0.05 ‰, making it difficult to estimate accurately the original martian composition before volatile loss. An original composition similar to that of Queen's Mercy (H6), which has δ^{87}Rb of +0.05 ‰, may be more reasonable than the very light Rb isotopic composition (Kesen (H4), which is –1 ‰ for δ^{87}Rb), as the former gives a fractionation factor of –0.033 ‰ between vapor and melt which is more or less consistent with the

calculated equilibrium fractionation factor between vapor and Rb-feldspar using ab-initio calculations.

3.4.2 Rubidium isotopic compositions of chondrites

The Rb isotopic compositions of chondritic samples span a wider range than the variation among Earth, Moon and Mars samples. Among chondrites, carbonaceous chondrites show less variable δ^{87}Rb values, from +0.03 to +0.2 ‰. Enstatite chondrites show larger variation of –0.24 to +0.3 ‰. In contrast, ordinary chondrites show significant variation of Rb isotopic compositions from –1 to +0.2 ‰.

3.4.2.1 Enstatite chondrites

High precision measurements of isotopic compositions of refractory elements show that enstatite chondrites have indistinguishable isotopic composition from the Earth (*e.g.*, Qin et al., 2010; Young et al., 2016; Zhang et al., 2014), meaning that enstatite chondrites could have been

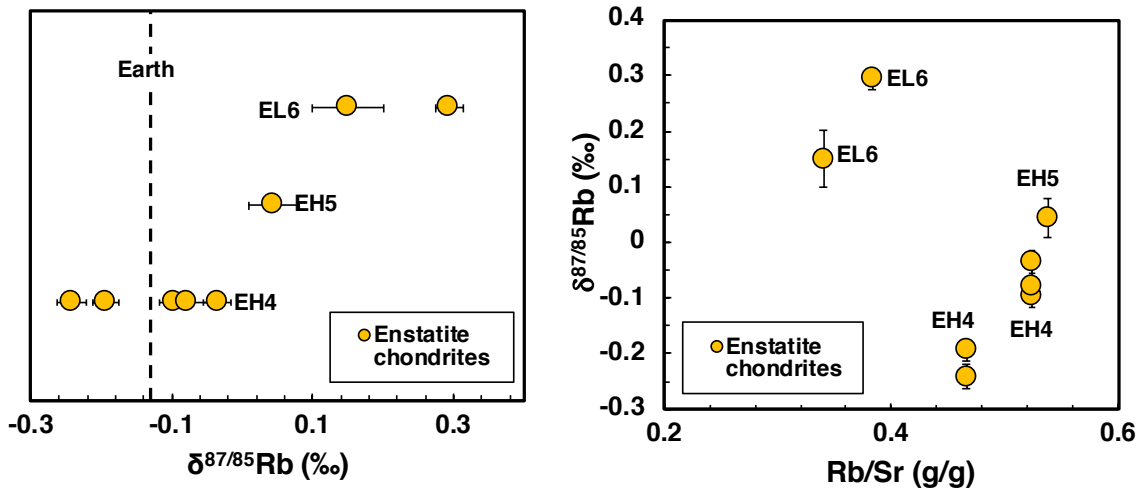

Figure 3.28 Rb isotopic compositions of enstatite chondrites (left panel) and Rb isotopic compositions plotted versus Rb/Sr ratios (right panel). The average δ^{87}Rb values of the EH4 enstatite chondrites is similar to that of the Earth. The EH5 and EH6 chondrites are heavier.

the major building blocks of the Earth. Dauphas (2017) investigated the accretion history of the Earth by looking at isotopic compositions of various elements that record different stages of Earth's accretion and found that enstatite chondrites always represented a large fraction of the materials accreted by the Earth through the Earth's history. Enstatite chondrites represent ~50 % of the material accreted to the Earth during the first 0–60 % mass accretion of the Earth, and the rest of Earth's accretion (60–100 % mass accretion) are almost 100 % enstatite chondrites (Dauphas, 2017).

In terms of moderately volatile elements, zinc isotopic compositions of low metamorphic grade enstatite chondrites (EL3, EH3, EH4, EH5) are very similar to that of the Earth, while EL6 chondrites showed significantly heavy Zn isotopic composition (Moynier et al., 2011). Potassium isotopic compositions of various types of enstatite chondrites show an average of terrestrial value, although big variations have been observed among enstatite chondrites (Zhao et al., 2019). Five enstatite samples were measured in this study for their Rb isotopic compositions including two aliquots of Abee (EH4), three aliquots of Indarch (EH4), Saint-Sauveur (EH5), Hvittis (EL6) and Pillistfer (EL6). The average Rb isotopic compositions of EH4 chondrites is similar to that of the Earth (Fig. 3.29). The EH5 and EL6 chondrites are progressively heavier. This might be suggesting that metamorphism has an effect on the Rb isotopic composition of the enstatite chondrites, but EH chondrites and EL chondrites could be from different parent bodies and could not be compared directly with each other.

It has been known that EH chondrites have more volatiles compared with EL chondrites (*e.g.*, Wasson and Kallemeyn, 1988). On the plot where Rb isotopic compositions are plotted versus Rb/Sr ratios (Fig. 3.29), EH and EL chondrites show two different groups, with EH chondrites containing more Rb. Within EH chondrites, there seems to be a trend between Rb

isotopic compositions and Rb/Sr ratios. More samples need to be measured to confirm the trend, but if any, the potential trend seems to be opposite to what one would expect from Rb volatile loss through evaporation.

The best estimate of the Rb isotopic composition of bulk enstatite chondrites would be to do an average over less metamorphosed EH4 chondrites. The average value is –0.13 ‰ ± 0.17 ‰ (the error is the 2 standard deviation of the measured δ^{87}Rb values of EH4 chondrites), which is the same as the estimated bulk Earth composition (–0.13 ‰ ± 0.03 ‰), confirming that Earth is mainly accreted from materials with enstatite isotopic compositions.

3.4.2.2 Carbonaceous chondrites

The Rb isotopic variation of carbonaceous chondrites is small compared with ordinary chondrites and enstatite chondrites, ranging from +0.03 to +0.2 ‰. The range is a factor of two smaller than that reported in Pringle and Moynier (2017), which is –0.2 to +0.2 ‰ (all the chondrites discussed are meteorite falls, as the meteorite finds can have very fractionated Rb isotopic compositions resulted from weathering). Whether this is due to the sample heterogeneity of carbonaceous chondrites is not known. The average (± 2 standard deviation) of all the carbonaceous chondrites in this study is +0.10 ± 0.09 ‰, slightly higher than the average value of +0.02 ± 0.25 ‰ reported in Pringle and Moynier (2017).

The Rb isotopic averages for CI chondrites (samples in this study are Orgueil and Ivuna), CM chondrites (Murchison and Mighei), CV chondrites (Allende and Vigarano) and CO chondrites (Lance and Ornans) are 0.16 ± 0.07 ‰, 0.12 ± 0.02 ‰, 0.07 ± 0.04 ‰ and 0.07 ± 0.1 ‰ respectively. Pringle and Moynier (2017) suggested a relationship between δ^{87}Rb values and the Rb/Sr ratios among carbonaceous chondrites. They claimed that there was a trend toward light Rb isotopes when Rb/Sr ratio decreases, suggesting a mixing between a volatile-rich isotopically-

heavy reservoir with a volatile-depleted isotopically-light reservoir rather than volatile loss due to evaporation. The trend is less clear with our data when plotting δ^{87}Rb values versus the Rb/Sr ratios of individual chondrites (Fig. 3.30), but is better when plotting Rb isotopic compositions versus the average Rb/Sr ratio of each group. However, the slope of the trend is much shallower than that in Pringle and Moynier (2017) due to the smaller range of Rb isotopic variations in our samples. More measurements are needed to tell which slope is more statistically significant.

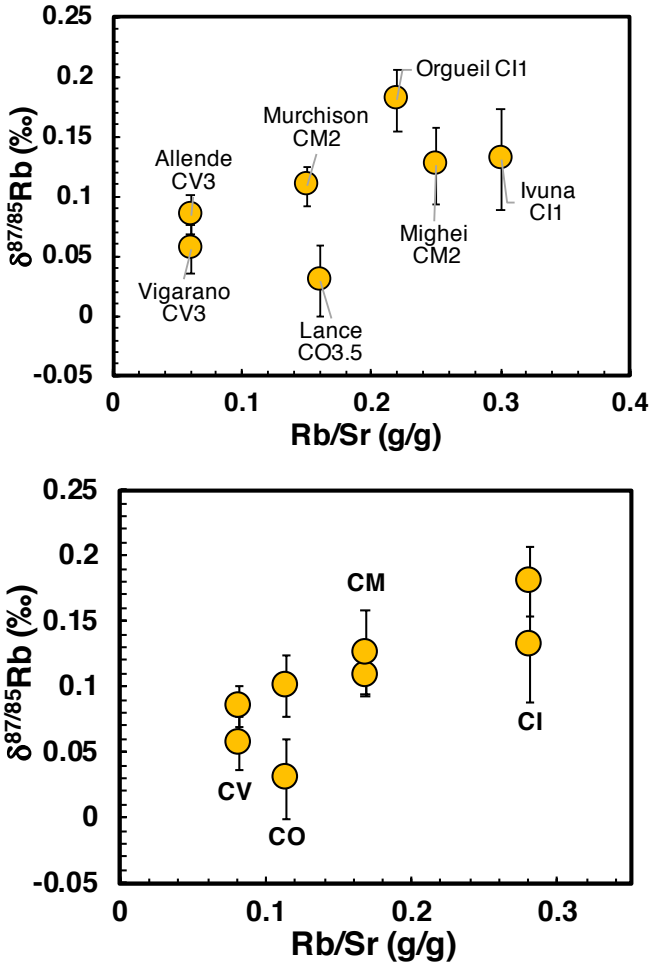

Figure 3.29 Top panel: Rb isotopic compositions of carbonaceous chondrites versus Rb/Sr ratios (g/g) for individual chondrites. Rb/Sr ratios are from MetBase. Ornans is not plotted here due to the unknown Rb/Sr ratio. Bottom panel: Rb isotopic compositions versus average Rb/Sr ratio of each chondritic group. The average Rb/Sr ratio of each group is from Wasson and Kallemeyn (1988).

The positive trend between Rb isotopic compositions and Rb/Sr ratios is not one would expect for volatile loss through evaporation, as during evaporation samples with more Rb depletion would have heavier δ^{87}Rb values. No K isotopic trend has been reported for carbonaceous chondrites. Another isotopic system that has been measured, which might be comparable to Rb in the sense that it is also volatile is copper. A positive trend between Cu isotopic compositions and volatile/refractory elemental ratios has been observed for carbonaceous chondrites (Luck et al., 2003). Because Cu isotopic compositions also seemed to correlate with oxygen isotopic anomalies in these samples, the trend of Cu isotopes versus volatile/refractory ratios was attributed to a mixing between a CI-like reservoir (not depleted) and a refractory reservoir like CAIs which has nucleosynthetic Cu anomalies. They further claimed that volatile Cu was preserved in the refractory reservoir initially as ^{63}Ni which was more refractory.

Rb has only two isotopes, like Cu, and nucleosynthetic anomalies cannot be distinguished from mass-dependent isotope fractionation. A partial condensation process may explain the trend between Rb isotopic compositions versus Rb/Sr ratios, but cannot explain that different carbonaceous chondrite types have different refractory isotopic anomalies (Warren, 2011). CAIs showing nucleosynthetic isotopic anomalies need to be involved to explain the isotopic anomalies in carbonaceous chondrites. However, Rb is a volatile element and if the Rb isotopic composition of carbonaceous chondrites reflect nucleosynthetic anomalies, the question arises regarding how Rb could be condensed within refractory CAIs. One possibility is that the reservoir that contributes to the isotopic anomalies of carbonaceous chondrites was isotopically similar to CAIs but with volatiles condensed to some extent. The reservoir, which mixed later with a nondepleted CI-like reservoir to form carbonaceous chondrites, has low Rb/Sr ratio and light Rb isotopic composition due to partial condensation of Rb.

3.4.2.3 Ordinary chondrites

Ordinary chondrites are not depleted in Rb compared with CI chondrites. The average Rb/Sr ratios of H, L and LL groups are similar, ~0.28-0.29 (Wasson and Kallemeyn, 1988), and are similar to the ratio of CI chondrites (0.28). The most pristine sample among the measured ordinary chondrites in this study is Krymka, which is a LL3.2 and has a δ^{87}Rb value of –0.41 ± 0.04 ‰. The value is comparable to the value reported by Pringle and Moynier (2017), which is –0.37 ± 0.02 ‰. Krymka is the only ordinary chondrite they measured, and they claimed that the light Rb isotopic composition reflected either metamorphism or the bulk Rb isotopic composition of ordinary chondrites. The Rb samples measure here include two H chondrites, two L chondrites and three LL chondrites. Their Rb isotopic compositions show quite large variation, from –1 to +0.2 ‰ (Fig. 3.31). Large K isotopic variation among ordinary chondrites has also been observed (Ku and Jacobsen, 2019). Whether Krymka could represent bulk Rb isotopic composition of ordinary chondrites is not clear. No clear trend between Rb isotopic compositions and the metamorphic grades is observed for the three LL chondrites, suggesting that metamorphism is not likely to be responsible for the large Rb isotopic variation.

It has been suggested that the building blocks of Mars consisted of ~85 % H ordinary chondrites based on oxygen isotopes (Lodders and Fegley, 1997). It is therefore maybe reasonable to use the Rb isotopic composition of bulk Mars to estimate that of ordinary chondrites. One complexity is that Rb is a volatile element, and volatile loss during Mars formation may have modified the Rb isotopic composition of the Mars. As discussed in Sect. 3.4.1, it is very difficult for Mars to lose volatiles during its formation and the isotopic modification of Mars due to volatile loss should not be significant. Mars is even less volatile depleted compared with the Earth (Fig. 3.1), maybe due to its smaller size comparted with the Earth (*e.g.*, Dauphas et al., 2015). The bulk

Earth has bulk Rb isotopic composition the same as that of the enstatite chondrites (Sect. 3.4.2.1) which are its main building blocks. Therefore, the bulk Rb isotopic composition of the Mars (+0.1 ‰) most likely reflects or at least should be very close to the bulk Rb isotopic composition of H ordinary chondrites. Given that the oxygen isotopic difference between H, L and LL chondrites

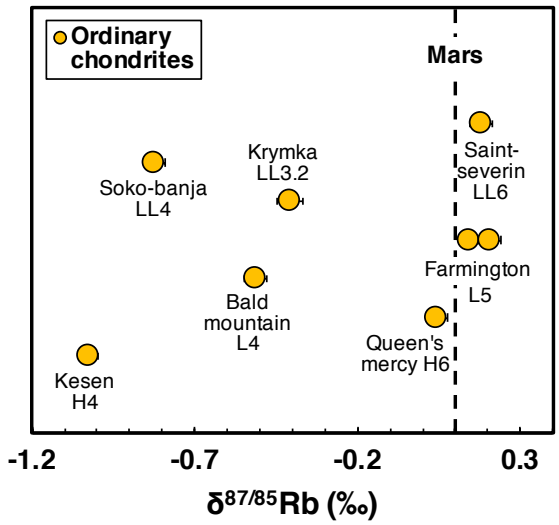

Figure 3.30 Rb isotopic compositions of ordinary chondrites. The bulk Mars is also plotted for reference. Mars is thought to form from mainly H chondrite-like composition according to their oxygen isotopes (Lodders and Fegley, 1997).

are small, it is may be reasonable to suspect that bulk ordinary chondrites should have a Rb isotopic composition near +0.1 ‰.

Interestingly, the measured ordinary chondrites which have Rb isotopic compositions similar to bulk Mars are the three most metamorphosed samples (H6, L5 and LL6). In contrast, the less metamorphosed samples show lighter Rb isotopic compositions (Fig. 3.31). One possibility is that the less metamorphosed samples are isotopically heterogeneous (*e.g.*, due to the heterogeneous compositions of chondrules in them) but metamorphism led to diffusion and homogenization of Rb. This could be tested by measuring samples with large mass. The current

mass digested for each sample is only 100 mg, which is usually from a homogenized powder of ~100–300 mg.

Large K isotopic variation has been observed for chondrules in ordinary chondrite Bishunpur (LL3.1) and Semarkona (LL3.0). Eleven chondrules in Bishunpur have $\delta^{41}K$ values ranging from –15.5 to +12 ‰ (Alexander et al., 2000). Twenty eight Semarkona chondrules show a range of –9.5 to +17.8 ‰ for $\delta^{41}K$ (Grossman, 2005). Scale to Rb, the variation of $\delta^{87}Rb$ values would be smaller by a factor of ~2 ($[(39/41)^{0.43}–1]/[(85/87)^{0.44}–1]$), assuming kinetic isotope fractionation because the K isotopic variation could be relevant to evaporative volatile loss during chondrule formation. Here we use a Mathematica model to estimate how the Rb isotopic composition variation of chondrules would affect the measured isotopic composition of ordinary chondrites. Clearly, the higher the sampled mass, the more likely that the sampled portion is representative of bulk composition. We therefore calculate the Rb isotopic composition variation versus the sampled mass.

In the model (See Appendix for a computer program), the isotopic compositions of 28 chondrules from Bishunpur and Semarkona are used to represent the possible isotopic compositions. The isotopic compositions are compared to the bulk composition and the isotopic differences are given to the chondrules (*i.e.*, the bulk is at zero). Each chondrule isotopic composition has its fixed Rb/Al ratio, calculated by assuming that $(Rb/Al)_{chondrule}/(Rb/Al)_{bulk} = (K/Al)_{chondrule}/(K/Al)_{bulk}$ ratio because K/Al ratios of chondrules were reported together with their K isotopic compositions. The size (mass is calculated by assuming a constant density) distribution of chondrules is assumed to follow that was reported by (Nelson and Rubin, 2002). Matrix is assumed to have bulk Rb isotopic composition and bulk Rb/Al ratio.

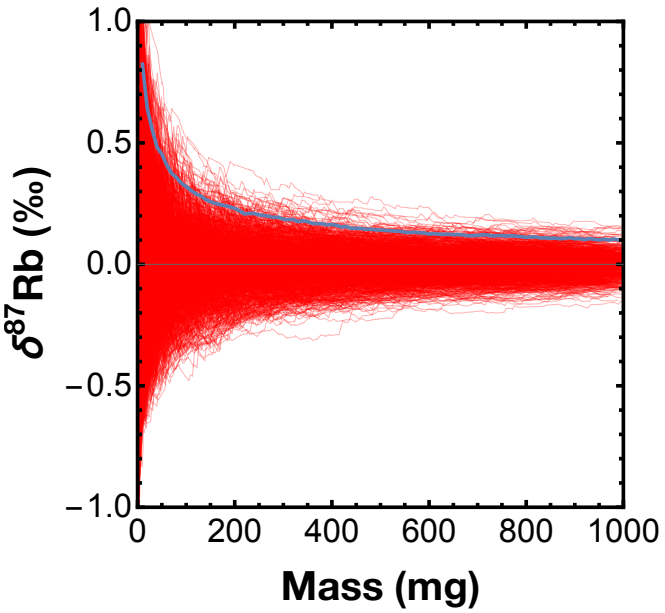

Figure 3.31 Modeled Rb isotopic composition deviation from bulk versus the sample mass (red lines). The 2 standard deviations of isotopic composition deviation at each mass is shown as the blue curve.

The program picks chondrules randomly, and each time a piece of matrix having a mass of 30 % the picked mass (chondrule + matrix) is also picked, until the total mass reaches a desired total mass. The isotopic composition evolution is recorded as the sampled mass grows. The process is repeated for 1000 times, and all the 1000 paths are plotted versus sampled mass on the same plot to see the isotopic composition deviation at a certain mass (Fig. 3.32). The result showed that significant isotopic variation could be expected for low sample masses. Usually, a Rb isotopic analysis digests ~100 mg sample powder, but a sample powder is usually prepared from a piece of rock with a larger mass ~100 mg to 300 mg. For a sample mass of 200 mg, Rb isotope could vary from bulk composition by ± 0.3 ‰ due to the nugget effect of chondrules. The large Rb isotopic variation in ordinary chondrites from –1 to +0.2 ‰ may not be entirely due to the nugget effect of chondrules, but the variation caused by nugget effect is quite large and further Rb isotope measurements on large sample masses are needed.

3.5 Conclusions

In this chapter, a new Rb isotope measurement method was developed and high-precision Rb isotopic analyses were performed for various planetary bodies, including the Earth-Moon system, Mars and chondrites. The high precision Rb isotopic analyses allowed us to precisely determine the Rb isotopic compositions of the bulk Earth and Moon (Fig. 3.22). This was done by plotting the Rb isotopic compositions (δ^{87}Rb values, relative to NIST SRM984) of samples versus their La/U ratios. Trends were observed in the plots, which likely reflected magmatic differentiation. Then bulk Rb isotopic compositions were determined by looking at the δ^{87}Rb values at CI chondritic La/U ratio. Bulk Earth and Moon were estimated to be –0.13 ± 0.01 ‰ and +0.03 ± 0.03 ‰ respectively.

The Rb isotopic compositions of the Earth and the Moon were used to understand why the Moon is depleted in moderately volatile elements compared to the Earth. The Moon is isotopically heavier than the Earth by +0.16 ± 0.04 ‰. Using literature data, the K isotopic difference between the Moon and the Earth was estimated, and the Moon is isotopically heavier than the Earth by 0.41 ± 0.07 ‰. The Rb and K isotopic fractionations between the Moon and the Earth are consistent with Rb and K evaporation into a medium that was ~99% saturated. Such saturation could be achieved by MRI-powered viscous drainage of vapor onto Earth in a partially vaporized protolunar disk.

The bulk Rb isotopic composition of Mars was estimated using the same way as that used for estimating bulk Earth and Moon. The δ^{87}Rb value is +0.10 ± 0.03 ‰. The isotopic composition and the volatile depletion of Mars could be explained by evaporative volatile loss from the precursor materials under near-equilibrium conditions.

A positive correlation between Rb isotopic compositions of different types of carbonaceous chondrites and their Rb/Sr ratios was observed. The trend is opposite to what would be expected for Rb loss by evaporation. It is likely that the trend was produced by mixing between a CI-like nondepleted component with a heavy Rb isotopic composition and a high Rb/Sr ratio, and a reservoir similar to the CAI reservoir but with volatile elements such as Rb partially condensed, which had a light Rb isotopic composition and a low Rb/Sr ratio.

EH4 enstatite chondrites have on average Rb isotopic composition the same as the bulk Earth, further confirming that enstatite chondrites and Earth are likely from the same isotopic reservoir. However, the EH5 and EL6 chondrites are shifted towards heavier Rb isotopic compositions, and the reason is still not clear.

Ordinary chondrites show the largest Rb isotopic variation from –1 to +0.2 ‰. Literature data suggested that chondrules in ordinary chondrites had large K isotopic variations. Large Rb isotopic variation among chondrules is therefore expected. Modeling with the K isotopic variation of chondrules showed that Rb isotopic variation in chondrules could not explain the entire isotopic variation in ordinary chondrites. Further studies on larger mass ordinary chondrite samples are needed to investigate the reason for the large Rb isotopic variation.

References

Akram, W., Schönbächler, M., 2016. Zirconium isotope constraints on the composition of Theia and current Moon-forming theories. Earth and Planetary Science Letters 449, 302–310.

Albarède, F., Albalat, E., Lee, C.T.A., 2015. An intrinsic volatility scale relevant to the Earth and Moon and the status of water in the Moon. Meteoritics & Planetary Science 50, 568–577.

Alexander, C.O., Grossman, J.N., Wang, J., Zanda, B., Bourot-Denise, M., Hewins, R.H., 2000. The lack of potassium-isotopic fractionation in Bishunpur chondrules. Meteoritics & Planetary Science 35, 859–868.

Anders, E., Ebihara, M., 1982. Solar-system abundances of the elements. Geochimica et Cosmochimica Acta 46, 2363–2380.

Brewer, K.N., Todd, T.A., Wood, D.J., Tullock, P.A., Sebesta, F., John, J., Motl, A., 1999. AMP-PAN column tests for the removal of ^{137}Cs from actual and simulated INEEL high-activity wastes. Czechoslovak Journal of Physics 49, 959–964.

Cameron, A.G., Ward, W.R., 1976. The origin of the Moon. Lunar and Planetary Science 7, 120.

Canup, R.M., 2012. Forming a Moon with an Earth-like composition via a giant impact. Science 338, 1052–1055.

Canup, R.M., 2004. Dynamics of lunar formation. Annual Review of Astronomy and Astrophysics 42, 441–475.

Canup, R.M., Asphaug, E., 2001. Origin of the Moon in a giant impact near the end of the Earth's formation. Nature 412, 708–712.

Canup, R.M., Visscher, C., Salmon, J., Fegley, B., Jr, 2015. Lunar volatile depletion due to incomplete accretion within an impact-generated disk. Nature Geoscience 8, 918–921.

Carballido, A., Desch, S.J., Taylor, G.J., 2016. Magneto-rotational instability in the protolunar disk. Icarus 268, 89–101.

Charnoz, S., Michaut, C., 2015. Evolution of the protolunar disk: Dynamics, cooling timescale and implantation of volatiles onto the Earth. Icarus 260, 440–463.

Clayton, R.N., 1993. Oxygen isotopes in meteorites. Annual Review of Earth and Planetary Sciences 21, 115–149.

Clayton, R.N., Mayeda, T.K., 1996. Oxygen isotope studies of achondrites. Geochimica et Cosmochimica Acta 60, 1999–2017.

Coetzee, C.J., 1972. The separation of a sodium-rubidium mixture on an ion-exchanger. A laboratory experiment. Journal of Chemical Education 49, 33.

Craig, H., Gordon, L.I., 1965. Deuterium and oxygen 18 variations in the ocean and the marine atmosphere. Pisa, Consiglio nazionale delle richerche, Laboratorio de geologia nucleare.

Cuk, M., Stewart, S.T., 2012. Making the Moon from a fast-spinning Earth: a giant impact followed by resonant despinning. Science 338, 1047–1052.

Dauphas, N., 2017. The isotopic nature of the Earth's accreting material through time. Nature 541, 521.

Dauphas, N., Burkhardt, C., Warren, P.H., Teng, F.-Z., 2014. Geochemical arguments for an Earth-like Moon-forming impactor. Philosophical Transactions of the Royal Society A: Mathematical, Physical and Engineering Sciences 372, 20130244.

Dauphas, N., Meheut, M., Blanchard, M., Zeng, H., Galli, G., Canup, R.N., Visscher, C., Nie, N., 2018. Can Lunar Formation Theories Be Tested with K Isotopes? Lunar and Planetary Science 49, #2481.

Dauphas, N., Poitrasson, F., Burkhardt, C., Kobayashi, H., Kurosawa, K., 2015. Planetary and meteoritic Mg/Si and δ^{30}Si variations inherited from solar nebula chemistry. Earth and Planetary Science Letters 427, 236–248.

Dauphas, N., Pourmand, A., Teng, F.-Z., 2009. Routine isotopic analysis of iron by HR-MC-ICPMS: How precise and how accurate? Chemical Geology 267, 175–184.

Dauphas, N., Reisberg, L., Marty, B., 2001. Solvent extraction, ion chromatography, and mass spectrometry of molybdenum isotopes. Analytical Chemistry 73, 2613–2616.

Dauphas, N., Roskosz, M., Alp, E.E., Golden, D.C., Sio, C.K., Tissot, F., Hu, M.Y., Zhao, J., Gao, L., Morris, R.V., 2012. A general moment NRIXS approach to the determination of equilibrium Fe isotopic fractionation factors: application to goethite and jarosite. Geochimica et Cosmochimica Acta 94, 254–275.

Davis, A.M., 2006. Volatile evolution and loss. In Meteorites and the Early Solar System II (eds. Lauretta D. S., McSween H.Y.Jr.), University of Arizona Press, Tucson, 295–307.

Day, J.M., Moynier, F., 2014. Evaporative fractionation of volatile stable isotopes and their bearing on the origin of the Moon. Philosophical Transactions of the Royal Society A: Mathematical, Physical and Engineering Sciences 372, 20130259.

Dybczyński, R., 1972. Effect of resin cross-linking on the cation-exchange separation of alkali and alkaline earth metals on sulphonic cation exchangers. Journal of Chromatography A 72, 507–522.

Elkins-Tanton, L.T., Burgess, S., Yin, Q.-Z., 2011. The lunar magma ocean: Reconciling the solidification process with lunar petrology and geochronology. Earth and Planetary Science Letters 304, 326–336.

Faris, J.P., 1960. Adsorption of elements from hydrofluoric acid by anion exchange. Analytical Chemistry 32, 520–522.

Fedkin, A.V., Grossman, L., Ghiorso, M.S., 2006. Vapor pressures and evaporation coefficients for melts of ferromagnesian chondrule-like compositions. Geochimica et Cosmochimica Acta 70, 206–223.

Gale, A., Dalton, C.A., Langmuir, C.H., Su, Y., Schilling, J.G., 2013. The mean composition of ocean ridge basalts. Geochemistry, Geophysics, Geosystems 14, 489–518.

Gammie, C.F., Liao, W.-T., Ricker, P.M., 2016. A hot big bang theory: Magnetic fields and the early evolution of the protolunar disk. Astrophysical Journal 828, #58.

Govindaraju, K., 1994. Compilation of working values and sample description for 383 geostandards. Geostand Geoanal Res 18: 1–158.

Grossman, J.N., 2005. Alkali elemental and potassium isotopic compositions of Semarkona chondrules. Meteoritics & Planetary Science 40, 541–556.

Hartmann, W.K., Davis, D.R., 1975. Satellite-sized planetesimals and lunar origin. Icarus 24, 504–515.

Herzog, G.F., Moynier, F., Albarède, F., Berezhnoy, A.A., 2009. Isotopic and elemental abundances of copper and zinc in lunar samples, Zagami, Pele's hairs, and a terrestrial basalt. Geochimica et Cosmochimica Acta 73, 5884–5904.

Hin, R.C., Coath, C.D., Carter, P.J., Nimmo, F., Lai, Y.-J., Strandmann, von, P.A.P., Willbold, M., Leinhardt, Z.M., Walter, M.J., Elliott, T., 2017. Magnesium isotope evidence that accretional vapour loss shapes planetary compositions. Nature 549, 511.

Hosono, N., Karato, S.-I., Makino, J., Saitoh, T.R., 2019. Terrestrial magma ocean origin of the Moon. Nature Geoscience 12, 418–423.

Ireland, T.J., Tissot, F., Yokochi, R., Dauphas, N., 2013. Teflon-HPLC: A novel chromatographic system for application to isotope geochemistry and other industries. Chemical Geology 357, 203–214.

Kato, C., Moynier, F., Valdes, M.C., Dhaliwal, J.K., Day, J.M., 2015. Extensive volatile loss during formation and differentiation of the Moon. Nature Communications 6, 7617.

Ku, Y., Jacobsen, S.B., 2019. Potassium isotope variations in chondrites. Lunar and Planetary Science 50, #1675.

Li, Y., Wang, W., Huang, S., Wang, K., Wu, Z., 2019. First-principles investigation of the concentration effect on equilibrium fractionation of K isotopes in feldspars. Geochimica et Cosmochimica Acta 245, 374–384.

Lock, S.J., Stewart, S.T., Petaev, M.I., Leinhardt, Z., Mace, M.T., Jacobsen, S.B., Cuk, M., 2018. The origin of the Moon within a terrestrial synestia. Journal of Geophysical Research: Planets 123, 910–951.

Lodders, K., 2003. Solar system abundances and condensation temperatures of the elements. Astrophysical Journal 591, 1220.

Lodders, K., Fegley, B., Jr, 1997. An oxygen isotope model for the composition of Mars. Icarus 126, 373–394.

Luck, J.M., Othman, D.B., Barrat, J.A., Albarède, F., 2003. Coupled ^{63}Cu and ^{16}O excesses in chondrites. Geochimica et Cosmochimica Acta 67, 143–151.

Lugmair, G.W., Shukolyukov, A., 1998. Early solar system timescales according to ^{53}Mn-^{53}Cr systematics. Geochimica et Cosmochimica Acta 62, 2863–2886.

Martin, A., Synge, R.M., 1941. A new form of chromatogram employing two liquid phases: A theory of chromatography. Biochemical Journal 35, 1358–1368.

McDonough, W.F., Sun, S.S., 1995. The composition of the Earth. Chemical Geology 120, 223–253.

Moynier, F., Albarède, F., Herzog, G.F., 2006. Isotopic composition of zinc, copper, and iron in lunar samples. Geochimica et Cosmochimica Acta 70, 6103–6117.

Moynier, F., Paniello, R.C., Gounelle, M., Albarède, F., Beck, P., Podosek, F., Zanda, B., 2011. Nature of volatile depletion and genetic relationships in enstatite chondrites and aubrites inferred from Zn isotopes. Geochimica et Cosmochimica Acta 75, 297–307.

Murthy, V.R., Geology, W.G.C., 1970, 1970. K Rb fractionation by plagioclase feldspars. Chemical Geology 6, 265–271.

Nelson, F., Rush, R.M., Kraus, K.A., 1960. Anion-exchange studies. XXVII. Absorbability of a number of elements in HCl-HF solutions. Journal of the American Chemical Society 82, 339–348.

Nelson, V.E., Rubin, A.E., 2002. Size-frequency distributions of chondrules and chondrule fragments in LL3 chondrites: Implications for parent-body fragmentation of chondrules. Meteoritics & Planetary Science 37, 1361–1376.

O'neill, H.S.C., 1991. The origin of the Moon and the early history of the Earth—A chemical model. Part 1: The Moon. Geochimica et Cosmochimica Acta 55, 1135–1157.

Pahlevan, K., Stevenson, D.J., 2007. Equilibration in the aftermath of the lunar-forming giant impact. Earth and Planetary Science Letters 262, 438–449.

Paniello, R.C., Day, J.M.D., Moynier, F., 2012. Zinc isotopic evidence for the origin of the Moon. Nature 490, 376–379.

Philip Horwitz, E., Chiarizia, R., Dietz, M.L., 1992. A novel strontium-selective extraction chromatographic resin. Solvent Extraction and Ion Exchange 10, 313–336.

Pierazzo, E., Melosh, H.J., 2000. Melt production in oblique impacts. Icarus 145, 252–261.

Prettyman, T.H., Hagerty, J.J., Elphic, R.C., Feldman, W.C., Lawrence, D.J., McKinney, G.W., Vaniman, D.T., 2006. Elemental composition of the lunar surface: Analysis of gamma ray spectroscopy data from Lunar Prospector. Journal of Geophysical Research 111(E12).

Pringle, E.A., Moynier, F., 2017. Rubidium isotopic composition of the Earth, meteorites, and the Moon: Evidence for the origin of volatile loss during planetary accretion. Earth and Planetary Science Letters 473, 62–70.

Qin, L., Alexander, C.M.O., Carlson, R.W., Horan, M.F., Yokoyama, T., 2010. Contributors to chromium isotope variation of meteorites. Geochimica et Cosmochimica Acta 74, 1122–1145.

Reufer, A., Meier, M.M., Benz, W., Wieler, R., 2012. A hit-and-run giant impact scenario. Icarus 221, 296–299.

Richter, F.M., 2004. Timescales determining the degree of kinetic isotope fractionation by evaporation and condensation. Geochimica et Cosmochimica Acta 68, 4971–4992.

Richter, F.M., Davis, A.M., Ebel, D.S., Hashimoto, A., 2002. Elemental and isotopic fractionation of Type B calcium-, aluminum-rich inclusions: experiments, theoretical considerations, and constraints on their thermal evolution. Geochimica et Cosmochimica Acta 66, 521–540.

Richter, F.M., Janney, P.E., Mendybaev, R.A., Davis, A.M., Wadhwa, M., 2007. Elemental and isotopic fractionation of Type B CAI-like liquids by evaporation. Geochimica et Cosmochimica Acta 71, 5544–5564.

Richter, F.M., Mendybaev, R.A., Christensen, J.N., Ebel, D., Gaffney, A., 2011. Laboratory experiments bearing on the origin and evolution of olivine-rich chondrules. Meteoritics & Planetary Science 46, 1152–1178.

Ringwood, A.E., Kesson, S.E., 1977. Basaltic magmatism and the bulk composition of the moon. The Moon 16, 425–464.

Rudge, J.F., Reynolds, B.C., Bourdon, B., 2009. The double spike toolbox. Chemical Geology 265, 420–431.

Saxena, P., Elkins-Tanton, L., Petro, N., Mandell, A., 2017. A model of the primordial lunar atmosphere. Earth and Planetary Science Letters 474, 198–205.

Sharp, Z.D., Barnes, J.D., Brearley, A.J., Chaussidon, M., Fischer, T.P., Kamenetsky, V.S., 2007. Chlorine isotope homogeneity of the mantle, crust and carbonaceous chondrites. Nature 446, 1062.

Sharp, Z.D., Shearer, C.K., McKeegan, K.D., Barnes, J.D., Wang, Y.Q., 2010. The chlorine isotope composition of the Moon and implications for an anhydrous mantle. Science 329, 1050–1053.

Smit, J.V.R., Jacobs, J.J., Robb, W., 1959a. Cation exchange properties of the ammonium heteropolyacid salts. Journal of Inorganic and Nuclear Chemistry 12, 95–103.

Smit, J.V.R., Robb, W., Jacobs, J.J., 1959b. Cation exchange on ammonium molybdophosphate—I: The alkali metals. Journal of Inorganic and Nuclear Chemistry 12, 104–112.

Smith, J.V., Anderson, A.T., Newton, R.C., Olsen, E.J., Wyllie, P.J., 1970. A petrologic model for the Moon based on petrogenesis, experimental petrology, and physical properties. The Journal of Geology 78, 381–405.

Snyder, G.A., Taylor, L.A., Neal, C.R., 1992. A chemical model for generating the sources of mare basalts: Combined equilibrium and fractional crystallization of the lunar magmasphere. Geochimica et Cosmochimica Acta 56, 3809–3823.

Strelow, F., 1960. An ion exchange selectivity scale of cations based on equilibrium distribution coefficients. Analytical Chemistry 32, 1185–1188.

Strelow, F.W., Rethemeyer, R., Bothma, C., 1965. Ion exchange selectivity scales for cations in nitric acid and sulfuric acid media with a sulfonated polystyrene resin. Analytical Chemistry 37, 106–111.

Thompson, C., Stevenson, D.J., 1988. Gravitational instability in two-phase disks and the origin of the Moon. Astrophysical Journal 333, 452–481.

Tian, Z., Chen, H., Fegley, B., Lodders, K., Barrat, J.A., Wang, K., 2018. Potassium isotope differences among chondrites, Earth, Moon, Mars, and 4-Vesta – Implication on the planet accretion mechanisms. Lunar and Planetary Science 49, #1276.

Touboul, M., Kleine, T., Bourdon, B., Palme, H., Wieler, R., 2007. Late formation and prolonged differentiation of the Moon inferred from W isotopes in lunar metals. Nature 450, 1206–1209.

Wang, K., Jacobsen, S.B., 2016. Potassium isotopic evidence for a high-energy giant impact origin of the Moon. Nature 538, 487–490.

Ward, W.R., 2012. On the vertical structure of the protolunar disk. The Astrophysical Journal 744, 140.

Warren, P.H., 2011. Stable-isotopic anomalies and the accretionary assemblage of the Earth and Mars: A subordinate role for carbonaceous chondrites. Earth and Planetary Science Letters 311, 93–100.

Wasson, J.T., Kallemeyn, G.W., 1988. Compositions of chondrites. Philosophical Transactions of the Royal Society of London. Series A, Mathematical and Physical Sciences 325, 535–544.

Wood, J.A., Dickey, J.S., Marvin, U.B., Powell, B.N., 1970. Lunar anorthosites. Science 167, 602–604.

Young, E.D., Kohl, I.E., Warren, P.H., Rubie, D.C., Jacobson, S.A., Morbidelli, A., 2016. Oxygen isotopic evidence for vigorous mixing during the Moon-forming giant impact. Science 351, 493–496.

Young, E.D., Shahar, A., Nimmo, F., Schlichting, H.E., Schauble, E.A., Tang, H., Labidi, J., 2019. Near-equilibrium isotope fractionation during planetesimal evaporation. Icarus 323, 1–15.

Yu, Y., Hewins, R.H., Alexander, C.M.O.D., Wang, J., 2003. Experimental study of evaporation and isotopic mass fractionation of potassium in silicate melts. Geochimica et Cosmochimica Acta 67, 773–786.

Zhang, J., Dauphas, N., Davis, A.M., Leya, I., Fedkin, A., 2012. The proto-Earth as a significant source of lunar material. Nature Geoscience 5, 251–255.

Zhang, J., Huang, S., Davis, A.M., Dauphas, N., Hashimoto, A., Jacobsen, S.B., 2014. Calcium and titanium isotopic fractionations during evaporation. Geochimica et Cosmochimica Acta 140, 365–380.

Zhang, Z., Ma, J., Zhang, L., Liu, Y., Wei, G., 2018. Rubidium purification via a single chemical column and its isotope measurement on geological standard materials by MC-ICP-MS. Journal of Analytical Atomic Spectrometry 33, 322–328.

Zhao, C., Bloom, H., Chen, H., Tian, Z., Koefoed, P., Lodders, K., Wang, K., 2019. Potassium isotopic compositions of enstatite chondrites and aubrites. Lunar and Planetary Science 50, #2689.

4 CONCLUSIONS AND PERSPECTIVES

Of all the methods that have been used to understand the history of the Earth and other planetary bodies, stable isotope tracers are among the most useful. The small-scale variability of isotopic ratios (usually in ‰ level) can give an effective indication of large scale geological and geochemical processes. Recent progress in multicollector inductively coupled plasma mass spectrometry (MC-ICPMS), allowing measurement of almost all the elements on the periodic table, has spurred wide interests in applying existing isotope tracers to previously unanswerable questions and in developing new isotopic tracers that have great potential. In this dissertation, I first applied Fe isotopes to trace the formation of two spectacular geological objects: banded iron formations (BIFs) which represent the oldest sedimentary rocks on Earth, and martian hematite spherules. Then, I presented a newly-developed Rb isotope tracer and applied it to the formation of the Moon and the volatile depletion history of planetary bodies.

In chapter 1, I reviewed some basic concepts in stable isotope geochemistry, including mass-dependent and mass-independent isotope fractionation, equilibrium and kinetic isotope fractionation, and mass dependent fractionation laws. I then briefly introduced some background information on stable Fe and Rb isotopic systems and some achievements and problems of using these two isotopic tracers.

Chapter 2 was dedicated to Fe isotopes. It started with the Fe isotope measurement method, including sample preparation, purification using extraction chromatography, and mass spectrometry. The remainder of the chapter utilized Fe isotopes in testing the UV photo-oxidation of Fe as a possible pathway to the precipitation of banded iron formations and martian hematite spherules. UV photo-oxidation is the only scenario that does not involve life among the three scenarios (UV photo-oxidation, O_2-mediated oxidation and anoxygenic photosynthesis) that have

been proposed to explain Fe oxidation and precipitation under a low-oxygen atmosphere on ancient Earth. In this work, Fe UV photo-oxidation experiments were conducted. The run products of these UV photo-oxidation experiments were measured for their Fe isotopic compositions and the mass dependent isotope fractionation law they followed. They showed that 1) the Fe UV photo-oxidation process is a Rayleigh distillation process, 2) the Rayleigh fractionation factor between the Fe(III) precipitate and the aqueous Fe(II) is +1.2 ± 0.1‰ for δ^{56}Fe, comparable to the isotope fractionation factors for O_2-mediated oxidation and anoxygenic photosynthesis, and consistent with the observed isotopic variation in natural BIFs, 3) the mass-dependent isotope fractionation law for UV photo-oxidation is the high-temperature equilibrium law, and IF-G (a BIF sample that was measured at the requisite high precision) follows the same law, further suggesting that precipitation of BIFs through Fe UV photo-oxidation is a viable process.

I then explored the possibility of forming martian hematite spherules via UV photo-oxidation. The quantum yield of UV photo-oxidation was estimated to be ~0.07 Fe atoms oxidized per photon absorbed based on the photo-oxidation experiments. An elaborate model using the quantum yield was developed to calculate the timescale of UV photo-oxidation on ancient Mars. In fact, photo-oxidation is quite effective (*e.g.*, it takes only ~50 years to fully oxidize the Fe in a body of water 100 meters deep), and is very likely responsible for Fe precipitation on Mars. Following this, I investigated the Fe isotopic compositions of hematite spherules and associated lithologies from Hawaii, which are a terrestrial analogue of martian hematite spherules. The study showed that compared to other weathering processes (palagonite alteration, high-T dry oxidation, steam vent alteration, and near-neutral to alkali hydrothermal alteration), acid-sulfate alteration of basaltic rocks - which is considered to have provided Fe source for the martian hematite spherules- is the one that could fractionate Fe isotopes significantly, with a fractionation factor of 0.24 ‰ for

δ^{56}Fe between the isotopically-light acid-sulfate fluid and the isotopically-heavy residue. This is the first estimate of Fe isotope fractionation during acid-sulfate alteration, and is consistent with the fact that the two hematite-rich samples showed very fractionated and different Fe isotopic compositions. The Fe isotopic compositions of the products of acid-sulfate alteration point to a complex history of hematite spherule formation. It is clear that hematite formation on Mars should also have caused large Fe isotopic variations, and Fe isotope studies on future returned martian hematite samples will provide insights into the surface processes that have shaped ancient Mars.

The focus of Chapter 3 was the development and use of a new isotopic tracer of Rb isotopes. Rb is a trace element, has geochemical behaviors similar to that of major element K, and has a great potential in tracing volatile loss processes due to the fact that it is a moderately volatile element (with a half condensation temperature of ~800 K). Due to its low abundance in rocks (the Rb/K ratio in Earth is about 1/400 by weight), and its extremely similar behaviors to K, the major challenge of Rb isotope measurement is the Rb purification method. The chapter first explained the Rb purification method that I developed over the past several years. Then the Rb isotopic data obtained by using the method on the Earth-Moon system, Mars, and chondrites were reported and discussed. The most compelling question solved in this chapter was how the Moon lost its moderately volatile elements. The Rb isotopic composition of the bulk Moon is isotopically heavier than the bulk Earth by +0.16 ± 0.04 ‰; this heavy Rb isotope-enrichment in the Moon is incompatible with the classical giant impact model or the synestia model in which the lunar volatile depletion is caused by partial condensation, as this would enrich the Moon in light Rb isotopes. The value is more consistent with a model in which the vapor phase of a two-phase proto-lunar disk (a magma layer at the midplane overlain by a vapor layer) is caught in magnetorotational instability, becomes highly viscous, and is drained to the Earth and then replenished by magma

evaporation. This model could quantitatively explain the isotope fractionation of Rb and other moderately volatile elements (K, Zn, etc.) in the Moon relative to the Earth.

The Rb isotopic compositions of the Mars and chondrites show some interesting, yet perplexing, results: 1) the bulk Mars is heavier than the Earth and the Moon, though it is less depleted in volatiles, 2) the less metamorphosed enstatite chondrites (EH4) have average Rb isotopic composition similar to the Earth, confirming that enstatite chondrites are the major isotopic building blocks of the Earth. More metamorphosed enstatite chondrites, however, are shifted to heavier values, 3) there is a positive relationship between Rb isotopic compositions versus the Rb/Sr ratios of carbonaceous chondrite groups, which is the opposite of what would be expected for evaporative volatile loss, and 4) there is a very large Rb isotopic variation (from –1 to +0.2 ‰) among ordinary chondrites, and the reason for the variation is still not clear. These are the questions that require follow-up investigations, and a better understanding of these issues would significantly improve our understanding of the ubiquitous volatile element depletion of planetary bodies.

Until now, the Rb isotopic system has only been applied to high-temperature volatile loss processes. No study on Rb isotope fractionation under low-temperature conditions such as weathering, or fluid-rock interactions has been performed. Yet, the recent progress on K isotopic measurement method enables some studies on K isotope fractionation under low temperature conditions. Preliminary K isotope data have been reported regarding continental weathering and subduction processes, which have shown large K isotope fractionation. Rb has a very similar bond strength to K, and usually substitutes K in most minerals (except for several minerals such as plagioclase and illite), and thus it can be expected that Rb would be also sensitive to these processes. Using Rb isotopes- potentially coupled with K isotopes- to investigate weathering and

subduction processes would be another exciting future direction, and would provide new insights into these large-scale, important geological processes.

APPENDIX

The following code describes the model used to calculate the nugget effect of chondrules on bulk Rb isotopic compositions of chondrites and was run in Mathematica. Words in blue are comments.

(*chondrule database. total=28 chondrules; first column are chondrule diameters in mm which will be changed to follow a size distribution reported in literature later, second column are K/Al ratios of chondrules normalized to the bulk. The matrix K/Al ratio is assumed to be the bulk value. Third column are δ^{41}K values*)

```
cd = {{0.5, 1.3, -0.4},
  {0.5, 0.43, -0.8},
  {0.5, 0.4, -0.1},
  {0.5, 0.0065, -6.4},
  {0.5, 0.011, 2.4},
  {0.5, 0.397, 0.23},
  {0.5, 0.097, -6.29},
  {0.5, 1.6, 2.28},
  {0.5, 0.088, -3.988},
  {0.5, 0.195, -0.2},
  {0.5, 0.41, 0.133}, (*above and including this line is Bishunpur from Alexander et al., 2000, below is Semarkona from Grossman, 2005*)
  {0.5, 1.65, 2.791},
  {0.5, 2.2, 3.7},
  {0.5, 1.4, 3.75},
```

{0.5, 1.6, 2.2},

{0.5, 1.1, 3.6},

{0.5, 0.075, 9.121},

{0.5, 0.49, 2.9},

{0.5, 0.087, -1.55},

{0.5, 0.45, 5.862},

{0.5, 0.15, -0.05},

{0.5, 0.39, 0.5},

{0.5, 0.062, 8.2},

{0.5, 2.1, 2.043},

{0.5, 2, 8.6},

{0.5, 0.39, -1.4},

{0.5, 0.035, 2.4},

{0.5, 1.6, 0},

{0.5, 0.061, 12.5},

{0.5, 0.12, 2.4},

{0.5, 1.3, 0.8},

{0.5, 1.6, 2.2},

{0.5, 0.086, -1.2},

{0.5, 1.6, 0},

{0.5, 0.0049, -9.5},

{0.5, 0.98, 0.2},

{0.5, 0.385, 5.413},

```
    {0.5, 1.8, 2.7},
    {0.5, 1.65, 6.312}
    };
l = Length[cd[[All, 1]]];
rm = RandomVariate[NormalDistribution[0.72, 0.8], l]; (*0.72, 0.8 are φ-units size distribution from Nelson and Rubin, 2002*)
cd[[All, 1]] = 2^-rm; (*random chondrule diameters in mm*)
cd[[All, 3]] = cd[[All, 3]]/2.2; (*δ41K is converted to δ87Rb*)
cd[[All, 1]] = (4/3)*3.14159*(cd[[All, 1]]/2000)^3*3000000*1000;
(*diameter is converted to mass in mg*)

dav = Total[cd[[All, 1]]*cd[[All, 2]]*cd[[All, 3]]]/Total[cd[[All, 1]]*cd[[All, 2]]];
(*the bulk Rb/Al ratio is calculated. K/Al ratio is used, assuming K/Al is the same as Rb/Al when normalized to matrix*)

cd[[All, 3]] = cd[[All, 3]] - dav; (*δ87Rb in individual chondrules*)
x = 0.7; (*chondrule fraction; the rest is assumed to have bulk composition*)
massmax = 1000; (*approximate maximum mass in mg*)
n = Round[massmax*x / Mean[cd[[All, 1]]]]; (*approximate number of chondrules that need to be added to reach a given mass*)
```

```
m = Table[0, {3}, {n}]; (*Table that contains the output of the simulation; chondrule (and accompanying matrix) are added one by one until n are added and the Rb isotopic composition is calculated*)

(*trj compiles all trajectories*)
tn = 500; (*Number of trajectories calculated*)
trj = Table[0, {tn}, {n}]; (*trj is the y-axis (δ87Rb) of the trajectories*)
xrj = Table[0, {tn}, {n}]; (*xrj is the x-axis (mass) of the trajectories*)

For[j = 1, j <= tn, j++,
 rd = RandomInteger[{1, l}]; (*Initialize with 1st chondrule*)
 m[[1, 1]] = cd[[rd, 1]]/x;(*Mass of chondrule plus matrix*)
 m[[2, 1]] = (1 - x) + x*cd[[rd, 2]]; (*Rb/Al ratio of chondrule plus matrix*)
 m[[3, 1]] = x*cd[[rd, 2]]*cd[[rd, 3]]/((1 - x) + x*cd[[rd, 2]]); (*Rb isotopic composition of chondrule plus matrix*)
 For[i = 2, i <= n, i++,
  rd = RandomInteger[{1, l}];
  m[[1, i]] = m[[1, i - 1]] + cd[[rd, 1]]/x; (*Mass*)
  m[[2, i]] = (m[[2, i - 1]]*m[[1, i - 1]] + cd[[rd, 1]]*cd[[rd, 2]] + cd[[rd, 1]]*(1 - x)/x)/(m[[1, i - 1]] + cd[[rd, 1]]/x); (*Rb/Al*)
  m[[3, i]] = (m[[2, i - 1]]*m[[1, i - 1]]*m[[3, i - 1]] + cd[[rd, 1]]*cd[[rd, 2]]*cd[[rd, 3]])/(m[[2, i - 1]]*m[[1, i - 1]] + cd[[rd, 1]]*cd[[rd, 2]] + cd[[rd, 1]]*(1 - x)/x) (*δ87Rb*)
 ];
```

```
trj[[j, All]] = m[[3, All]];
xrj[[j, All]] = m[[1, All]];
]

(*Calculation of the standard deviation of Rb isotopic composition at each mass*)
sevx = Table[1.0*i*massmax/100, {i, 100}]; (*Masses where the standard deviation will be calculated*)
sevy = sevx*Indeterminate; (*2 *standard deviation*)

For[i = 1, i <= 100, i++,
pol = Position[xrj, x_ /; sevx[[i]] - sevx[[1]]/2 < x < sevx[[i]] + sevx[[1]]/2];
sevy[[i]] = StandardDeviation[Extract[trj, pol]]*2 (*Calculates 2*stdev of the δ87Rb values that fullfill the criterion above*)
];

Show[ (*Plot the results*)
ListLinePlot[#, PlotRange -> {{0, 1000}, {-1, 1}}, PlotStyle -> {{Opacity[0.3], Red, Thin}},
FrameLabel -> {Style["Mass (mg)", Black, FontFamily -> "Helvetica Neue", FontSize -> 22, Bold], Style["δ87Rb (‰)", Black, FontFamily -> "Helvetica Neue", FontSize -> 22, Bold]},
AspectRatio -> 1, Frame -> True, FrameStyle -> Directive[Black, Thick], FrameTicksStyle -> Directive[FontSize -> 18, Black]] &@ Table[Transpose@{xrj[[i]], trj[[i]]}, {i, Length@xrj}],
```

```
ListLinePlot[Transpose[{sevx, sevy}], PlotRange -> {{0, 1000}, {0, 1}}, PlotStyle ->
{Thick, Turquoise}]
]
```